

M0010109+P

Modelling of Freeze Layer Formation and Refractory Wear in Direct Smelting Processes

Andrew Paul Campbell

Ph.D.

December 2002

Thesis
UNIVERSITY OF GREENWICH LIBRARY

Modelling of Freeze Layer Formation and Refractory Wear in Direct Smelting Processes

Andrew Paul Campbell

Centre for Numerical Modelling and Process Analysis
School of Computing and Mathematical Sciences
the University of Greenwich
London, United Kingdom.

A thesis submitted in partial fulfilment of the requirements of the University of Greenwich for the degree of Doctor of Philosophy.

This research programme has been carried out in collaboration with:

Hismelt Corporation Pty. Ltd.

and

the office of the Chief Technologist, Rio Tinto Technology.

December 2002

Copyright © 2002 University of Greenwich

All Rights Reserved. Except as permitted under current legislation, no part of this work may be photocopied, stored in a retrieval system, published, adapted, transmitted, recorded or reproduced in any form or by any means, without the prior permission of the copyright owner. Enquiries should be addressed to the University of Greenwich.

The right of the University of Greenwich to be identified as the author of this work has been asserted in accordance with the Copyright, Designs and Patents Act 1988.

I certify that this work has not been accepted in substance for any degree, and is not concurrently submitted for any degree other than that of Doctor of Philosophy (PhD) of the University of Greenwich. I also declare that this work is the result of my own investigations except where otherwise stated.

Andrew Campbell

ABSTRACT

The work discussed in this thesis is aimed at examining the formation of freeze layers and refractory wear on water-cooling elements within direct smelting processes through the use of computational modelling techniques. The motivation of performing this work is to examine the cooling of regions of the Smelt Reduction Vessel of the HIs melt process closer to the molten bath material. HIs melt is a novel process for the production of pig iron which has been under development by Rio Tinto and is now being commercialised.

The previous work performed in this area has been reviewed with particular focus on the refractory wear mechanisms as the solidification algorithms have been thoroughly implemented within the Computational Fluid Dynamics (CFD) framework PHYSICIA used within this work. The governing equations along with the Finite Volume discretisations of these equations are set out within this thesis. Some comment is made about the solution methods used, and how boundary conditions are implemented. The Free-surface flow and Solidification governing relationships are also described as these are important for investigating the formation of freeze layers.

The implementation of the refractory wear mechanisms are discussed in some detail. The three mechanisms implemented are for the penetration of slag into the refractory, the corrosion of the refractory by this penetrated slag; and the erosion of the refractory by the bulk flow of slag within the furnace. To be able to reasonably predict refractory wear, it is necessary to make the properties of the materials within the system temperature dependent.

During the pilot plant trials at the HIs melt® Research and Development facility, located in Kwinana Western Australia, accretions formed on the end of the solids injection lances. These accretions have been termed Elephant's Trunks. With the imminent construction of the Development Plant which injects the iron bearing feeds at an elevated temperature rather than at ambient temperatures used on the pilot plant, the formation of these pipe-like accretions under both the cold and hot injection conditions have been examined. This work provides confidence that the freeze layers predicted from the model will reflect those formed within the furnace.

To evaluate the effectiveness of the refractory wear mechanisms, data from experimental and the HIsmelt pilot plant have been modelled. Sections of refractory samples from an induction furnace test and a rotary slag test have been modelled. The results are in agreement with the profile and affected regions of the sectioned refractory test pieces. A part of the HIsmelt pilot plant Smelt Reduction Vessel (SRV) has been modelled for the period of campaign 8-1 & 8-2 (just over 20 days). The predicted wear is in agreement with the measurements taken after the vessel had been cooled.

To bring together freeze layer formation with the refractory wear mechanisms, a water-cooled element was modelled for the sloping slag section. The results show the growth of a small freeze layer that is consistent with the small freeze layer seen on the upper cooling panels of the pilot plant SRV. This model is an ideal tool to evaluate different water-cooling strategies for HIsmelt and other similar direct smelting processes.

This work has developed models that predict the formation of freeze layers and refractory wear within direct smelting processes. The models have focused on slag-refractory interactions and further work would be needed to extend the refractory wear models to account for metal-refractory interactions. To examine spalling, stress calculations could be performed to determine when this may occur.

ACKNOWLEDGEMENTS

Firstly I must recognise the support of HIs melt Corporation Pty. Ltd. and RioTinto Technology Development. HIs melt and Rio Tinto Technology Development have kindly financially supported this project. Special mention must be made regarding the support from various employees at various locations throughout the Rio Tinto family.

Rod Dry and Carolyn McCarthy at HIs melt who have provided valuable project guidance and data regarding the operation of the HIs melt HRDF pilot plant.

Chris Cross from the Office of the Chief Technologist, Rio Tinto Technology for his guidance and for the great support by making contact with the various operations within the Rio Tinto group that my research applies to. Mark Davis and Ian Barton-Jones from Rio Tinto Technical Services Limited have provided support and encouragement for this work.

Françoise Cardarelli from Rio Tinto Iron and Titanium in Tracy, Quebec Canada for supplying the rotary slag test information.

My supervisors for this project, Professor Mark Cross and Professor Koulis Pericleous, for providing support and bringing their experience to this project which is very much appreciated. Nick Croft has provided much support with the CFD code PHYSICA used in this research.

Finally I must thank my wife, Wendy, for her support whilst completing my PhD.

TABLE OF CONTENTS

ABSTRACT	V
ACKNOWLEDGEMENTS	VII
TABLE OF CONTENTS	IX
LIST OF FIGURES	XIII
LIST OF TABLES	XVII
NOMENCLATURE	XIX
INTRODUCTION	1
1.1 THE HISMELT® PROCESS	1
1.2 MODELLING OF THE HISMELT PROCESS	5
1.2.1 Bath Model.....	5
1.2.2 Top-space Model.....	7
1.2.3 Application of Modelling Results	8
1.3 OBJECTIVES OF THE RESEARCH PROGRAMME	8
1.4 PHYSICS INVOLVED	11
1.5 REVIEW OF RELEVANT WORK	11
1.5.1 Refractory Wear	11
1.5.2 Furnace Design and Freeze Layer Formation	27
1.5.3 Previous Modelling of Refractory Wear	30
1.6 PHYSICAL PROPERTIES	30
1.6.1 Slag Viscosity.....	31
1.6.2 Slag Surface tension and Contact Angle	31
1.6.3 Phase Equilibria Calculations	32
1.7 OUTLINE OF WORK.....	33
COMPUTATIONAL MODELLING FRAMEWORK	35
2.1 GOVERNING EQUATIONS	35
2.1.1 Finite Volume Discretisations of Governing Equations	37
2.2 DIFFERENCING SCHEMES	43
2.2.1 Two Point Schemes	44
2.2.2 Higher Order Schemes	49

2.2.3	Concluding Remarks	52
2.3	BOUNDARY CONDITIONS	52
2.3.1	Fixed Value	53
2.3.2	Fixed Flux	54
2.3.3	Constant Pressure Boundaries	54
2.4	SOLVERS	54
2.4.1	Explicit and Semi-implicit Treatment	54
2.4.2	Pressure – Velocity Coupling	58
2.4.3	Unstructured Code	59
2.5	FREE-SURFACE	60
2.5.1	Donor-Acceptor Method	60
2.5.2	GALA	61
2.5.3	Stability	61
2.6	SOLIDIFICATION	61
2.6.1	Liquid Fraction	62
2.6.2	Heat Sources	62
2.6.3	Momentum Sources	63
IMPLEMENTATION OF REFRACTORY WEAR MECHANISMS.....		65
3.1	REFRACTORY WEAR MECHANISMS	65
3.1.1	Penetration	66
3.1.2	Corrosion	70
3.1.3	Erosion	74
3.2	THE DYNAMIC DOMAIN	75
3.2.1	Refractory Presence Momentum Sink Term	76
3.3	TIMESCALES	77
3.3.1	Flow	77
3.3.2	False Time-stepping	78
3.3.3	Reactions	78
3.4	PHYSICAL PROPERTIES	78
3.4.1	Materials	78
3.4.2	Density	81
3.4.3	Viscosity	81
3.4.4	Thermal Conductivity	81
3.4.5	Specific Heat	82
3.4.6	Refractory Properties	82
3.4.7	Slag Properties	83
FREEZE LAYER APPLICATION: HISMELT ELEPHANT TRUNKS.....		91
4.1	DESCRIPTION OF THE PROCESS	91
4.2	DATA GATHERING	92

4.3	MODEL FORMULATION.....	93
4.3.1	Domain.....	93
4.3.2	Jet Expansion.....	94
4.3.3	Boundary Conditions.....	95
4.3.4	Cases Examined.....	97
4.4	VERIFICATION OF ASSUMPTIONS.....	98
4.4.1	Mesh Refinement.....	98
4.4.2	Interface Heat Transfer.....	99
4.5	RESULTS AND DISCUSSION.....	102
4.6	CONCLUDING REMARKS.....	106
VALIDATION OF REFRACTORY WEAR MODELS.....		107
5.1	INDUCTION FURNACE TEST.....	107
5.1.1	Description of the Process.....	107
5.1.2	Data Gathering.....	108
5.1.3	Experimental Setup.....	109
5.1.4	Model Formulation.....	110
5.1.5	Verification of Assumptions.....	111
5.1.6	Results and Discussion.....	112
5.1.7	Conclusions.....	114
5.2	HISMELT HRDF PILOT PLANT RESULTS.....	115
5.2.1	Experimental Setup.....	115
5.2.2	Data Gathering.....	116
5.2.3	Model Formulation.....	118
5.2.4	Verification of Assumptions.....	122
5.2.5	Results and Discussion.....	124
5.2.6	Concluding Remarks.....	126
APPLICATION TO SIMILAR SMELTING PROCESSES.....		127
6.1	DESCRIPTION OF THE PROCESS.....	127
6.2	EXPERIMENTAL SETUP.....	128
6.2.1	Slag and Refractory Chemistry Considerations.....	129
6.3	DATA GATHERING.....	131
6.4	MODEL FORMULATION.....	132
6.4.1	Free-surface.....	132
6.4.2	Mesh Considerations.....	135
6.4.3	Simulation Time.....	136
6.4.4	Model Simplification.....	136
6.4.5	Free-surface Location.....	137
6.4.6	Shear.....	138
6.4.7	Temperature.....	139

6.5	VERIFICATION OF ASSUMPTIONS	140
6.6	RESULTS AND DISCUSSION	144
6.7	CONCLUDING REMARKS.....	146
APPLICATION OF REFRACTORY WEAR AND FREEZE LAYER MODELLING		147
7.1	OBJECTIVES OF MODELLING THE WATER-COOLED STAVE.....	147
7.2	WATER-COOLED ELEMENTS.....	147
7.2.1	Dynamic Nature of the Process	148
7.3	MODEL FORMULATION.....	149
7.4	OBSERVED RESULTS.....	151
7.5	BOUNDARY CONDITIONS.....	152
7.6	RESULTS AND DISCUSSION	152
7.6.1	Sensitivities.....	156
7.7	CONCLUDING REMARKS.....	158
CONCLUSIONS.....		159
8.1	SUMMARY OF FINDINGS	159
8.2	RESEARCH ACHIEVEMENTS	160
8.3	LIMITATIONS OF THE WORK	161
8.4	FUTURE WORK	161
8.4.1	Application to Other Refractory Slag Systems	162
8.4.2	Application to Metal.....	162
8.4.3	Spalling Mechanisms	162
8.4.4	Alternative Cooler Designs	163
8.4.5	Investigate Heat Pipe Technology.....	163
8.4.6	Porous Flows	164
8.5	CONCLUDING REMARKS.....	164
GLOSSARY.....		165
APPENDICES		167
A	HISMELT COMMERCIAL DEVELOPMENT PLANT	168
A1	General Flowsheet Arrangement.....	168
A2	Pre-treatment	170
A3	Off-gas Treatment	173
A4	Energy recovery and re-use	173
B	CD-ROM CONTENTS.....	175
REFERENCES		177

LIST OF FIGURES

Figure 1.1 – The Development timeline for the HIs melt Process	2
Figure 1.2 – The Horizontal Smelt Reduction Vessel ²	3
Figure 1.3 – The Vertical Smelt Reduction Vessel ³	4
Figure 1.4 – A Conceptual 3-D View of the Commercial HIs melt development plant	4
Figure 1.5 – The Various Stages of the Coal Particles’ Traverse of the Bath.....	6
Figure 1.6 – The Post-combustion Reactions ²	8
Figure 1.7 – HIs melt HRDF Vertical SRV showing a water-cooled stave	9
Figure 1.8 – Plan view of the Pipe layout for water-cooled stave depicted in Figure 1.7 ¹⁹ ..	10
Figure 1.9 – Magnesite Chrome Ore (left) and resultant fired refractory product (right)	12
Figure 1.10 – Schematic Representation of Penetration	13
Figure 1.11 – Penetration and Corrosion behaviour for a steelmaking slag with the various specimens tested by Yu et al. ²⁸	16
Figure 1.12 – Penetration and Corrosion behaviour for various slags tested against a MgO refractory after Yu et al. ²⁸	16
Figure 1.13 – Schematic Representation of Corrosion.....	17
Figure 1.14 – Schematic Representation of Erosion.....	22
Figure 1.15 - Flow observed by Sandhage and Yurek ³² in their rotating cylinder work.	22
Figure 1.16 – Button or Sessile Drop Test	25
Figure 1.17 – Crucible, Cavity, Cup or Brick Test	25
Figure 1.18 – Dipping, Immersion or Finger Test.....	25
Figure 1.19 – Induction Furnace Test.....	26
Figure 1.20 – Rotary Slag Test Apparatus Showing the Main Cylinder.....	27
Figure 1.21 - Comparison of Heat Fluxes for various Water-cooling Systems ⁵¹	29
Figure 2.1 – Mesh Terminology	36
Figure 2.2 – Divergence Theorem Representation.....	38
Figure 2.3 - Non-Orthogonal Control Volume	40
Figure 2.4 – Control Volume for steady one-dimensional convection and diffusion illustration	44
Figure 2.5 – Value for ϕ calculated from the Exact Solution for various Peclet Numbers..	47
Figure 2.6 – Comparison of the different Differencing Schemes’ Accuracy.....	49
Figure 2.7 – Control Volume for Van Leer Scheme	51

Figure 2.8 – Boundary condition applied to a control volume	53
Figure 2.9 – Control Volume for unsteady one-dimensional conduction.....	55
Figure 2.10 – Illustration of how latent heat can be applied to Specific Heat	63
Figure 3.1 – Flowchart for Refractory Mechanisms	66
Figure 3.2 – Flowchart for the Penetration Calculation.....	68
Figure 3.3 – Location Vectors	69
Figure 3.4 – MTDATA plot of phases present against temperature	71
Figure 3.5 – Comparison of Arrhenius and Linear Scaling Functions	72
Figure 3.6 – Flowchart for the Corrosion Calculation.....	73
Figure 3.7 – Flowchart for the Erosion Calculation.....	74
Figure 3.8 – Measured Thermal Conductivity Values	82
Figure 3.9 – Measured and Fitted Surface Tension Values.....	83
Figure 3.10 – MTDATA plot of Solid and Liquid Phase Totals for Hlsmelt Slag.....	84
Figure 3.11 – Equation used for Contact Angle	85
Figure 3.12 - Slag Viscosity Measurements by Zhang and Jahanshi ⁷⁶	85
Figure 3.13 - Revised Viscosity Relationship	86
Figure 3.14 - Comparison of Original and Revised Viscosity Equations	87
Figure 3.15 - Induction Furnace results for the Original and revised Viscosity Relationships	88
Figure 3.16 - Adjustment Made to Contact Angle	89
Figure 3.17 - Results after Revising Contact Angle Relationship.....	90
Figure 4.1 - Trunk Formation.....	91
Figure 4.2 - Injection Lance Arrangement in the Hlsmelt Vessel.....	92
Figure 4.3 - Lance General Arrangement	93
Figure 4.4 – Axi-symmetric Wedge Domain	94
Figure 4.5 – Computational Domain and Mesh Regions	94
Figure 4.6 – Liquid Fraction Contours for Fixed Interface Temperature for the HRDF case	96
Figure 4.7 - Lance Dimensions	97
Figure 4.8 - Standard Mesh.....	98
Figure 4.9 - Mesh Refinement Results.....	99
Figure 4.10 - 600°C Temperature Rise, HRDF case	100
Figure 4.11 - HRDF cold injection liquid fraction contours	102
Figure 4.12 – HRDF cold injection temperature contours	102
Figure 4.13 - 6m cold injection liquid fraction contours	103
Figure 4.14 – 6m Cold Injection Temperature Contours	103

Figure 4.15 - 6m hot injection liquid fraction contours.....	104
Figure 4.16 – 6m Hot injection Temperature Contours	104
Figure 4.17 - Transient Nature of 6m Hot Case	105
Figure 4.18 - Trunk Growth Comparison.....	106
Figure 5.1 – Induction Furnace Schematic	107
Figure 5.2 – Results from the Induction furnace Test.....	108
Figure 5.3 – Results from the Induction furnace Test for the Magnesium-Chrome Refractory Indicating the location of the Slag; Metal and Extent of affected Refractory.....	109
Figure 5.4 – Section of the Induction furnace that is modelled.....	110
Figure 5.5 – Schematic of the Model	110
Figure 5.6 – Total Mesh View.....	111
Figure 5.7 – Comparison of Results with various mesh sizes.....	112
Figure 5.8 – Comparison of Results with different inflow conditions	112
Figure 5.9 – Model Results after running for 5 hours with the results of the induction furnace test (inset picture).....	113
Figure 5.10 – Rate of Penetration at the centre of the domain with Respect to time	113
Figure 5.11 – Metal and Slag Chemistry for Campaign 8-1 ³	116
Figure 5.12 – Refractory Wear Measurements after Campaign 8-2	117
Figure 5.13 – Bath Model results Supplied by Mark Davis	119
Figure 5.14 – Mesh of HIs melt HRDF pilot plant model indicating the slag flow boundary conditions	120
Figure 5.15 – General Bath Flow pattern on Bath Model Results	121
Figure 5.16 – Liquid Turbulent Viscosities Supplied by Mark Davis	122
Figure 5.17 – Refractory Wear Contour Sensitivity to Inflow Boundary Condition.....	123
Figure 5.18 – Refractory Wear Contour Sensitivity to Mesh Density.....	124
Figure 5.19 – Predicted Refractory wear for Campaign 8-2 compared to measured results.	125
Figure 6.1 – Rotary Slag Test Arrangement.....	127
Figure 6.2 – Test Piece Dimensions	128
Figure 6.3 - FACT calculation for the RTIT Slag.....	130
Figure 6.4 - FACT calculation for the Marcast refractory	130
Figure 6.5 - FACT calculation for 90% Marcast Refractory with 10% RTIT Slag.....	131
Figure 6.6 – Picture of the MARCAST 561 SP Sample tested with Molten Slag after Sectioning.	132
Figure 6.7 – Picture of the MARCAST 561 SP Sample tested with Molten 4.5% Carbon Metal after Sectioning.	132
Figure 6.8 – Free-surface Rotating Gravity Vector.....	134
Figure 6.9 – Mesh developed for the Rotary Slag Test that follows the refractory location	135

Figure 6.10 – Mesh developed for the Rotary Slag Test showing the initialised location of the refractory (shaded black).....	136
Figure 6.11 – Free-surface Location.....	137
Figure 6.12 – Co-located Averaged Shear Values.....	139
Figure 6.13 – Temperature Conditions for the Rotary Slag Test.....	140
Figure 6.14 – Standard (red) and Double Density Mesh (green).....	141
Figure 6.15 – Standard (red) and Half Density Mesh (blue).....	141
Figure 6.16 – Standard (red) and $\frac{3}{4}$ Density Mesh (black).....	141
Figure 6.17 – 0.5 Refractory Contours for the Mesh Sensitivity Cases.....	142
Figure 6.18 – 0.5 Penetration Contours for the Mesh Sensitivity Cases.....	143
Figure 6.19 – Temperatures taken down the centre of the meshes.....	144
Figure 6.20 – Result from Rotary Slag Test.....	145
Figure 7.1 – Various Refractory Retaining Techniques.....	148
Figure 7.2 - Schematic of the Area of the Vessel Modelled.....	150
Figure 7.3 - Schematic of the extent of the Computational Domain.....	150
Figure 7.4 - Schematic of the Mesh Developed for the Water-Cooled Stave Model.....	151
Figure 7.5 – Progression of Wear Around Cooling Pipes over time.....	152
Figure 7.6 - Results after running model for simulated 10 days with an elevated temperature of 1923K.....	153
Figure 7.7 - Temperature Profile at a height of 4.3m after 10 days at 1923K and a further 2 days at 1723K.....	154
Figure 7.8 - Results after running model for a further 2 days at normal operating temperature of 1723K.....	155
Figure 7.9 – Growth of Freeze Layers with respect to Time.....	155
Figure 7.10 – Refractory locations for the various meshes tested after 10 days at the elevated temperature of 1923K.....	156
Figure 7.11 – View of the Base Case and Coarse Mesh results for Penetration.....	157
Figure 7.12 - Effect of different in-flow boundary condition model on refractory position after running model for 10 days at 1923K.....	158
Figure 8.1 - General Arrangement of the HIs melt Flowsheet.....	168
Figure 8.2 – Process Flow Diagram for the Commercial HIs melt development plant.....	169
Figure 8.3 – Proposed HIs melt Commercial Development Plant Layout.....	170

LIST OF TABLES

Table 2.1 - Definition of Terms in the Generic Transport Equation.....	37
Table 2.2 – A(P) Function for the different schemes.....	49
Table 2.3 – Values for the Integral of T_p for various weighting factors	56
Table 2.4 – CFL Limits for different dimensionalities.....	58
Table 3.1 – Slag Compositions	79
Table 3.2 – Refractory Compositions	80
Table 3.3 – Values used for Material Properties	81
Table 4.1 - Lance Dimensions for the various cases (in meters).....	98
Table 4.2 - Injection Velocities for the Various Cases.....	98
Table 4.3 – Calculation Quantities	100
Table 4.4 – Jet Temperature Rise	101
Table 6.1 – RTIT Slag Composition	129
Table A.1 – Direct Reduction Processes ¹³⁰	172
Table B.1 – Publication List.....	175
Table B.2 – Summary of Models Included on the CD-ROM.....	176

NOMENCLATURE

Roman Letters

A	Area	m^2
<u>A</u>	System Matrix	
C	Constant	
C_p	Specific Heat	$\text{J.kg}^{-1}\text{K}^{-1}$
CV	Control Volume	
C	Concentration	kg.m^{-3}
D	Hydraulic Diameter	m
D	Diffusion Coefficient	m^2s
E	Energy	J
F	Convection Coefficient	
<u>F</u>	Vector Field	
H	Enthalpy	J
J	Dissolution Rate	$\text{kg.m}^{-2}\text{s}^{-1}$
K	Permeability Coefficient	m^2
L	Latent Heat	J.kg^{-1}
M	Molecular Weight	g.mol^{-1}
P	Pressure	Pa
Q	Energy Transfer	W.m^{-2}
R	Universal Gas Constant	$8.314 \text{ J.mol}^{-1}\text{K}^{-1}$
S	Source	
S	Surface	m^2
T	Period	s
T	Temperature	K
V	Volume	m^3
<u>b</u>	Source Vector	
d	Distance	m
e	Natural Logarithm	2.718281
f	Fraction	
h	Heat Transfer Coefficient	$\text{W.m}^{-2}\text{K}^{-1}$
k	Reaction Rate	s^{-1}
k	Thermal Conductivity	$\text{W.m}^{-1}\text{K}^{-1}$
l	Length	m
\dot{m}	Mass Rate	kg.s^{-1}
n	Normal	

\underline{n}	Unit Outward Normal	
\underline{p}	Penetration Vector	
\underline{q}	Flow Rate	$\text{m}^3 \text{s}^{-1}$
r	Radius	m
t	Time	s
u	Velocity	$\text{m} \cdot \text{s}^{-1}$
\underline{u}	Velocity Vector	$\text{m} \cdot \text{s}^{-1}$
x	Distance, direction x-axis	m
y	Distance, direction y-axis	m
z	Distance, direction z-axis	m

Greek Letters

Γ	Diffusion Coefficient	
α	Interpolation Factor	
γ	Surface Tension.....	$\text{N} \cdot \text{m}^{-1}$
δ	Centre-face distance	m
δ	Boundary layer thickness	m
θ	Contact Angle.....	$^\circ$
μ	Dynamic Viscosity	$\text{kg} \cdot \text{s}^{-1} \text{m}^{-1}$
ν	Kinematic Viscosity.....	$\text{m}^2 \text{s}^{-1}$
ζ	Time-Temperature Integral	$\text{m} \cdot \text{s}^{-1}$
π	Mathematical Constant.....	3.141592654
ρ	Density	$\text{kg} \cdot \text{m}^{-3}$
τ	Shear Stress	$\text{N} \cdot \text{m}^{-2}$
ϕ	Solved Variable/Quantity	

Sub-scripts

A	Adjacent Element
C	Constant
D	Darcy
E.....	Control Volume to the East
O	Old/Previous Value
P.....	Current Element
P.....	Proportional Component
S.....	Surface
V	Volume
W	Control Volume to the West
e	Face between the Current and East Control Volumes
f.....	Face
i.....	Element Number
l.....	lower

- s..... solid
u..... upper
w Face between the Current and West Control Volumes
 δ Centre-face distance
 ϕ Solved variable

Super-scripts

- O Old/Previous Value
W Weymann Equation pre-exponential term

Mathematical Operators

- %..... Modulus
 ∂ Partial Differential
 Δ Gradient, rate of change
 ∇ Divergence
 Σ Summation
 $\sqrt{\quad}$ Square Root

Dimensionless Groups

- CFL..... Courant, Friedrichs, Lewy Number
Nu Nusselt Number
Pe..... Peclet Number
Re..... Reynolds Number

The work discussed in this thesis is aimed at examining the formation of freeze layers and refractory wear on water-cooling elements within direct smelting processes through the use of computational modelling techniques. The motivation of performing this work is to examine the cooling of regions of the Smelt Reduction Vessel of the HIs melt process closer to the molten bath material. HIs melt is a novel process for the production of pig iron which has been under development by Rio Tinto and is now being commercialised.

1.1 The HIs melt® Process

The iron making industry has attempted to produce iron by the direct smelting of iron ore and ground coal for many years. Brotzmann¹ advocated the use of Post Combustion (PC) for emerging direct smelting processes that would compete with the traditional blast furnace approach. Brotzmann also noted that there is a price to be paid for the amount of preparatory work required to produce coke and sinter, along with the environmental problems that need to be mastered in the production of these blast furnace feed stocks.

The core of the HIs melt process works by smelting ground ore and coal in a molten metal bath. The reduction reactions occurring within the bath produce gases, predominantly Carbon Monoxide and Hydrogen, which along with the nitrogen injection carrier gas eject metal and slag into the gas reaction space above the bath in the form of droplets. In this gas space the gases produced in the reduction of the ore react with the oxygen in the Hot Air Blast (HAB) from the top space tuyeres. These exothermic reactions (called Post Combustion) provide thermal energy which is transferred to the droplets of slag and metal which fall back to the bath – providing the bath the energy it requires to sustain the reduction of ore.

The HIs melt process has been under development for approximately twenty years² and it has primarily been supported by Rio Tinto. The process was originally based on the K-OBM and KMS steelmaking processes of Klöckner-Werke. The smelt reduction concept was successfully tested in a 60t OBM converter, and a small scale pilot plant was designed and built at Klöckner's Maxhütte steelworks in southern Germany.

Figure 1.1 shows the timeline for the various stages of development for the process, in particular from the late 1980's and early 1990's the HIs melt Research and Development Facility (HRDF) was constructed to test a larger scale vessel, in Kwinana Western Australia. The first Smelt Reduction Vessel (SRV), a horizontal rotating vessel as illustrated in Figure 1.2, suffered from high refractory wear in the region of the hot blast jet³. This horizontal vessel nevertheless demonstrated that it was possible to obtain good post combustion from such a smelting process. Novel techniques were developed that are fundamental to the vessels that have been subsequently developed – in particular the swirling HAB Tuyere and top injection of ore and other solid raw materials.

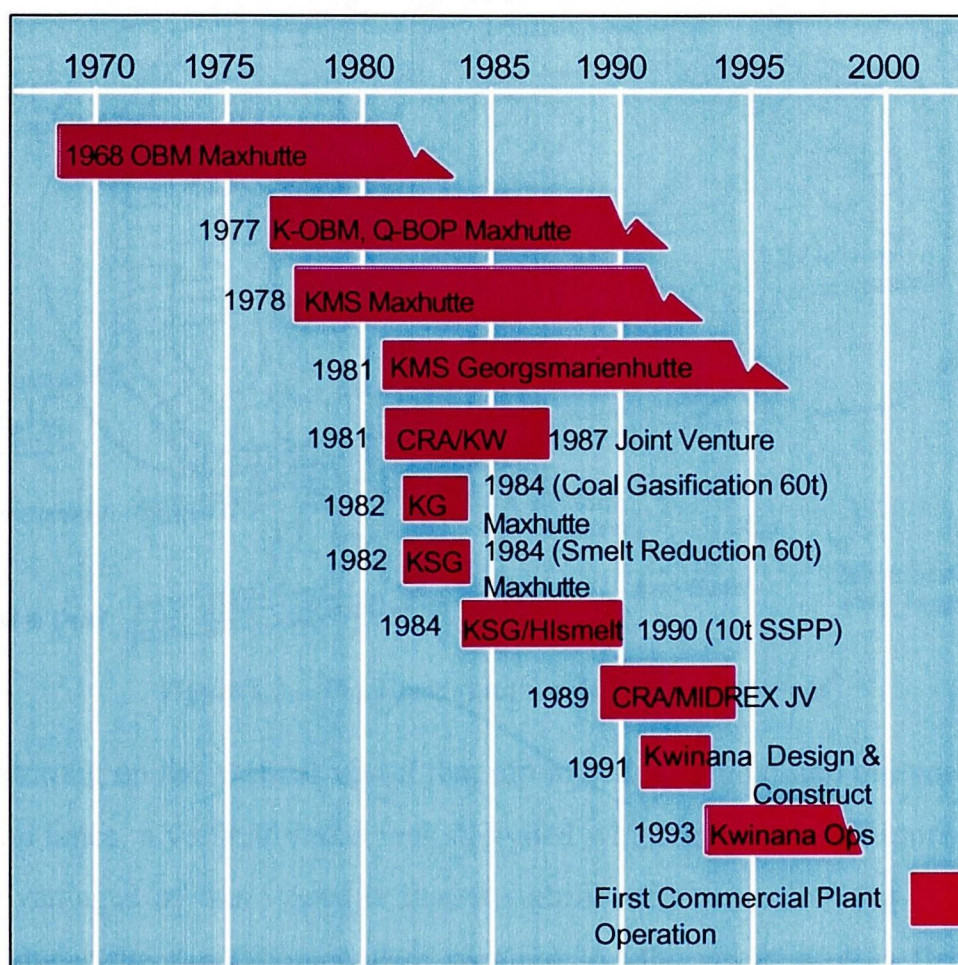


Figure 1.1 – The Development timeline for the HIs melt Process⁴

One important point to understand about the horizontal vessel is the use of bottom injection of the coal and ore into the bath. This then necessitated that the vessel should be able to rotate to move the bottom tuyeres clear of the molten bath material for maintenance. Water-cooling could not be applied to the vessel as it would become submerged when the furnace is rotated.

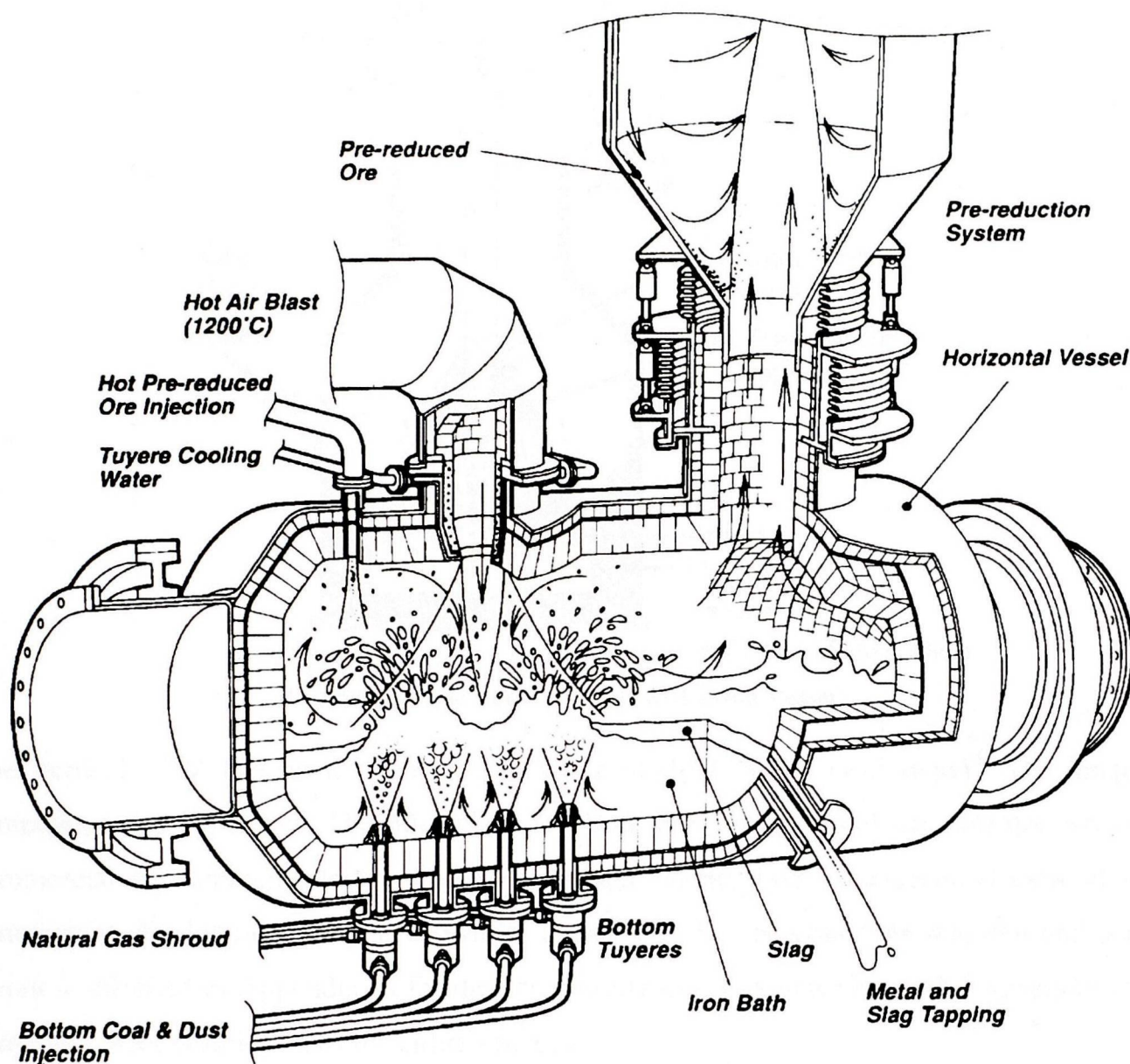


Figure 1.2 – The Horizontal Smelt Reduction Vessel²

After demonstrating on the vertical vessel that top injection of coal and ore was possible using a side injection lance, a vertical vessel was designed which is shown in Figure 1.3. One of the significant advantages of this vessel is that it significantly simplifies the engineering of the design and reduces the capital investment required. As the vessel now is fixed in place, the top part of the vessel is water-cooled – the area of significant wear in the operation of the horizontal vessel.

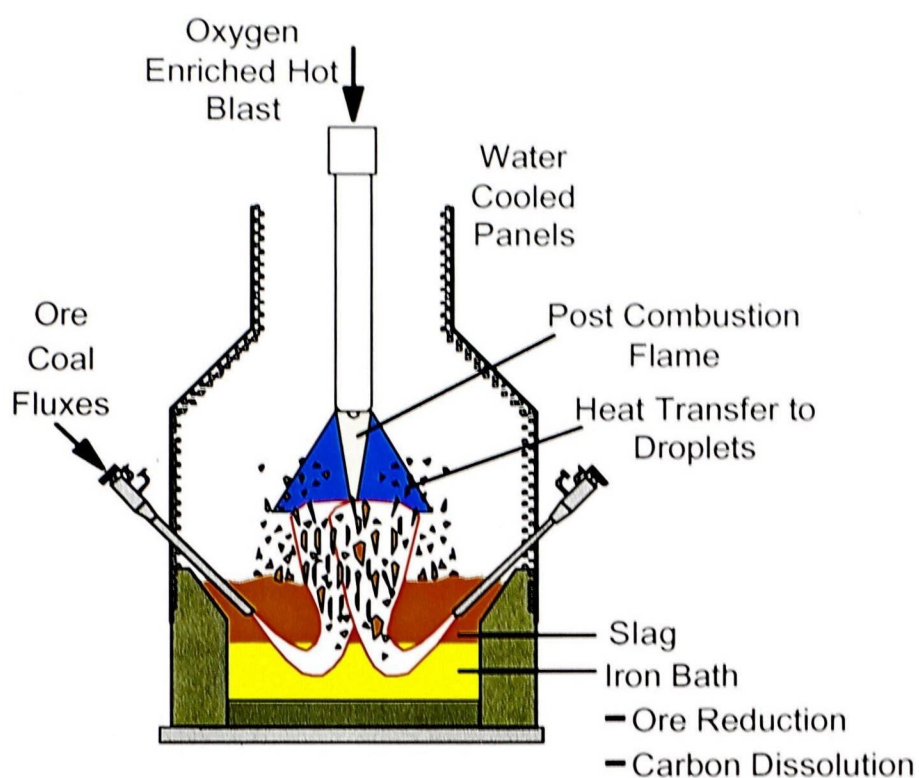


Figure 1.3 – The Vertical Smelt Reduction Vessel³

The vertical SRV has been operated in excess of 3000 hours (132 days)⁵. The longest campaign ran for 38 days. The pilot plant has been put into care and maintenance whilst a commercial development plant is under design and construction. A conceptual view of the commercial development plant is shown in Figure 1.4. The process flow diagram and plant layout is attached in Appendix A for the commercial development plant. This appendix also contains a brief description of the entire process.



Figure 1.4 – A Conceptual 3-D View of the Commercial Hismelt development plant⁶

The refractory used in the horizontal vessel is a Magnesia-Chrome refractory pre-fired brick manufactured by Vietsch-Radex in Austria. Within the vertical SRV design this refractory is used for the hearth region and the sloping section up to the side wall water-cooled panels. The

panels have a high Chromia content castable slip cast around them. Due to the restrictions in North America on the disposal of these bricks, due to the carcinogenic links⁷ made with Cr^{6+} - the only chromium ion soluble in water. It is possible to limit the formation of Cr^{6+} by adjusting the slag chemistry and the cooling rate of the refractory⁸.

1.2 Modelling of the Hismelt Process

Computational modelling techniques have been used extensively in the design, control and optimisation phases in each stage of the development of the Hismelt process. A summary of this computational modelling has been written by Davis et al.². The modelling work was initially undertaken by a group of workers at CHAM, and more recently at Rio Tinto Research and Technology; CSIRO Division of Minerals; and the University of Greenwich⁹.

The modelling has focused on the core smelting unit of the process. To make the modelling task manageable, the process has been partitioned into three distinct zones. These zones have been named as:

- Bath Zone
- Transition Zone
- Top-space

The bath zone, as the name suggests, refers to the molten bath of metal and slag. The top-space identifies the continuous gas space at the top of the vessel. The area located between these two zones has a significant amount of liquid iron and slag running through the gas, and is therefore named the transition zone. The various zones allow for specific models to be employed in each area to properly account for the different physical and chemical effects.

As a significant amount of gas is injected into the bath, along with the gases evolved from the reduction and coal devolatilisation processes, the bath is highly mixed. The modelling of this region was more involved as modelling techniques needed to be developed for this region of the process. An artificial split was introduced to allow two models to be developed: a Bath model for the mixing, reduction and devolatilisation; and a top-space model to model the gas space above the bath that also includes the transition zone. The split, even though there is no distinct boundary in the process, allowed the development of the process to proceed.

1.2.1 Bath Model

The bath contains many phases: gas; liquid metal, liquid slag, particles of coal and ore of various sizes. The gas and liquid phases are modelled using an Eulerian - Eulerian technique.

This technique treats the gas and liquid phases as a continuum mathematically. The volume fraction of each phase is calculated across the domain. The small scale structure is smoothed over to make the calculation feasible using current computing power. However, the smaller scale bubble structure is important for heat and mass transfer considerations and is accounted for with sub-grid models¹⁰.

Inter-Phase-Slip Algorithm¹¹ (IPSA) developed by Spalding is used to distinguish between the metal and slag phases within the “liquid” phase. Lagrangian particle tracking is used to monitor the location of the solid particles (mainly coal and ore) through the bath. Source terms are added into the momentum and continuity equations to account for the injection of this material and the gas evolved by the material as it is rapidly heated. Figure 1.5 shows how particles move through the bath and the various mechanisms that are involved.

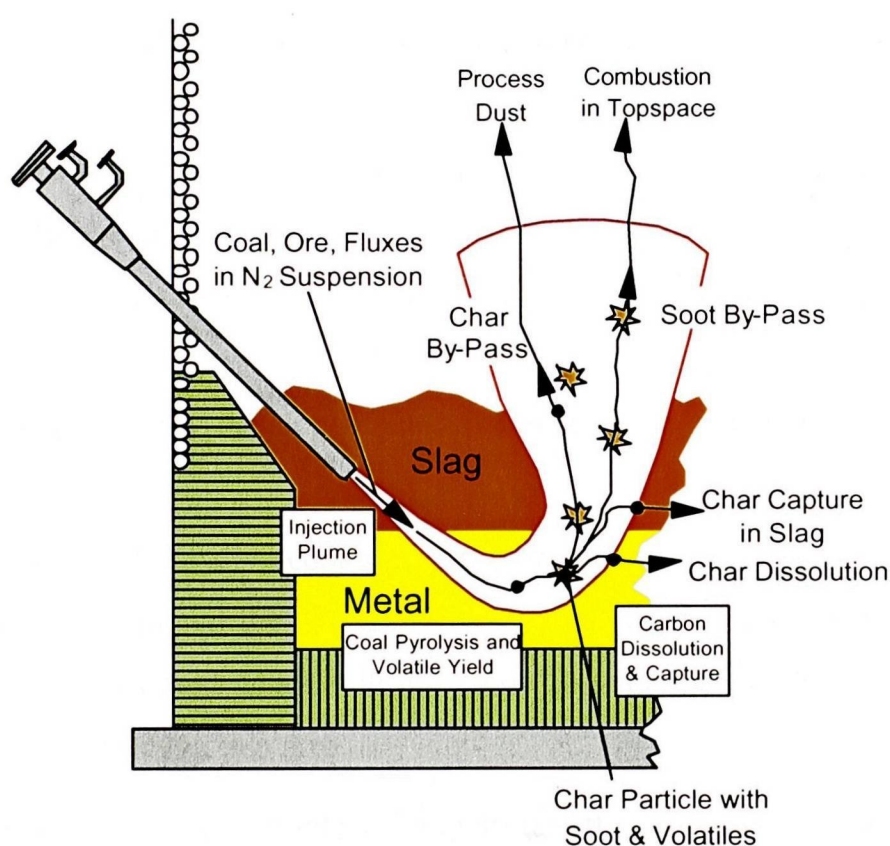


Figure 1.5 – The Various Stages of the Coal Particles' Traverse of the Bath¹²

There are several benefits from the motion of the gas through the bath. A large scale recirculation is set up by the large volumes of gas moving upward in the bath. This provides for excellent mixing of the bath. Additionally, large flow rates of gas that cause channelling in the liquid leads to the generation of splash of the metal and slag into the gas space above the bath. This material is important as it is the primary mechanism for the transport of energy from the top gas reacting space back to the bath.

To model the complexity of the bath, a full three dimensional model has been developed^{2,10,13,14}. To obtain information regarding the important features of the bath, transient runs are required. The model has been validated against water models, and small scale iron and tin¹⁵ bath models. The bath model gives important predictions of the general flow pattern within the bath and top-space. By necessity the location of the gas plumes and the droplets of metal and slag are also calculated.

1.2.2 Top-space Model

The top-space model has been developed^{16,13} to model the gas space above the bath, including the reactions (Figure 1.6), heat and mass transfer that are occurring in this region of the process. To simplify the model formulation, five sub models have been developed²:

- a turbulent reacting gas space model;
- a Lagrangian particle tracking formulation for the treatment of the liquid phase;
- a model of the heat and mass transfer between the two phases due to combustion;
- a two-phase six-flux radiation model to calculate radiant fluxes^{17,18}; and
- a specifically developed gas turbulence model for regions with high swirl.

The top-space model additionally accounts for the transition zone – the region where droplets of metal and slag have entered the top ‘gas space’ above the bath. The surface of the bath is likely to have fingers of liquid which will not be diffuse enough to allow the continuous flow of the top space gases through this area.

Due to the ballistic nature of the droplets flying around the top space, it is inappropriate to use a single velocity within each cell for these droplets – this would be taking an Eulerian - Eulerian or ‘two fluids’ approach. Rather the droplets are modelled using Lagrangian particle tracking techniques. The break-up of droplets is determined by testing against a critical Weber number, and the droplet is reduced in size if a break-up event has occurred. Additionally the decarburisation of the droplets is also considered and is controlled by gas boundary layer diffusion.

The top air tuyeres use swirl to increase post combustion with only a minor sacrifice being made with heat transfer efficiency. The swirl also softens and spreads the jet to create a larger

area where the gases produced by the smelting reactions in the bath are post combusted. The location of the jet is influenced by various factors and the top space model allows it's location to be optimised to maximise the performance of the process.

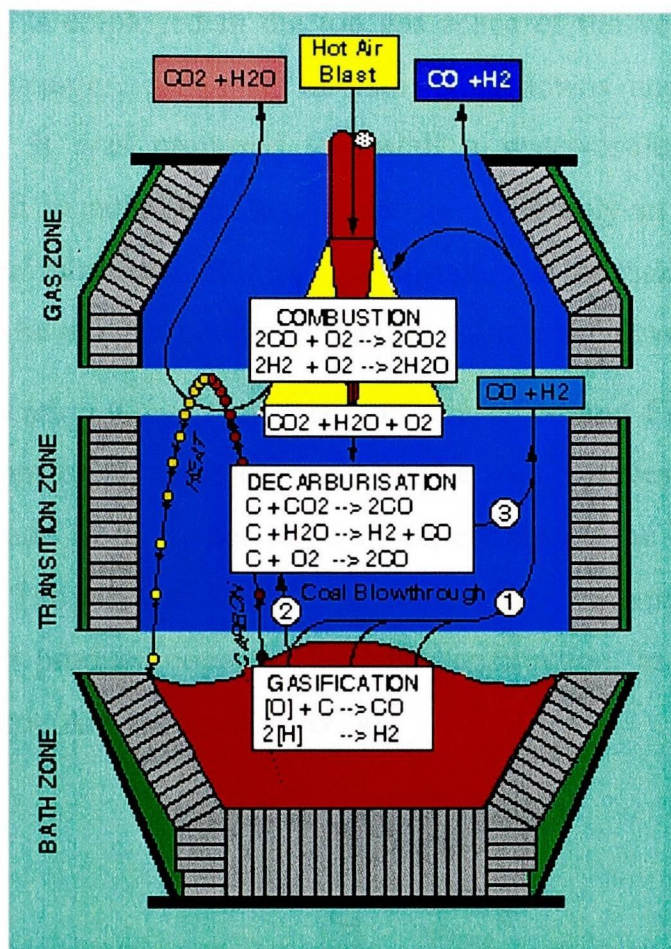


Figure 1.6 – The Post-combustion Reactions²

1.2.3 Application of Modelling Results

The results of the modelling provide further information in the design and operation of the SRV. In particular the distribution of mass within the fountain of droplets is critical in determining the post combustion and heat transfer efficiency within the top-space model. The models are an important design tool: to guide the placement of the injection lances; the locating of tap-holes; and scaling plant design from the pilot plant scale to the full sized commercial development plant.

1.3 Objectives of the Research Programme

During the operation of the pilot plant, the sloping refractory region above the hearth was slowly wearing away. It is projected that this part of the lining will need to be replaced after approximately a year. To replace the refractory will involve shutting the plant down for several weeks to remove the spent lining, install and pre-heat the new lining. The ultimate aim

is to minimise, or if possible eliminate, the refractory wear in this region. One possible solution is to install water-cooled elements into this region.

In the design of the vertical SRV, that has been successfully operated on a pilot plant scale, extensive water-cooling is employed in the top gas space of the vessel. This water-cooling operated for many campaigns, subjected to many shut-downs and start-ups without any operational difficulties. It was proposed to install a water-cooled stave in the sloping refractory section, which is called the “slag zone” (as it is only in contact with slag). The staves were designed and fabricated, although not installed as the risk involved with installing them was determined to be too great at that particular point in the development of HIs melt.

Figure 1.7 shows the location where they were to be installed and Figure 1.8 shows in more detail how they were constructed from copper pipe. Generally staves are constructed in solid blocks or plates and made from copper or steel, depending on the heat loads that they are expected to experience. The block and plate type coolers are commonly used in blast furnaces and in flash smelters to produce copper. The pipe construction, as employed currently by HIs melt, is used in Electric Arc Furnaces (EAF's).

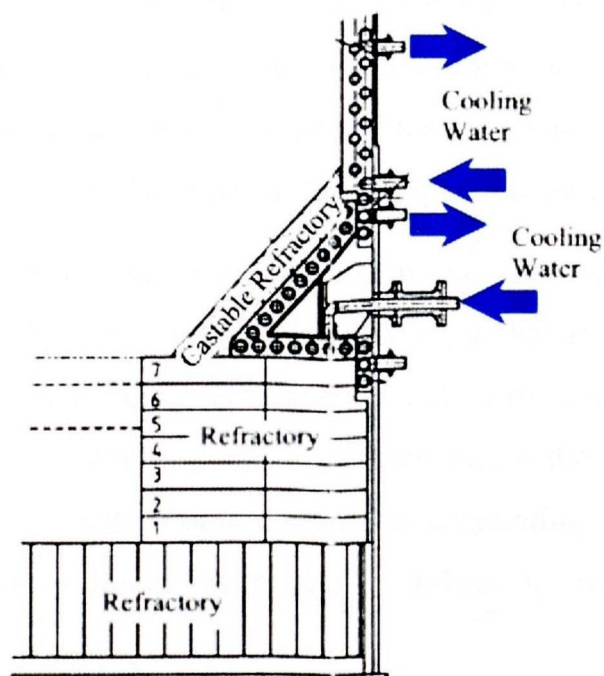


Figure 1.7 – HIs melt HRDF Vertical SRV showing a water-cooled stave ¹⁹

It is commonplace when using water-cooling in smelting applications, to coat the hot face of the water-cooling element with a layer of castable refractory material. This layer helps to protect the element from process perturbations. In some smelters, liquid metal has penetrated the cooling element and come into contact with the cooling water causing an explosion. Some manufacturers have introduced slotted grooves into the hot face of the cooler to try and ensure

that some of the cooling element has castable in these grooves to help protect the element in these situations.

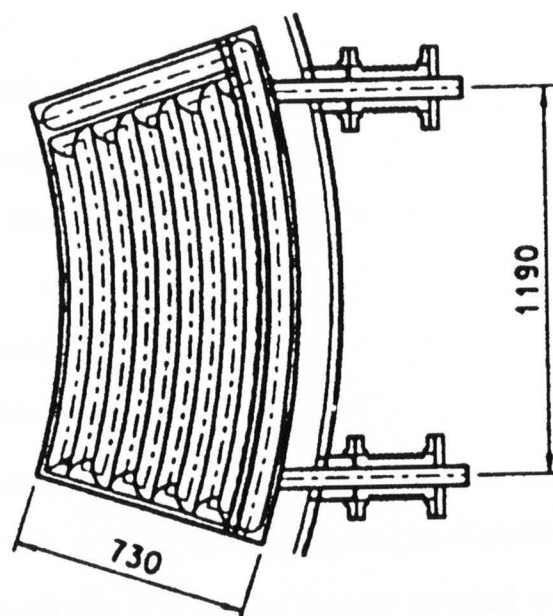


Figure 1.8 – Plan view of the Pipe layout for water-cooled stove depicted in Figure 1.7¹⁹

The prime motivation for undertaking this work is to characterise and to provide further understanding of how freeze layers form on water-cooled elements. To be able to model this system effectively, a methodology is developed to predict the thickness of the refractory layer applied to the water-cooled element. The importance of creating a mechanism to predict this thickness is that this refractory layer has a direct impact on the heat transfer occurring.

The first objective of this work is to develop refractory wear mechanisms to be able to adequately predict the thickness of the refractory layer that is applied to the hot face of the water-cooled element that is being worn away by the process. The second objective of this work is to be able to effectively model the freeze layers that are forming on water-cooled elements. A model of the water-cooling elements accounting for the wear of the refractory layer and the formation of freeze layers can be utilised to evaluate different water-cooling designs.

1.4 Physics Involved

To model this problem a variety of physics needs to be captured – in particular:

- Fluid Flow;
- Turbulence;
- Heat Transfer;
- Phase Change;
- Chemical Reactions;
- Radiation;
- Free-surfaces; and
- Thermal Stress

PHYSICA²⁰ is a CFD code that has been developed at the University of Greenwich, Greenwich, London, UK. It is a finite volume unstructured mesh code. Its main appeal is that the above physics are all available and can be closely coupled within the same code. Another advantage of PHYSICA is the ability to add additional physics as and when required, a facility that has been used in this work.

1.5 Review of Relevant Work

A significant amount of work has been performed on the properties and performance of refractories under their service conditions. In particular, work to describe the mechanisms that lead to refractory wear form the basis for the refractory wear modelling performed here is summarised. As freeze layers and accretions are also modelled, the work that has examined these processes is also covered within this section. A very detailed review of wear mechanisms has been prepared by Lee and Zhang²¹.

1.5.1 Refractory Wear

Refractories are a complex material with several phases and pore structures. Refractories are produced as pre-fired shapes, or as unfired materials that are mixed and installed in-situ using casting or spray like techniques (gunning) before firing. On firing refractories the phase's present change and bonds between the various constituent raw materials are formed. Figure 1.9 shows the different structures of Magnesium-Chrome refractories after they have been fired for a period of time. Impurities generally find their way to the boundaries between the predominant phases. Improvements in refractory quality have been made recently by obtaining raw materials with low compositions of these impurities²².

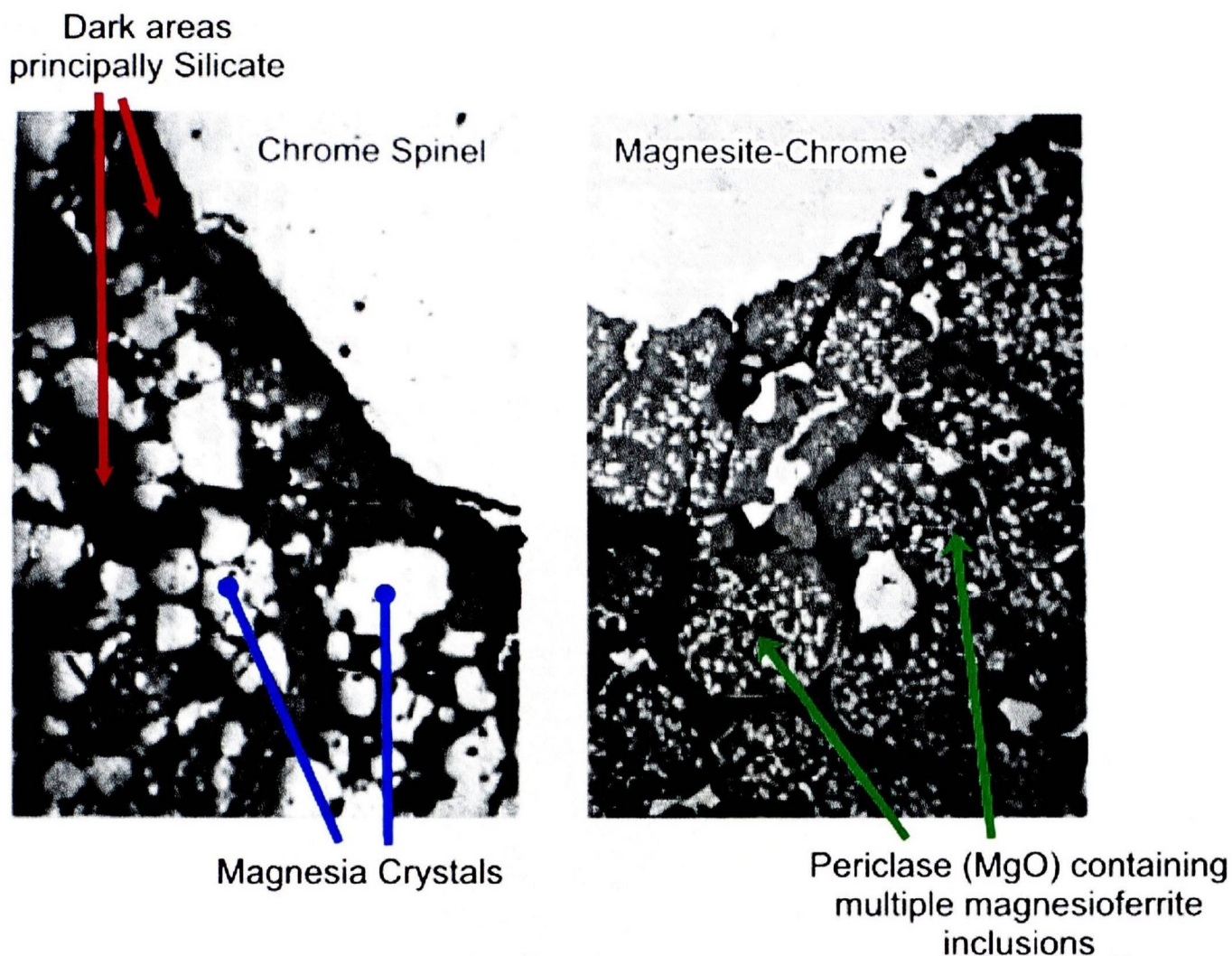


Figure 1.9 – Magnesite Chrome Ore (left) and resultant fired refractory product (right)²³

Chemical, thermal and mechanical stresses are the main factors involved with the wear of refractory linings²⁴. Refractory wear mechanisms can be simply summarised by grouping them into three sequential steps. The first step is for the slag* to *penetrate* the refractory. Secondly the material that has penetrated the refractory reacts with or dissolves the refractory that it is in contact with - *Corrosion* (Chemical Wear). The structure of the refractory is weakened by the infiltrating material such that the flow of material within the smelter can *erode* the refractory surface (Mechanical Wear).

On a global scale the cycling of the furnace or ladle can lead to build up of stresses in the penetrated refractory due to the differences in thermal expansion of the refractory and the penetrated region. If the stress levels are sufficient, the penetrated layer may shear away from the refractory in a process called spalling. As the region of the process that this work examines is completely submerged in slag, the refractory is not expected to be exposed to this thermal cycling and this mechanism is therefore not examined in this work.

* this could also be some other sort of melt (matte, metal, glass) or gaseous components that are able to penetrate the structure of the refractory and then be able to interact with the refractory.

Penetration, corrosion and erosion are discussed in some detail in the following sections. Work carried out by other workers is also summarised and discussed, with specific reference to the refractories used in this modelling work – Magnesia-Chrome and High Alumina spinel forming low cement castables.

1.5.1.1 Penetration

When refractory comes into contact with slag, slag will be absorbed into its pores as shown in Figure 1.10. For virgin refractory, the penetration of slag into its pores is initially quite fast compared to the penetration that occurs afterwards.

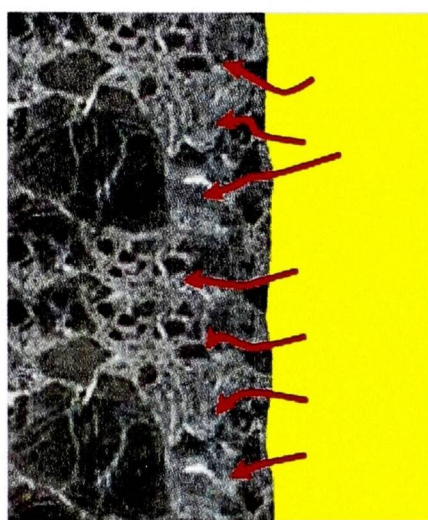


Figure 1.10 – Schematic Representation of Penetration

The commonly used theoretical models for penetration are based on capillary flow²¹. This approach is also used to describe flows within porous media²⁵. The Laplace equation of capillarity (Equation 1.1), also known as the Laplace-Young Equation, can be used to calculate the pressure drop (ΔP) created by the capillary action of the pores (of radius r) within the refractory.

$$\Delta P = \frac{2\gamma \cos\theta}{r} \quad (1.1)$$

where γ is Surface Tension ($\text{N}\cdot\text{m}^{-1}$)

θ is the contact or wetting angle between refractory and slag

By using Poiseuille's law (Equation 1.2) with the Laplace equation of capillarity (Equation 1.1), a penetration rate as shown in Equation 1.3 can be determined.

$$\frac{dl}{dt} = \frac{r^2 \Delta P}{8\mu l} \quad (1.2)$$

$$\frac{dl}{dt} = \frac{r\gamma \cos\theta}{4\mu l} \quad (1.3)$$

where l is the current depth of penetration (m)

t is time (s)

μ is the dynamic viscosity of the slag ($\text{kg}\cdot\text{s}^{-1}\cdot\text{m}^{-1}$)

Although temperature is not explicitly stated within Equation 1.1 to Equation 1.3, it has a large implicit effect as the properties of the slag are temperature and composition dependant. The temperature dependence of these properties is covered later in this chapter in the section that deals with the slag viscosity.

Mukai and several co-workers²⁶ examined the penetration of MgO refractories. This was performed by using in-situ X-ray images recorded over time and examining the microstructures of the refractory samples at the completion of the tests. They concluded that the penetration of slag increases with: increasing pore radius; increasing total iron concentration within the slag; increasing temperature of the slag; and decreasing slag basicity. The conclusions of Mukai et al. are consistent with the theoretical models derived from capillary forces (Equation 1.3).

Kuromitsu et al.²⁷ examined the interaction between alumina and binary glasses by placing glass powders onto well sintered dense alumina. The alumina disks and glass powder were fired at 850°C using a 10°C.min⁻¹ heating rate. They found that the reaction layer grew uniformly and that the growth rate was directly proportional to the square root of time. From this they concluded that the driving force for slag penetration was the capillary driving force.

Before discussing these results of Kuromitsu et al. the relationship of penetration with time requires further description. On integrating Equation 1.3 from $t=0$ to t and $l=0$ to l and assuming that the physicochemical properties of the slag remain constant gives:

$$l^2 = \left[\frac{r\gamma \cos \theta}{2\mu} \right] \cdot t \quad (1.4)$$

which can be re-written as

$$l = K \cdot t^{1/2} \quad (1.5)$$

where

$$K = \left[\frac{r\gamma \cos \theta}{2\mu} \right]^{1/2}$$

In this form, K is known as the penetration coefficient. Mukai et al.²⁶ also use this formulation in their work and comment that their results follow this during the initial part of the penetration of virgin refractory. From the work of Kuromitsu et al. it could be construed that Equation 1.5 will hold true for extended periods of time. Kuromitsu et al. have only heated their samples for a period of 10 minutes which will correspond to the initial period of penetration. Their assumption that the physicochemical properties of the slag (pore size, surface tension, contact angle, and viscosity) are constant is an important one as this is only likely to be reasonable for the initial part of the penetration process. These quantities will change with changing temperature and local composition which will change due to any local reactions, dissolution and diffusion taking place.

Yu, Mukai, Kawasaki, and Furusato²⁸ tested five different types of refractories to investigate the relationship between corrosion and penetration for magnesia refractories. The tests were carried out in an induction furnace with the slag temperature controlled to 1873 ± 10 K. Samples were fixed to the end of a water-cooled stainless steel rod and inserted into the furnace allowed to equilibrate and dipped into the slag for 60 – 1800 seconds (1 – 30 minutes). After the tests were completed, the refractory samples were sectioned and the penetration depth measured using an optical microscope. Some of their results are shown in

Figure 1.11 and Figure 1.12. From a modelling point of view, this work shows how penetration is related to time (Equation 1.5).

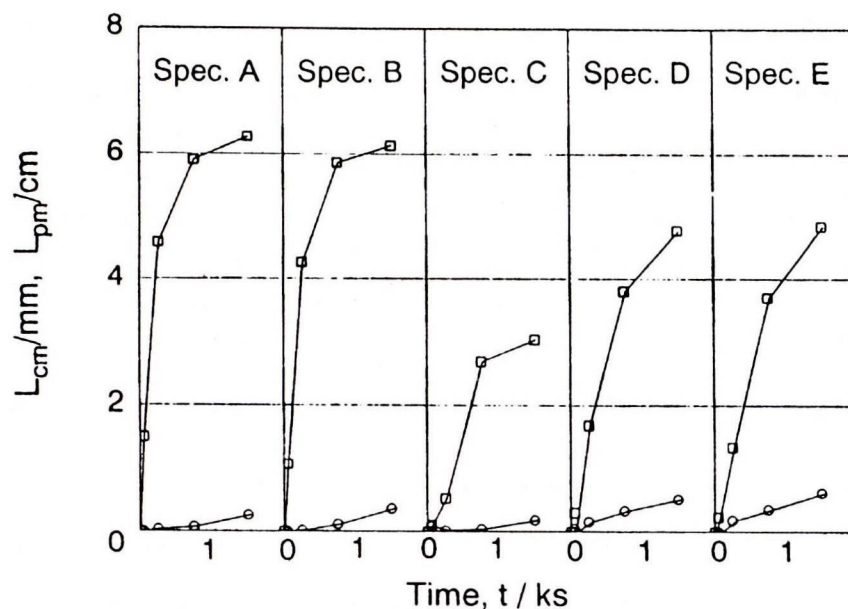


Fig. 4. Penetration and corrosion behavior of slag No.4 on the specimens.

□: Penetration depth, L_{pm} ,
○: Corrosion depth in the slag, L_{cm} .

Figure 1.11 – Penetration and Corrosion behaviour for a steelmaking slag with the various specimens tested by Yu et al.²⁸

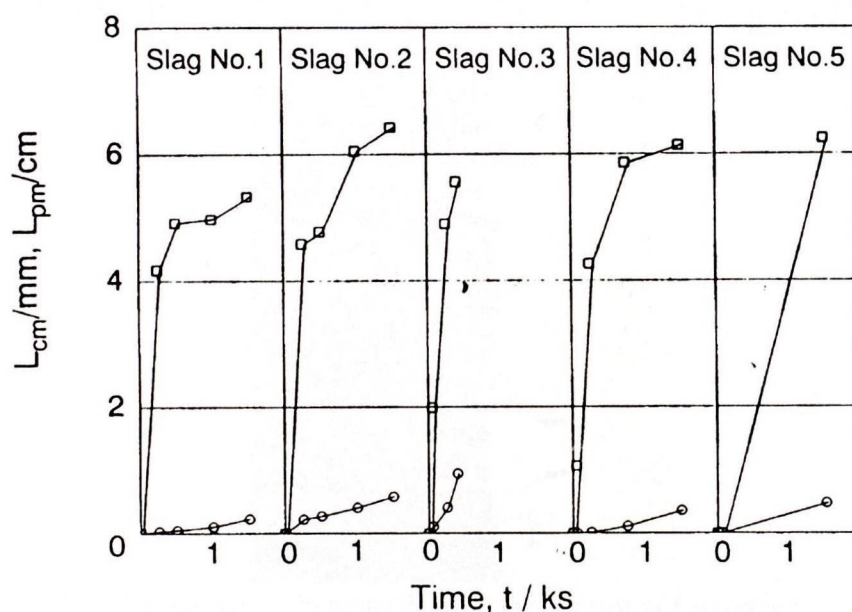


Fig. 5. Penetration and corrosion behavior of the slags on specimen B at 1873K.

□: Penetration depth, L_{pm} ,
○: Corrosion depth in the slag, L_{cm} .

Figure 1.12 – Penetration and Corrosion behaviour for various slags tested against a MgO refractory after Yu et al.²⁸

Bradley, Li and Stott have treated alumina based refractories with a CO₂ laser²⁹ and a xenon arc lamp³⁰. This heating of the surface melts the top layer of the refractory causing densification to occur in this layer. The aim of this process is to close off the pores within the surface layer to hinder or stop the penetration. In the work using the CO₂ laser, the refractory is heated to limit the thermal shock encountered during the surface treatment. Thermal shock testing has also been performed without any detrimental effects observed. This approach to reducing the routes for slag to penetrate is quite novel, although the usefulness of refractories treated in this way would have to be examined for their suitability for particular service conditions. In particular the surface layer would need to withstand any corrosion or erosive effects of the process.

In summary penetration is a complex multi-physics phenomenon. The most significant factor is the temperature dependence of the physicochemical properties - surface tension, contact angle, and viscosity. These properties will be impacted on the local scale by the interaction of the slag with the refractory along with any diffusion that may be taking place.

1.5.1.2 Corrosion

Corrosion is the chemical attack of refractory by molten slag, metal or matte. This process has two basic steps – the reaction between the refractory and slag; and the transport of the reaction products away from the reaction site²¹. These processes are depicted by Figure 1.13.

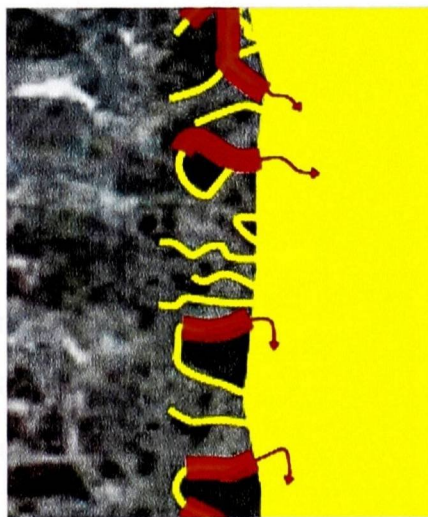


Figure 1.13 – Schematic Representation of Corrosion

Some authors³¹⁻³³ have examined corrosion under the action of forced convection. This work concludes that there is a relationship between the rotation rate (the method of creating forced convection or flow) and the wear that occurs. This work fits more naturally as an examination of the erosion taking place, and this work is discussed in more detail in the next section on erosion. This is not such a clear cut distinction as the shear exerted by 1-2ms⁻¹ flow will be

sufficient to erode the refractory on its own – its structure must be weakened in some way by the interaction with slag intrinsically linking erosion to corrosion.

The topic of corrosion has received extensive attention by researchers for some period of time. Lee and Zhang²¹ have reviewed the work by many authors and summarise the way that various refractories corrode when they come into contact with molten slag. The broad two forms of dissolution: direct[†] and indirect dissolution are covered here. The literature regarding magnesia-chrome and high alumina refractories is examined in some depth as these are the refractories examined in this work.

Direct Dissolution occurs when the refractory dissolves *directly* in the slag. The amount of dissolution will depend on the reaction rate of the dissolution of the refractory by the slag. If this is first order with respect to the reactant species, the dissolution rate (J) can be expressed as²¹:

$$J = K \frac{A_c}{A_o} C_m \quad (1.6)$$

where A_c is the actual area of refractory
 A_o is the apparent area of the refractory
 C_m is the concentration of the reactant in the melt; and
 K is the first order rate constant.

The dissolution rate may be the rate-limiting step in this process, although the removal of the reaction products through convection and/or diffusion may well limit the corrosion occurring. To limit the dissolution of the refractory into the slag it is commonplace to operate metallurgical processes with sufficient levels of particular components. At HIs melt, dolomite is used as a flux to maintain MgO at a sufficient level to minimise corrosion. Additionally the slag basicity (a ratio of slag components – see the glossary for more detailed information on the various ways slag basicity can be calculated) is generally controlled as it has been shown by many authors to have an effect on corrosion rates.

Indirect Dissolution occurs when the refractory interaction with the slag produces a solid product or a stable boundary layer, which is then dissolved by the slag. The layer is formed by the concentration of the reaction products in the local area. It is worthwhile to comment that the slag may well be interacting with the refractory from within the pores and cracks through which it has penetrated. This leads to a reasonably tortuous path back to the bulk slag, making

the diffusion or convection of the reaction products difficult and the limiting step within this process. In some cases a solid layer will form that will protect the refractory from further wear. When this occurs, the dissolution (J , $\text{kg}\cdot\text{m}^{-2}\cdot\text{s}^{-1}$) can be expressed in terms of the diffusion through this layer as²¹:

$$J = D \frac{(C_{sat} - C_{slag})}{\delta} \quad (1.7)$$

where D is the Diffusion coefficient ($\text{m}^2\cdot\text{s}$)
 δ is the boundary layer thickness (m)
 C_{sat} is the saturation composition in the slag ($\text{kg}\cdot\text{m}^{-3}$)
 C_{slag} is the composition of the component in the slag ($\text{kg}\cdot\text{m}^{-3}$)

Rehner and Toma³⁴ have mathematically modelled the corrosion of refractories by glass melts. They have modelled this process by modelling the diffusion of some of the melting agents (alkaline and alkaline-earth oxides) from the glass into the refractory and the resulting displacement of the resulting composition into the melt. The melting agents are modelled using Fick's second law:

$$\frac{\partial C}{\partial t} = \nabla(D\Delta C) \quad (1.8)$$

where C is the composition of the component of interest and D is the diffusion coefficient for this component which is temperature dependent in the Arrhenius form:

$$D = D_0 e^{-\frac{E}{RT}} \quad (1.9)$$

where E is the activation energy of the reaction (J)
 R is the universal gas constant of $8.314 \text{ J}\cdot\text{mol}^{-1}\cdot\text{K}^{-1}$
 T is the temperature (K)

Results are presented to show that this model reflects reality. The concern with this approach is that it does not appear to account for the penetration of the refractory by the melt that it is in contact with as has been shown by Kuromitsu et al.²⁷ Therefore any interaction between the refractory and glass will not be accounted for.

[†] direct dissolution is also known as congruent or homogeneous dissolution

Corrosion of Magnesia-Chrome Refractories

In testing for penetration Yu, Mukai, Kawasaki and Furusato also examined the corrosion of refractories in dipping tests²⁸. Various refractory samples were attached to the end of a stainless steel rod. The rod was then inserted into molten slag within a heated furnace. They found that the corrosion rate is related to the penetration rate. From this they concluded that by preventing penetration, it should be feasible to prevent corrosion and spalling effects within the refractory.

Chen and Wu have also examined the corrosion of magnesia-chrome refractories along with MgO-CaO refractories³⁵. The cylindrical sample has two Molybdenum end caps fitted to its ends and is attached to a Molybdenum rod. The sample is then inserted into molten slag within a furnace and rotated. For the steelmaking slags tested in this work the dissolution rate of the magnesia-chrome refractories was found to be lower than the MgO-CaO refractories. They found that by increasing the basicity, leads to an increase in the dissolution of the magnesia-chrome refractories, whereas the MgO-CaO refractory decreased.

Ichikawa, Minato, and Horita examined the corrosion resistance of magnesia-chrome bricks to low basicity slag³⁶. They comment that it is generally accepted that the corrosion resistance improves with increasing MgO and Cr₂O₃ composition. Corrosion tests are carried out on samples of varying compositions in an arc heated rotary slag test with a composition by weight of 60% CaO and 40% SiO₂. After testing the samples were sectioned and the penetration and corrosion measured along the length of the sample. They concluded that the corrosion with respect to low basicity slag is strongly linked to the Al₂O₃ content, with Fe₂O₃ composition having little effect. By reducing the content of SiO₂ and Al₂O₃ as far as possible, increasing the MgO and Cr₂O₃ contents the corrosion resistance can be improved.

All of this work concludes that the slag will penetrate and corrode the refractory through the weak points of the refractory. These weak points may well be the pores of the refractory, although lower melting point phases form between the major refractory phases from the impurities within the raw materials that the refractories are manufactured from. These impurities, as such as SiO₂, form phases with lower melting points than the bulk of the refractory. These phases are easier to weaken and disrupt the structure of the refractory as they are generally located at the boundaries of the predominant phases present. In recent years a significant improvement in the performance of refractories has been achieved through improving the purity of the raw materials used in their manufacture²².

In the work discussed here, and other work on the corrosion of magnesia-chrome refractories³⁷ direct dissolution is found to occur.

Corrosion of High Alumina Castables

Bates has investigated the corrosion behaviour of refractory oxides in molten silicate slags³⁸. Two test methods were used: plates of the oxides were dipped into the molten slag; and secondly the refractory oxide being tested is shaped like a crucible and the molten slag is placed inside and heated to the test temperature. For the alumina test gehlenite ($2\text{CaO}\cdot\text{Al}_2\text{O}_3\cdot\text{SiO}_2$) was found to have formed on the interface with the slag.

Guha³⁹ also has examined the dissolution of polycrystalline alumina in slag of a composition by weight of 37.5% CaO, 37.5% SiO_2 , and 25% Al_2O_3 . The specimens were exposed to molten slag for a period of 1 to 10 hours at a temperature from 1400 to 1500°C. He found that the dissolution of the Al_2O_3 into the slag was through a liquid boundary layer as had been found by others^{31,32,40-42} previously. This boundary layer is saturated with gehlenite ($2\text{CaO}\cdot\text{Al}_2\text{O}_3\cdot\text{SiO}_2$) during the initial stages of the dissolution process. As the dissolution progresses an interface of $\text{CaO}\cdot 2\text{Al}_2\text{O}_3$ is formed between the liquid boundary layer and the Al_2O_3 . With time this layer reacts further with Al_2O_3 to form $\text{CaO}\cdot 6\text{Al}_2\text{O}_3$ at the interface. The $\text{CaO}\cdot 6\text{Al}_2\text{O}_3$ is significantly larger than Al_2O_3 in molar volume and this causes the interface to break up and allow slag to penetrate into the bulk of the specimen. This penetrating slag then becomes saturated in Al_2O_3 and anorthite ($\text{CaO}\cdot\text{Al}_2\text{O}_3\cdot 2\text{SiO}_2$) crystallises from the melt. No further reactions take place as anorthite is compatible with $\text{CaO}\cdot 6\text{Al}_2\text{O}_3$ and Al_2O_3 .

Zhang et al.⁴³ and Lee et al.⁴⁴ have also performed similar work to Guha and Bates that has been described above. The conclusion by all of these workers is that the dissolution of alumina occurs indirectly.

1.5.1.3 Erosion

The literature suggests that erosion occurs through the thinning of the boundary layer that then helps to accelerate other processes within the refractory wear, in particular the direct or indirect dissolution of refractory into the slag²¹. As already mentioned in the above section regarding corrosion, the weakening of the refractory structure by the penetrated slag may well accelerate the erosion of the refractory. The schematic of this process is shown in Figure 1.14.

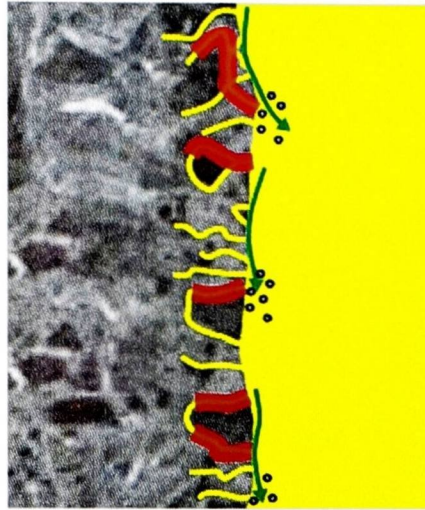


Figure 1.14 – Schematic Representation of Erosion

Dunkl and Bruckner³³ have investigated the forced “corrosion” of refractories through the use of a rotating cylinder face. The advantage of this method is that the boundary layer thickness (Prandtl flow boundary layer and Nernst diffusion layer) is independent of the dimensions of the cylinder face. It can be shown that the “corrosion” rate is proportional to the square root of the angular velocity. Dunkl and Bruckner present results of their test work and show that this relationship between “corrosion” rotational speeds holds true. Similar work with the same findings has also been carried out by Sandhage and Yurek^{31,32} and Figure 1.15 shows the flows that they observed in their work.

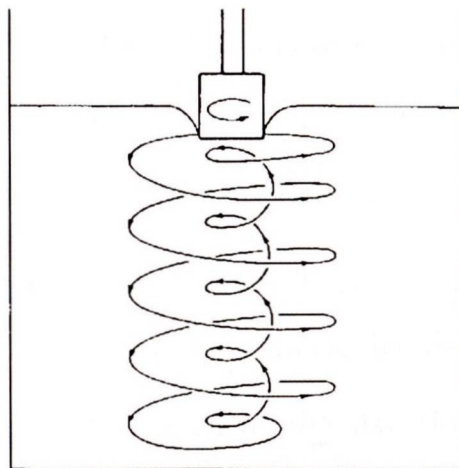


Figure 1.15 - Flow observed by Sandhage and Yurek³² in their rotating cylinder work.

Some corrosion will inevitably occur, and in fact will be assisted by the reduction of the boundary layer due to the induced flow caused by the rotation of the refractory specimen. It may well be that the “corrosion” is in fact erosion due to the shear generated by the flow of slag on the refractory. The shear forces developed by the flow of slag provide a way to erode the refractory. This can be calculated from Newton’s Law of Viscosity⁴⁵.

$$\tau = \mu \left. \frac{du_x}{dy} \right|_{wall} \quad (1.10)$$

To examine the physics of the erosion mechanism, literature regarding soil erosion was examined to see if there was an expression of a force balance that was useful. The US Department of Agriculture has produced a model for predicting soil erosion⁴⁶. Of particular interest is their relationship to predict the amount of soil that is picked up with water which is shown in equation 1.11. This equation is valid when the hydraulic shear stress exceeds the critical shear stress of the soil.

$$D_f = D_c \left(1 - \frac{G}{T_c} \right) \quad (1.11)$$

where D_f = Rill erosion Rate ($\text{kg}\cdot\text{s}^{-1}\text{m}^{-2}$)
 D_c = Detachment Capacity ($\text{kg}\cdot\text{s}^{-1}\text{m}^{-2}$)
 G = Sediment Load ($\text{kg}\cdot\text{s}^{-1}\text{m}^{-1}$)
 T_c = Sediment transport Capacity ($\text{kg}\cdot\text{s}^{-1}\text{m}^{-1}$)

When the critical shear stress exceeds the detachment capacity, D_c ($\text{kg}\cdot\text{s}^{-1}\text{m}^{-2}$) can be expressed as:

$$D_c = K_r (\tau_f - \tau_c) \quad (1.12)$$

where K_r = Geometry Parameter ($\text{s}\cdot\text{m}^{-1}$)
 τ_f = Threshold Shear Value (Pa)
 τ_c = Shear Stress acting on the soil due to the flow (Pa)

From these equations it can be seen that once the shear stresses developed by the fluid (in this case water), exceed the forces holding the soil in place that the soil is eroded away.

A simple calculation of the shear developed by the slag flowing past refractory at $1\text{--}2 \text{ ms}^{-1}$ gives values of shear that range from $0.2 - 12 \text{ N}\cdot\text{m}^{-2}$. The technical specification of the refractory⁴⁷ indicates that the hot modulus of rupture at 1500°C is $6 \times 10^6 \text{ N}\cdot\text{m}^{-2}$. By comparing this with the values of shear developed, we can see that virgin refractory will not be eroded by the flow of the slag by itself.

The conclusion is that the refractory has to first be penetrated and weakened by the slag. Therefore for erosion to take place the shear developed in the slag exceeds the effective hot modulus of rupture of *penetrated* refractory. The effective hot modulus of rupture will be some fraction of the value for un-penetrated refractory. As the time-temperature quantity

represents the degree of reaction that has taken place, this could be used in a relationship to predict the effective hot modulus of rupture.

1.5.1.4 Thermal Effects

Temperature has an important part to play with refractory wear. Cycling of temperature may cause stresses to build up due to dissimilar thermal expansion rates and melting points for different parts of the refractory. Finally the slag refractory interactions will also be dependent on the prevailing temperature.

Refractories have many phases present within them, which behave differently²². The most notable effect is where penetrated refractory is subjected to temperature cycling – like a ladle that is repetitively filled and emptied. In this situation the penetrated refractory expands and contracts at a different rate to the virgin refractory causing stresses to build up to a point where the penetrated refractory shears away from the bulk – a process that is called spalling. This mechanism can also be responsible for causing cracks within refractories. As the temperature conditions are kept constant during modelling the thermal stresses are not examined.

When lower melting point phases are present, usually formed from impurities within the raw materials such as silica, these sometimes will melt and disrupt the structure of the refractory leading to poor performance. The penetration of slag is highly dependent on the temperature. The penetration is calculated from the slag viscosity, surface tension and contact angle – all of which are dependent on temperature. The interaction of the refractory with the slag will also be a function of temperature. The Arrhenius law indicates that reaction rates of chemical reactions are exponentially related to the temperature.

1.5.1.5 Standard Test Procedures

The standard test methods used to measure the performance of refractories can be grouped into two broad categories: Static; and Dynamic tests. These procedures are described here to provide background information for the models that are created for the induction furnace and rotary slag tests. The other tests are also described briefly to provide an insight into the degree that they reflect the slag chemistry and temperature profiles that refractories come into contact with in industrial applications.

Many of the tests are used to measure the relative effectiveness of a suite of refractories against each other. Generally at the end of these tests, the test specimens are removed from the furnace. After they have been cooled they are sectioned and polished to allow proper

measurement of the wear and to examine the effect of the slag on the phases within the refractory.

Static

Static tests involve a piece of refractory that is either a flat plate, or has a hole or cavity machined into it which are illustrated in Figure 1.16 and Figure 1.17. The refractory is heated to the required temperature and molten slag is dropped into place and the slag and refractory is held at the test temperature for a period of time.



Figure 1.16 – Button or Sessile Drop Test

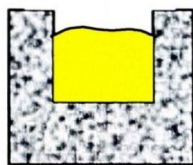


Figure 1.17 – Crucible, Cavity, Cup or Brick Test

The main advantage of the static tests is that they are quick and simple to perform for a large number of samples. The biggest disadvantage is that the slag can easily become saturated in the products of any reaction between the slag and refractory. An alternative method is to immerse a refractory finger within slag, with both the refractory specimen and slag heated in a furnace as illustrated in Figure 1.18. It is possible in the finger test to use a large volume of slag, thus minimising the effect of slag chemistry on the test results.

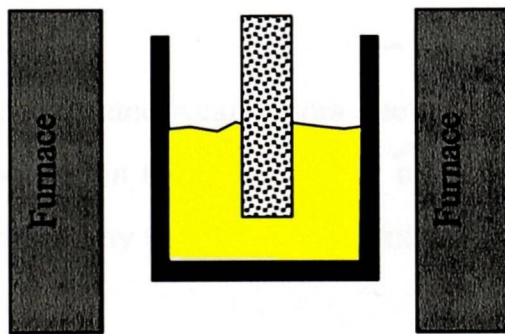


Figure 1.18 – Dipping, Immersion or Finger Test

All of these tests suffer from the fact that they are carried out under isothermal conditions. The service conditions for refractories usually involve a significant temperature gradient which is an important factor in the penetration of slag into the refractory..

Dynamic Tests

The benefit of using a dynamic test over a static one is that the presence of flow reduces the boundary layer which can lead to an increased amount of corrosion. The rotating finger test simply rotates the test piece in the finger test (shown in Figure 1.18).

Induction Furnace

This test is carried out by fitting several different refractory test pieces to the inside wall of an induction furnace. Metal and slag are added, with the metal being heated by the induction coil. Flow is induced in the metal by the electromagnetic force which then causes flow within the slag layer.

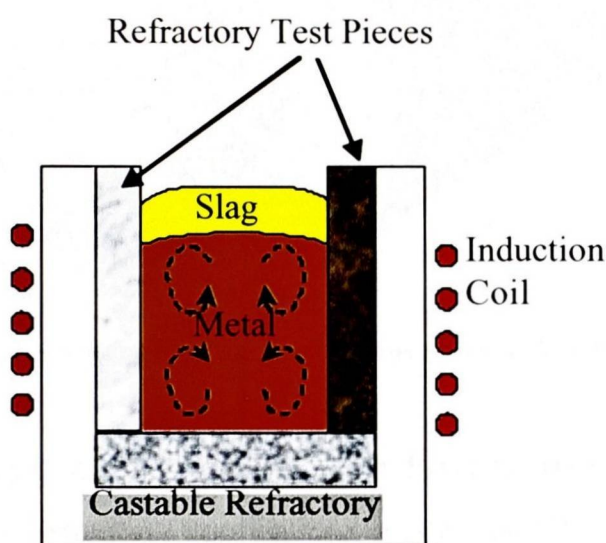


Figure 1.19 – Induction Furnace Test

One of the advantages of this test is that it is possible to set up a temperature gradient and the atmosphere is also easily controlled. It is possible to control the flow of metal in the induction furnace by varying the current and frequency of the coil, although this is constrained by the temperature required for the test.

At the metal-slag interface, accelerated wear occurs due to the movement of the interface due to the flow of metal and slag within the furnace. The refractory is oxidised by the slag, and oxides on the surface are removed by the wash of the metal²⁶.

Rotary Slag Test

In the Rotary Slag test the refractory samples are cut and inserted into the inside of a rotary kiln that has open ends. Figure 1.20 shows the cylindrical furnace with the six refractory samples visible on the ends. The kiln is tilted slightly and a fresh supply of slag is continuously added to the furnace to prevent the build up of any reaction products between

refractory and slag. A gas burner is used to heat and melt the slag. This method is described in the standard ASTM C874-85⁴⁸.

This is a popular test as it is possible to test several samples simultaneously. The gas burner in the centre of the furnace sets up a temperature gradient through the refractories, although the flame may alter the oxidation state of the iron within the slag.

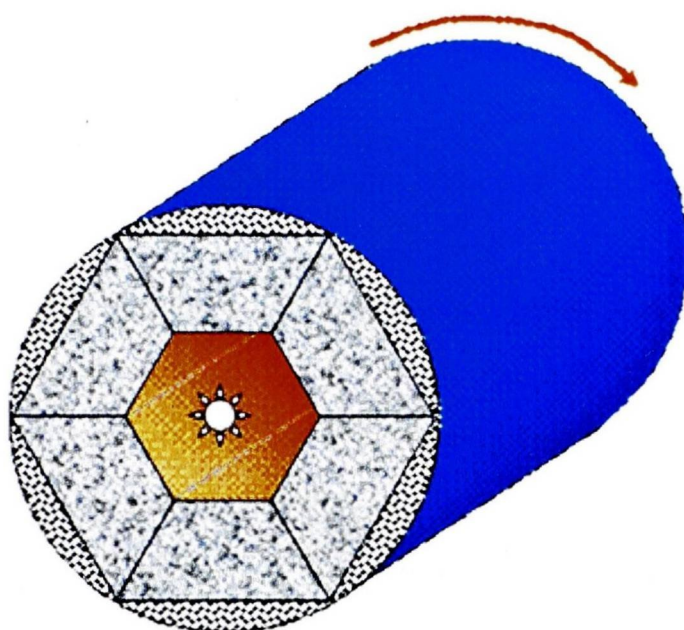


Figure 1.20 – Rotary Slag Test Apparatus Showing the Main Cylinder

1.5.2 Furnace Design and Freeze Layer Formation

One of the most intensive smelting applications in Pyrometallurgy is the Outokumpu Flash Smelting of Copper. These flash smelters are operating at 150-400%⁴⁹ of their design operating capacity. As the process intensity has increased, the cooling requirements for the furnace have also changed. Their use is described here as it is useful information on the design and use of water-cooled elements.

The increase in process intensity has been primarily due to the reliable supply and production of oxygen⁴⁹. These improvements in process intensity give at equilibrium, heat fluxes of 20-250 kW.m⁻², which will peak at up to 5000 kW.m⁻² when the molten slag comes in direct contact with the furnace cooling system if the accretion breaks off⁵⁰. During normal operation the refractory will wear back to an equilibrium thickness of 15-75 mm⁵⁰ which leads to problems with holding and attaching the refractory to the cooler. Understanding the fluid flow and heat transfer characteristics is important for successfully cooling any furnace⁴⁹.

With the advent of higher process intensities within the flash smelters, various furnaces have required increased cooling to meet the new production rates and to solve problems with

excessive refractory wear⁵¹. In the retrofitting of such furnaces^{52,53} one or more of the following improvements were made⁵¹:

- The slag zone has been stabilised using copper water-cooled elements
- Air-cooled copper fins were added to the outside of the vessel to increase the heat transfer and reduce the penetration into the refractory
- Water-cooled copper tap-holes
- Instrumentation to monitor furnace and water-cooling system performance
- Binding Systems to promote tight brick joints that are resistant to matte/metal or slag leaks.

There are various types of cooling available for the side wall of furnaces, depending on the intensity of the process. These types include⁵¹:

- Forced air-cooled copper fins attached to the shell plate in the metal/matte zone to maintain the temperature of the shell plate within acceptable limits and minimising metal/matte penetration into the brickwork.
- Water-cooled copper finger coolers that penetrate the furnace brickwork⁵⁴; the water passages are limited to the portion of the cooler outside the wall.
- Externally cooled copper plate coolers, which are similar to the finger coolers in that water remains outside the wall, but offer higher heat removal capability.
- Internally cooled copper plate coolers, which are cast copper plates with internal water cooling that provide higher heat removal capacity.
- Copper waffle coolers, which are cast copper elements with internal water cooling to offer the highest heat removal capacity.

The difference between these different systems is their different cooling duties which are summarised in Figure 1.21. The different types of coolers will be suited to different parts of the furnace depending on the process conditions in that region. Over-cooling is inefficient as extra energy will be required to supply this requirement.

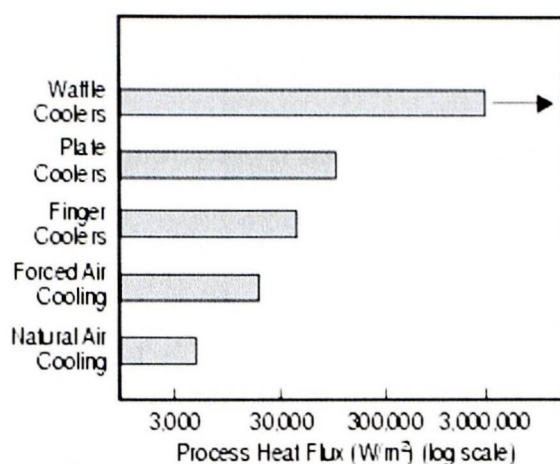


Figure 1.21 - Comparison of Heat Fluxes for various Water-cooling Systems⁵¹

1.5.2.1 Solidification

Solidification, or other changes of phase, are coupled processes. The fundamental aspect of the process is that the fraction of the material that is liquid (and the balance being solid) is a function of temperature. For pure materials the phase change will occur at a fixed temperature, but for other materials (alloys and mixtures) this occurs over a range of temperatures. It is important to recognise that on any change of phase the energy balance is impacted by the amount of energy consumed or released in the phase change – the latent heat.

Solidification is also closely coupled to the momentum relationships in that the presence of solid or partially solid material will retard the flow of material. The flow is also important to the energy or temperature of the systems and this demonstrates how the solidification is closely coupled with the energy and momentum calculations of the system.

Computational Modelling of Solidification

The modelling of coupled solidification is one area that has received a significant amount of attention by many authors. Sampson and Gibson have examined the solidification of liquid metal flowing through a circular pipe^{55,56}. They model the system using a two dimensional model of the pipe for laminar and turbulent flow.

By using computational fluid dynamics (CFD), it is possible to model more complex geometries and flows. Hibbert, Markatos, and Voller⁵⁷ used the CFD code PHOENICS to model the solidification within a pipe. Their model compares well with the results obtained by Lazaridis⁵⁸.

Voller and Prakash⁵⁹ have modelled the freezing of a thermal cavity successfully. Schneider and Beckerman⁶⁰ have successfully modelled the freezing of a Lead-Tin alloy in a square

cavity that was cooled from one side. The filling of moulds in casting operations are even more complex and have been effectively modelled by several workers⁶¹⁻⁶³.

The computational modelling of solidification has had a significant amount of work and the techniques are well defined.

Accretion Formation

Much of the work regarding the formation of accretions from submerged nozzles or tuyeres has been directed to applications within the steel industry where bottom blowing techniques are used. Kyllö and Gray⁶⁴ performed work for HIs melt regarding the bottom tuyeres for the horizontal smelt reduction vessel. From their review of the literature, they found that for a pipe like accretion to form, when an inert gas is used, will require a high pressure. Physical⁶⁵ and mathematical⁶⁶ modelling has been performed for “mushroom” or hemispherical type accretions that are found to form in steelmaking applications, with results that correspond to the observed accretions in the systems being studied.

1.5.3 Previous Modelling of Refractory Wear

Many people have modelled refractory wear. Most of this modelling has involved the use of finite element techniques to model the thermo-mechanical behaviour of the refractory⁶⁷⁻⁷³. This work generally involves modelling the thermal behaviour of the refractories whilst also analysing the stresses that build up during service. As the temperature variations within the refractory are not likely to vary significantly the stresses within the refractories have not been calculated.

No other work has been located that describes a closely coupled model for examining freeze layers and refractory wear. It is this fact that makes this work unique in its approach to this problem.

1.6 Physical Properties

The physical properties are important whenever a system is being modelled. The properties of the slag are important within this system. The main effect considered here is the temperature dependence of Viscosity, Contact Angle and Surface Tension, along with the affect of the chemical reactions involved. This particularly impacts the penetration rate (Equation 1.3).

1.6.1 Slag Viscosity

The penetration of slag into refractory has a large dependency on the viscosity (μ) of the slag. There has been significant work to model not only the temperature dependency of the slag, but also the variation due to its composition^{74,75}. Various models have been proposed for modelling the viscosity of metallurgical slags.

The Weymann equation (1.13) has been found to provide the best fit for the temperature dependence of most glasses and slags.

$$\mu = A^W T e^{\frac{E_\mu^W}{RT}} \quad (1.13)$$

where A^W is the pre-exponential term;
 E_μ is the activation energy; and
 T is the Temperature (K)

The structure of slag changes with changing compositions. For silicate slags, the pure silica network breaks down into rings and/or chain structures as basic metal oxides are added. To account for these changes a relationship is developed to calculate the activation energy based on the composition of the slag.

Zhang and Jahanshahi have measured viscosities for various slags in their work towards a generic approach to modelling slag viscosities⁷⁶. One of these slags is similar to the typical Hismelt slag composition.

1.6.2 Slag Surface tension and Contact Angle

The Surface Tension and Contact Angle have been shown to be temperature dependent by several authors⁷⁷⁻⁸⁰. Notably most of this work relates to metals and their alloys, although Zhang, Shu, and Wei⁷⁸ have correlated surface tension against various temperatures and slag compositions. They note that the surface tension of a pure liquid can be correlated in the following manner:

$$\gamma = \gamma_0 + \frac{d\gamma}{dT} \cdot T \quad (1.14)$$

where γ is the surface tension ($\text{N}\cdot\text{m}^{-1}$)
 γ_0 is the surface tension from the previous time-step ($\text{N}\cdot\text{m}^{-1}$)

As for other thermodynamic properties (in particular Gibbs energy), it is easier to express the surface tension in terms of the sum of the ideal values for each of its components, and then adjust by subtracting the excess energy⁸¹. In this way it is possible to build up a database of

information to help predict compositions of various slags. The surface tension and contact angle relationships used are described within the implementation chapter.

1.6.3 Phase Equilibria Calculations

The CALPHAD (Computer Coupling of Phase Diagrams and Thermo-chemistry) method was developed to set out common principles for the calculation of chemical and phase equilibria⁸². The basis for these calculations is the assembled, critically assessed thermodynamic data with their binary, ternary and higher order combinations⁸³.

There are many software packages that have been developed to perform these calculations, although there are two packages in widespread industrial use. The first is MTDATA⁸⁴ which has been developed at the National Physical Laboratory, Teddington UK. The second is F*A*C*T⁸⁵ which has been developed at the Centre for Research in Computational Thermochemistry at École Polytechnique, Montreal Canada. There are some differences in the way that these packages function (MTDATA uses the Compound Energy model⁸⁶, whereas F*A*C*T uses Quasichemical model⁸⁶), although they both perform the same underlying function.

The aim of these calculations is to determine the equilibrium state of the system that has been defined. To define a system the amount of the components, temperature, and pressure need to be stated. From the laws of thermodynamics, it is known that the system will minimise the Gibbs free energy to achieve equilibrium. From the databases of thermodynamic data, the Gibbs free energy for the various possible species can be calculated. A minimisation is performed to satisfy all the constraints within the system – as such as the amount of each component or element defined at the start of the calculation.

These software packages are particularly useful in predicting phase transformations. Additionally due to the underlying thermodynamics, other useful information about the system can be obtained such as:

- Specific Heat
- Liquidus and Solidus Temperatures
- Latent heat of Fusion

There is a cautionary note to the use of these packages – the databases should be checked to ensure they contain information on all of the phases that are likely, and possible to be present. This is where significant work is being undertaken to extend the already quite extensive databases that have been critically assessed.

1.7 Outline of Work

The fundamental aim of this work is to characterise and understand the freeze layers that form on water-cooled elements within a direct smelting context as such as HIs melt. To be able to achieve this, the main task is to be able to characterise the wearing refractory layer that is applied to the hot face of these cooling elements. The modelling of the slag solidifying as a freeze layer uses well defined computational techniques. The uniqueness of this work is the modelling of the entire system in a closely coupled manner. No previous work has been located that has examined the solidification and refractory wear in the same model.

To model these freeze layers and refractory wear a finite volume (FV) framework is used, which is described in Chapter 2. The refractory wear mechanisms of penetration, corrosion and erosion identified in reviewing the literature have been implemented within the Finite Volume – Unstructured Mesh (FV-UM) code PHYSICA.

The penetration is modelled by using a transport equation to solve a scalar variable for the location of the slag within the domain – either in the bulk slag or in penetrating the refractory. The penetration front is driven by capillary forces which are indirectly dependent on temperature. The physical properties of slag viscosity, surface tension, and contact angle with the refractory all require a temperature dependent relationship to adequately model this system. From the penetration of the refractory, the amount of refractory that will be corroded or eroded during a time-step is calculated and the scalar variable tracking the amount of refractory is adjusted accordingly.

To assist in development and provide verification of the refractory wear mechanisms various models have been developed. Results from induction furnace test work have been used to guide the adjustment of the parameters that influence the penetration mechanism. Data from the HIs melt pilot plant trials and rotary slag refractory wear tests have also been modelled to provide further validation of the refractory wear mechanisms.

To better understand how accretions form, the pipe like “elephants trunks” that form on the end of the solids injection lances were modelled. In combining this modelling of accretions with the refractory wear mechanisms, the elements required to characterise and understand freeze layer formation on water-cooled elements are available. These elements are then applied to create a model of the commercial plant design that is about to be built. This model provides a tool to evaluate designs for the cooling of the lower regions of the direct smelting furnaces.

COMPUTATIONAL MODELLING FRAMEWORK

This chapter sets out the computational framework technology by describing the Computational Fluid Dynamics technique used in this work. Initially the governing equations are set out along with the Finite Volume discretisations of these equations. Some comment is made about the solution methods used, and how boundary conditions are implemented. The Free-surface flow and Solidification governing relationships are also described as these are important for investigating the formation of freeze layers.

The first step in the numerical treatment of a problem using Computational Fluid Dynamics (CFD) techniques is to divide the computational domain into sub volumes – creating a mesh. The sizes of the individual cells or elements need to be small enough to capture the changes within the domain. For this reason meshes of different sizes need to be used to ensure that the answer obtained is independent of the size of the mesh elements.

Once the mesh has been generated the different physical phenomena need to be solved. The problem is initialised with values and given boundary conditions. The problem is then solved using a numerical solution technique: finite difference; finite element; or finite volume.

2.1 Governing Equations

To be able to perform the required calculations, values are calculated and stored at different locations within the domain. The first step in setting up any calculation domain is to create the sub-volumes. One such sub-volume is shown in Figure 2.1 and they are referred to interchangeably as elements or control volumes (CV). When all of the outlines of these volumes of the domain are visualised together, the resulting picture looks like a mesh – another common term used for the computational domain. The corners of the control volumes are known as grid points.

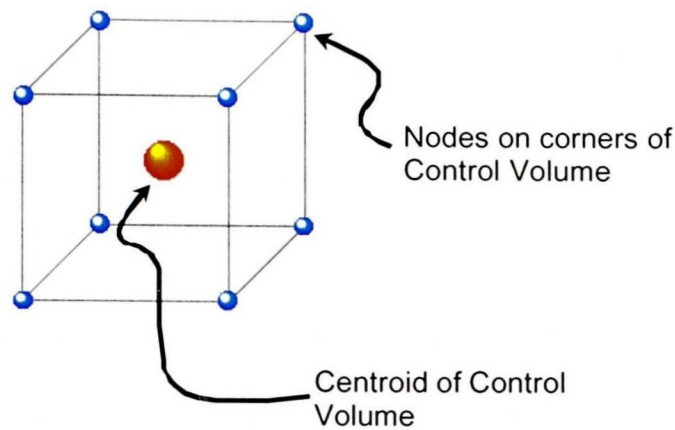


Figure 2.1 – Mesh Terminology

Finite Difference (FD) methods solve for the values of the unknowns (ϕ) at the node points of the grid. Taylor series expansions are commonly used to create finite difference approximations of the derivatives of ϕ in terms of the nodal values and its immediate neighbours. The derivatives appearing in the governing equations are replaced by finite differences which produce an equation for ϕ at each node point.

Finite Element (FE) methods use piecewise functions (linear or quadratic) to describe the local changes in the unknown variables (ϕ). The governing equations are satisfied when the exact solution of ϕ is obtained. When the approximating functions are used in the governing equations, they will not exactly hold. The residuals are minimised yielding a set of equations for the unknown coefficients in the approximating functions.

Finite Volume (FV) methods were initially developed as a special form of the finite difference method. Integration across each control volume within the solution domain for the governing equations distinguishes FV methods from all the other CFD techniques. One of the main attractions of this technique is the clear association of the numerical technique and the laws of conservation. Over a specified control volume this takes the general form as described in Equation 2.1.

$$\left[\begin{array}{c} \text{Rate of increase} \\ \text{of } \phi \text{ of} \\ \text{fluid element} \end{array} \right] + \left[\begin{array}{c} \text{Net rate of} \\ \text{flow of } \phi \text{ out} \\ \text{of fluid element} \end{array} \right] = \left[\begin{array}{c} \text{Rate of increase} \\ \text{of } \phi \text{ due to} \\ \text{diffusion} \end{array} \right] + \left[\begin{array}{c} \text{Rate of increase} \\ \text{of } \phi \text{ due to} \\ \text{sources} \end{array} \right] \quad (2.1)$$

These finite volume techniques have been described by Patankar⁸⁷ and more recently Versteeg and Malalasekera⁸⁸. The general form illustrated in Equation 2.1 is written mathematically in Equation 2.2. This governing equation is also known as the *transport equation* as it effectively ‘transports’ the calculated quantity through the calculation domain.

$$\underbrace{\frac{\partial(\rho\phi)}{\partial t}}_{\text{transient}} + \underbrace{\nabla(\rho u\phi)}_{\text{convection}} = \underbrace{\nabla(\Gamma_\phi\Delta(\phi))}_{\text{diffusion}} + \underbrace{S_\phi}_{\text{sources}} \quad (2.2)$$

Equation 2.3 is a generic form of the transport equation (Equation 2.2). Table 2.1 describes the various terms for the common phenomena that are described in this general form.

$$\underbrace{\frac{\partial}{\partial t} \int_V \mathbf{A}\phi dV}_{\text{transient}} + \underbrace{\int \mathbf{B}(\underline{u} \cdot \underline{n}) dS}_{\text{convection}} = \underbrace{\int_S \Gamma_\phi \Delta\phi ndS}_{\text{diffusion}} + \underbrace{\int_V \mathbf{C} dV}_{\text{sources}} \quad (2.3)$$

Phenomenon	ϕ	A	B	Γ_ϕ	C
Continuity	1	ρ	ρ	0	S_{mass}
Velocity	u	ρ	ρu	μ	$S_u - \nabla P$
Heat Transfer	h	ρ	ρh	$\frac{k}{C_p}$	S_h
Scalar	ϕ	ρ	$\rho\phi$	$\rho\nu$	S_ϕ

Table 2.1 - Definition of Terms in the Generic Transport Equation

To be able to solve the governing equations across the domain, they are discretised to give a form that can be used to compute the quantity being calculated.

2.1.1 Finite Volume Discretisations of Governing Equations

An approximation can be made for each term within Equation 2.2, such that it can be expressed in a linear matrix form:

$$\underline{A}\phi = \underline{b} \quad (2.4)$$

The integration of the transport equation(s) across a control volume produces a discretised equation based on the centroid of the element. The discretised form has convection and diffusion fluxes along with the rate of change of the particular variable being solved (ϕ). The discretisation of each term of the transport equation (Equation 2.2) is now discussed in turn.

2.1.1.1 Convection Term

The convection term is transformed into a surface integral using the divergence theorem⁸⁹ (Equation 2.5) as shown in Equation 2.6.

$$\iiint_V \nabla(\underline{F}) dV = \iint_S \underline{F} \cdot \underline{n} dS \quad (2.5)$$

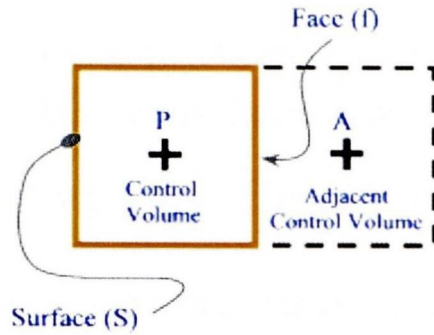


Figure 2.2 – Divergence Theorem Representation

$$\iiint_V \nabla(\rho \underline{u} \phi) dV = \iint_S \rho (\underline{u} \cdot \underline{n}) \phi dS \quad (2.6)$$

The velocity (\underline{u}) is the relative velocity of the fluid. In all the cases that are examined in this work, a static mesh has been employed, and therefore the relative velocity is equivalent to the fluid velocity.

To evaluate the surface integral, it is split up into integrals for each of the bounding faces of the control volume, which produces the following summation where the subscript f denotes a face evaluation.

$$\iint_S \rho (\underline{u} \cdot \underline{n}) \phi dS \approx \sum_f \rho_f (\underline{u} \cdot \underline{n})_f A_f \phi_f \quad (2.7)$$

As the values are calculated for the centroid, assumptions are required to obtain estimated values at the face for this integrand. The Hybrid scheme (see section 2.2.1.2) is used as standard in this work. Depending on the relative strength of convection to diffusion, face values are either up-winded or approximated at the face. Hence, the density can be taken to be the upwind element value of density which can be calculated in the following manner.

$$\rho_f = \begin{cases} \rho_P, & (\underline{u} \cdot \underline{n})_f > 0.0 \\ \rho_A, & (\underline{u} \cdot \underline{n})_f < 0.0 \end{cases} \quad (2.8)$$

where A refers to the Adjacent upwind element
 P refers to the current element being examined

To calculate the normal component of the velocity at the face, the Rhie – Chow⁹⁰ interpolation method is used. Finally an approximation is required to determine the value of ϕ at the face – as such as the upwind or arithmetic average which are covered in more detail in the sections describing how the transport equation is discretised.

2.1.1.2 Diffusion Term

By applying the divergence theorem, as already described above with relation to the convection term, the following surface integral is obtained:

$$\iiint_V \nabla \cdot \{\Gamma_\phi \Delta(\phi)\} = \iint_S \Gamma_\phi \Delta(\phi) \underline{n} dS \quad (2.9)$$

This can be simplified as $\Delta(\phi) \underline{n}$ is equal to the gradient of ϕ in the direction of the normal.

By summing the integral across each of the bounding faces of the control volume, Equation 2.10 can be written.

$$\sum_f \left(\int_f \Gamma_\phi \frac{\partial \phi}{\partial n} dS \right) \quad (2.10)$$

In a truly orthogonal mesh, a line constructed between the two elements either side of a face will be normal to the plane that the face resides. In this case it is possible to approximate the normal gradient of ϕ with Equation 2.11. Applying this approximation to the sum of the faces yields the discretised form written in Equation 2.12.

$$\frac{\partial \phi}{\partial n} \approx \frac{\phi_A - \phi_P}{d_{AP}} \quad (2.11)$$

$$\sum_f (\Gamma_\phi)_f A_f \left(\frac{\phi_A - \phi_P}{d_{AP}} \right) \quad (2.12)$$

The last task remaining is determining how to calculate the value of Γ_ϕ at the face. One possible method is to take an arithmetic mean as follows:

$$\begin{aligned} (\Gamma_\phi)_f &= \alpha_f (\Gamma_\phi)_P + (1 - \alpha_f) (\Gamma_\phi)_A \\ \alpha_f &= \frac{d_{Af}}{d_{Af} + d_{fP}} \end{aligned} \quad (2.13)$$

The arithmetic mean is suitable when ϕ is the velocity. For other quantities, such as heat transfer, the harmonic mean (Equation 2.14) is more appropriate. When $(\Gamma_\phi)_A$ is zero the flux of ϕ is expected to also be zero – whereas the arithmetic mean will approximate the value of Γ_ϕ at the face with $\alpha_f (\Gamma_\phi)_P$, which is not expected to be zero. Additionally if $(\Gamma_\phi)_A$ is significantly smaller than $(\Gamma_\phi)_P$, the diffusion of ϕ from P to the face will encounter a relatively smaller resistance than the diffusion of ϕ from A to the face. Therefore it is

Figure 2.3 Two-Orthogonal-Cell Control Volume

expected that $(\Gamma_\phi)_f$ will be related to $(\Gamma_\phi)_A$, and inversely on α_f . Equation 2.13 suggests otherwise with $(\Gamma_\phi)_f = \alpha_f (\Gamma_\phi)_P$.

$$(\Gamma_\phi)_f = \frac{(\Gamma_\phi)_P (\Gamma_\phi)_A}{\alpha_f (\Gamma_\phi)_P + (1 - \alpha_f) (\Gamma_\phi)_A} \quad (2.14)$$

The harmonic mean gives the desired results, in particular:

- $(\Gamma_\phi)_f$ is zero when either $(\Gamma_\phi)_A$ or $(\Gamma_\phi)_P$ are zero
- $(\Gamma_\phi)_f \approx \frac{(\Gamma_\phi)_A}{\alpha_f}$ when $(\Gamma_\phi)_P \gg (\Gamma_\phi)_A$

Non-Orthogonal Considerations

In the process of integrating the diffusion term over a control volume leads to the estimation of the derivative of ϕ with respect to the face normal. In a truly orthogonal or structured mesh this derivative can be estimated by the formula

$$\frac{\partial \phi}{\partial n} = \frac{\phi_A - \phi_P}{d_{AP}} \quad (2.15)$$

Figure 2.3 depicts a non-orthogonal control volume which shows how the line connecting the centroids of the adjacent elements is not parallel to the face normal and the angle (θ) is no longer 90° . This makes the estimation of the derivative above inaccurate and requires adjustment. Taking v to be the vector connecting the adjacent element centroids then

$$\frac{\partial \phi}{\partial v} = \frac{\phi_A - \phi_P}{d_{AP}} \quad (2.16)$$

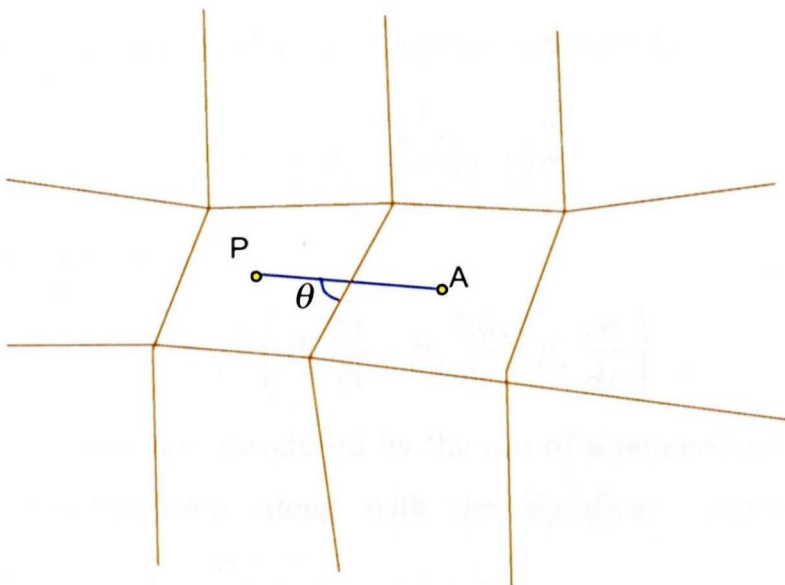


Figure 2.3 - Non-Orthogonal Control Volume

The normal to the face can be written with a component in the direction of \underline{v} with a tangential component $\underline{\beta}$ in the form:

$$\underline{n} = (\underline{v} \cdot \underline{n})\underline{v} + \underline{\beta} \quad (2.17)$$

With this it is possible to express the differential in terms of the vector connecting the element centroids as

$$\frac{\partial \phi}{\partial n} = (\underline{v} \cdot \underline{n}) \frac{\partial \phi}{\partial v} + \underline{\beta} \frac{\partial \phi}{\partial t} \quad (2.18)$$

where t is the unit vector in the direction of $\underline{\beta}$. To be able to calculate the differential t is expressed as the Cartesian components of $\underline{\beta}$. When this is done the differential can be written as

$$\frac{\partial \phi}{\partial n} = (\underline{v} \cdot \underline{n}) \frac{\partial \phi}{\partial v} + \beta_x \frac{\partial \phi}{\partial x} + \beta_y \frac{\partial \phi}{\partial y} + \beta_z \frac{\partial \phi}{\partial z} \quad (2.19)$$

Now the problem is a function of the Cartesian derivatives of ϕ on the faces of the control volume. To calculate the Cartesian derivatives of ϕ for the centroid of an element, the derivative is integrated across the control volume in the following manner

$$\int_V \frac{\partial \phi}{\partial x} dV = V \left\{ \frac{\partial \phi}{\partial x} \right\}_p \quad (2.20)$$

and by applying the divergence theorem

$$\begin{aligned} \int_V \frac{\partial \phi}{\partial x} dV &= \int_S \phi n_x dS \\ &= \sum_f A_f \phi_f n_x \end{aligned} \quad (2.21)$$

The effect of the non-orthogonal mesh is to change the diffusion to

$$D_f = A_f \frac{(\Gamma_\phi)_f}{d_{AP}} (\underline{u} \cdot \underline{n})_f \quad (2.22)$$

which leads to an extra source of

$$A_f (\Gamma_\phi)_f \left(\beta_x \frac{\partial \phi}{\partial x} + \beta_y \frac{\partial \phi}{\partial y} + \beta_z \frac{\partial \phi}{\partial z} \right) \quad (2.23)$$

Croft⁹ has shown how errors are introduced by the use of a non-orthogonal mesh for a heat transfer and fluid flow problem, along with the significant improvements that these corrections provide.

2.1.1.3 Source Term

The source term is an important term within the governing equations. It allows for sources (and sinks also) to be added to the variable being calculated. This is particularly useful when phenomena are interacting with one another.

In many instances the source is dependent on the variable ϕ being solved; therefore it is desirable to make the discretised equations reflect this fact. The source term is linearized as the discretised equation is solved using techniques for linear algebraic equations. The source is then expressed in the form⁸⁷:

$$S_{\phi} = S_C - S_P \phi_P \quad (2.24)$$

That is the source term is linearized to a constant (S_C) and a proportionality factor (S_P)* to multiply the quantity being solved (ϕ). The way that the source is linearized is important, as it affects the speed and stability of the solution. To maintain the diagonal dominance of the set of equations, S_P must be non-negative.

For speed, as much of the source should be placed in the linear ($S_P \phi$) part⁹. The speed will be reduced if S_C is increased in magnitude. Large changes in S_P and S_C may lead to issues with the stability of the solution process.

It is not uncommon for Equation 2.24 to be written in the coefficient (Co) and value (Val) form of Equation 2.25. The advantage of this form is that the value of the solved variable (ϕ) is known and can be directly used in this formulation.

$$S_{\phi} = Co(Val - \phi) \quad (2.25)$$

where

$$S_C = Co \cdot Val$$

$$S_P = Co$$

On integrating the linearized source term over the control volume for values at its centroid, gives the contribution:

$$V_P (S_C - S_P \phi_P) \quad (2.26)$$

* It should be noted that S_P does not refer to the source evaluated at the point 'P' but rather the part of the source term that is proportional to the solved variable ϕ

2.1.1.4 Transient Term

Integrating the transient term across a control volume leads to the following equation:

$$\int_t^{t+\Delta t} \int_V \frac{\partial(\rho\phi)}{\partial t} dV \cdot dt \quad (2.27)$$

For a stationary mesh, the volume of the control volume (V) is not changing and it is possible to reverse the order of the integration. Equation 2.27 becomes:

$$\int_V (\rho\phi - \rho^o\phi^o) dV \quad (2.28)$$

where the super-script 'O' refers to the value at the previous time-step. Assuming that the control volume can be represented by the value at the centroid of the control volume, denoted by P, the above equation can be approximated as

$$\int_V (\rho_P\phi_P - \rho_P^o\phi_P^o) dV \quad (2.29)$$

If fully implicit assumptions are made, the integration of the other terms (convection, diffusion and source) in the equation with respect to time leads to a factor of Δt applied to each of them. The entire equation is divided by Δt to leave the transient term only dependent on the time step size that is selected. This leads to the transient term being:

$$\frac{(V_P\rho_P\phi_P - V_P^o\rho_P^o\phi_P^o)}{\Delta t} \quad (2.30)$$

2.2 Differencing Schemes

The integration of the transport equation(s) across a control volume produces a discretised equation based on the centroid of the element. The discretised form has convection and diffusion fluxes along with the rate of change of the particular variable being solved (ϕ).

A common illustration^{87,88} for discretisations is a steady one-dimensional convection and diffusion problem. In this case the transport equation reduces to Equation 2.31, which when integrated across a control volume as shown in Figure 2.4 produces the resulting discretised Equation 2.32.

$$\frac{d}{dx}(\rho u\phi) = \frac{d}{dx}\left(\Gamma \frac{d\phi}{dx}\right) \quad (2.31)$$

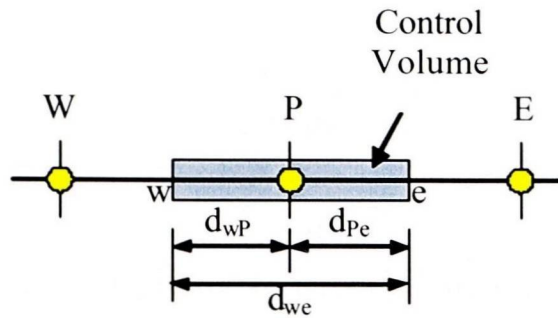


Figure 2.4 – Control Volume for steady one-dimensional convection and diffusion illustration

$$(\rho u \phi)_e - (\rho u \phi)_w = \left(\Gamma \frac{d\phi}{dx} \right)_e - \left(\Gamma \frac{d\phi}{dx} \right)_w \quad (2.32)$$

The difficulty in evaluating this equation is calculating the values for ϕ at the faces of the control volume. Various schemes are used to calculate the value of ϕ at the faces, with the simplest using two points on either side of the face. Higher order schemes use more points to provide a better estimation of ϕ at the face.

2.2.1 Two Point Schemes

There are several two point schemes in use. The Central is the simplest being a simple average. The upwind scheme uses the flow conditions to improve the estimation of ϕ at the face. The Hybrid scheme is a combination of the Central and upwind schemes. The Exponential and Power law schemes are practically exact solutions for ϕ at the face. The accuracy of these schemes can be seen from examining various Peclet numbers. The Hybrid scheme is the default differencing scheme used by PHYSICA and it has been used in this work.

2.2.1.1 Central Scheme

The simplest method is to average the two points either side of the face (Equation 2.33) which is why this method is called the Central Differencing scheme.

$$\begin{aligned} \phi_e &= \frac{1}{2}(\phi_E + \phi_P) \\ \phi_w &= \frac{1}{2}(\phi_W + \phi_P) \end{aligned} \quad (2.33)$$

By substituting Equation 2.33 into Equation 2.32 the following is obtained:

$$\frac{1}{2}(\rho u)_e(\phi_E + \phi_P) - \frac{1}{2}(\rho u)_w(\phi_P + \phi_W) = \frac{\Gamma_e(\phi_E - \phi_P)}{(\delta x)_e} - \frac{\Gamma_w(\phi_P - \phi_W)}{(\delta x)_w} \quad (2.34)$$

where Γ_e and Γ_w are calculated using an arithmetic mean. To simplify the system we define the following:

$$\begin{aligned} F &\equiv \rho u \\ D &\equiv \frac{\Gamma}{\delta x} \end{aligned} \quad (2.35)$$

It is customary to rearrange the equation in terms of the cell centred value and the other adjacent cell values as is shown in Equation 2.36.

$$a_p \phi_p = a_E \phi_E + a_w \phi_w \quad (2.36)$$

where:

$$\begin{aligned} a_E &= D_e - \frac{F_e}{2} \\ a_w &= D_w - \frac{F_w}{2} \\ a_p &= D_e + \frac{F_e}{2} + D_w - \frac{F_w}{2} \\ &= a_E + a_w + (F_e - F_w) \end{aligned}$$

It is possible for a_E and a_w to become negative, possibly causing unrealistic results. Patankar⁸⁷ reports that a solution may diverge unless the flows being studied had a low Peclet number (ie. Low values of F/D).

2.2.1.2 Upwind Scheme

The problems of the Central Differencing scheme are caused by the inaccuracy of the approximation to calculate the value at the face. The Upwind scheme uses the value of ϕ of the point upwind of the face, for the value of ϕ at the face. In terms of the standard form this becomes:

$$a_p \phi_p = a_E \phi_E + a_w \phi_w \quad (2.37)$$

where:

$$\begin{aligned} a_E &= D_e + \max(-F_e, 0) \\ a_w &= D_w + \max(F_w, 0) \\ a_p &= D_e + \max(F_e, 0) + D_w + \max(-F_w, 0) \\ &= a_E + a_w + (F_e - F_w) \end{aligned}$$

From Equation 2.37 it can be seen that a_E and a_W can not become negative – and hence the problem with the central difference scheme is solved. The disadvantage of this scheme is that an artificial diffusion is introduced into the solution.

2.2.1.3 Exponential Scheme

The governing equation (Equation 2.31) can be solved exactly if Γ and ρu are taken to be constant over the domain $0 \leq x \leq l$ used with the boundary conditions:

$$\begin{aligned}\phi &= \phi_0 \Big|_{x=0} \\ \phi &= \phi_l \Big|_{x=l}\end{aligned}\tag{2.38}$$

The exact solution to the governing equation is given by Equation 2.39 where the Peclet number (Pe) is defined by Equation 2.40. The Peclet number gives the strength of convection and diffusion relative to each other.

$$\frac{\phi - \phi_0}{\phi_l - \phi_0} = \frac{e^{\frac{Pe x}{l}} - 1}{e^{Pe} - 1}\tag{2.39}$$

$$\begin{aligned}Pe &\equiv \frac{\rho u l}{\Gamma} \\ &\equiv \frac{\text{Convection}}{\text{Diffusion}}\end{aligned}\tag{2.40}$$

Figure 2.5 shows that the relationship between ϕ and x is only linear, and an acceptable approximation for low Peclet Numbers. When Pe is large, the value of ϕ at the interface ($x = l/2$) is nearly equal to the value at the upwind boundary. This is what the upwind scheme assumes, although it is used for large values of $|\text{Pe}|$.

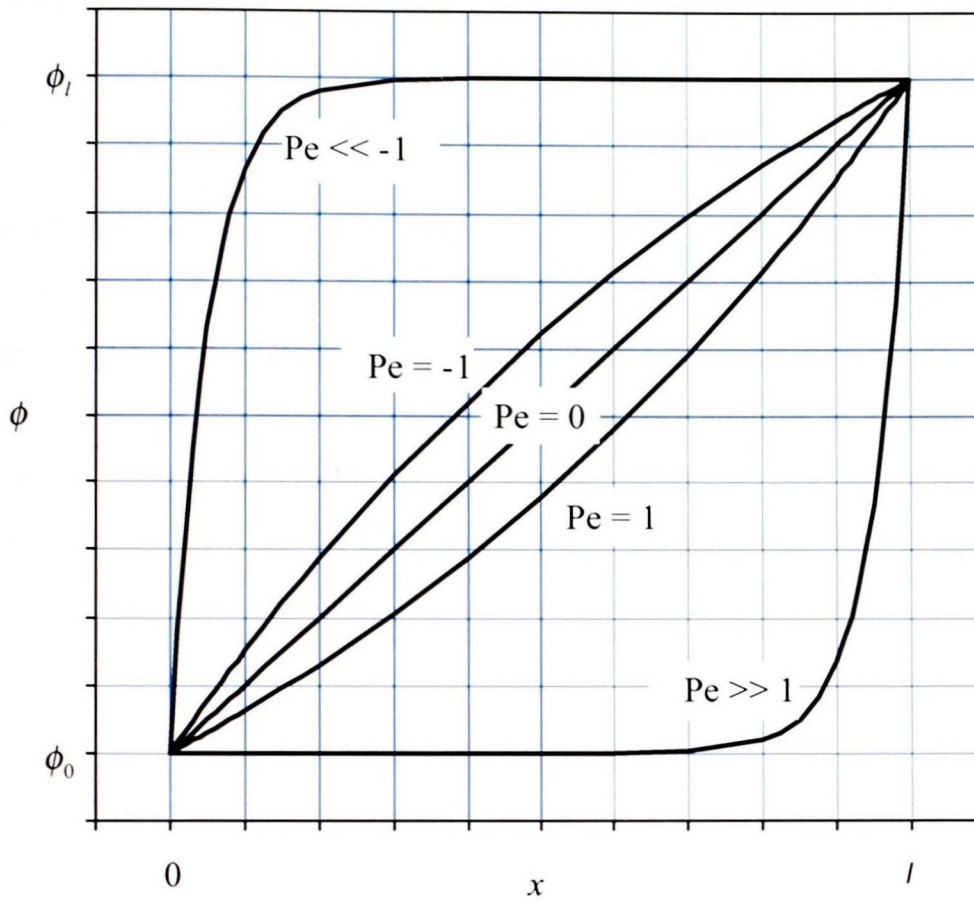


Figure 2.5 – Value for ϕ calculated from the Exact Solution for various Peclet Numbers

For large values of $|Pe|$, $\frac{d\phi}{dx}$ is zero at the interface. In this situation the diffusion is nearly absent. In the upwind scheme the diffusion is calculated from a linear relationship and therefore the diffusion is over-estimated for high values of $|Pe|$.

The Exponential Scheme is based on this exact solution of the governing equation. Patankar⁸⁷ derives the Exponential Scheme and in the standard form is:

$$a_p \phi_p = a_e \phi_e + a_w \phi_w \quad (2.41)$$

where:

$$a_e = \frac{F_e}{e^{\frac{D_e}{\Delta x}} - 1}$$

$$a_w = \frac{F_w e^{\frac{D_w}{\Delta x}}}{\frac{F_w}{\Delta x} - 1}$$

$$a_p = a_e + a_w + (F_e - F_w)$$

There is a computational cost for calculating the exponentials. Even though this result is desirable, the result is not exact for two and three dimensional problems and the extra expense does not deliver the benefits of the extra computing time.

2.2.1.4 Hybrid Scheme

The Hybrid scheme developed by Spalding⁸⁷ reduces to the central differencing scheme for Peclet numbers $-2 \leq Pe \leq 2$. Outside of this range the Upwind Scheme is used in which there is no diffusion. As the name suggests it uses a combination of central difference and Hybrid, although it was developed as an approximation to the exact solution already described. The standard form for the Hybrid scheme is shown in Equation 2.42.

$$a_p \phi_p = a_E \phi_E + a_W \phi_W \quad (2.42)$$

where:

$$\begin{aligned} a_E &= \max\left(-F_e, D_e - \frac{F_e}{2}, 0\right) \\ a_W &= \max\left(F_w, D_w + \frac{F_w}{2}, 0\right) \\ a_p &= a_E + a_W + (F_e - F_w) \end{aligned}$$

2.2.1.5 Power Law

For the Hybrid Scheme, the results depart from the exact solution at $Pe = \pm 2$. A better approximation was devised by Patankar⁸⁷ called the power-law scheme. Equation 2.43 summarises the calculation by this scheme. Patankar also comments that the power law scheme is recommended for convection-diffusion problems, although the Hybrid scheme will be sufficient in many situations.

$$a_E = D_e \cdot \max\left\{0, \left(1 - \frac{0.1|F_e|}{D_e}\right)^5\right\} + \max\{0, -F_e\} \quad (2.43)$$

2.2.1.6 Summary

The standard discretised form can be generalised for these cases by different choices of the function $A(|Pe|)$ as shown in Equation 2.44. The functions $A(|Pe|)$ for each of the different schemes already mentioned are listed in Table 2.2 and are plotted for a range of Peclet numbers in Figure 2.6. This figure powerfully depicts the relative accuracy of the various

schemes. Patel and Markatos⁹¹ have evaluated these schemes and others for two dimensional convection and diffusion.

$$a_P \phi_P = a_E \phi_E + a_W \phi_W \quad (2.44)$$

where:

$$a_E = D_e A(|Pe_e|) + \max\{-F_e, 0\}$$

$$a_W = D_w A(|Pe_w|) + \max\{F_w, 0\}$$

$$a_P = a_E + a_W + (F_e - F_w)$$

Scheme	Formula for A(Pe)
Central Difference	$1 - 0.5 Pe $
Upwind	1
Hybrid	$\text{Max}(0, 1 - 0.5 Pe)$
Power Law	$\text{Max}(0, \{1 - 0.1 Pe \}^5)$
Exponential (exact)	$\frac{ Pe }{e^{ Pe } - 1}$

Table 2.2 – A(|P|) Function for the different schemes

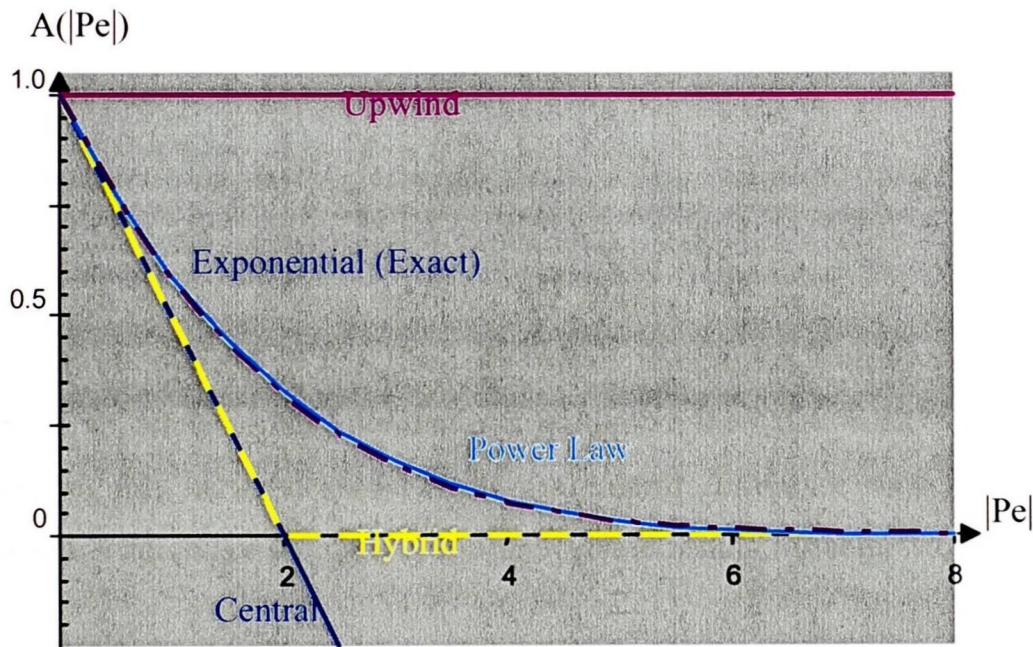


Figure 2.6 – Comparison of the different Differencing Schemes' Accuracy

2.2.2 Higher Order Schemes

Higher order differencing schemes use the values from more than the adjacent element to the face that is currently being examined. The QUICK, SMART, and Van Leer differencing schemes are described here.

2.2.2.1 QUICK

The Quadratic Upstream Interpolation for Convective Kinetics (QUICK) scheme developed by Leonard⁹² calculates the face values for ϕ from a quadratic function that passes through the values of the cells on either side of the face and the cell on the upstream side of these cells. For one-dimensional convection-diffusion problems can be summarised as shown in Equation 2.45 taken from Versteeg and Malalasekera⁸⁸.

$$a_P \phi_P = a_W \phi_W + a_E \phi_E + a_{WW} \phi_{WW} + a_{EE} \phi_{EE} \quad (2.45)$$

where:

$$\begin{aligned} a_P &= a_W + a_E + a_{WW} + a_{EE} + (F_e - F_w) \\ a_W &= D_w + \frac{6}{8} \alpha_w F_w + \frac{1}{8} \alpha_e F_e + \frac{3}{8} (1 - \alpha_w) F_w \\ a_{WW} &= -\frac{1}{8} \alpha_w F_w \\ a_E &= D_e - \frac{3}{8} \alpha_e F_e - \frac{6}{8} (1 - \alpha_e) F_e - \frac{1}{8} \alpha_w F_w \\ a_{EE} &= \frac{1}{8} (1 - \alpha_e) F_e \\ \alpha_w &= \begin{cases} 1, & F_w > 0 \\ 0 & F_w < 0 \end{cases} \\ \alpha_e &= \begin{cases} 1, & F_e > 0 \\ 0 & F_e < 0 \end{cases} \end{aligned}$$

The implementation of this scheme involves the addition of source terms, which can be problematic as the coefficients as described above can be negative. Improvements to QUICK have been made to alleviate this problem, in particular the QUICKER⁹³ algorithm. The QUICK algorithm has better accuracy than the central difference and hybrid schemes, although it suffers from minor overshoots and unbounded results for complex flows⁸⁸.

2.2.2.2 SMART

The SMART scheme was devised to solve the problem of unbounded results experienced with the QUICK formulations. Further detail of this scheme can be found in the work of Gaskell and Lau⁹⁴.

2.2.2.3 Van Leer

In using first order differencing schemes, such as Hybrid and Upwind, to solve for the advection of a scalar variable (Equation 2.47) through a computational domain, the interface

is smeared and the interface quality is poor. Various methods can be employed to reduce the smearing to an acceptable level. One method that has been used in this work is the Van Leer scheme which is a transient scheme based on Godunov's numerical treatment of the Lagrangian flow equations⁹⁵⁻⁹⁹. The Van Leer scheme implemented⁶² in PHYSICA is described here using the control volume shown in Figure 2.7.

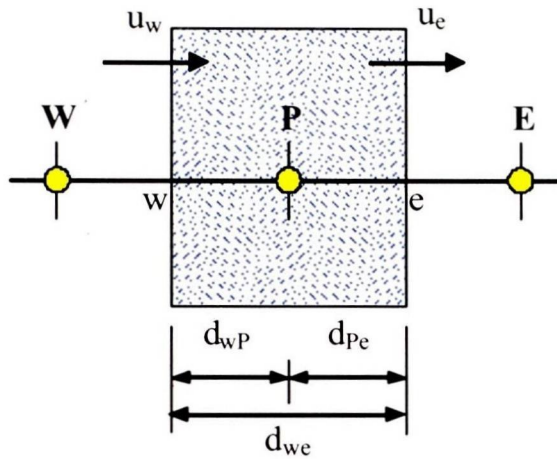


Figure 2.7 – Control Volume for Van Leer Scheme

Initially the fluxes of the solved variable at the faces of the control volume need to be calculated. This is achieved by using the upwind method, which for the east (e) face can be calculated in the following way.

$$\phi_e = \begin{cases} \phi_P, & u_e > 0 \\ \phi_E, & u_e < 0 \end{cases} \quad (2.46)$$

Second order terms are introduced by the Van Leer interpolation in time and space to reduce the smearing. These terms are derived from the solution of:

$$\frac{\partial \phi}{\partial t} + \nabla \cdot (\phi u) = 0 \quad (2.47)$$

which can be discretised for a one dimensional problem to produce the following equation:

$$\phi_P = \phi_P^O - \frac{\delta t}{\delta x} (u_e \phi_e - u_w \phi_w) \quad (2.48)$$

This equation relates the cell centred value (ϕ_p) to the values at the faces. The Van Leer scheme uses the local gradients of ϕ to determine the values at the face in the following manner.

$$\phi_e = \begin{cases} \phi_p + \frac{\delta x}{2} \left[\frac{\partial \phi}{\partial x} \right]_P \left[1 - \frac{u_e \Delta t}{\Delta x} \right] & u_e > 0 \\ \phi_p - \frac{\delta x}{2} \left[\frac{\partial \phi}{\partial x} \right]_E \left[1 + \frac{u_e \Delta t}{\Delta x} \right] & u_e < 0 \end{cases} \quad (2.49)$$

The gradient term is given by

$$\left[\frac{\partial \phi}{\partial x} \right]_P = \begin{cases} \frac{2 \operatorname{sgn}(\delta_e)}{\delta x} \min(|\delta_e|, \frac{1}{2}(|\delta_e| + |\delta_w|), |\delta_w|) & \operatorname{sgn}(\delta_e) = \operatorname{sgn}(\delta_w) \\ 0, & \text{Otherwise} \end{cases} \quad (2.50)$$

with

$$\begin{aligned} \delta_e &= \phi_E - \phi_P \\ \delta_w &= \phi_P - \phi_W \\ \operatorname{sgn}(\delta_e) &= \begin{cases} +1, & \delta_e \geq 0 \\ -1, & \delta_e < 0 \end{cases} \end{aligned}$$

This implementation is explicit in respect to time as values for ϕ are required at the beginning of each time-step. This will also require the time-step size to obey the CFL limit for stability which is described in the section about explicit solution methods.

2.2.3 Concluding Remarks

The various differencing schemes described in this section are implemented within the unstructured framework of PHYSICA. The Hybrid scheme is used by default unless the user selects one of the other schemes that have been implemented.

2.3 Boundary Conditions

At the extremities of the domain being examined, the condition or value at the boundary will be known – in particular where the material or fluid is moving into the domain at that particular point. The boundary condition gives the value of the variable being solved, which is on the face of a control volume as illustrated by Figure 2.8.

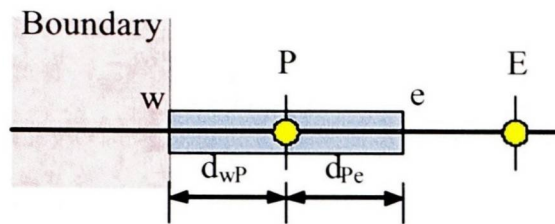


Figure 2.8 – Boundary condition applied to a control volume

The main two boundary conditions, Fixed Value and Fixed Flux, are described further along with the constant pressure boundary conditions. For further information about these boundary conditions and others, readers are directed to read the work by Versteeg and Malalasekera⁸⁸.

Boundary conditions are implemented using source terms which can be linearized as:

$$S_{\phi} = Co(Val - \phi) \quad (2.51)$$

2.3.1 Fixed Value

When the value of the solved variable (ϕ) is known at the face of a control volume, a fixed value boundary condition exists. This is also known as the Dirichlet boundary condition. This lends itself naturally to the coefficient value formulation of the source term linearization (Equation 2.25). The value term is set to the value of ϕ whereas the coefficient links (through diffusion and convection) this known value of ϕ to the value of ϕ that is calculated at the centroid of the control volume. This can be summarised as:

$$Co = A \frac{\Gamma_{\phi}}{\delta_{wP}} + \max(-C_{\phi} \underline{u} \cdot \underline{n}A, 0.0) \quad (2.52)$$

$$Val = \phi_{fix}$$

The above method is used in PHYSICA for setting the fixed value boundary conditions. When the mesh is staggered such that the control volume centres align with the boundaries the cell centred value can be directly set using

$$Co = 10^{10} \quad (2.53)$$

$$Val = \phi_{fix}$$

when this is substituted into the discretised form it gives

$$(a_p + 10^{10})\phi_p = \sum a_{nb}\phi_{nb} + 10^{10}\phi_{fix} \quad (2.54)$$

and if a_p and a_{nb} are negligible, this reduces to

$$\phi_p = \phi_{fix} \quad (2.55)$$

2.3.2 Fixed Flux

To set the rate, such as a heat transfer rate, at which a solved variable (ϕ) enters a control volume, again uses constants to make certain terms within the calculation insignificant. This is also known as the Neumann boundary condition. In PHYSICA this is achieved by setting the coefficient and value to the following values.

$$\begin{aligned} Co &= A \cdot 10^{-10} \\ Val &= \frac{\dot{\phi}_{fix}}{A \cdot 10^{-10}} \end{aligned} \quad (2.56)$$

2.3.3 Constant Pressure Boundaries

In PHYSICA a constant pressure boundary is treated as a fixed value boundary condition, although to solve pressure the pressure correction is calculated. At points where the pressure is fixed using a boundary condition, the correction is set to zero.

2.4 Solvers

The solution of the system of equations takes place by one of the well known matrix solution techniques. PHYSICA uses the Jacobi preconditioned Conjugate Gradient method (JCG). The explicit[†] solution is described in a little detail here as it is important for the discussion of the Courant, Friedrichs, Lewy stability criterion that follows.

2.4.1 Explicit and Semi-implicit Treatment

In particular for solving problems involving free-surface flows, the solution is more accurate if it is solved explicitly. The transport of a scalar variable (ϕ) in unsteady flow can be written in the general form:

$$\frac{\partial(\rho\phi)}{\partial t} + \Delta(\rho u\phi) = \Delta(\Gamma_{\phi} \nabla\phi) + S_{\phi} \quad (2.57)$$

[†] when the current value is dependent on the previous time -step value

To solve equation 2.57, it is integrated across a control volume (CV). Additionally each of the terms must be integrated across a finite time-step (Δt). By replacing the volume integrals with surface integrals for the convective and diffusive terms, as has been previously shown in Equations 2.6 and 2.9 respectively, we obtain:

$$\begin{aligned} \int_{CV} \left(\int_t^{t+\Delta t} \frac{\partial}{\partial t} (\rho\phi) dt \right) dV + \int_t^{t+\Delta t} \left(\int_A n \cdot (\rho u \phi) dA \right) dt \\ = \int_t^{t+\Delta t} \left(\int_A n \cdot (\Gamma \nabla \phi) dA \right) dt + \int_t^{t+\Delta t} \int_{CV} S_\phi dV dt \end{aligned} \quad (2.58)$$

To illustrate these implicit and semi-implicit schemes, the one-dimensional unsteady heat conduction problem by Versteeg and Malalasekera⁸⁸ is used. The unsteady heat conduction in one dimension is governed by the equation:

$$\rho C_p \frac{\partial T}{\partial t} = \frac{\partial}{\partial x} \left(k \frac{\partial T}{\partial x} \right) + S \quad (2.59)$$

The control volume is taken to be:

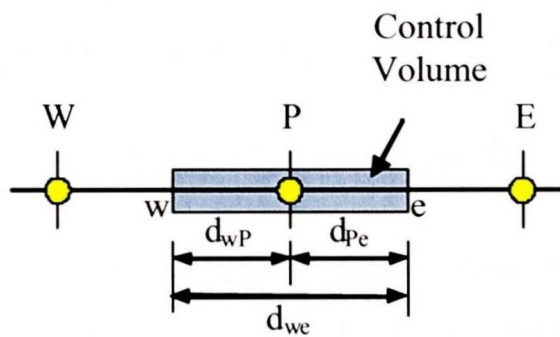


Figure 2.9 – Control Volume for unsteady one-dimensional conduction

On integrating Equation 2.59 over its control volume and the time-step (Δt) produces:

$$\int_t^{t+\Delta t} \int_{CV} \rho C_p \frac{\partial T}{\partial t} dV dT = \int_t^{t+\Delta t} \int_{CV} \frac{\partial}{\partial x} \left(k \frac{\partial T}{\partial x} \right) dV dT + \int_t^{t+\Delta t} \int_{CV} S dV dt \quad (2.60)$$

which can be re-written as:

$$\int_w^e \left[\int_t^{t+\Delta t} \rho C_p \frac{\partial T}{\partial t} dt \right] = \int_t^{t+\Delta t} \left[\left(kA \frac{\partial T}{\partial x} \right)_e - \left(kA \frac{\partial T}{\partial x} \right)_w \right] dt + \int_t^{t+\Delta t} \bar{S} \Delta V dt \quad (2.61)$$

where A is the face area; ΔV is its volume which is equal to $A\Delta x$; Δx is the width of the control volume; and \bar{S} is the average value of the source.

When the temperature at the point P is taken to be the temperature across the entire control volume and using a first order (backward) differencing scheme, the left hand side can be written as:

$$\int_{CV} \left[\int_t^{t+\Delta t} \rho C_p \frac{\partial T}{\partial t} dt \right] dV = \rho C_p (T_p - T_p^0) \Delta V \quad (2.62)$$

by applying central differencing to the diffusion terms on the right hand side of Equation 2.61 gives

$$\begin{aligned} \rho C_p (T_p - T_p^0) \Delta V = & \int_t^{t+\Delta t} \left[\left(k_e A \frac{T_E - T_p}{\delta x_{EP}} \right) - \left(k_w A \frac{T_p - T_w}{\delta x_{PW}} \right) \right] dt \\ & + \int_t^{t+\Delta t} \bar{S} \Delta V dt \end{aligned} \quad (2.63)$$

To be able to evaluate the right hand side of Equation 2.63, an assumption has to be made about the variation of T_p , T_e , and T_w with respect to time. This could involve taking the temperature at time t , $t + \Delta t$, or a combination of the temperatures at both points in time. To generalise the different possible approaches that may be taken, the integral of T_p (I_T) can be expressed in terms of a weighting factor α that ranges between 0 and 1 as follows:

$$I_T = \int_t^{t+\Delta t} T_p dt = [\alpha T_p + (1 - \alpha) T_p^0] \Delta t \quad (2.64)$$

In Table 2.3, the values for three weighting factors have been listed. For $\alpha = 0$ the temperature at time t is used; whereas for $\alpha = 1$ the temperature at time $t + \Delta t$ is used. For $\alpha = \frac{1}{2}$ the temperatures at the old and current times are equally weighted.

Weighting factor α	Integral Value I_T	Name Given to Scheme
0	$T_p^0 \Delta t$	Explicit
$\frac{1}{2}$	$\frac{1}{2} (T_p + T_p^0) \Delta t$	Crank-Nicholson
1	$T_p \Delta t$	Fully Implicit

Table 2.3 – Values for the Integral of T_p for various weighting factors

Substituting Equation 2.64 for T_W and T_E into Equation 2.63 and dividing through by $A\Delta t$ produces:

$$\begin{aligned} \rho C_P (T_P - T_P^O) \Delta V = & \alpha \left[\frac{k_e (T_E - T_P)}{\delta x_{EP}} - \frac{k_w (T_P - T_W)}{\delta x_{PW}} \right] \\ & + (1 - \alpha) \left[\frac{k_e (T_E^O - T_P^O)}{\delta x_{EP}} - \frac{k_w (T_P^O - T_W^O)}{\delta x_{PW}} \right] + \bar{S} \Delta x \end{aligned} \quad (2.65)$$

This can be re-arranged to give:

$$\begin{aligned} a_P T_P = & a_W [\alpha T_W + (1 - \alpha) T_W^O] + a_E [\alpha T_E + (1 - \alpha) T_E^O] \\ & + [a_P^O - (1 - \alpha) a_W - (1 - \alpha) a_E] T_P^O + b \end{aligned} \quad (2.66)$$

where

$$\begin{aligned} a_P &= \alpha (a_W + a_E) + a_P^O \\ a_P^O &= \rho C_P \frac{\Delta x}{\Delta t} \\ a_W &= \frac{k_w}{\delta x_{WP}} \\ a_E &= \frac{k_e}{\delta x_{PE}} \\ b &= \bar{S} \Delta x \end{aligned}$$

The final form of the discretised equation depends on the value of α . When $\alpha = 0$ the temperature values at the old time t are used to evaluate the value of T_P at the new time $t + \Delta t$. This resulting scheme is called explicit. For $0 < \alpha \leq 1$ the resulting schemes are termed implicit. A scheme where $\alpha = 1$ is termed fully implicit and when $\alpha = 1/2$ it is called the Crank-Nicolson scheme.

One of the key advantages of the implicit method is that it can tolerate much larger time-steps than the explicit methods. In particular for the explicit schemes, the time-step must be limited for stability reasons. In this work the CFL Number is used as the stability criterion.

2.4.1.1 CFL Number

The Courant, Friedrichs, Lewy (CFL) number¹⁰⁰ is a measure of the progression of the flow through an individual element within a particular time-step. The CFL number is calculated as:

$$CFL = \frac{|u| \Delta t}{\Delta x} \quad (2.67)$$

Explicit schemes are linked to the previous time-step values of the variable being solved. For these schemes instability arises when the flow “jumps” an element within a single time-step. Due to geometrical considerations¹⁰¹ the CFL number should be limited to values less than or equal to those listed in Table 2.4. This limit is also known as the Courant Condition or Courant Criterion.

Dimensionality	Limit
1D	$\frac{1}{\sqrt{1}} = 1$
2D	$\frac{1}{\sqrt{2}} = 0.707$
3D	$\frac{1}{\sqrt{3}} = 0.577$

Table 2.4 – CFL Limits for different dimensionalities

The implementation of CFL number within PHYSICA is by calculating the maximum CFL number within the domain. This value is used along with the targeted CFL number to ratio the old time-step value to obtain the size of the next time-step (Equation 2.68). The maximum time-step and rate of change can also be set.

$$\Delta t = \Delta t^0 \frac{CFL_{\text{target}}}{CFL_{\text{max}}^0} \quad (2.68)$$

2.4.2 Pressure - Velocity Coupling

To solve for a variable ϕ , when convection is important, the local velocity field is required. The velocity is calculated as part of the solution process as do the other flow variables. The main source into the momentum equations is the pressure gradient. The momentum equations are intrinsically linked to each other and the continuity equation. An additional problem in solving such a set of equations are the non-linear terms contained within the convective terms of the momentum equation. Patankar and Spalding⁸⁸ originally came up with the SIMPLE solution procedure for this problem.

2.4.2.1 SIMPLE

The acronym SIMPLE stands for *Semi-Implicit Method for Pressure-Linked Equations*. This method, developed by Patankar and Spalding⁸⁸, takes a guessed pressure field from which new velocities are calculated. A corrected pressure field is then calculated through solving the variables that impact the flow field. The process starts again, and repeated until a satisfactory result is obtained.

The main approximation used in SIMPLE is the omission of velocity corrections from neighbouring elements to derive the pressure correction field. To improve convergence Patankar⁸⁷ revised this method – it is called SIMPLER, which stands for SIMPLE revised.

2.4.2.2 SIMPLER

The velocities are calculated in the same way as in SIMPLE as the pressure correction equation corrects the velocities reasonably well, but does not correct the pressure. In SIMPLER, the pressure is derived directly without the use of a correction.

2.4.2.3 SIMPLEC

Van Doormaal and Raithby¹⁰² developed SIMPLEC (SIMPLE-consistent). It is based on the SIMPLE method, and the momentum equations are manipulated so that the velocity correction within SIMPLEC omits terms that are less significant than those omitted in the SIMPLE formulation.

2.4.2.4 Concluding Remarks

SIMPLE is a straight forward procedure to implement and has been used widely in CFD calculations. The improved calculation of the pressure field in SIMPLER is reported to give a 30 - 50% saving of computer time whilst using 30% more equations and is therefore used as the default in many commercial CFD codes⁸⁸. The further refined methods (as such as SIMPLEC) have varying usefulness depending on how closely the momentum and other scalar equations are coupled.

The SIMPLEC method is used in this work for pressure correction. The SIMPLEC method is default method used within PHYSICA, alternatively the SIMPLE algorithm has also been implemented.

2.4.3 Unstructured Code

PHYSICA is a Finite Volume – Unstructured Mesh (FV-UM) code. Traditionally CFD codes have used meshes that are constructed in a structured way. This allows for the code to explicitly know how the elements are connected together. Unstructured codes take approximately 4 to 4.5 times as long⁹ to perform the calculation as a structured code. Unstructured codes however are more economical in other ways, in particular for complex geometries that are unsuited to structured meshes.

PHYSICA was selected due to its functionality in being able to model the various physical phenomena present in the system examined. The meshes generated in this work are essentially structured meshes.

2.5 Free-surface

Free-surface modelling is used to predict the location of material in the domain as the surface is free to move due to the flow, sources and sinks of the fluid. In this work a free-surface is calculated for the location of the slag in a rotating furnace. A free-surface is calculated using a scalar marker variable (ϕ). The biggest problem that has to be addressed with free-surfaces is the numerical smearing of the free-surface variable. This occurs when any face of an element contains fluid, as it can influence all of the other faces within the element.

In the Scalar Equation Algorithm (SEA)^{103,104} the tracking variable or fluid marker ranges between 0 and 1, with a value of 1 indicating that the element is completely occupied by the fluid. Equation 2.69 is solved to obtain the values of ϕ throughout the domain.

$$\frac{\partial \phi}{\partial t} + \underline{u} \cdot \nabla \phi = 0 \quad (2.69)$$

To limit the numerical smearing in the calculation of free-surfaces within PHYSICA the advection of ϕ uses one of the following schemes:

- Upwind;
- Van Leer; or
- Donor-Acceptor Method.

The Upwind and Van Leer methods have already been discussed in the treatment of differencing schemes.

2.5.1 Donor-Acceptor Method

In the Donor-Acceptor¹⁰⁵ method the upwind element is termed the donor, whilst the downwind element is termed the acceptor. The method calculates the normal to the free-surface interface through the use of derivatives¹⁰⁶. This information is then used to calculate the fluxes through individual faces. One of the disadvantages of the donor-acceptor method is that it can not provide detailed information about the free-surface within a control volume¹⁰⁵.

2.5.2 GALA

The GALA (GAs Liquid Analyser) algorithm can also be employed to help in the calculation of the free-surface. The GALA algorithm takes the continuity equation

$$\frac{\partial \rho}{\partial t} + \nabla \cdot (\rho u) = 0 \quad (2.70)$$

and rewrites it in a form that conserves volume rather than mass. With ϕ ranging from 0 to 1 the density can be expressed as

$$\rho = \rho_1 + \phi(\rho_2 - \rho_1) \quad (2.71)$$

and when this is substituted into Equation 2.70 gives

$$\frac{\partial \rho_1}{\partial t} + \frac{\partial \phi(\rho_2 - \rho_1)}{\partial t} + \nabla \cdot (u \rho_1) + \nabla \cdot (u \phi(\rho_2 - \rho_1)) = 0 \quad (2.72)$$

and if the density of each fluid is assumed to be constant

$$(\rho_2 - \rho_1) \frac{\partial \phi}{\partial t} + (\rho_2 - \rho_1) \nabla \cdot (u \phi) + \rho_1 \nabla \cdot (u) = 0 \quad (2.73)$$

given Equation 2.69 produces the volume conservation equation

$$\nabla \cdot u = 0 \quad (2.74)$$

2.5.3 Stability

For numerical stability it is generally advisable to keep the Courant Number below 0.35. The net effect of this constraint is that the time-steps can become quite small for small meshes – leading to long simulation times.

2.6 Solidification

For the numerical modelling of the phase change process, the common approach is to modify the governing equation for energy – Enthalpy (Equation 2.76) or Temperature¹⁰⁷ (Equation 2.75). Solidification is a coupled system, linking the liquid fraction with the temperature and flow conditions. This is achieved through the use of extra source terms in the heat and momentum governing equations to account for the latent heat and presence of solid material respectively.

$$\frac{\partial(\rho C_p T)}{\partial t} + \nabla \cdot (\rho u C_p T) = \nabla \cdot \left\{ \left(k + \frac{C_p \rho v_l}{\sigma_t} \right) \Delta(T) \right\} + S_T \quad (2.75)$$

$$\frac{\partial(\rho H)}{\partial t} + \nabla(\rho u H) = \nabla \left\{ k \Delta \left(\frac{H}{C_p} \right) \right\} + \nabla \left\{ \frac{\rho v_t}{\sigma_t} \Delta(H) \right\} + S_H \quad (2.76)$$

2.6.1 Liquid Fraction

The solidification algorithms start by calculating the liquid fraction within each cell. For pure systems the solidification occurs at a single temperature, whereas for mixtures this occurs over a temperature range with solid phases co-existing with the liquid. This transition between liquid and solid is referred to as the “mushy” region by several workers in this area.

The simplest way to equate the temperature to liquid fraction is to use a linear relationship⁵⁹ between the liquidus (T_l) and solidus (T_s) temperatures as is shown in Equation 2.77.

$$f_{liquid} = F(T) = \begin{cases} 0 & T < T_s \\ 1 & T > T_l \\ \frac{T - T_s}{T_l - T_s} & \text{Otherwise} \end{cases} \quad (2.77)$$

2.6.2 Heat Sources

On any change of phase the latent heat (L) is either used or returned from the system. To account for this, a source is added to the heat transfer calculations that is equal to the change in liquid fraction multiplied by the latent heat. This is shown in Equation 2.78.

$$-L \frac{\partial f}{\partial t} \quad (2.78)$$

To account for the transfer of latent heat, an extra source equal to the Latent Heat by the liquid fraction is multiplied by the continuity equation. Therefore this leads to the total source arising due to solidification being:

$$-L \frac{\partial f}{\partial t} - L \nabla(\rho \underline{u} f) \quad (2.79)$$

An alternative method to applying a source in this manner is to make the specific heat reflect the latent heat. Figure 2.10 shows how a temperature dependent function can reflect the specific heat. The integral, as shown by the shading in this figure, is equal to the latent heat.

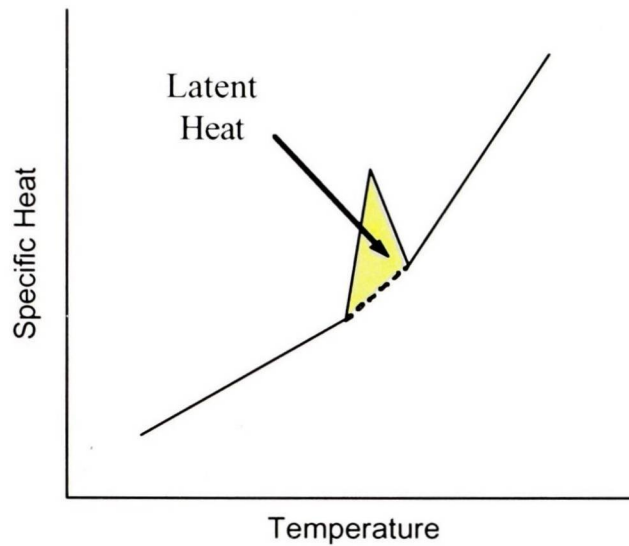


Figure 2.10 – Illustration of how latent heat can be applied to Specific Heat

To apply this heat source directly can lead to the system cycling or oscillations within the solution steps. On solidification, the latent heat is credited back to the system. This extra heat can potentially re-melt the liquid, which can then re-solidify and continue cycling in this way. To overcome this problem the Voller and Prakash method^{59,107} is used for updating the liquid fraction within PHYSICA, although there are other correction methods by Voller and Brent¹⁰⁸ that are also implemented.

2.6.3 Momentum Sources

As the liquid turns to solid, the flow is retarded by the presence of these solid phases. The technique that is used to accomplish this either modifies the viscosity of the liquid directly creating an effective viscosity, or by applying a source term to the momentum equations.

An example of the way that the effective viscosity is calculated is given in Equation 2.80⁶³. The use of this effective viscosity is suitable for the early stages of equiaxed solidification.

$$\mu_{eff} = \mu_l \left(\frac{1}{1 - F_\mu \frac{f_s}{f_c}} \right)^2 \quad (2.80)$$

$$\text{where } F_\mu = 0.5 - \frac{1}{\pi} \tan^{-1}(100(f_s - f_c)) \quad (2.81)$$

An alternative method is to approximate the flow as a Darcy flow through a porous medium²⁵. This is achieved by applying a momentum sink to the momentum equations.

$$S_D = \frac{F_D \mu u}{K} \quad (2.82)$$

The Darcy source term shown in Equation 2.82 includes a switching function F_D that tends towards zero as the amount of solids decreases. The permeability constant (K) can be calculated from the Kozeny-Carmen equation⁶³ (Equation 2.83) for regions where the solidification is dendritic.

$$K = C \frac{d^2 (1 - f_s)^3}{f_s^2} \quad (2.83)$$

where C is a constant and d is the characteristic dimension.

IMPLEMENTATION OF REFRACTORY WEAR MECHANISMS

This chapter discusses how the various refractory wear mechanisms have been implemented within the CFD code PHYSICA. The bulk of this chapter is related to the refractory wear mechanisms of: penetration; corrosion; and erosion. The second part of this chapter deals with the properties that are used in all of the models and how they are calculated within the dynamic domains used in this work.

3.1 Refractory Wear Mechanisms

The general calculation scheme is shown by the flowchart in Figure 3.1. The degree of penetration is solved using a transport equation, which is intrinsically solved with the other solved variables within PHYSICA. After the solution procedure for a particular time-step is completed, calculations are performed for the corrosion and erosion mechanisms. The Other Physics referred to in the flow chart refer to the other solved quantities: Heat Transfer; Fluid; Flow; Phase Change; and Free-surface calculations.

The time-step size is calculated from the progression of the penetration front based on a Courant Number limit and a minimum step size of 0.01s. As penetration progresses quickly in un-penetrated refractory the time-step is initialised to 0.01s. This value is then limited to values that will capture the chemistry (900s) or free-surface movement (0.4s) when this is used.

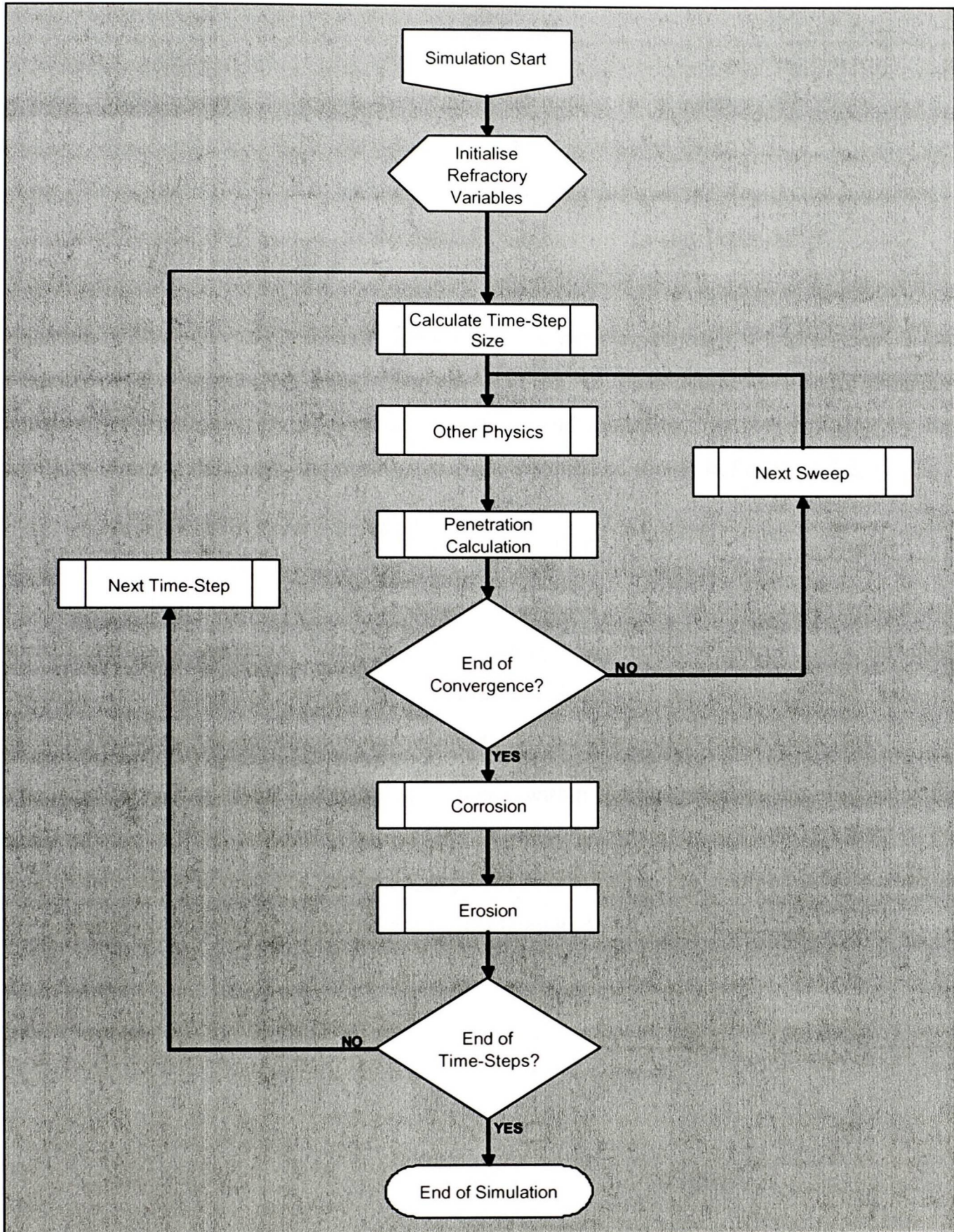


Figure 3.1 – Flowchart for Refractory Mechanisms

3.1.1 Penetration

Penetration has been examined by many authors^{21,26}, and the consensus is that the penetration of refractory is a capillary force driven flow. The rate of penetration can be calculated from Equation 3.1.

$$\frac{dl}{dt} = \frac{r\gamma \cos \theta}{4\mu l} = u_{pen} \quad (3.1)$$

where

- r is the radius of the pore in the refractory (m)
- γ is the surface tension of the slag ($\text{N}\cdot\text{m}^{-1}$)
- θ is the contact or wetting angle of the slag on the refractory
- μ is the dynamic viscosity of the slag ($\text{kg}\cdot\text{s}^{-1}\text{m}^{-1}$)
- l is the current penetration depth of slag into refractory (m)

Equation 3.1 provides the necessary progression of the slag through refractory and is the velocity of the penetration front. This velocity can be used within a general transport equation⁸⁸ formulation. By neglecting convection and assuming that the diffusion by the capillary forces is dominant, the penetration can be written as shown in Equation 3.2.

$$\frac{\partial \phi_{pen}}{\partial t} + \nabla(u_{pen} \phi_{pen}) = 0 \quad (3.2)$$

Equation 3.1 demonstrates how the penetration is affected by the viscosity, contact angle and surface tension of the slag – which are all temperature dependent. Figure 3.2 is a flowchart outlining the basic steps within the penetration calculation. As the penetration rate (or velocity) is dependent on the current penetration, this is the first step in this procedure.

The penetrating slag is not accounted for directly within the heat transfer calculations as the small amount of slag penetration would lead to a very small source term being added to the heat transfer calculations. The materials properties will adjust to the change in the location of the penetration front as the properties are recalculated as a part of the solution procedure.

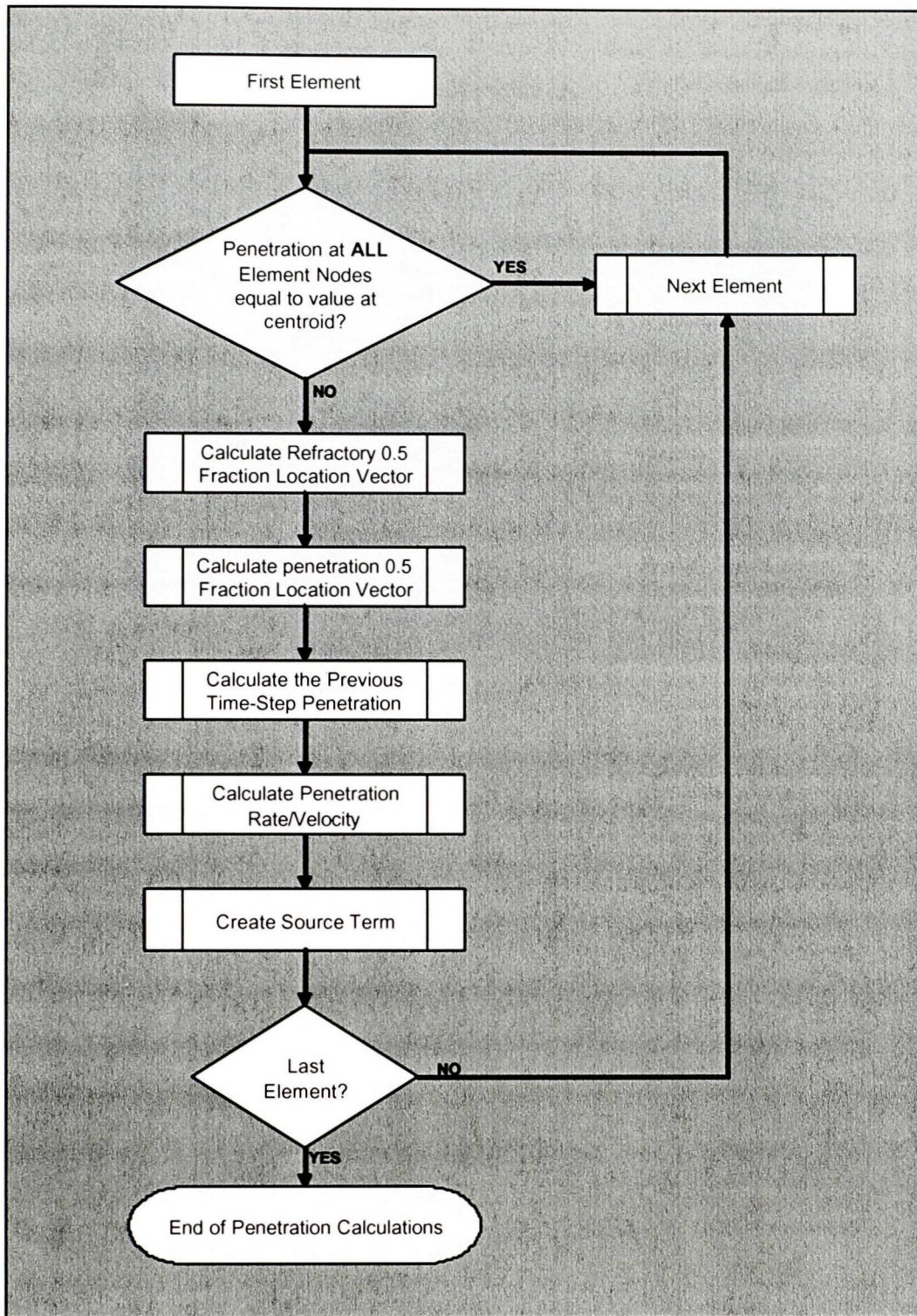


Figure 3.2 – Flowchart for the Penetration Calculation

To calculate the current penetration, vectors are calculated to locate the 0.5 fraction contours for the refractory and penetration variables. Figure 3.3 illustrates how the vectors locate the 0.5 contours for the refractory and the slag. The current penetration is easily calculated from the difference between these two vectors. To calculate the location vectors, values at the nodes or corners of the control volumes are determined by averaging the adjacent elemental values. If there is no difference between the value at the centroid and nodes, the next element is examined.

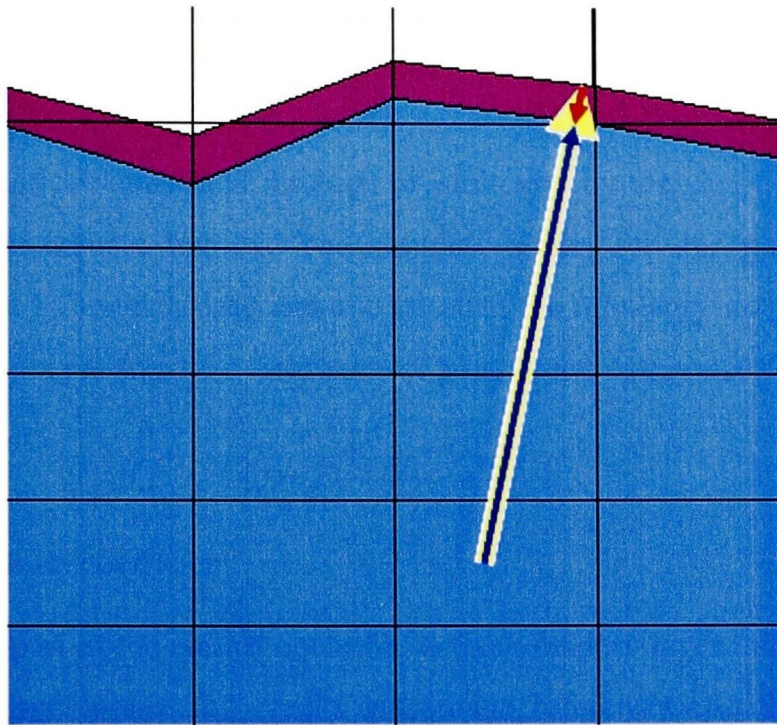


Figure 3.3 – Location Vectors

The velocity of the slag penetration front is calculated using Equation 3.1. Equation 3.3 is the general form of the transport equation. The difficulty of the way that the convection term is implemented in PHYSICA is that it uses the velocity that is calculated for the bulk fluid in this way:

$$\frac{\partial(\rho\phi)}{\partial t} + \nabla(\rho\mathbf{u}\phi) = \nabla\{\Gamma_{\phi}\Delta\phi\} + S_{\phi} \quad (3.3)$$

The calculated penetration velocity needs to be substituted for the bulk velocity. The simplest way to achieve this is to turn off the convection term, along with the diffusion term that is not required, and insert a source term to represent the convection of the penetration front through the domain. The transient term shown in Equation 3.3 is adjusted to remove density from the coefficient.

The source term for the convection of the solved penetration variable is:

$$S_{pen} = \sum_{nb} u_{pen}|_f (\phi_i - \phi) \quad (3.4)$$

To calculate the penetration velocity at each face (Equation 3.5), the magnitude of the velocity is multiplied by the unit penetration vector. The dot product with the opposite of the unit outward normal to the face resolves the vector into the direction of the face. As the penetration of refractory by slag is essentially a one-way process, the velocity through the face is limited to positive values only.

$$u_{pen}|_f = \max(u_{pen} \cdot \hat{p} \cdot -\hat{n}, 0) \quad (3.5)$$

3.1.2 Corrosion

Corrosion is the chemical attack and removal of refractory by the chemical reaction with the slag that comes into contact with it. The simplest model for this process is the Nernst Equation²¹ (Equation 1.7) which describes the rate that the refractory will dissolve into slag in terms of how far the slag is from the saturation of a particular component within the slag.

$$J = D \frac{(C_{sat} - C_{slag})}{\delta} \quad (3.6)$$

where D is the Diffusion coefficient.

The other important part of the Nernst equation, is the boundary layer thickness (δ). The slag is reacting within small pores and cracks within the refractory and the products of these reactions will build up in these sites unless they are removed through some process – most likely to be chemical diffusion. Therefore common slag practice involves ensuring that the slag is close to the saturation level for the major refractory component. On the macro scale, the boundary layer that will form between the refractory and the bulk slag will be small due to the flow of slag within these models.

To fully model the complete description of refractory configuration would entail a significant amount of detail regarding the location of pores, and the arrangement of phases and phase boundaries. This would lead to a large number of variables within the model. To model the corrosion mechanisms, it was decided to take an overall view of the interaction between the refractory and slag.

The simplified model is based on the fact that for the reactants involved (slag and refractory) will need to be held at or above a particular temperature for a period of time to be fully reacted. This process is analogous to cooking food – where the uncooked food is kept at an elevated temperature for a period of time. Supporting evidence for this formulation includes the common observation that higher operating temperatures of furnaces lead to increased refractory wear. Arrhenius law¹⁰⁹ (Equation 1.9) gives the relationship of reaction kinetics to temperature.

$$k = k_0 e^{\frac{E}{RT}} \quad (3.7)$$

Finally thermodynamic equilibrium calculations using MTDATA⁸² for a mixture of primarily refractory and slag for a range of temperatures indicate the phases that are present after the

system has been held at the particular temperature for a period of time. Figure 3.4 shows a plot of data obtained from calculations performed using MTDATA for a mixture of 90% Magnesium-Chrome refractory with 10% of a typical Hismelt slag.

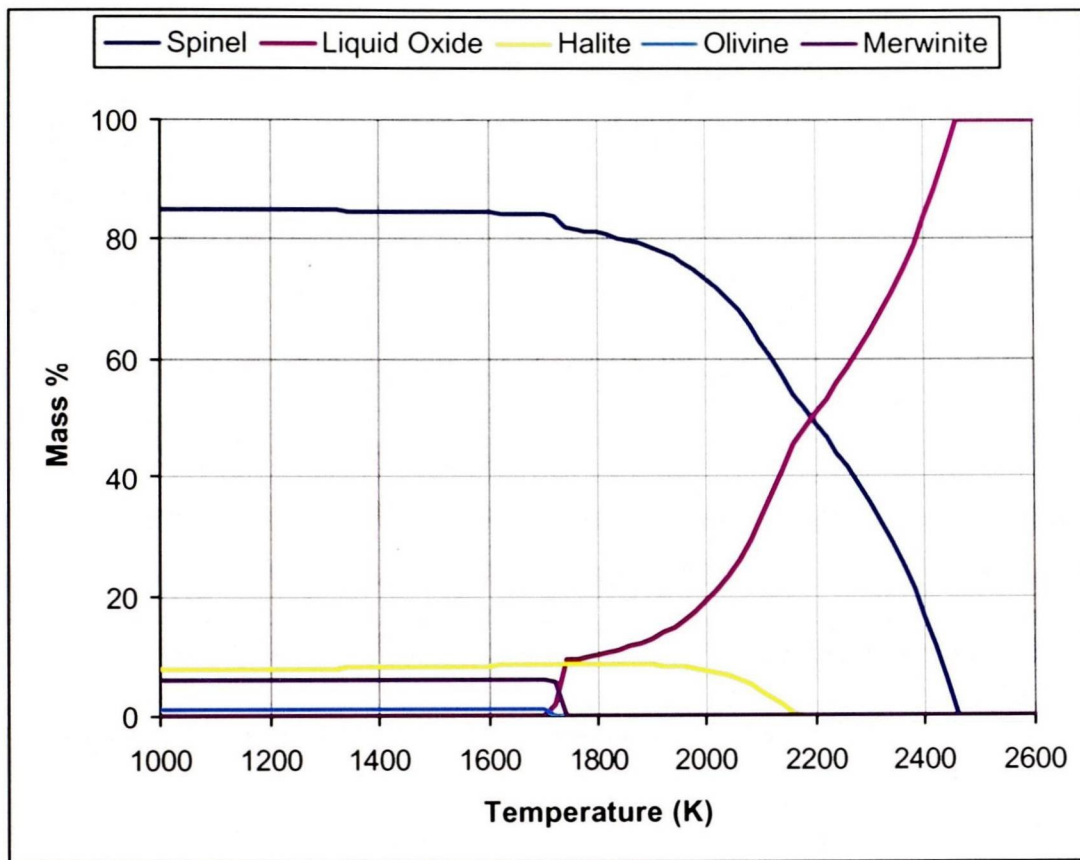


Figure 3.4 – MTDATA plot of phases present against temperature

To implement this formulation a method is required to track the temperature history of the refractory. This has been achieved by integrating across the volume of refractory that is within the reacting temperature range with respect to temperature and time. From the results of the MTDATA calculation for Magnesium-Chrome refractory and Hismelt slag (Figure 3.4) the reacting temperature range is 1680 – 2400K.

As the kinetics of the reactions involved will follow Arrhenius Law (Equation 1.9), a scaling function is used which is substituted in place of temperature in the integral. The constants (k_0 and E) are set to give 0.1 and 100 at the extremities of the reaction temperature range as is shown in Figure 3.5. The upper limit of 100 is used in determining, from the calculated integral, when and how much refractory is to be removed.

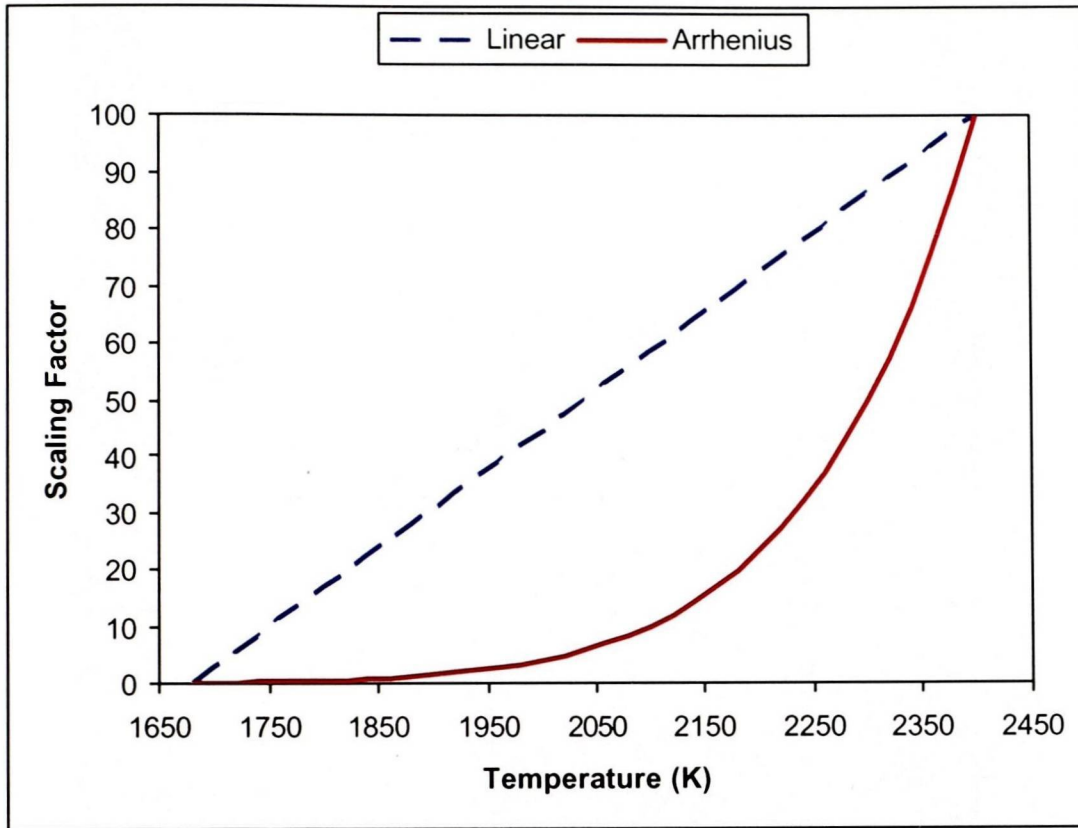


Figure 3.5 – Comparison of Arrhenius and Linear Scaling Functions

The Time-Temperature Integral (ζ) therefore can be written as:

$$\zeta = \sum_{n=0}^{timesteps} \left(k_0 e^{\frac{-E}{RT}} \times Volume_{Re_{act}} \times \Delta t_n \right) \quad (3.8)$$

To make use of this value, a small fixed volume is used to calculate the value that the integral needs to reach for this volume of refractory to be corroded. This quantity has been termed the “hurdle” value, which is determined in the following manner.

$$\zeta_{Hurdle} = 100 \times Volume_{Resolution} \times Reaction\ Time \quad (3.9)$$

The reaction time is a time factor that accounts for the period of time it takes for the reaction to occur. This factor has been selected on the basis of experience in heating up furnace linings gradually. At particular points of this process, the temperature is held for 1 – 2 hours to allow the phases to attain their equilibrium state. As this is expected to be in excess of the actual time, a value of 30 minutes has been used for this reaction time factor.

Figure 3.6 shows the sequence of the calculation steps for the corrosion mechanism, which are performed at the end of each time-step. Refractory is removed in multiples of the hurdle value. Once the refractory has been removed, the Time-Temperature integral is reduced to account for the refractory that is removed.

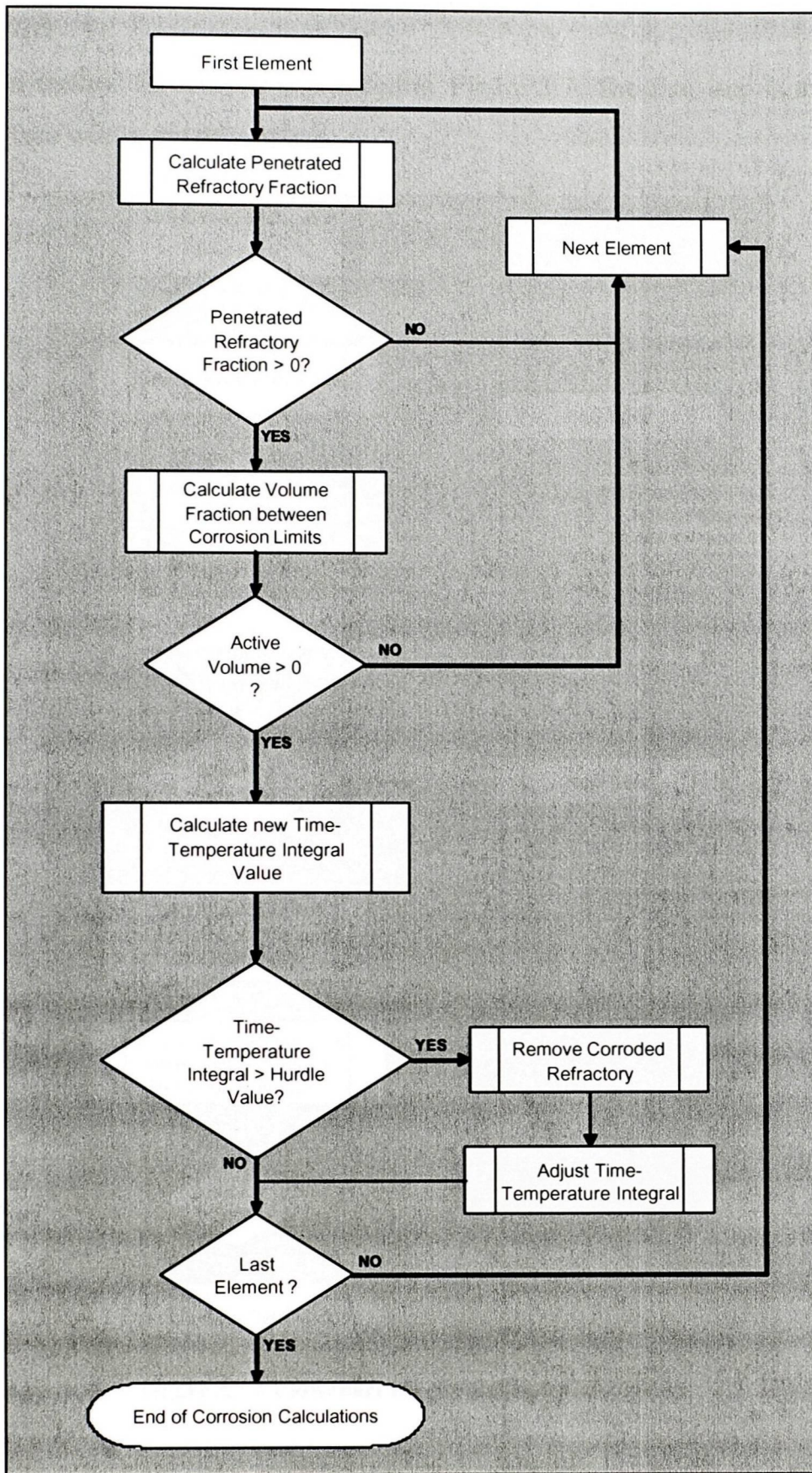


Figure 3.6 – Flowchart for the Corrosion Calculation

3.1.3 Erosion

The calculation method for erosion is outlined in Figure 3.7. The first step is to calculate the shear on each face within the domain.

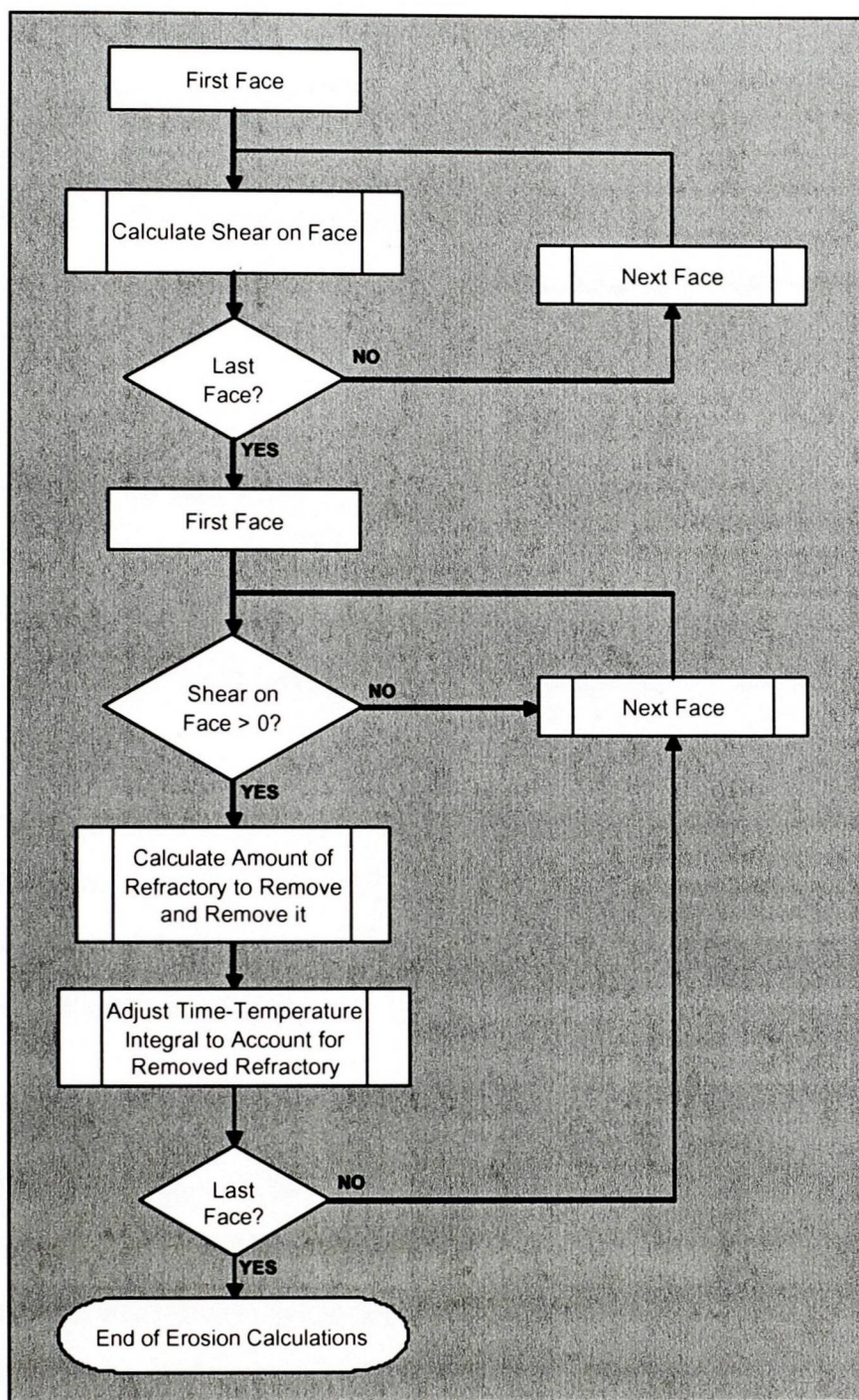


Figure 3.7 – Flowchart for the Erosion Calculation

For virgin unaffected refractory the Hot Modulus of Rupture is significantly greater than the shear that will be developed for a flow of slag moving at one or two meters per second. The structure of the refractory must be weakened by the penetrating slag that has reacted with the refractory structure. From the modelling of soil erosion⁴⁶, above a critical shear soil is removed and carried away by water. The same approach has been taken here where an upper and lower shear limit are set. A linear relationship between the lower and upper limit (Equation 3.10) is established to determine what amount of refractory can be removed.

$$f_{removed} = \begin{cases} 0 & \tau \leq \tau_{lower} \\ 1 & \tau \geq \tau_{upper} \\ \frac{\tau - \tau_{lower}}{\tau_{upper} - \tau_{lower}} & \text{Otherwise} \end{cases} \quad (3.10)$$

Erosion occurs by shaving off layers from the surface. The maximum thickness of the layer that can be removed is set as a parameter. As erosion is a transient process, this Refractory Removal Rate (RRR) is the thickness removed per unit of time (ms^{-1}). The refractory depth that potentially can be removed from an element in a particular time-step can be calculated from Equation 3.11.

$$R_{removed} = f_{removed} \cdot RRR \cdot \Delta t \quad (3.11)$$

As refractory can not be eroded when it is un-penetrated, the depth to be removed is checked to ensure that it has in fact been penetrated by slag. If the penetrated depth is smaller than the erosion depth calculated, the refractory removed is limited to the penetrated refractory. When refractory is removed, the time-temperature integral is adjusted to account for the removal of this refractory.

In this work corrosion is not a significant effect due to the slag practice of saturating the slag with the major component of the refractory. For other refractory systems, consideration needs to be given to the effect that the removal of refractory by the corrosion mechanism may have on the erosion predicted by the model.

3.2 The Dynamic Domain

As refractory is being worn away with time, the way that some elements work is changing. As refractory is removed, area becomes available for the slag to flow through. This dynamic nature of the mesh is tracked by using a variable to measure the fraction of each material within each element of the domain. These tracking variables are:

- Refractory (ϕ_{ref})

The refractory variable simply tracks the amount of refractory within each element regardless of whether it has been penetrated by slag or not.

- Penetration (ϕ_{pen})

As penetration is a diffusion like process, the penetration variable measures the amount of each element that has slag OR penetrated

refractory. This approach allows the use of the generic transport equation to model the progress of the slag penetrating into the refractory.

The tracking variables are updated at the end of each iteration. At the start of each iteration, the various properties are calculated based on the values of these tracking variables for each element – using a weighted average. Therefore as the domain changes, the properties within each element adjust to account for these changes.

The consequence of having the domain dynamically changing in this way is that a method is required to prevent flow within elements containing solid material. This is achieved through using an extra source term added to the momentum equations to slow and/or stop flow where solid material is present.

3.2.1 Refractory Presence Momentum Sink Term

To limit or stop flow within cells that contain an amount of refractory, a Darcy sink term is applied to the momentum equations. Darcy originally produced an empirical relationship based on experiments that he carried out for steady flow in a vertical column of homogeneous sand²⁵. A generalised form for Darcy's Law is:

$$\underline{q} = K \underline{u} \quad (3.12)$$

Darcy's law is only valid when the Reynolds number, based on the grain size of the porous media is below some value between 1 and 10. For the slag and refractories within this study the Reynolds number is approximately 0.0004.

In metal casting the permeability constant can be calculated based on the Kozeny-Carmen Equation which is primarily driven by the dendrite spacing in the mushy or semi-liquid region. The default permeability in PHYSICA is set to 1.0×10^{-10} which is designed for metal casting work. Nield and Bejan¹¹⁰ have tabulated permeability's (K) for various materials. In particular for concrete with a porosity of 0.12-0.34, its permeability is in the range from 4.8×10^{-15} to $2.2 \times 10^{-13} \text{ m}^2$.

The general form of the Darcy source as implemented within PHYSICA, using the default switching function, is shown in Equation 3.13. To prevent divide by zero errors occurring the liquid fraction value is bounded such that it never is zero in this equation, but rather a very small value.

$$S_D = \frac{\mu V}{K \frac{f_{liq}^3}{(1 - f_{liq})^2}} \quad (3.13)$$

When implementing this source, it became apparent that the source alone was insufficient to stop flow. The pressure correction equation was causing imbalances within the solution by trying to overcome the apparent continuity error with a large pressure correction. Adjustments to the code were required to make the interface between the refractory and slag act like a material boundary, so that PHYSICA would stop the pressure corrections at this point in the domain. This required a further variable that was used to indicate the location of the interface to the code. This variable was used in place of the standard method of examining the geometry for changes in the material.

3.3 Timescales

Due to the different phenomena involved in freeze layers and refractory wear different timescales apply. To adequately model these phenomena the time-steps must be able to resolve the different timescales. In practice the time-step is limited at the start by the fast initial penetration of virgin refractory by slag. After the penetration has slowed the time-step is limited by the chemical reaction limit.

3.3.1 Flow

Flow is an important phenomenon in the solution of the situations modelled in this work. The time-step must be small enough to capture the flow through the elements within the domain. This is particularly important for the cases where a scalar variable is solved explicitly, as is commonly the case for free-surface calculations.

The Courant, Friedrichs, Lewy (CFL) number is a measure of the flow through individual elements of the computational domain. In the free-surface calculations performed for the rotary slag test, the target CFL number is 0.3.

Within the penetration mechanism, the CFL number is also used to maintain stability within the calculations. On initial contact of refractory with slag, the penetration is relatively rapid to

the penetration that occurs after this initial period. The time-step is limited to produce a maximum progression of the penetration front through any control volume to 10%. To ensure that the penetration is manageable in the very first time-step, the time-step is set to 0.01s.

3.3.2 False Time-stepping

An alternative method to using quite small time-steps is to use false time stepping. This allows the flow calculations to sub-step in time to be able to properly account for the timescales involved.

3.3.3 Reactions

Refractory reactions do not necessarily take place instantly. The assumption made in setting up the corrosion mechanism is that if refractory is held at a sufficient temperature for an adequate period of time that it will be corroded by the slag. If the time-step is too large, the corrosion may be overlooked. In this work the time-step is limited to half the corrosion time factor (in this work the corrosion time factor has been set to 1800s - see section 3.1.2 for details regarding the time factor) which equals 900s.

3.4 Physical Properties

The physical properties of the materials are important to the accuracy of the final result from these models. Particular attention has been paid to the temperature dependence of some of these properties that has a direct impact on the refractory wear mechanism models.

The various material properties are calculated by performing a weighted average based on the volume fraction that is occupied by each of the constituent parts within the calculation. This is particularly important as, in this work, the domain is changing dynamically due to the wear and solidification that is taking place.

3.4.1 Materials

There are several complex materials in this problem that have different properties. These include slag, refractory and the furnace construction materials copper and steel. The values of their physical properties are summarised in this section, whilst a description of how these values have been used in this work is contained in the following sections.

3.4.1.1 Slag

Table 3.1 lists the slag compositions used in this work. The slag composition is a typical slag analysis taken from the HIs melt pilot plant test work. The Rio Tinto Iron & Titanium (RTIT)

slag analysis is the composition of the slag that was used in the rotary slag refractory wear test.

Component	Composition (mass%)	
	Hismelt	RTIT
Fe ₂ O ₃	4.3	
FeO		45
Al ₂ O ₃	16.64	5
CaO	38.85	27
Cr ₂ O ₃	0.036	
MgO	8.47	
MnO	0.343	
P ₄ O ₁₀	0.667	
S	0.119	
SiO ₂	30.76	11
K ₂ O	0.021	
TiO ₂	0.85	10
V ₂ O ₅	0.026	

Table 3.1 – Slag Compositions

The slag practice at Hismelt was to maintain approximately 8-9% MgO in the slag to minimise the corrosion of the Magnesium-Chrome refractories by the slag. The slag basicity was also controlled to be approximately 1.25. The slag used in this work has a basicity of 1.26.

The RTIT slag is a significantly different slag to the Hismelt slag. The processes employed at RTIT use electric arc furnaces to smelt ores with a high TiO₂ content. The slag has a high Iron Oxide (FeO) content which is known to be quite corrosive to refractories. The Iron reported in the Hismelt slag will actually represent some FeO due to the method that is used to analyse the slag sample.

3.4.1.2 Refractory

The refractories examined in this work are listed in Table 3.2. The ANKROM-S56 is the Magnesia-Chrome refractory used in the Hismelt pilot plant trials. The ANKOCAST is a spinel forming high Alumina refractory that Hismelt have been looking at using as a replacement for the Chromia* containing castable refractory that they currently use on their water-cooling panels. MARCAST-561-SP is a similar refractory that RTIT have tested in a rotary slag refractory wear test that has been used as part of the validation of this work.

* The leaching of Cr⁶⁺ into groundwater has been found to have serious health implications and therefore the disposal of materials containing Chromia, as such as spent refractory linings, is becoming cost prohibitive.

Component	Composition (mass %)		
	ANKROM-S56	ANKOCAST-ZV97M	MARCAST 561 SP
MgO	59	6	5.9
Al ₂ O ₃	6	92	92.7
Cr ₂ O ₃	19		
SiO ₂	0.5	0.8	1.1
Fe ₂ O ₃	14	0.1	
Na ₂ O		0.2	
CaO	1.3		0.1

Table 3.2 – Refractory Compositions

Typical values for Fire bricks used as a safety lining were not obtained as they are not exposed to the refractory wear mechanisms. Typical transport properties were used for the heat transfer calculations.

The ANKROM-S56 is magnesia-chrome brick used in the Hismelt horizontal and vertical vessels. It is manufactured using pressure and temperature to produce a dense brick with a small amount of porosity. The other two refractories being castable refractories will be supplied in a dry powdered form. The powder is then mixed with water and poured into a mould or sprayed on to the required surface in a technique called gunning. Before use the refractory, both castable and bricks, will be preheated in the furnace in stages from 500°C to 1500°C. This is performed to cure the castable by driving out any remaining moisture, but also to stabilise the phases present within the refractory structure.

3.4.1.3 Miscellaneous

Apart from the refractory and slag, air and steel values are used in some of the models. Typical transport properties were obtained for these materials. Table 3.3 contains the properties used in this work for all of the materials.

Property	Refractory			Slag	Air ¹¹¹	Steel ¹¹²
	ANKROM-S56 ⁴⁷	MARCAST 561 SP ¹¹³	Fireclay Brick ¹¹⁴			
Density ρ kg.m^{-3}	3270	3000	2000	2600	$= \frac{MP}{RT}$	7854
Viscosity (Dynamic) μ $\text{kg.s}^{-1}\text{m}^{-1}$	NOT FLOWING			$= \frac{3400}{T} - 1.32$	6.63E-05	NOT FLOWING
Thermal Conductivity k $\text{W.m}^{-1}\text{K}^{-1}$	$= f(T)$	2.08	0.3	1.0^{115}	60.5	0.128
Specific Heat C_p $\text{J.kg}^{-1}\text{K}^{-1}$	921	921	960	1255	1307	434

Table 3.3 – Values used for Material Properties

3.4.2 Density

The refractory and steel densities are well defined by measurements. The density of air has been simply calculated using the ideal gas law (Equation 3.14) assuming an average molecular weight of 29.

$$\rho = \frac{MP}{RT} \quad (3.14)$$

The slag density within the HIs melt vessel has been subject to considerable conjecture over time. In particular the degree to which the slag is aerated impacts on the effective density. The 2600 kg.m^{-3} figure was arrived at after analysing several campaigns to calculate the amount of slag in the vessel up to the slag notch.

3.4.3 Viscosity

The viscosity of air¹¹⁶ is taken to be a constant value of 663×10^{-7} Pa.s which is the value taken at 1900K. This is approximately the temperature of the flame (and it is assumed that the air is quite close to this temperature also). The slag viscosity is treated in the section discussing the properties of slag

3.4.4 Thermal Conductivity

The values for thermal conductivity were sourced from various references and technical data sheets obtained from suppliers. As the refractory suppliers had measured⁴⁷ the thermal conductivity for ANKROM-S56 (Figure 3.8), a polynomial (Equation 3.15) was fitted to

reflect this data. For other thermal conductivities in this work constant values were used as the temperature range for these materials is quite narrow.

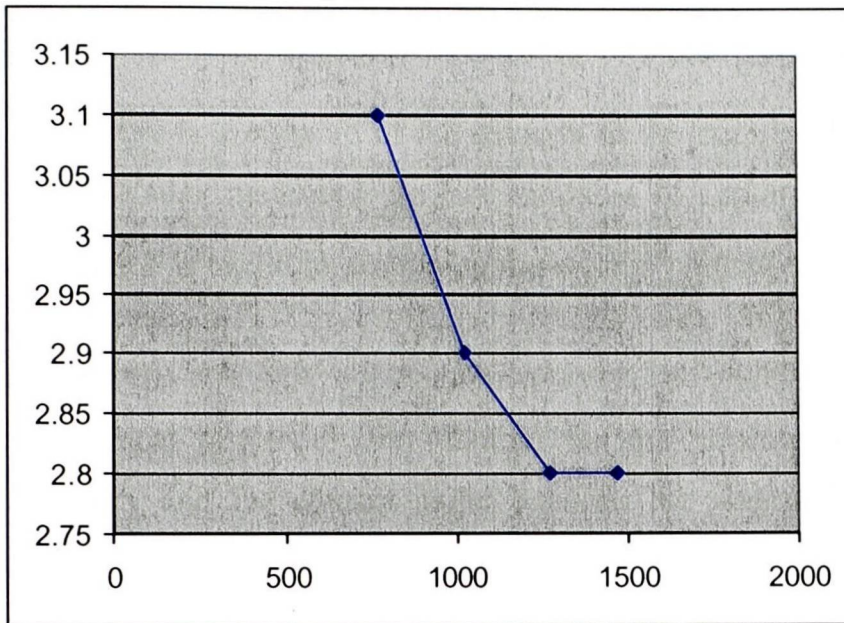


Figure 3.8 – Measured Thermal Conductivity Values

$$k = 5.6137 - 0.0061T + 5.0 \times 10^{-6} T^2 - 2.0 \times 10^{-9} T^3 + 2.0 \times 10^{-13} T^4 \quad (3.15)$$

3.4.5 Specific Heat

As for thermal conductivity, values have been sourced from data sheets and other standard references. The thermal conductivity for the slag was calculated based on the composition and the values for its constituent compounds.

3.4.6 Refractory Properties

Specific properties of the refractories are required for the refractory wear mechanisms. This includes the porosity and pore diameter of the refractory which is used in the penetration mechanism. The hot modulus of rupture is not used directly in the erosion mechanism as there is no simple way to link the modulus of rupture measured for virgin refractory to the shear that would be required to erode the refractory. To calculate this shear would necessitate the modelling of the complex phase and pore structure of the refractory.

The open porosity for the ANKROM-S56 magnesia-chrome refractory after impregnation is 14% by volume⁴⁷. No values have been obtained for the castable refractories and the same porosity (14%) is used for these materials also.

Veitsch-Radex indicate¹¹⁷ that the pore diameter for the ANKROM-S56 bricks ranges from 10 μ m to 30 μ m with an average pore diameter of 18 μ m. Experimental data from an induction furnace test, described later, is used to set the pore diameter. For the ANKROM refractory the

lower limit of 10 μm is used to match the induction furnace results. As there is no data available for the pore diameter for the MARCAST refractory, the same pore diameter is used. In reality it is likely to be about the same as for the ANKROM pre-cast shapes or slightly larger.

The hot modulus of rupture is a measure of the strength of the material. For the ANKROM-S56 refractory Veitsch-Radex measured the hot modulus of rupture to be 6 $\text{N}\cdot\text{mm}^{-2}$ at 1500°C⁴⁷. This information is useful in examining the erosion properties of the refractory.

3.4.7 Slag Properties

Additional thermo-chemical properties are required for the penetration mechanism. The surface tension, viscosity and the contact angle between the slag and refractory are all temperature dependent.

3.4.7.1 Surface Tension

Nexhip and Sun⁷⁷ measured the surface tension for a slag with composition by weight of 28% CaO – 42% SiO₂ – 20% Al₂O₃ – 10% MgO whilst measuring the dynamic wetting of refractories. This is not a perfect match for the Hismelt slag with the basicity being 0.67 (compared to 1.26) although the MgO and SiO₂ content are reasonably close. As no other data closer to the slags used in this work has been found, this is used as the best information available. A linear relationship (Equation 3.16) is fitted to this data, as used in this work.

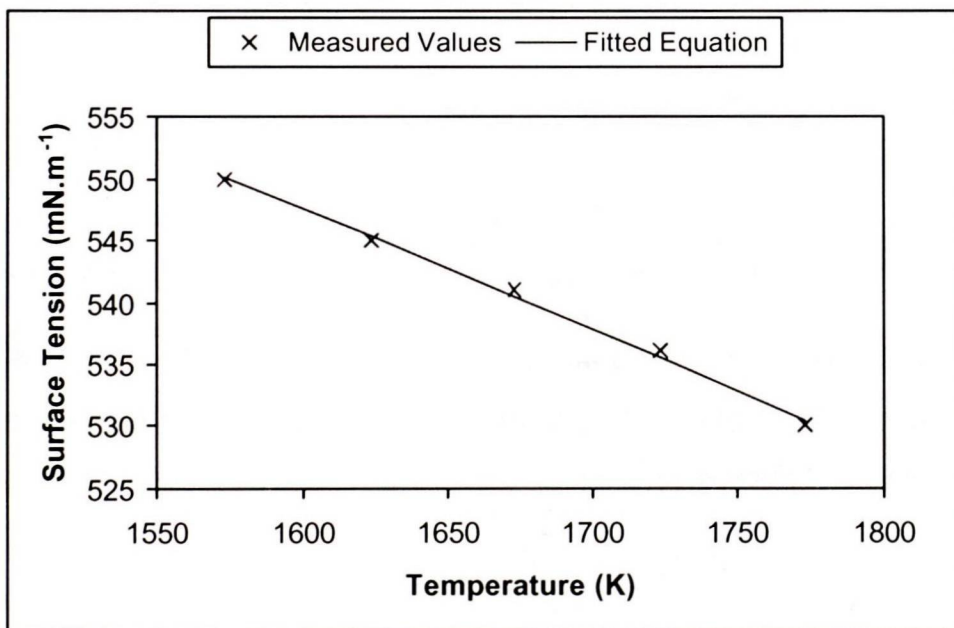


Figure 3.9 – Measured and Fitted Surface Tension Values

$$\gamma = 0.554611 - 2.88846 \times 10^{-6} T \quad (3.16)$$

3.4.7.2 Contact Angle

There is limited published work on the contact angle of slag with refractories. The use of the contact angle is in the penetration calculations, of which the fundamental equation is that of capillary action. Equation 3.17 is used to calculate the penetration front velocity and takes the cosine of the contact angle.

$$\frac{dl}{dt} = \frac{r\gamma \cos\theta}{4\mu l} = u_{pen} \quad (3.17)$$

As the contact angle tends towards 90° the cosine of the angle tends to zero. As the slag solidifies the penetration stops. Therefore for temperatures below the liquidus the contact angle is set to 90° preventing penetration. A plot of the liquid and solid fraction calculated for a typical HIs melt slag by MTDATA is shown in Figure 3.10.

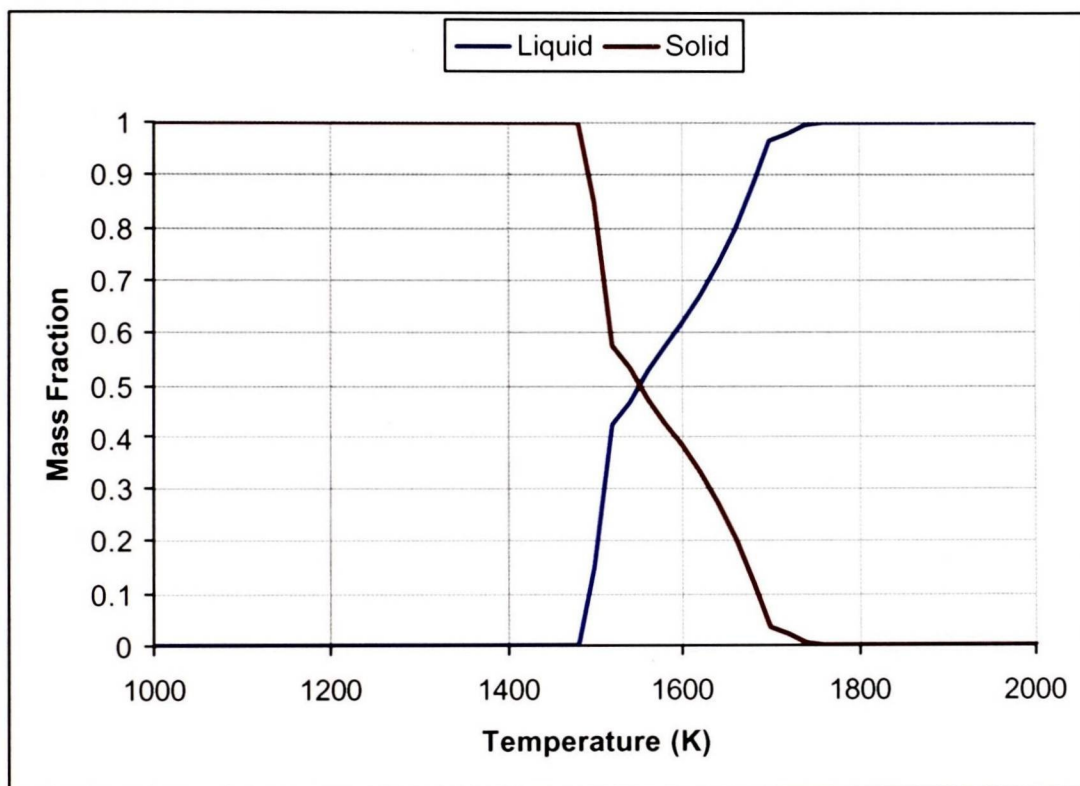


Figure 3.10 – MTDATA plot of Solid and Liquid Phase Totals for HIs melt Slag

To complete the description of the Contact Angle, modelling was carried out on the various systems where penetration information is available to find values that produce results that matched the observed data. Figure 3.11 shows the piece-wise equation used in this work.

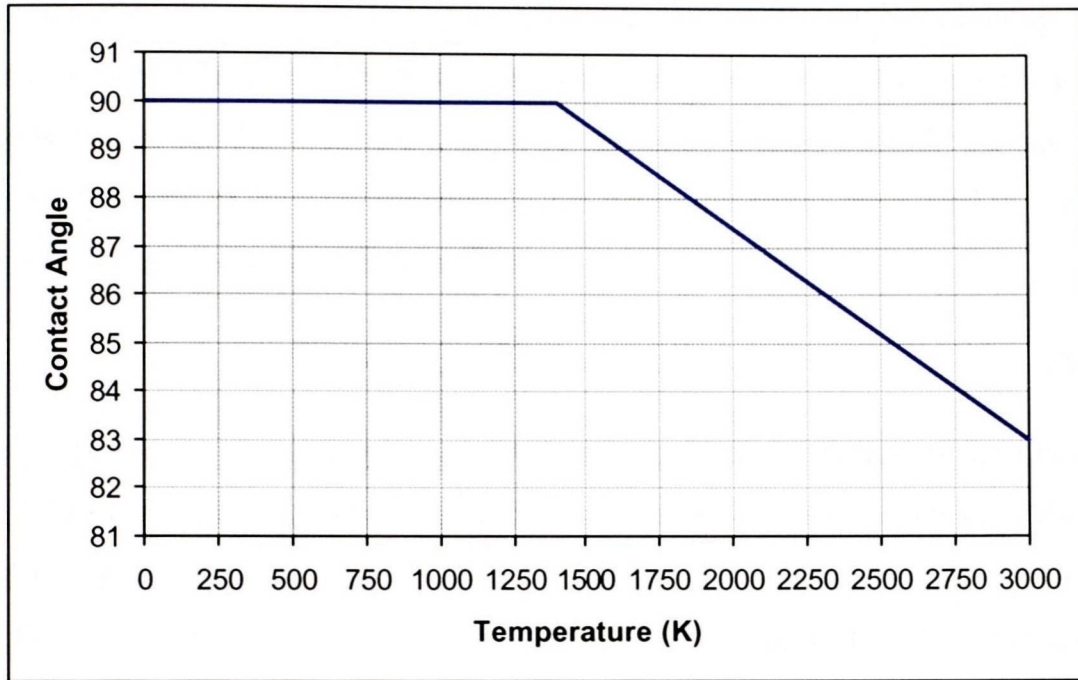


Figure 3.11 – Equation used for Contact Angle

3.4.7.3 Viscosity

The viscosity of slag is temperature dependent. Zhang and Jahanshahi⁷⁶ have measured viscosities for various slags in their work towards a generic approach to modelling slag viscosities. Some of their results are shown in Figure 3.12.

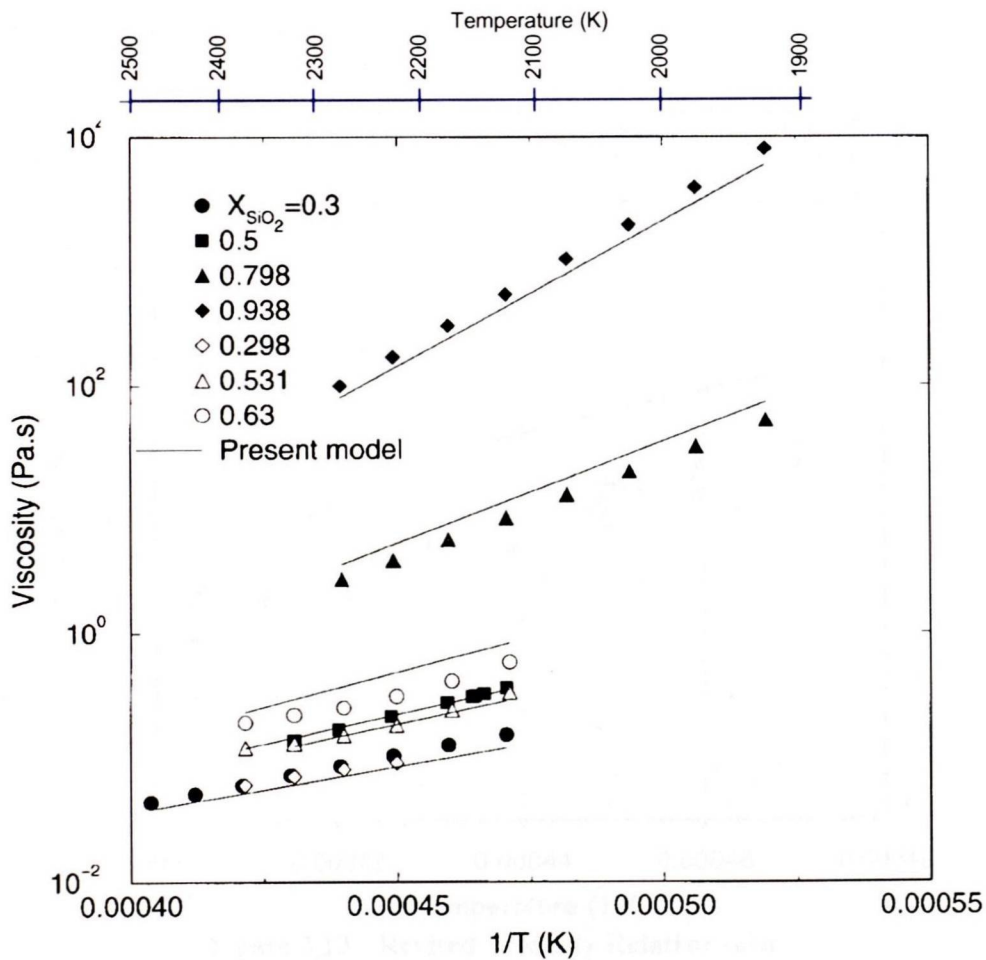


Figure 3.12 - Slag Viscosity Measurements by Zhang and Jahanshahi⁷⁶

One of the slags that they have measured is a Lime-Alumina-Silica slag containing 30% Silica – a slag that is similar to the HIs melt slag composition used in this work. In Figure 3.12 the measured viscosities for this slag are shown by the filled circles towards the bottom of the figure. To use this data in the CFD models for this work, the points were read by hand and the following linear relationship was developed.

$$\mu = \frac{3400}{T} - 1.32 \quad (3.18)$$

Sensitivity of Results to Slag Viscosity. After much work, the accuracy of the fitted equation (Equation 3.18) for viscosity was questioned. The last part of this chapter describes how the effect of the slag viscosity was investigated. By adjusting the contact angle relationship, the degree of freedom within the penetration mechanism, the results reflect the observations from the induction furnace test.

The accuracy of the fitted viscosity relationship arose from the use of a free digitising program Windig¹¹⁸ to more accurately read from the scanned image of the data presented by Zhang and Jahanshi in Figure 3.12. The digitised data has been plotted in Figure 3.13 along with the previous relationship (Equation 3.18) and a newly fitted linear relationship (Equation 3.19) to the digitised data. The error bars on the measured points give an indication of the errors involved in the digitising of the figure.

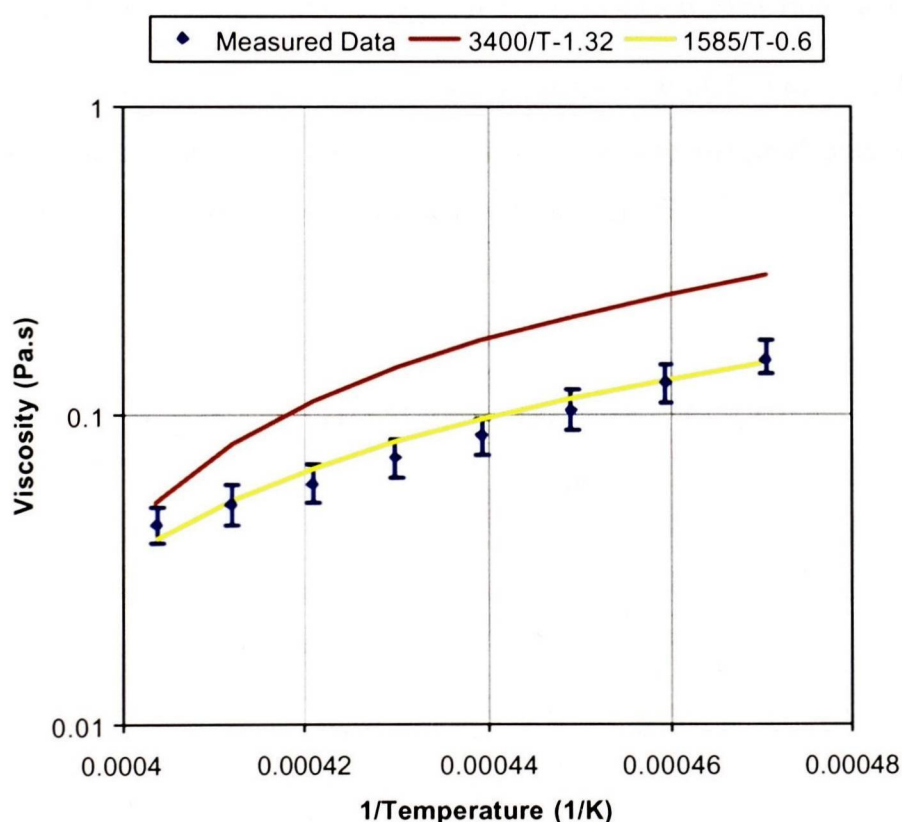


Figure 3.13 - Revised Viscosity Relationship

$$\mu = \frac{1585}{T} - 0.6 \quad (3.19)$$

The effect of this revision is not insignificant as is demonstrated when the viscosity is plotted against Temperature rather than its reciprocal (Figure 3.14). It is this lower temperature range that is of interest as this has a significant impact on the penetration.

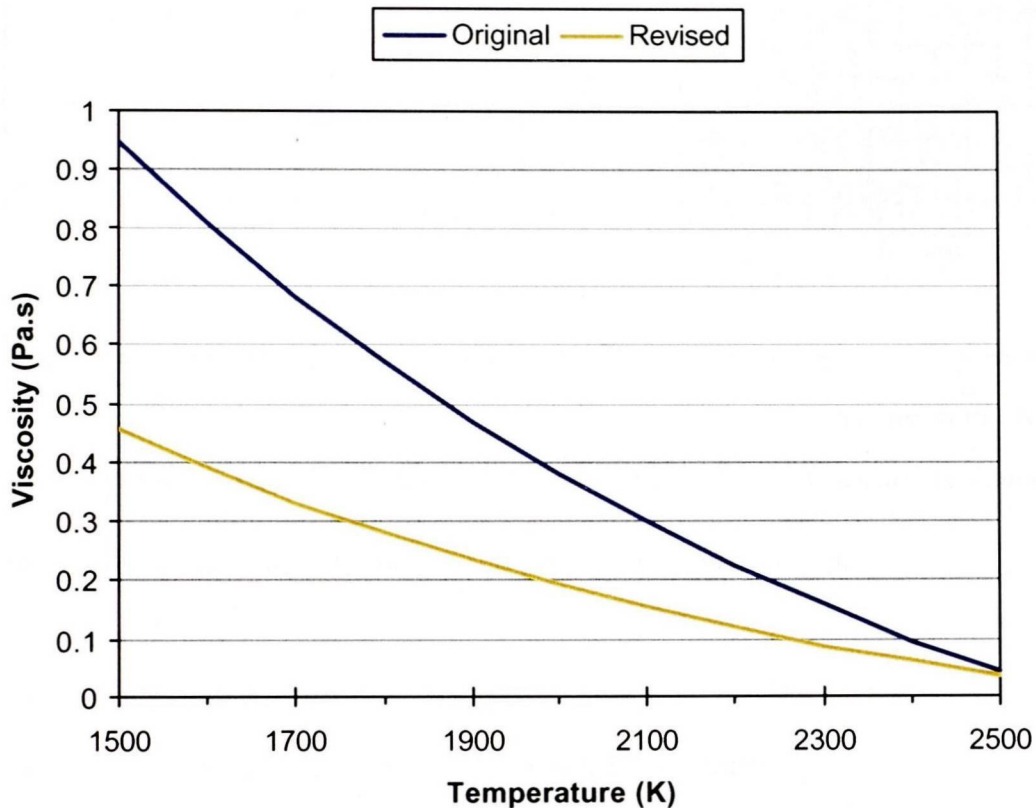


Figure 3.14 - Comparison of Original and Revised Viscosity Equations

To examine the impact on the results the induction furnace model, which is described fully in a following modelling section, has been run using both the original and revised viscosity relationships and the penetration front is shown in Figure 3.15.

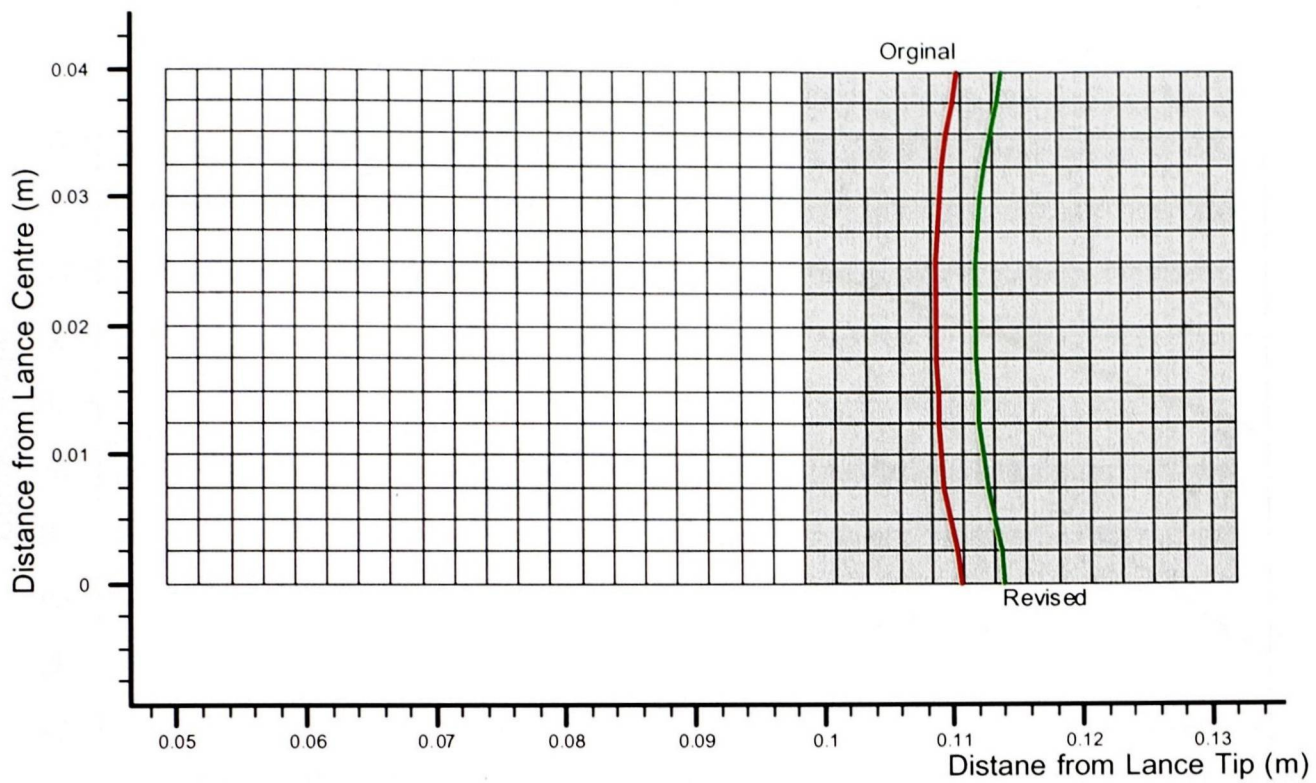


Figure 3.15 - Induction Furnace results for the Original and revised Viscosity Relationships

The parameters that are used in calculating the penetration rate include:

- Pore Radius;
- Slag Surface Tension;
- Contact Angle between the Slag and Refractory;
- Slag Viscosity; and
- Current Penetration Depth.

The Contact Angle is used in the Induction furnace model as a tuning parameter to adjust the penetration rate to match the measured penetration as the other quantities are reasonably well defined. As a piecewise function is used to describe the temperature dependency of the contact angle, the value at 3000K was adjusted to obtain the required penetration. The adjusted contact angle relationship is shown in Figure 3.16.

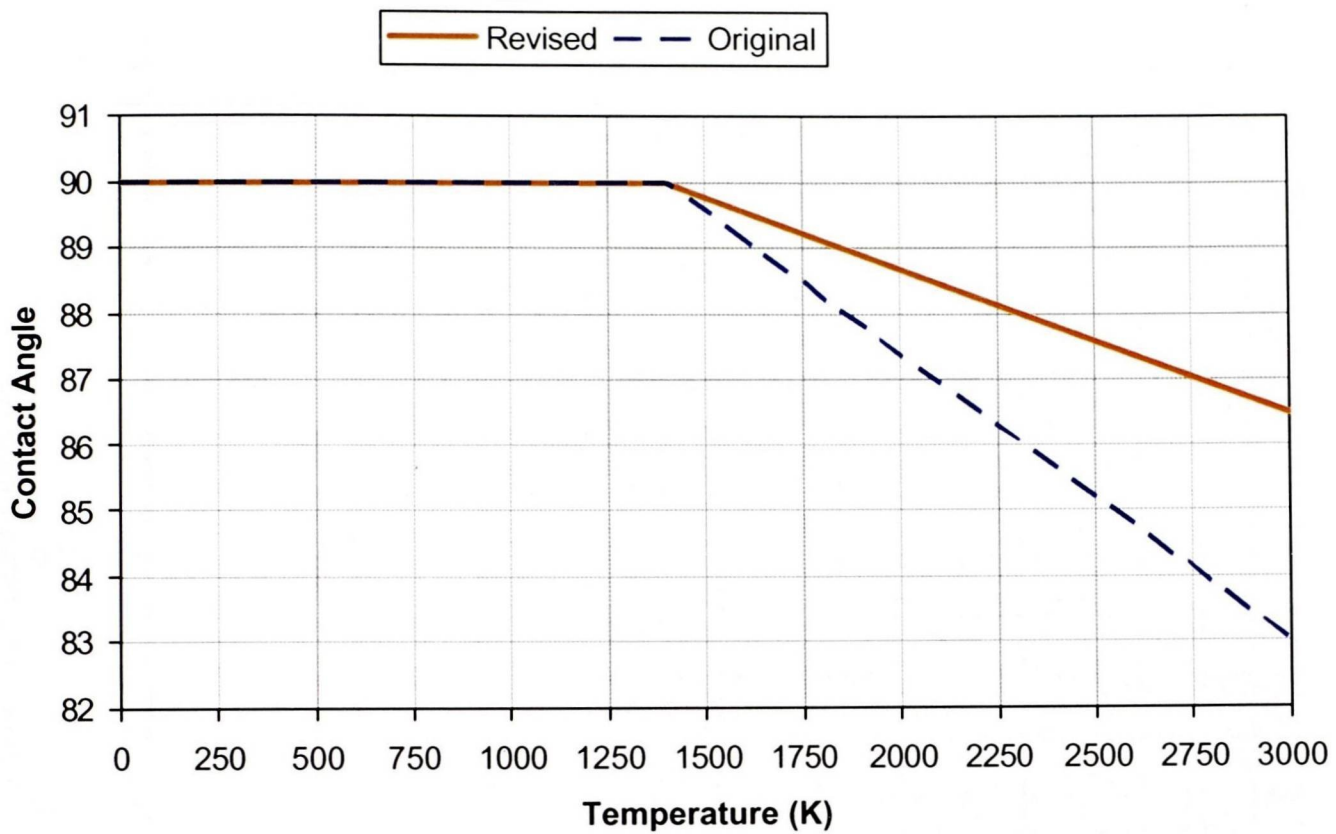


Figure 3.16 - Adjustment Made to Contact Angle

Figure 3.17 shows the results from the induction furnace cases run. The red and green contours are the previously presented penetration fronts for the two different viscosity relationships. The dashed yellow line is for the revised viscosity relationship with the contact angle temperature relationship also adjusted.

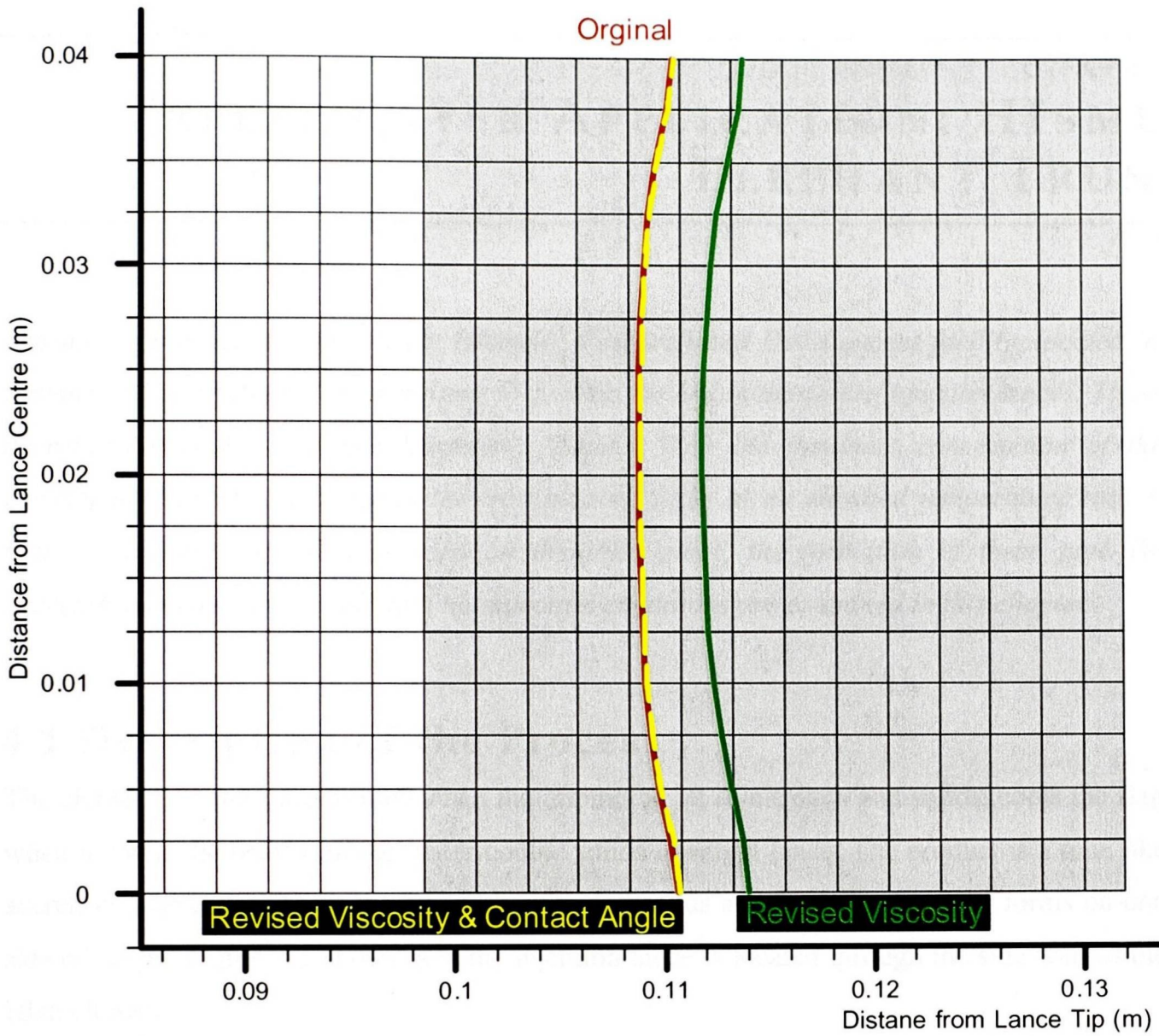


Figure 3.17 - Results after Revising Contact Angle Relationship

Using the original version of the temperature dependent viscosity relationship (Equation 3.18) is no different to using the revised equation with the adjusted piecewise contact angle relationship. This is not surprising as the contact angle is inversely proportional to the slag viscosity in the calculation of the penetration velocity (Equation 3.17).

FREEZE LAYER APPLICATION: HISMELT ELEPHANT TRUNKS

During the pilot plant trials at the HIs melt[®] Research and Development facility, located in Kwinana Western Australia, accretions formed on the end of the solids injection lances. These accretions have been termed Elephant's Trunks. With the imminent construction of the Development plant which injects the iron bearing feeds at an elevated temperature rather than at ambient temperatures used on the pilot plant, the formation of these pipe-like accretions under both the cold and hot injection conditions are examined in this chapter.

4.1 Description of the Process

The elephant's trunks are formed when the impinging jet of nitrogen and solids, cools the slag when it enters the bath from the water-cooled solids injection lance. The product is a tube like accretion. Figure 4.1 shows the jet of nitrogen and solids and how the accretion forms on one side of the jet. Figure 4.2 shows how the injection lance is located through the side wall of the HIs melt SRV.

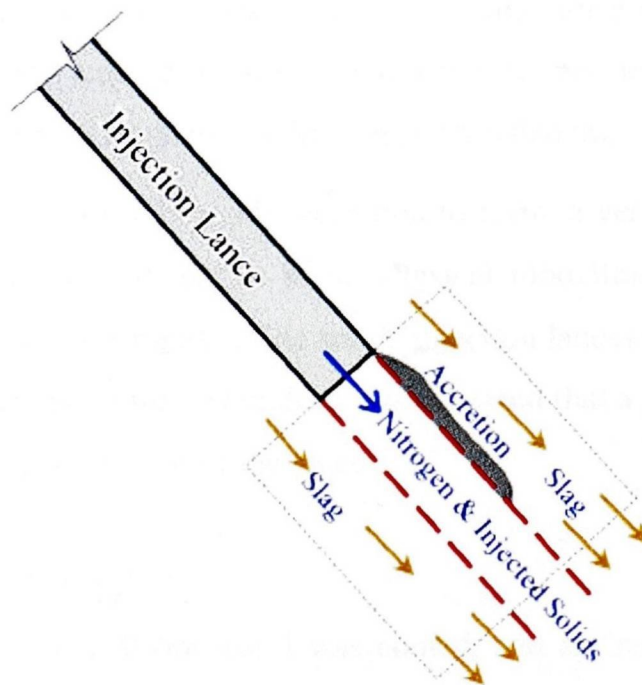


Figure 4.1 - Trunk Formation

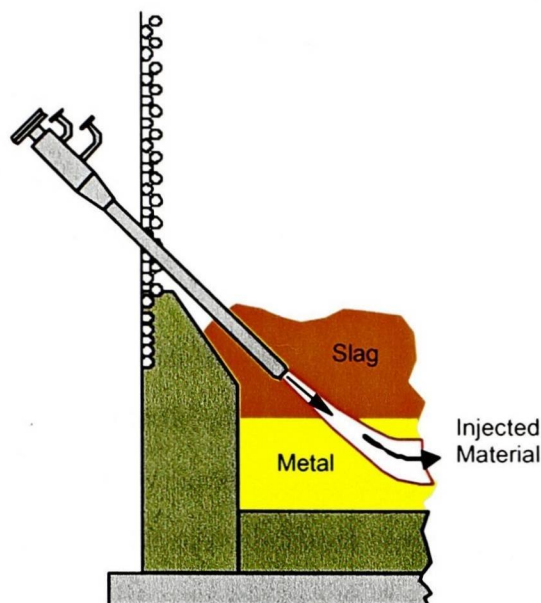


Figure 4.2 - Injection Lance Arrangement in the HIs melt Vessel

As it is important to get the solid material into the molten metal bath, the presence of these trunks is thought to improve the penetration of the solid particles injected into the bath. Within the design for the first commercial installation of HIs melt the use of hot injected material has been introduced. Modelling of the elephant's trunks is used to establish whether they will form under the hot injection conditions. Additionally this model provides further information regarding the solidification of slag as accretions – just as slag is frozen in the proximity of the water-cooling that is proposed for the sloping refractory slag zone.

There has been significant work examining accretions that form within iron smelting. Kyllö and Gray⁶⁴ performed a review of the work done on accretions for iron smelting applications. This particular review mostly covers work on bottom tuyeres and the porous hemispherical accretions. These types of accretions are also known as “Mushrooms” due to their shape.

Kyllö and Gray comment that for a pipe like accretion to form, a very high pressure is likely to be required. They also reported that in some physical modelling under sonic injection conditions, a pipe accretion forms rapidly. The solids injection lances operate at close to sonic conditions under significant pressures. Therefore it is expected that a pipe accretion will form quickly for the conditions near the exit of the lance.

4.2 Data Gathering

After every campaign the HIs melt 6m vessel was cooled, and an inspection of the inside of the SRV was carried out. It was routine to record the accretions that formed on the end of the injection lances. The trunks formed had a very smooth and straight inside surface. The trunks

mainly consisted of solidified slag. Towards the jet interface the accretion was dense, with no porosity present. Further away from the interface the structure became less ordered and droplets of metal were also present.

After Campaign 9-2 the elephant trunks measured 700mm in length. It is approximately at this length where the metal bath is located. Additionally a 20mm slag layer formed on the outside of the lance itself¹¹⁹.

4.3 Model Formulation

Only the regions near the injection lances are modelled. The boundary conditions are described for this model along with the various cases for the hot and cold injection.

4.3.1 Domain

The general arrangement of the lance when it is operating is shown in Figure 4.3. The lances are cooled with water. The solid particles are pneumatically conveyed with Nitrogen and are close to sonic velocities. The slag flows over the outside of the lance relatively slowly¹²⁰ – in the order of $1 - 2 \text{ ms}^{-1}$.

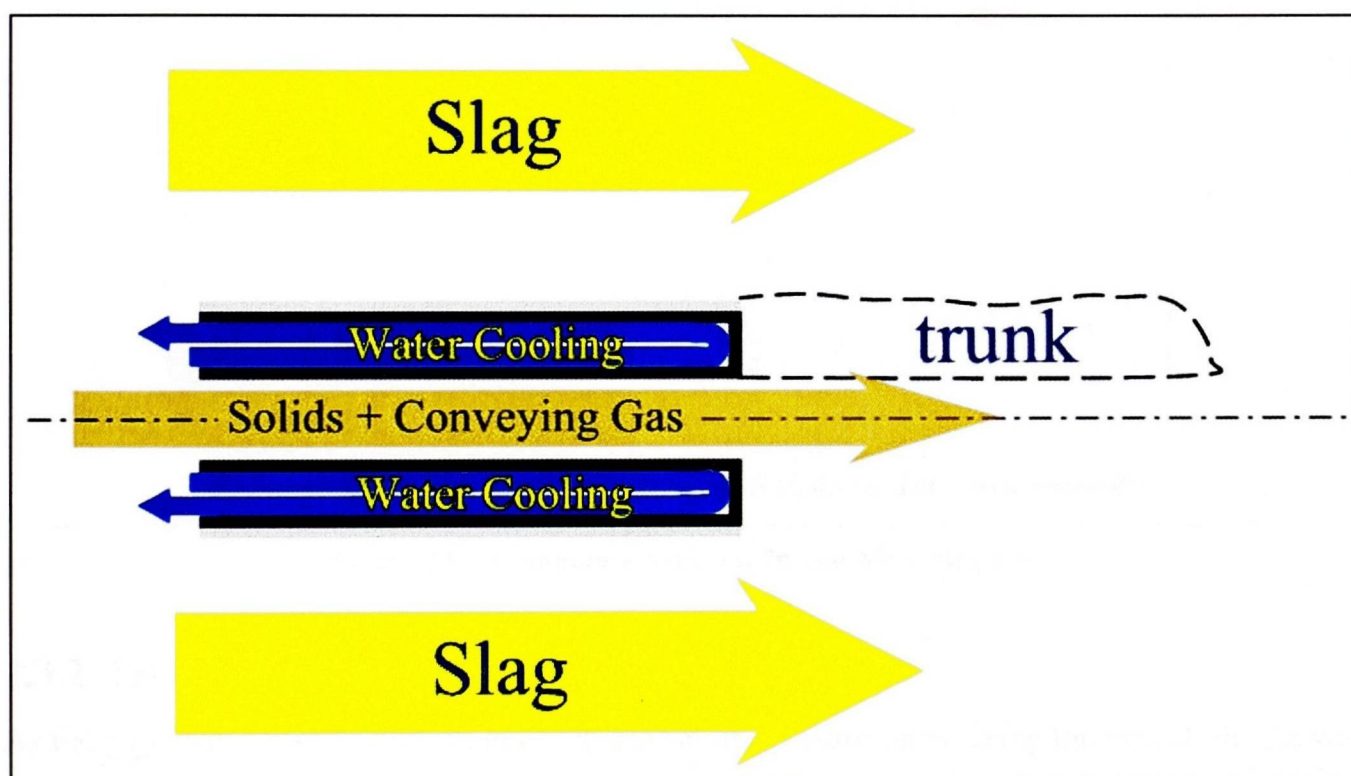


Figure 4.3 - Lance General Arrangement

To model this system an axi-symmetric wedge is used to model a part of the lance area. The outline of the domain used in this modelling work is shown in Figure 4.4.

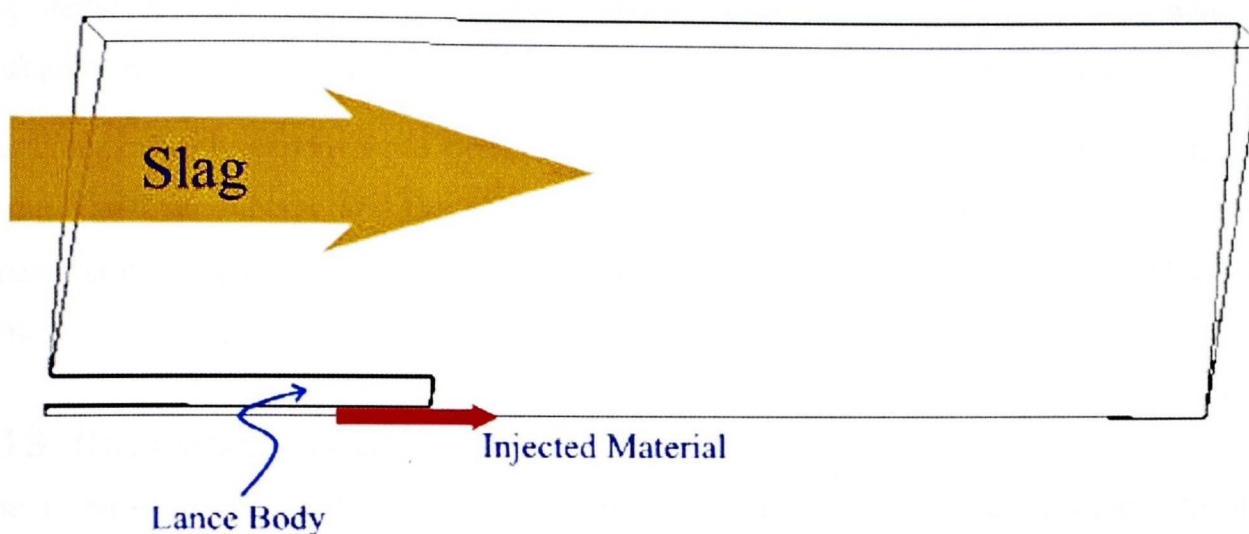


Figure 4.4 – Axi-symmetric Wedge Domain

To model the lance, a steel layer has been used along with a thin layer of refractory material on the outside of the lance. Figure 4.5 indicates how these layers are arranged within the model of the domain. Within the rest of the domain the slag liquid fraction is calculated with the balance being the solidified slag. The properties for the liquid and solid slag are calculated from the slag liquid fraction.

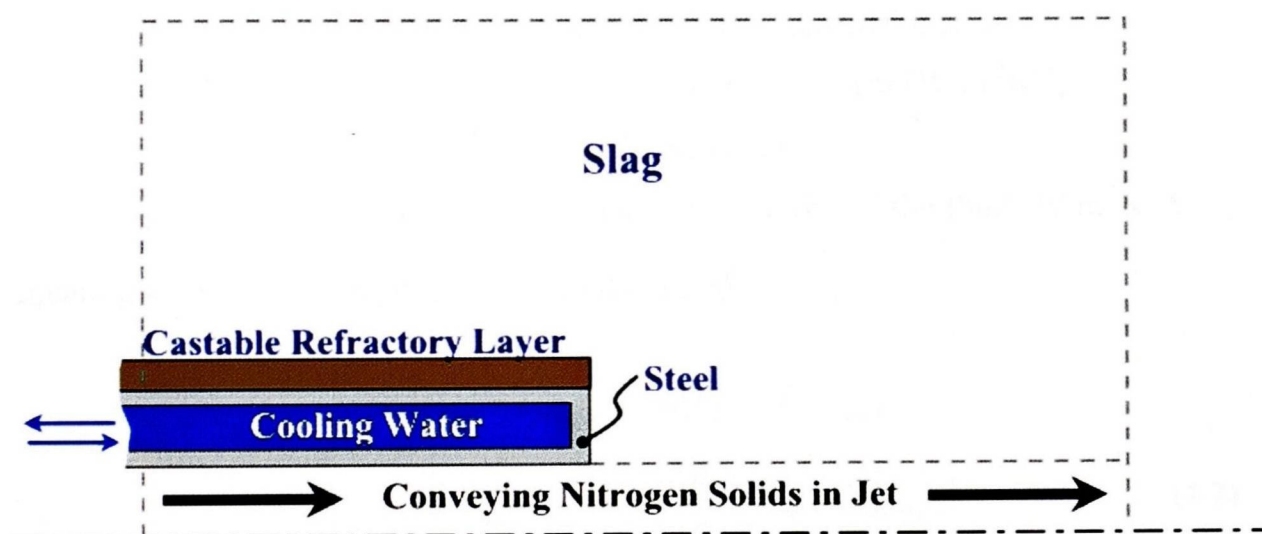


Figure 4.5 – Computational Domain and Mesh Regions

4.3.2 Jet Expansion

As the jet could possibly expand due to the drop of pressure on entering the vessel, the jet was tracked using a scalar variable. The scalar variable measures the fraction of the element that is made up of the jet material. To minimise the amount of numerical smearing occurring, the Van Leer differencing scheme was used.

The results showed negligible expansion of the jet within the area of interest that is modelled. This is not at all surprising due to the fact that the jet is not entirely a fluid, but rather a

suspension of solid particles (making up less than 5% of the total jet volume) within the Nitrogen carrier gas – leading to a large momentum to be associated with the jet.

It is comparatively expensive to perform the calculation of the jet due to the transient nature of the Van Leer scheme and the small time-steps required for stability (CFL limit). As the expansion of the jet is practically non-existent, the jet is assumed to flow straight through the domain.

4.3.3 Boundary Conditions

One of the most important boundary conditions is the interface between the jet and the slag. It is assumed that the slag is laminar whereas the jet is highly turbulent. To calculate the heat transfer at the interface the Dittus-Boelter¹²¹ equation (Equation 4.1) is used to calculate the Nusselt number (Nu) for turbulent internal flow within a pipe.

$$\begin{aligned} Nu_D &= 0.025 Re_D^{0.8} Pr^{0.4} \\ &= \frac{hD}{k} \end{aligned} \quad (4.1)$$

where

- Re is the Reynolds number calculated from the pipe diameter
- Pr is the Prandtl number (dimensionless)
- h is the heat transfer co-efficient ($W \cdot m^{-2} K^{-1}$)
- D is the pipe diameter (m)
- k is the thermal conductivity of the fluid ($W \cdot m^{-1} K^{-1}$)

by equating the flow of energy to and from the interface

$$\begin{aligned} \frac{k_{Slag}}{\delta} (T_{Slag} - T_{Interface}) &= h (T_{Jet} - T_{Interface}) \\ &= \frac{Nu_{\delta} k}{\delta} (T_{Jet} - T_{Interface}) \end{aligned} \quad (4.2)$$

$$k_{Slag} (T_{Slag} - T_{Interface}) = Nu_{\delta} k (T_{Jet} - T_{Interface})$$

where

- δ is the interface thickness (m)
- T is the temperature (K)

the temperature at the interface can be calculated as follows

$$\therefore T_{Interface} = \frac{k_{Slag} T_{Slag} - Nu_{\delta} k T_{Jet}}{k_{Slag} - Nu_{\delta} k} \quad (4.3)$$

As the jet was found not to expand, and the long simulation times (in the order of several days on a Sun Ultra 5) required, the jet part of the domain was removed. From the calculations

performed with the jet, the jet temperature was not increasing and therefore a 30°C fixed temperature boundary condition is used at the interface between the jet and slag. When the jet was modelled, the accretion forms quickly at the start of the simulation. Due to the existence of the solid material, there is no need to account for the shear that will be generated by the jet onto the liquid slag.

The blue shading within Figure 4.6 shows the solidification that is calculated for this situation. It should be noted that the metal bath will ‘wash’ away the trunk that is formed below the metal level – in the HRDF case shown this occurs at approximately 0.6-0.7m from the end of the lance¹²².

The physical properties for the jet are assumed to be constant when calculating the Reynolds and Prandtl numbers. The velocity was changed based on the design flow rates for each case which are listed in Table 4.2.

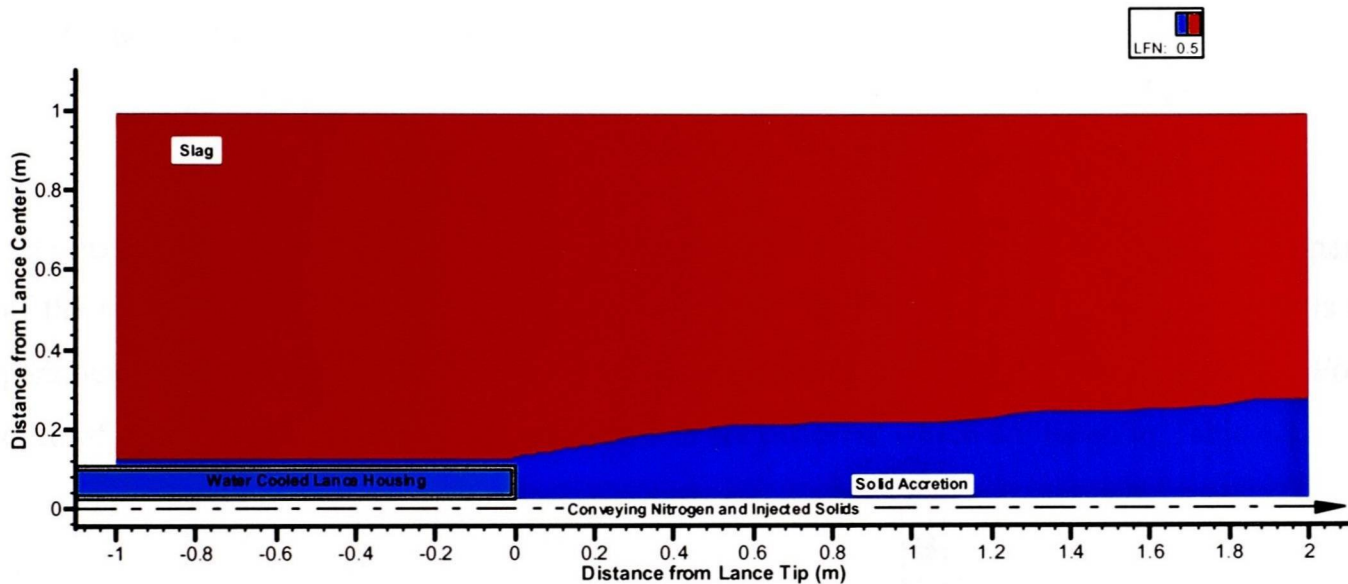


Figure 4.6 – Liquid Fraction Contours for Fixed Interface Temperature for the HRDF case

Slag enters from the lance end of the domain at 1450°C at a velocity of 2.0 ms⁻¹. The outlet is at the opposite end of the domain to the inlet, which is a constant pressure boundary. The inside surface of the lance is fixed to a temperature of 50°C, which is based on the exit water temperature observed on the pilot plant – a value which is a little conservative.

The boundary at the top of the domain is designed to be away from the area of greatest interest, and is some distance into the bath. The boundary is set to a fixed temperature of 1770K.

4.3.4 Cases Examined

There are three cases that have been modelled:

1. HRDF cold (30°C) solids injection

- 14.37 tph Ore
- 8.07 tph Coal
- $1.7 \text{ kNm}^3\text{h}^{-1}$ Nitrogen
- 1.36 tph Lime

2. 6m cold (30°C) solids injection

- 2.1 tph Ore
- 67.8 tph Coal
- $5.5 \text{ kNm}^3\text{h}^{-1}$ Nitrogen
- 13.7 tph Lime

3. 6m hot (600°C) ore injection

- 152 tph Ore
- $7.6 \text{ kNm}^3\text{h}^{-1}$ Nitrogen

The mass rates listed for each of the cases were used when the jet was being modelled as part of the system. These rates are used to calculate the velocity (Table 4.2) of the jet which is a parameter that feeds back into the model through the interface heat transfer coefficient. For each of the different cases, the lance dimensions are different which are listed in Table 4.1.

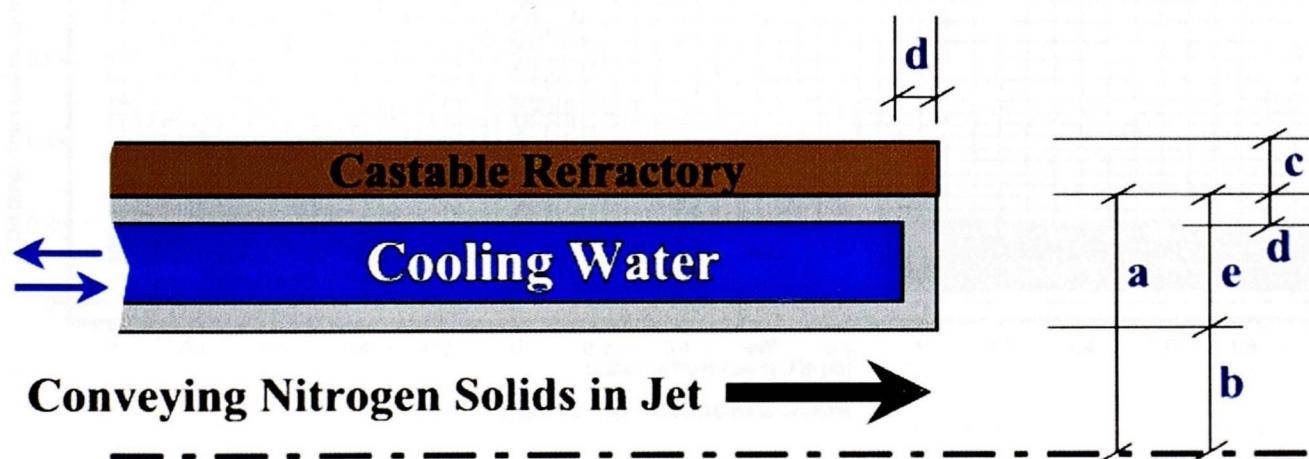


Figure 4.7 - Lance Dimensions

Case	a	b*	c*	d*	e*
HRDF Cold	0.112	0.025	0.015	0.012	0.087
6m Cold	0.141	0.032	0.015	0.015	0.110
6m Hot	0.204	0.046	0.015	0.022	0.158

Table 4.1 - Lance Dimensions for the various cases (in meters)

Case	Velocity (m s^{-1})
HRDF Cold	58
6m Cold	60
6m Hot	115

Table 4.2 - Injection Velocities for the Various Cases

4.4 Verification of Assumptions

To ensure the reliability of the results produced, different mesh densities and the sensitivity of the results is tested against the assumptions made in this model – that the interface temperature is constant.

4.4.1 Mesh Refinement

Through the process of developing this model, extra mesh density was added to the areas of particular interest – where the solidification is taking place. As a consequence of simulation experience, the mesh shown in Figure 4.8 was developed.

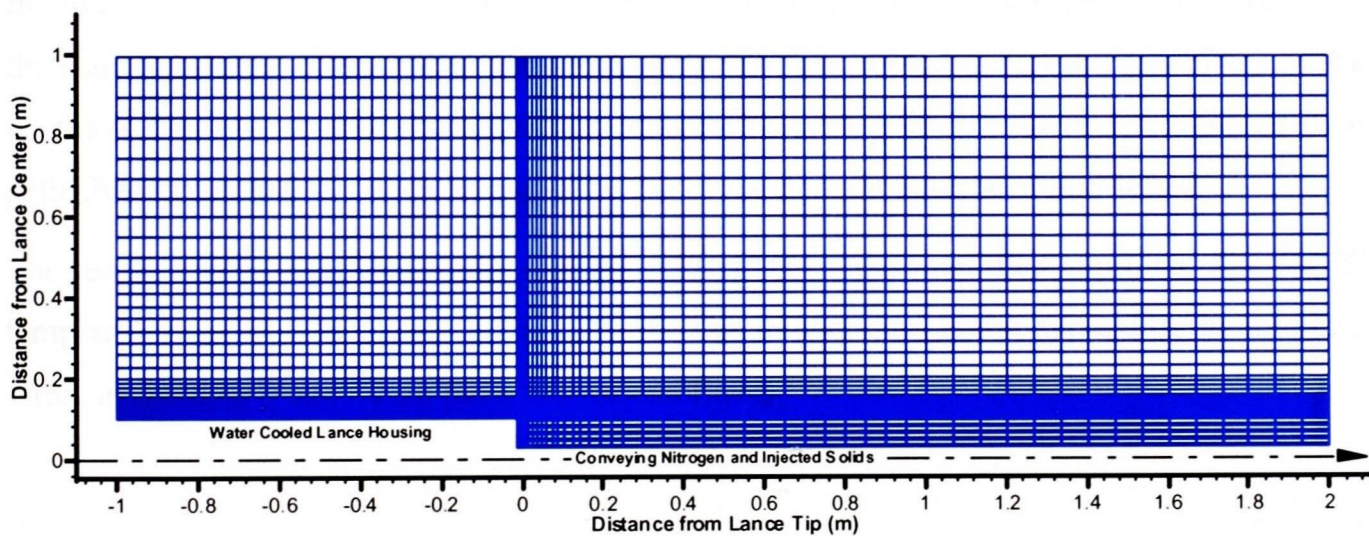


Figure 4.8 - Standard Mesh

To test the suitability of this mesh and to ensure that the results were not dependent on the size of the elements used, different mesh densities for the HRDF cold injection case were run. The 0.5 liquid fraction contours are plotted for these simulations in Figure 4.9.

* Dimension shown on Figure 4.7

The red contour shows the 0.5 liquid fractions for the Standard mesh shown in Figure 4.8. The green contour shows the result for a mesh with elements twice the size of the standard mesh (i.e. $\frac{1}{4}$ the number of elements). The blue contour shows the results for a mesh with elements half the size of the standard mesh. This result is similar to the standard mesh result and it is concluded, considering the cost of using a finer mesh, that the standard mesh is sufficient for modelling the lance accretions.

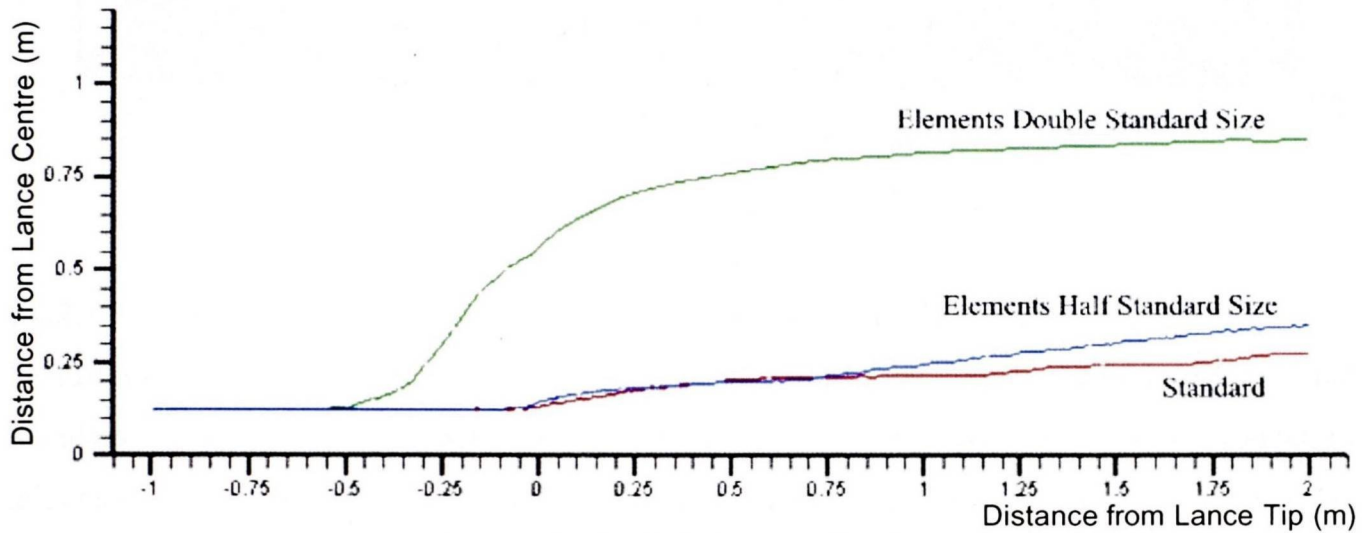


Figure 4.9 - Mesh Refinement Results

4.4.2 Interface Heat Transfer

In simplifying the model, a fixed temperature assumption was used for the interface between the slag and the jet. Two additional simulations were performed to test the sensitivity of the results to this assumption where the temperature of the jet is linearly increased along its flow path. 300°C and 600°C increases along the 2m of the domain have been performed.

The results from these simulations showed little effect on the trunk that is grown. The 600°C temperature rise case is shown in Figure 4.10. The temperature rise is applied to the interface – that is between 0 and +2 on the x-axis of this figure.

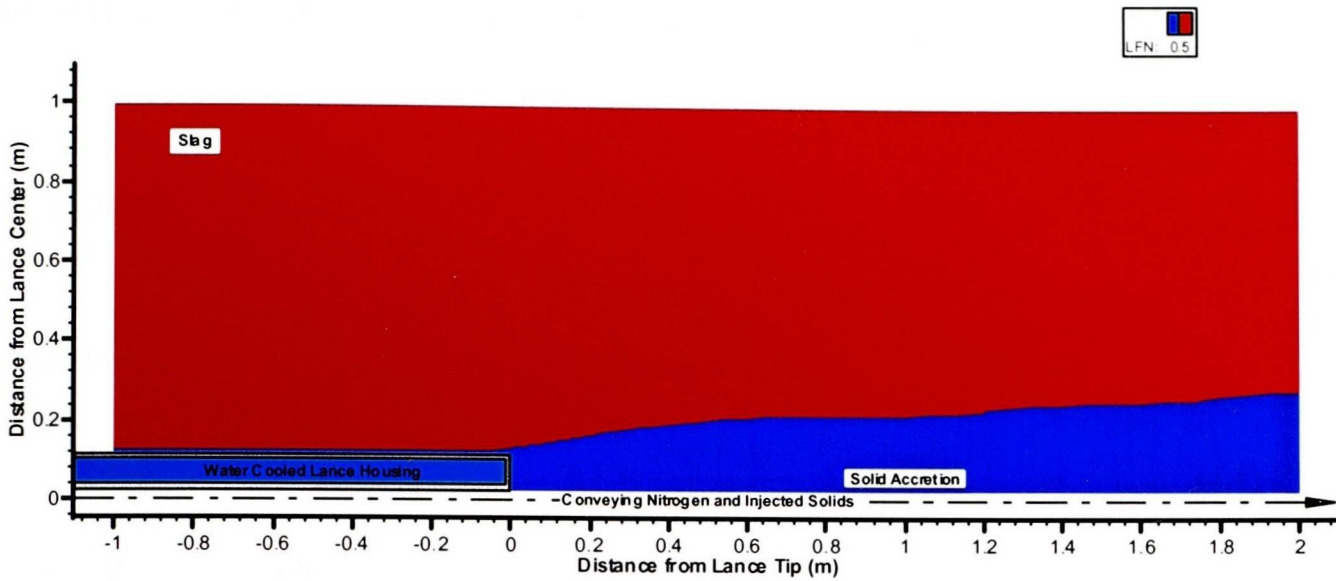


Figure 4.10 - 600°C Temperature Rise, HRDF case

4.4.2.1 Calculation of Increase in Temperature along the interface

To further verify the assumption of the constant interface temperature, a single dimensional calculation for the energy balance has been performed along the length of the model to calculate the rise in the jet temperature. These calculations are for the HRDF cold injection case.

Quantity	Value
$\frac{\Delta T}{\Delta x}$	50
Nu	31.72
k_{Jet}	0.3336
k_{Slag}	13.64
Diameter	0.05
δ	0.025
\dot{m}	7.14
$C_{p_{Jet}}$	980

Table 4.3 – Calculation Quantities

The results from this analysis are included in Table 4.4, are calculated from the properties listed in Table 4.4. The first step of the calculation is to calculate the slag temperature.

$$T_{slag} = T_0 + x \frac{\Delta T}{\Delta x} \quad (4.4)$$

The interface temperature is then calculated from a Nusselt Number (Equation 4.1) and the diffusion of energy from the interface.

$$T_{Interface,i} = \frac{k_{Slag} T_{Slag,i} - Nu_{\delta} k T_{Jet,(i-1)}}{k_{Slag} - Nu_{\delta} k} \quad (4.5)$$

from this the heat transfer is calculated on the slag side using

$$Q = \frac{k_{Slag}}{\delta} (T_{Slag,i} - T_{Interface,i}) \quad (4.6)$$

which is balanced on the jet side by

$$Q = \dot{m}Cp_{Jet} (T_{Jet,Out} - T_{Jet,in}) \quad (4.7)$$

this allows the temperature rise to be calculated from

$$\Delta T = \frac{Q\pi D^2 \Delta x}{\dot{m}Cp_{Jet}} \quad (4.8)$$

giving the temperature of the jet

$$T_{Jet,i} = T_{Jet,(i-1)} + \Delta T \quad (4.9)$$

This process is carried out iteratively to produce the temperature along the length of the domain which are listed in the table shown below.

Step Index	Distance from Lance Tip	Slag Temperature	Jet Temperature	Interface Temperature	Energy Transferred	Surface Area	Jet Temperature Rise
i	x m	T _{Slag} K	T _{Jet} K	T _{Interface} K	Q W.m ⁻²	S m ²	dT K
0	0.0	300	300.000				
1	0.1	305	300.003	302.816	1192	0.016	0.003
2	0.2	310	300.008	305.632	2383	0.016	0.005
3	0.3	315	300.016	308.450	3573	0.016	0.008
4	0.4	320	300.027	311.270	4763	0.016	0.011
5	0.5	325	300.040	314.090	5953	0.016	0.013
6	0.6	330	300.056	316.911	7141	0.016	0.016
7	0.7	335	300.075	319.734	8329	0.016	0.019
8	0.8	340	300.096	322.558	9516	0.016	0.021
9	0.9	345	300.120	325.383	10703	0.016	0.024
10	1.0	350	300.147	328.209	11889	0.016	0.027
11	1.1	355	300.176	331.036	13075	0.016	0.029
12	1.2	360	300.208	333.865	14259	0.016	0.032
13	1.3	365	300.243	336.694	15444	0.016	0.035
14	1.4	370	300.280	339.525	16627	0.016	0.037
15	1.5	375	300.320	342.357	17810	0.016	0.040
16	1.6	380	300.363	345.190	18992	0.016	0.043
17	1.7	385	300.408	348.025	20174	0.016	0.045
18	1.8	390	300.456	350.860	21355	0.016	0.048
19	1.9	395	300.507	353.697	22535	0.016	0.051
20	2.0	400	300.560	356.534	23715	0.016	0.053

Table 4.4 – Jet Temperature Rise

From these results it can be seen that the rise is small and it is valid to assume that there is no temperature rise in the jet. The reason for this result is due to the large mass rate – due to the high velocity.

4.5 Results and Discussion

The HRDF cold injection case presented in Figure 4.11, is consistent with the trunks observed once the vessel has been shut down. The temperature contours are plotted in Figure 4.12. From these results, and excluding gravity effects, it may well be concluded that the trunks may grow to quite a length. At the moment the trunks are “washed” away by the molten metal bath at approximately 0.7m from the end of the lance. It may be desirable from a safety point of view to move the lance further away from the bath, although whether the trunk has the strength to support its own mass is unknown. A stress analysis would need to be performed to answer this question.

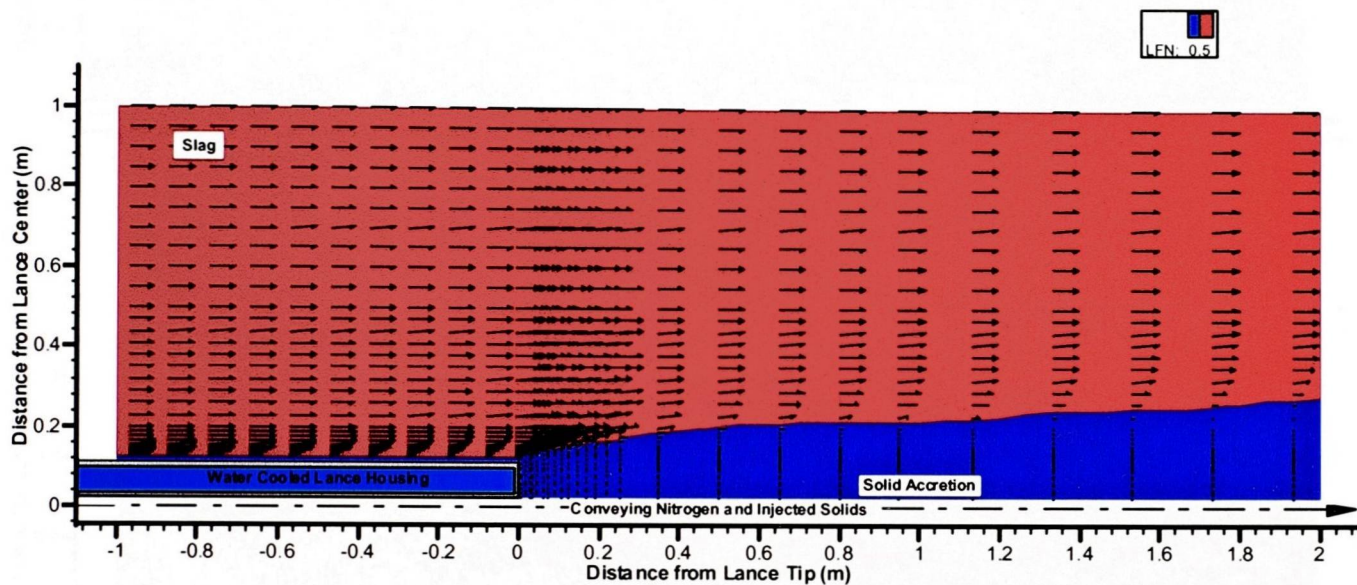


Figure 4.11 - HRDF cold injection liquid fraction contours

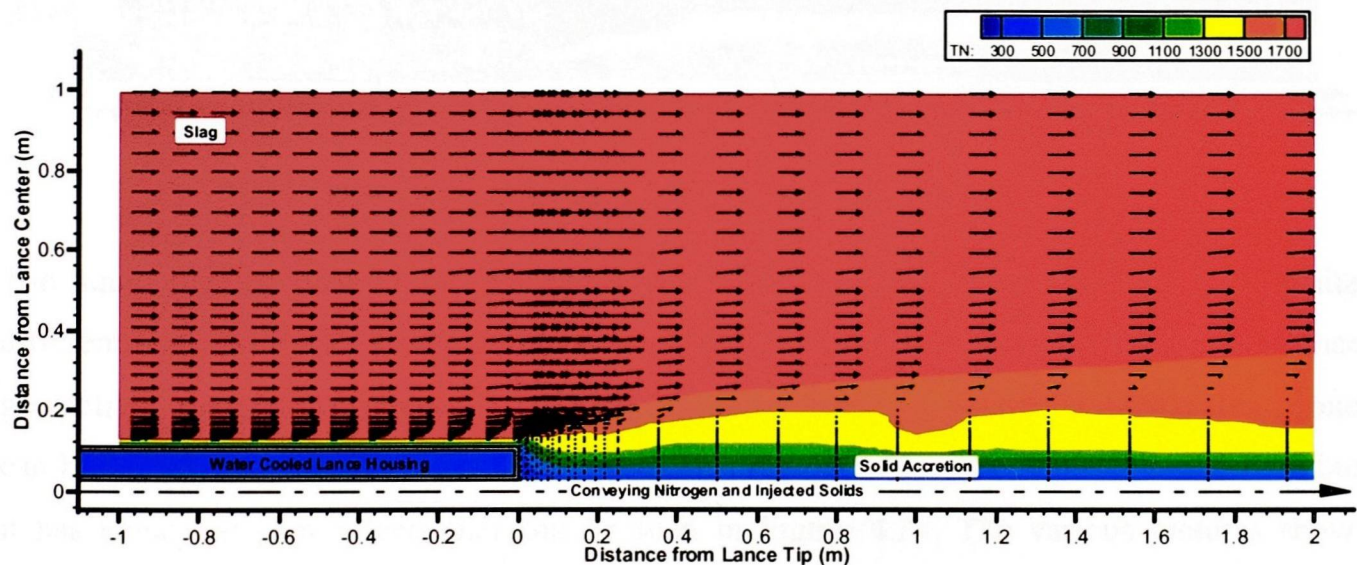


Figure 4.12 – HRDF cold injection temperature contours

Figure 4.13 shows the trunk formed in modelling the 6m cold injection case. The results are quite similar to the HRDF cold injection case. The temperature contours (Figure 4.14) show a lower temperature for the trunk near the end of the lance. The difference between the two

cases is the different internal diameters for the lances. This larger diameter leads to a larger area for heat transfer to take place, and therefore it is expected to produce a slightly different temperature profile to the HRDF case.

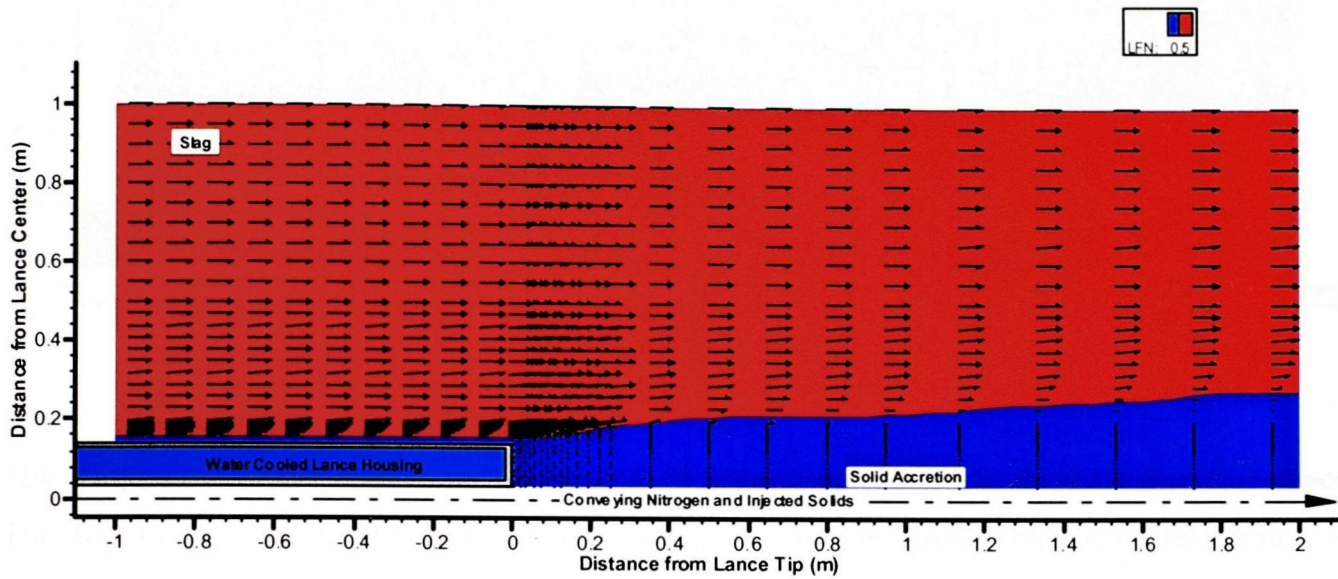


Figure 4.13 - 6m cold injection liquid fraction contours

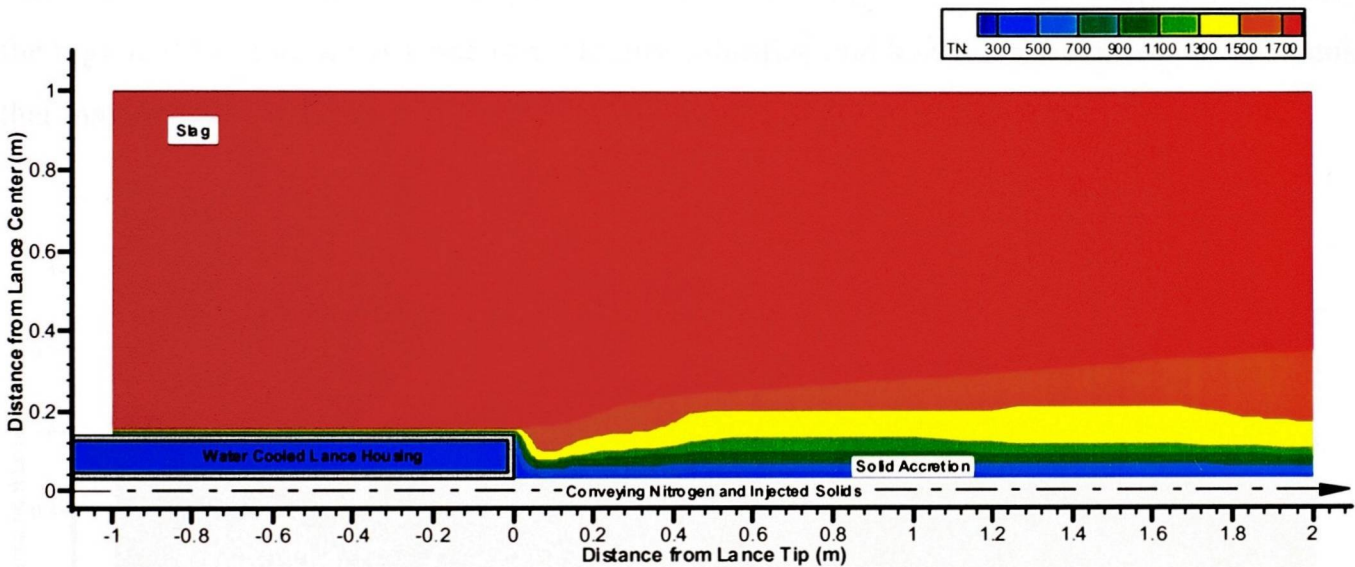


Figure 4.14 - 6m Cold Injection Temperature Contours

The liquid fraction contours for the 6m hot injection case shown in Figure 4.15, are quite different from the trunks grown in the two cold injection cases. Apart from the different lance geometries, the main difference is the temperature of the jet being 600°C . A “mushy” zone can be observed just off the end of the lance. This region is almost completely solidified, but it has some transient effects that can be seen in Figure 4.17. The various pictures show sequential snapshots of how the area near the end of the lance nearly re-solidifies and then re-melts which keeps cycling with time.

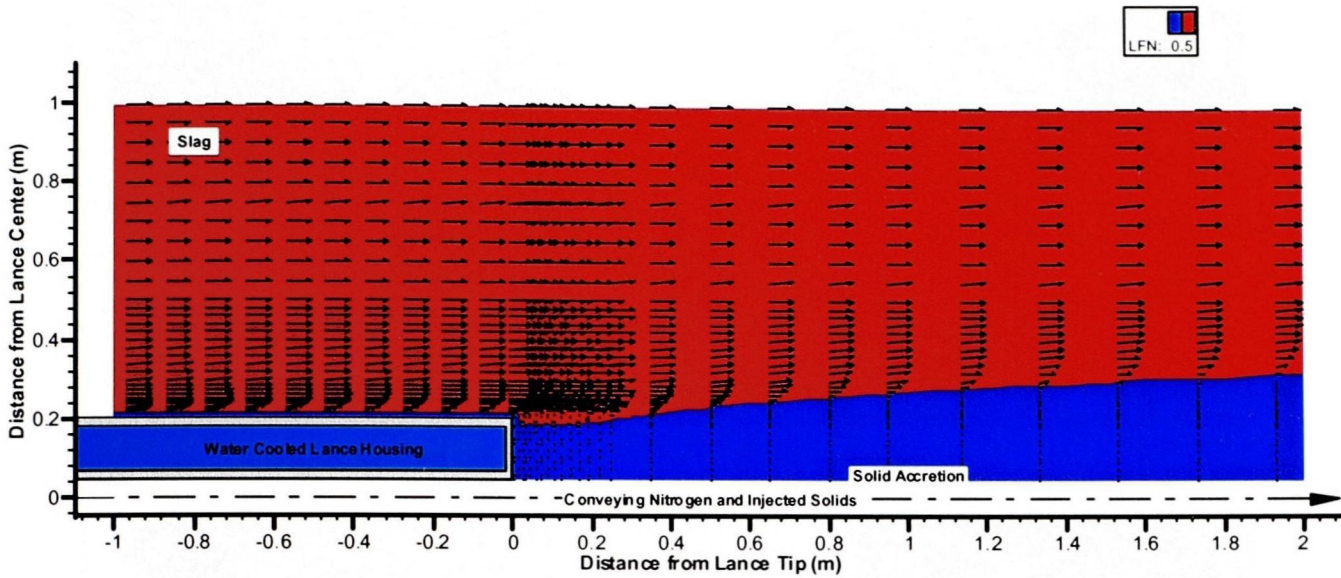


Figure 4.15 - 6m hot injection liquid fraction contours

The temperature contours shown in Figure 4.16 are quite different to the cold injection cases. The region adjacent to the lance is also hotter due to the small amount of re-circulation occurring from the slag flowing off the end of the lance body. The higher temperature of the solidified slag means that it will require less energy to heat and re-melt the trunk. Additionally the region at the end of the lance is not totally solidified and leads to a weak area of the trunk that may be liable to break away during operation.

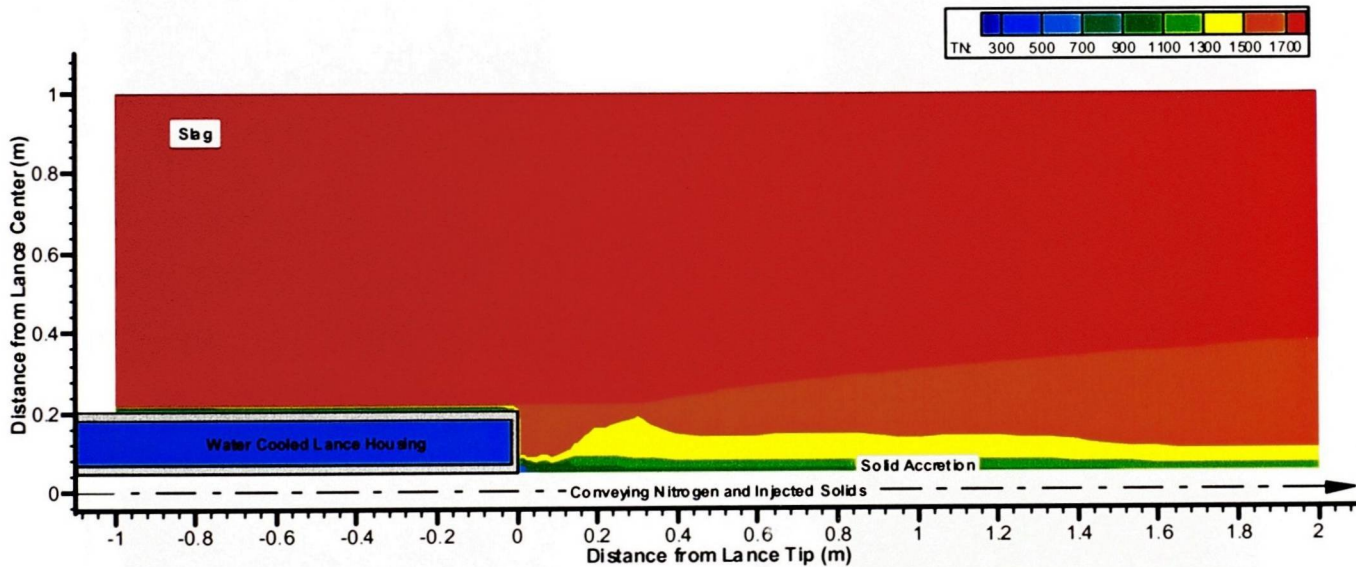


Figure 4.16 - 6m Hot injection Temperature Contours

The transient results shown in Figure 4.17 depict a sequential picture of the trunk that grows at the end of the lance. The mushy region shown, cycles through various stages of solidification due to the influence of the slag flow re-circulation.

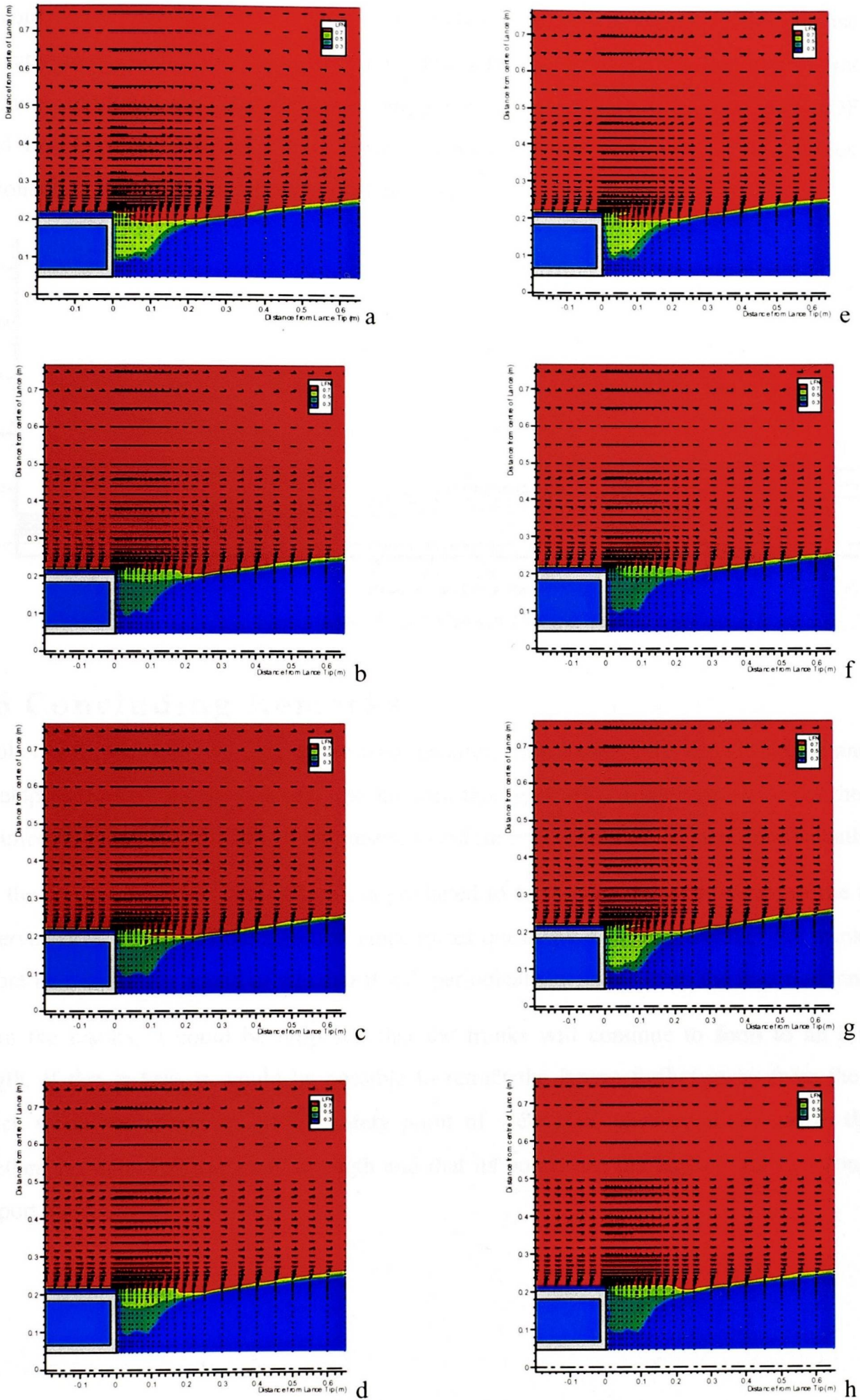


Figure 4.17 - Transient Nature of 6m Hot Case

To compare the results from the three cases modelled, the results have been scaled based on the ratio of the lance internal diameter to match the HRDF case. The 0.6 liquid fraction contours are plotted in Figure 4.18. The red, green, and blue contours refer to the HRDF, 6m Cold Injection, and the 6m Hot Injection respectively. This comparison demonstrates that reasonable trunks are grown in each of these cases.

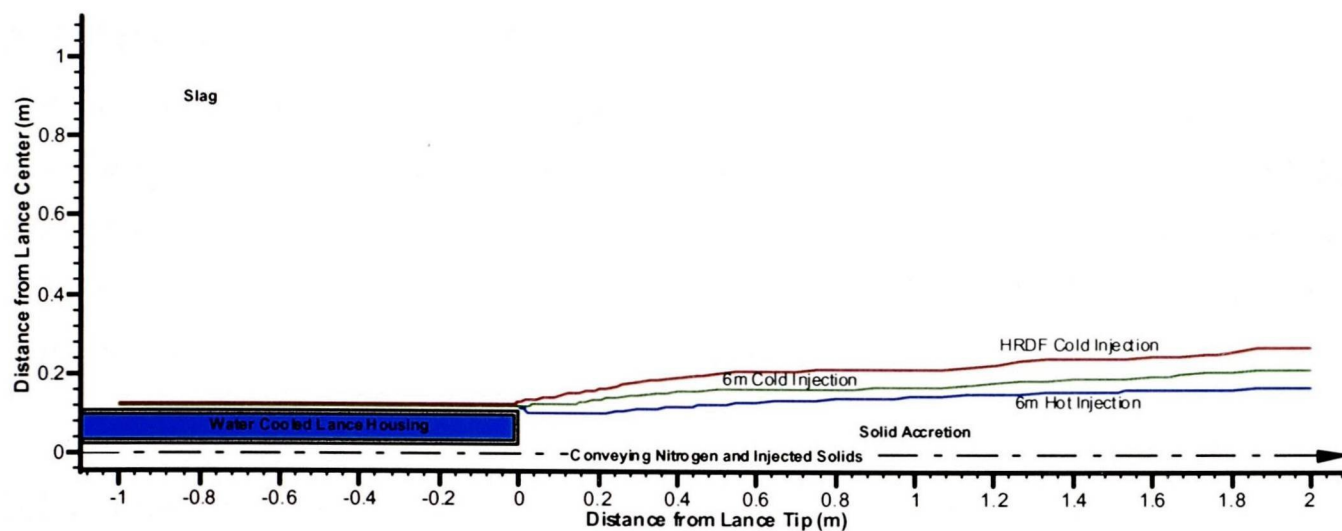


Figure 4.18 - Trunk Growth Comparison

4.6 Concluding Remarks

Stable trunks are predicted for the two cold injection cases examined – for the HRDF and 6m development plant. As the coal is to be injected through the cold injection lance for the first commercial plant, the trunks will be present to aid the penetration of the coal into the bath.

For the 6m hot injection case, a trunk is predicted to form. The transient nature of the trunk observed near the end of the injection lance raises questions regarding whether the trunk will in fact be structurally sound or whether it will periodically separate from the injection lance.

From the results, it could be proposed that the trunks will continue to form to an infinite length. If this is true, it would be possible to retract the lances further away from the bath which would be attractive from a safety point of view. The physical limitation to this is whether the trunk has sufficient strength and that its bond with the lance is strong enough to support itself.

5.1 Induction Furnace Test

The Induction Furnace test is a commonly used industrial test for refractory wear. The test pieces are fitted to the inside of an induction furnace, which is then filled with metal and slag and the furnace is run for a period of time. At the end of the test the samples are sectioned and their performance is analysed. The Induction Furnace is modelled to provide calibration of the penetration refractory wear mechanism.

5.1.1 Description of the Process

Induction furnaces use a coil to heat the metal within them. They range from large furnaces used in industry to smaller scale furnaces used in laboratory test facilities as illustrated in Figure 5.1. In testing refractories, a number of different refractories are used to line the furnace. The furnace is filled with metal, and if required a layer of slag. The furnace is operated for several hours, and after cooling the samples are sectioned and compared to each other for the worn and penetrated areas.

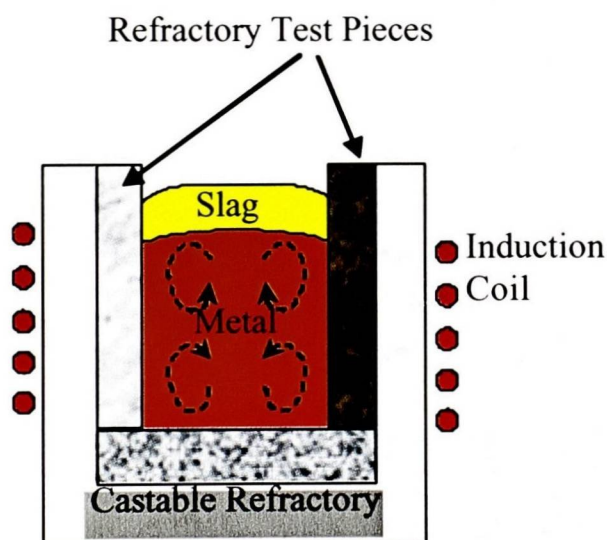


Figure 5.1 – Induction Furnace Schematic

It should be noted that the metal is required for all tests (even if the test is targeted towards examining slag resistance) for the inductive heating to take place. As with many refractory

tests the results are qualitative – that is the results should only be compared to the other refractory samples tested at the same time. No standards for this test procedure can be found.

5.1.2 Data Gathering

Vietsch-Radex* was commissioned to perform induction furnace tests on the existing magnesia-chrome refractory and other potential refractories that could be used in the HIs melt SRV. Although a detailed report was prepared at the time, only the scanned images of the sectioned refractory samples are available¹²³, which is shown in Figure 5.2.

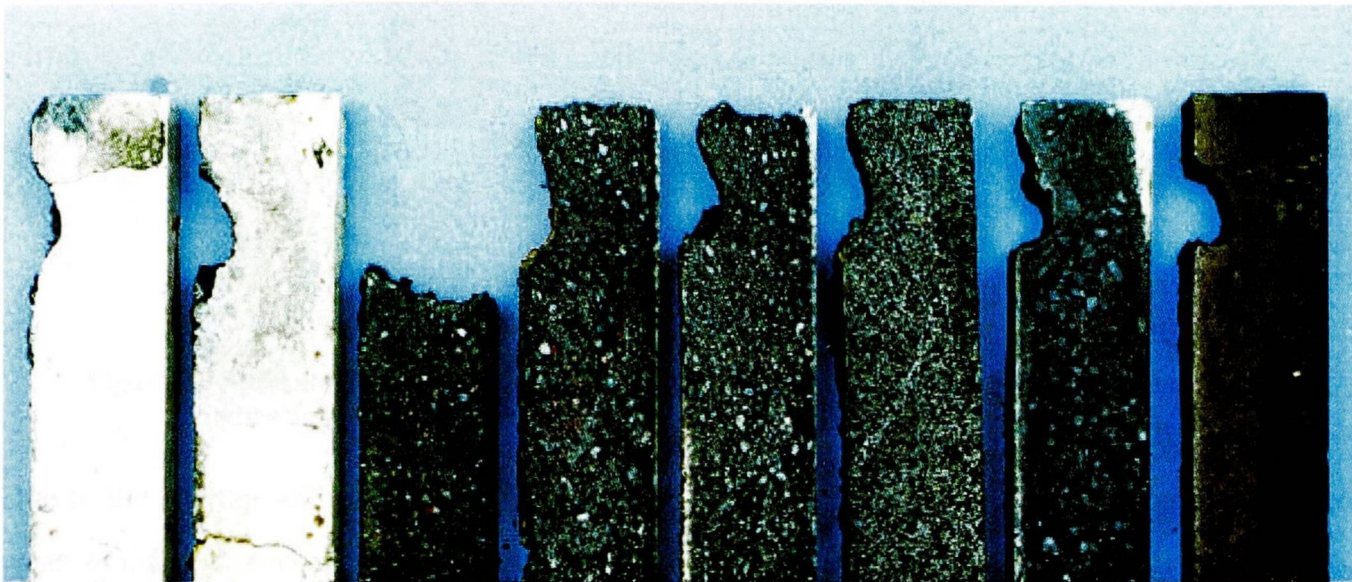


Figure 5.2 – Results from the Induction furnace Test

* Now part of RHI Refractories

Figure 5.3 highlights the extent of the affected refractory and the location of the metal and slag within the induction furnace with respect to the Magnesium-Chrome refractory sample.

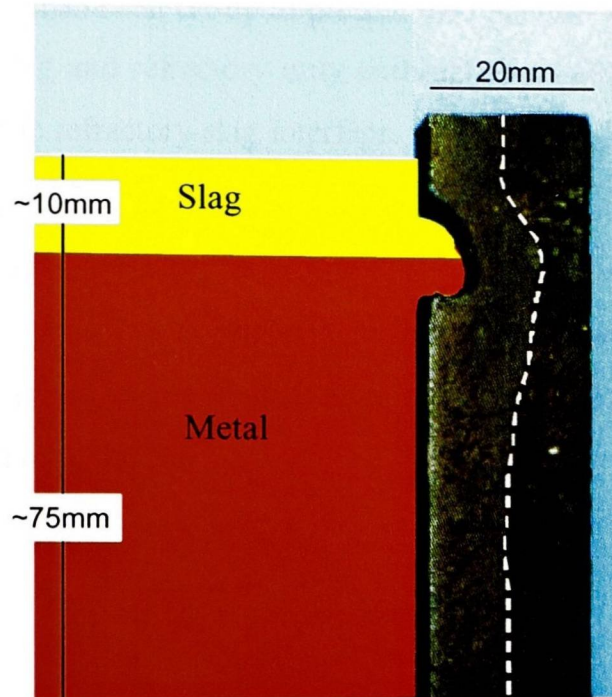


Figure 5.3 – Results from the Induction furnace Test for the Magnesium-Chrome Refractory Indicating the location of the Slag; Metal and Extent of affected Refractory

Due to the motion within the system caused by the heating of the metal, an area of accelerated wear occurs at the metal-slag interface with the refractory. This is caused by the slag oxidising the refractory structure, and then the metal level rises and washes away some of the oxidised refractory. This same effect was observed in the HIs melt pilot plant results at the metal slag interface that moved up and down due to the changing slag level between slag taps.

For the Magnesium-Chrome refractory sample shown in the above figures, the 20mm sample has been affected to approximately half the width at the top where it has been exposed to slag only. The Magnesium-Chrome refractory that is tested here is the ANKROM-S56 brand that was used in the HIs melt pilot plant trials.

5.1.3 Experimental Setup

As there is limited information available about this test a few assumptions have been made. As this work was aimed at comparing the performance of various refractories against those currently used at that time at HIs melt, the conditions would have been set up to be similar to those experienced in the HIs melt process. Simply this would be a HIs melt slag at the normal bath temperature (1450°C). As it is normal practice to run refractory wear tests for 5 hours, the model was set up to simulate 5 hours of real time exposure.

5.1.4 Model Formulation

Due to the nature of the data, the model is aimed at setting up the penetration parameters. Therefore a simple model has been set up to predict the penetration of slag into the refractory. The model consists of slag and refractory only and makes no attempt to model the dynamic action of the motion of the refractory-slag interface.

The small section of the furnace shown in Figure 5.4 is modelled. The model is set up using various layers of different materials (Figure 5.5). The slag is flowing in at the bottom part of the slag area at 1723K at 1ms^{-1} . A constant pressure outlet is applied to the rest of this face. The only other boundary condition that is applied is the cold face temperature for the refractory which is fixed to 300K.

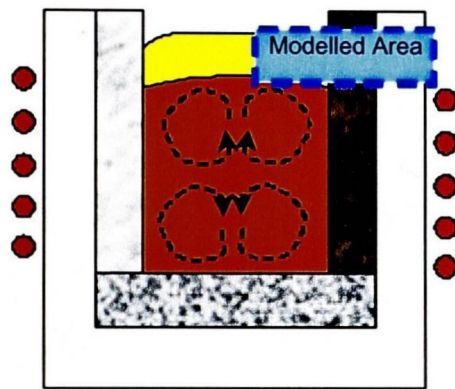


Figure 5.4 – Section of the Induction furnace that is modelled

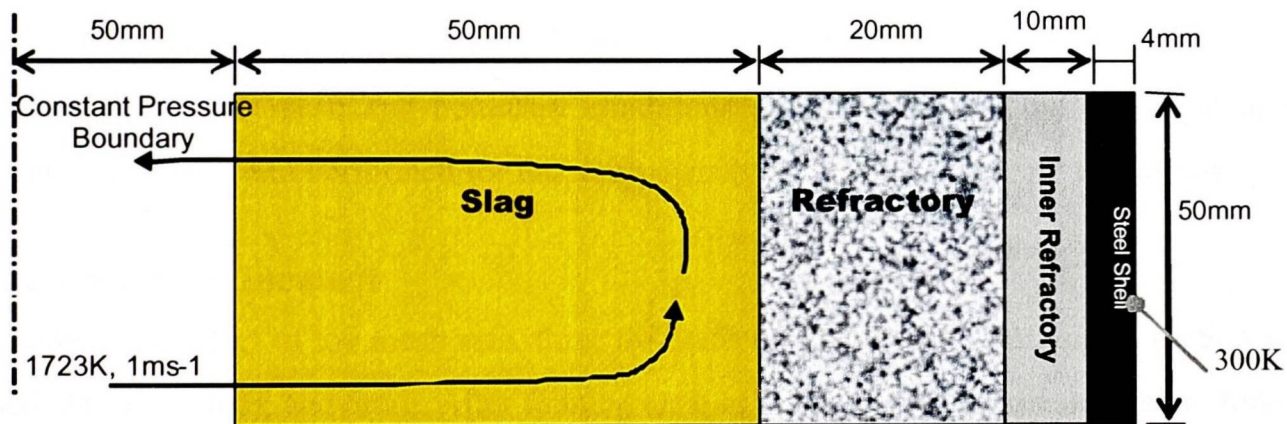


Figure 5.5 – Schematic of the Model

It is important to model the various layers within this model, as the change in refractory materials has a significant impact on the temperature profile of the system

From the inflow diameter of 15mm the Reynolds number is approximately 60. This indicates that the flow is not turbulent, and therefore its effects are not considered in this model. It is recognised that some turbulence will be generated by the slag changing direction at the furnace wall.

To capture the geometry of the furnace, a wedge like mesh has been created as is shown in Figure 5.6. The mesh is coloured black and orange to show the location of the refractory and slag respectively.

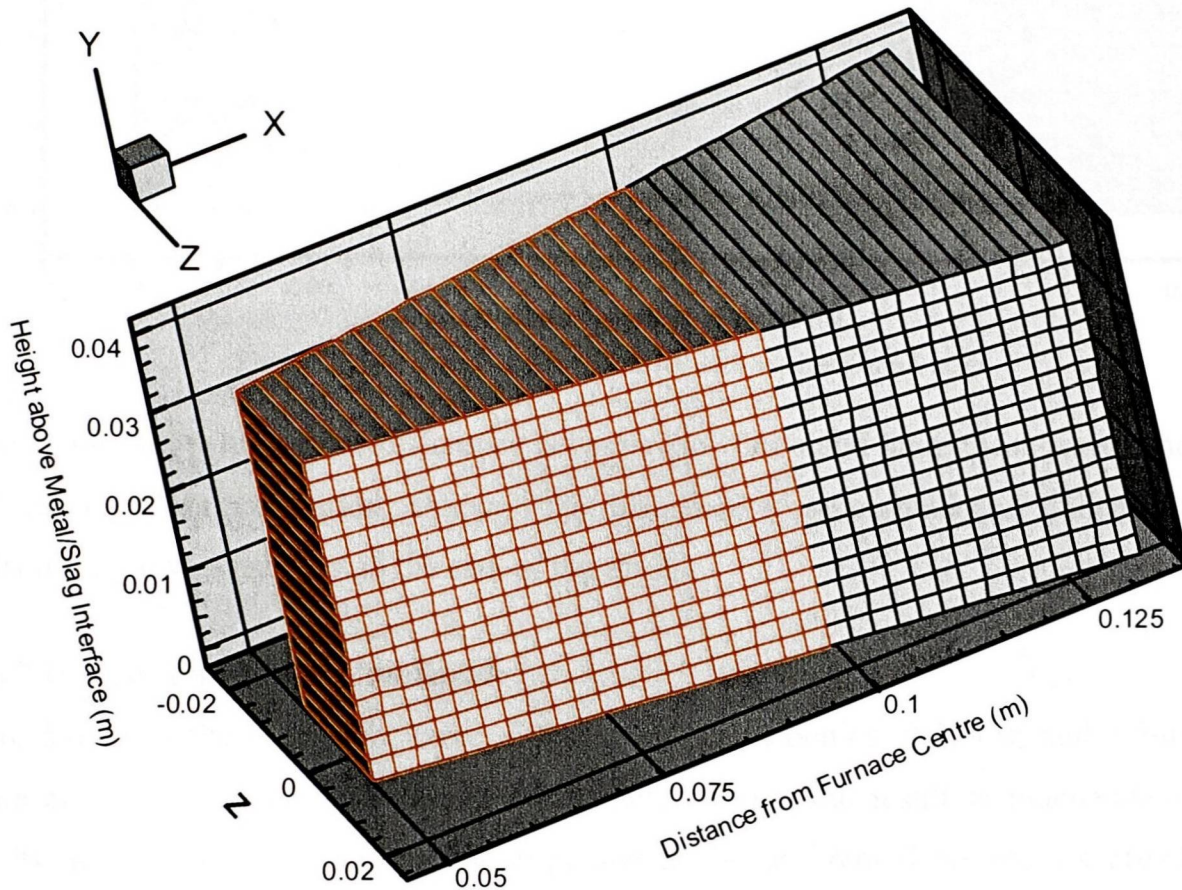


Figure 5.6 – Total Mesh View

5.1.5 Verification of Assumptions

To verify that the mesh and boundary conditions are not affecting the results obtained, sensitivities have been performed for the mesh density and inflow boundary conditions.

5.1.5.1 Mesh Refinement

To assess the effect of the mesh size, three different mesh sizes of square cross section were used: 25mm; 10mm; and 5mm. After running each of these meshes for the equivalent time for 5 hours operation, the penetration for each case is shown in Figure 5.7.

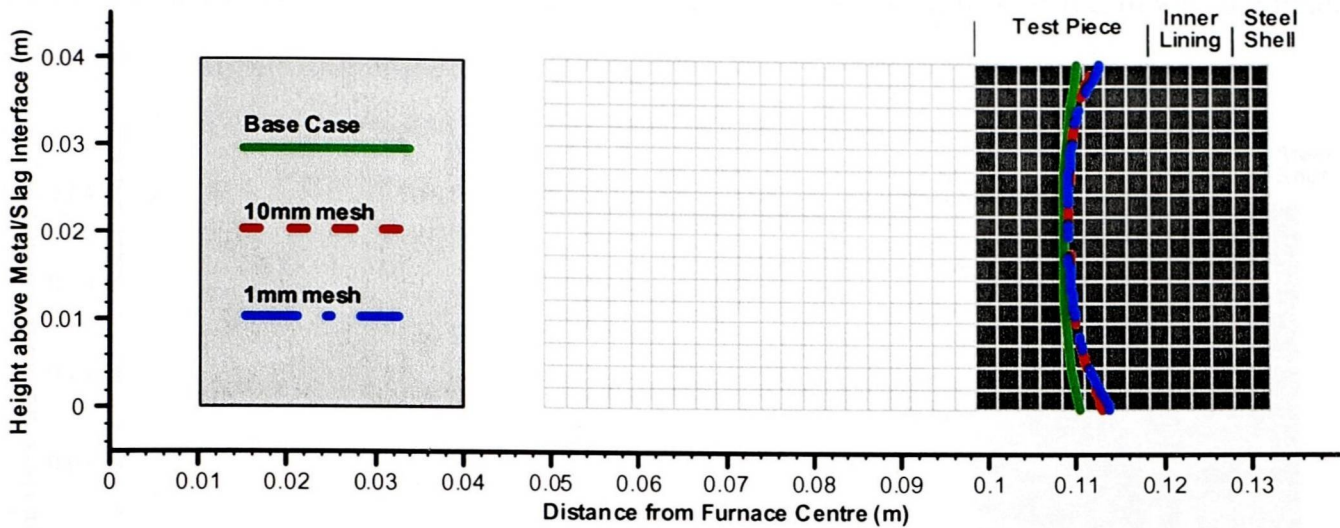


Figure 5.7 – Comparison of Results with various mesh sizes

These results show little to no difference between the 10mm and 5mm mesh sizes. The 25mm mesh displays less penetration, although the difference is quite small and indicates that the results have a low sensitivity to the size of the mesh.

5.1.5.2 Inflow Boundary Condition

Figure 5.8 show the results for three different inflow velocities: 0.5; 1.0; and 1.5ms⁻¹. The results are almost exactly the same, it is concluded that the result is independent of the velocity at this boundary. This is not surprising as the different flows are not affecting the temperature profile significantly.

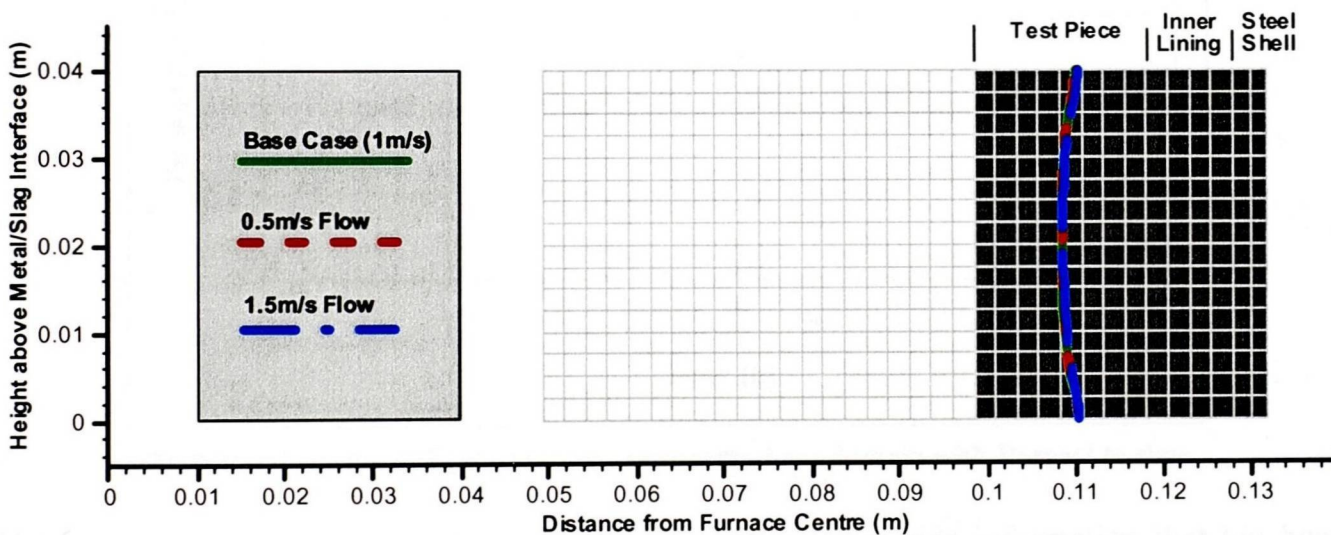


Figure 5.8 – Comparison of Results with different inflow conditions

5.1.6 Results and Discussion

The results (Figure 5.9) obtained from this model match the test work performed for Hlsmelt by Veitsch-Radex (inset picture). The progression of the penetration with respect to time (Figure 5.10) shows the initial fast penetration rate that then drops off markedly with time.

Again the measured value after 5 hours of operation matches well with the model predicted value.

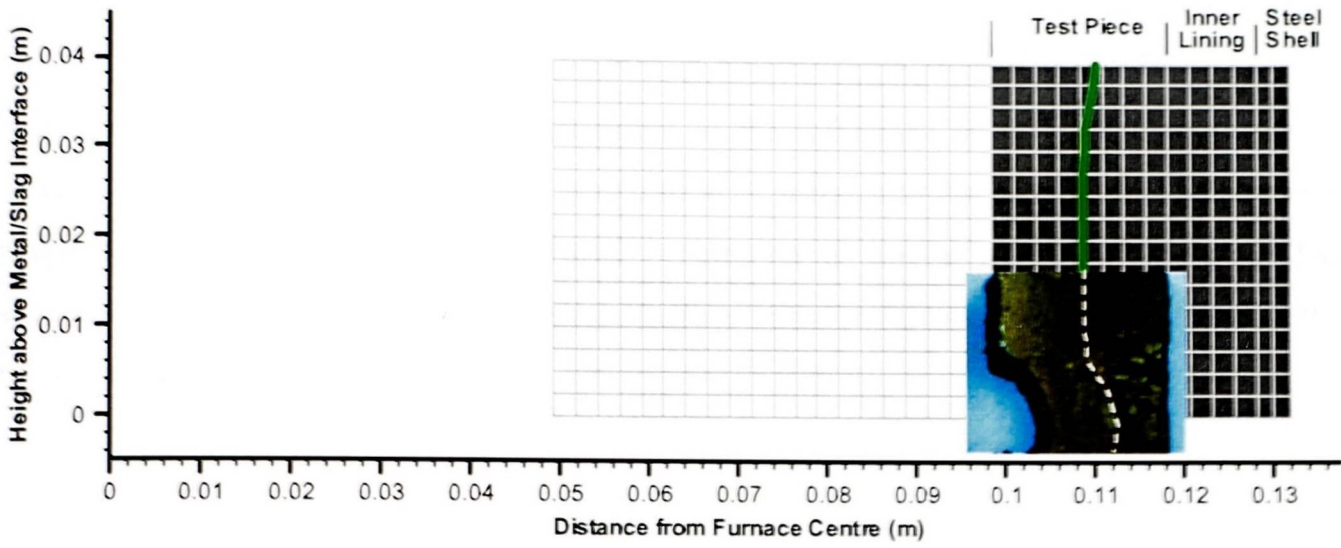


Figure 5.9 – Model Results after running for 5 hours with the results of the induction furnace test (inset picture)

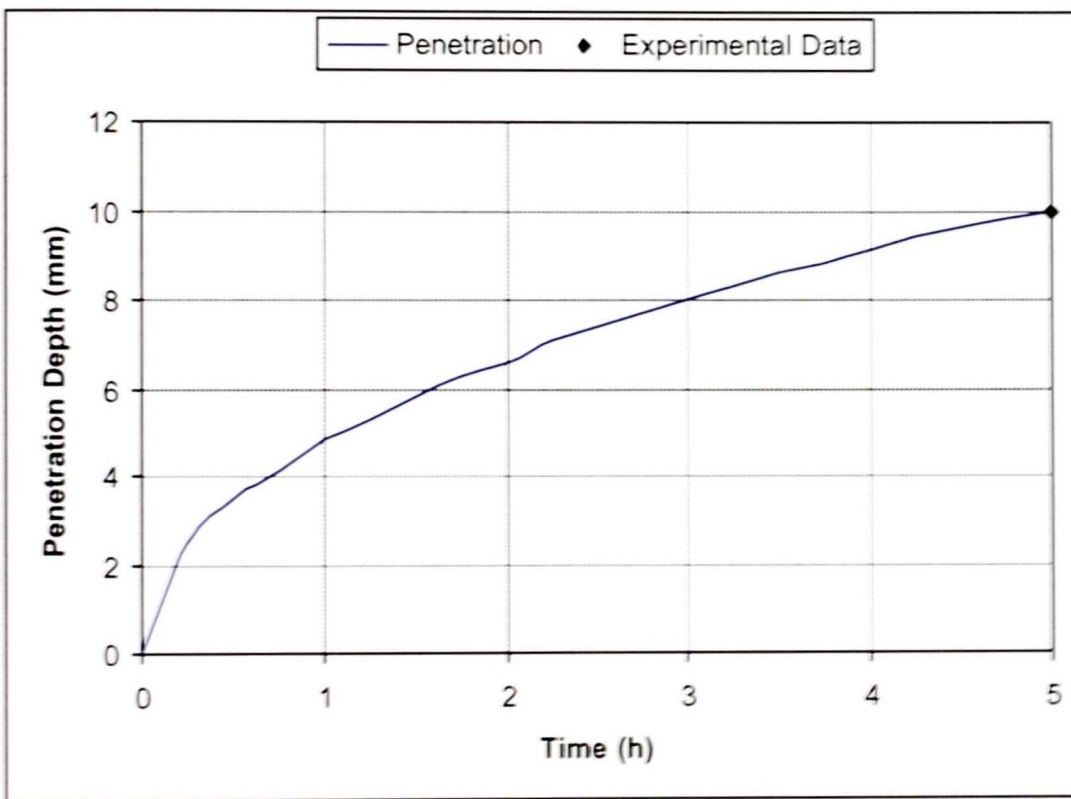


Figure 5.10 – Rate of Penetration at the centre of the domain with Respect to time

These results by themselves are not convincing, but they provide information that has been used to set up the penetration parameters for the other cases that have been examined.

5.1.7 Conclusions

The model of the induction furnace refractory wear test has been able to reproduce the penetration observed in the test work performed. This model has been able to set up the values for the penetration parameters that can be used in the modelling of other systems.

This work has only examined the penetration of the refractory by slag. From the pictures taken of the sectioned test pieces, the penetration of metal into the refractory is of a similar magnitude. It is suggested that the metal penetration is similar to that of the slag. The accelerated wear at the moving metal-slag interface with the refractory is not modelled in this present study.

5.2 HIs melt HRDF Pilot Plant Results

In the HIs melt process a large amount of molten slag and metal is thrown into the top gas reaction space by the gases that are produced in the reduction of the injected solid material. The droplets of predominantly slag fly around with a significant amount hitting the walls of the vessel with the balance falling back into the bath. The droplets hitting the wall run down and over the sloping slag section back to the bath. A model has been developed of the sloping refractory region and results obtained are compared to the measured wear profile taken after the campaigns.

5.2.1 Experimental Setup

A Campaign in the iron and steel industry refers to the period of time that a furnace or vessel is operated with a refractory lining. During a campaign, minor refractory repairs may be made but a campaign is not completed until it is decided to completely reline the vessel. At HIs melt, campaigns are broken down into separate operating periods. The period that is to be examined is the first two such periods of campaign 8 – campaign 8-1 and 8-2. Campaign 8-1 lasted for 195 hours (8.125 days). Campaign 8-2 lasted for 300 hours (12 ½ days) for a combined total operating time for the two sub-campaigns of 495 hours.

Any continuous process, as such as HIs melt, is best operated at steady conditions. During the start-up and shut-down, the process operates inefficiently. The chrome content is high in the slag at the start and slowly reduces as is shown in Figure 5.11. The only significant source of Chromia within the system is from the refractories, and the thinking at HIs melt is that this initial high level of Chromia in the slag is due to the spalling of the refractory due to the heat up of the vessel.

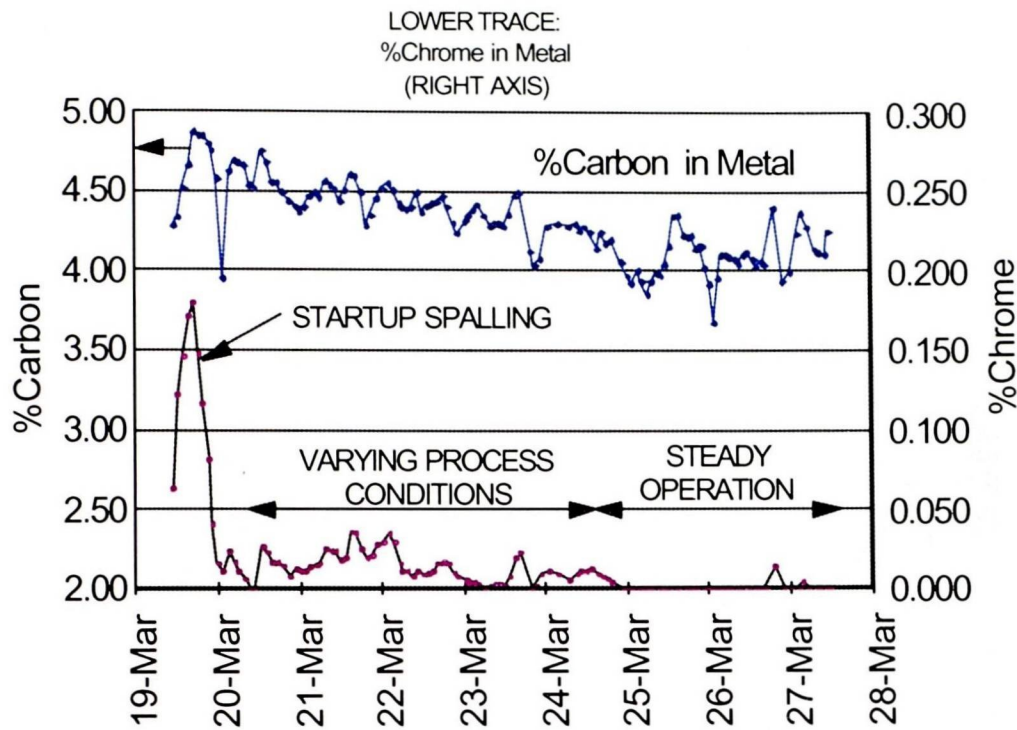


Figure 5.11 – Metal and Slag Chemistry for Campaign 8-1³

The vessel is gradually heated over several days as specified by the manufacturer to limit the amount of stress that is created by the thermal expansion of the bricks. Additionally the temperature is held at various points to ensure that the phases within the refractory have a chance to equilibrate. The heat up process is carried out using hot air and natural gas burners which may oxidise the surface of the refractories.

Each campaign aims to test various features of the process. Campaign 8-1 and 8-2 were testing the performance of various feed materials. Iron units were supplied through different types of iron ore to Direct Reduced Iron (DRI) and blends of DRI and iron ore. Different coals were also tested from low rank anthracites through to medium and high volatile coals. On changing the feed material to the vessel, the process would react causing the fluctuations that can be seen in the metal and slag chemistry (Figure 5.11) and bath temperature. Additionally various levels of oxygen enrichment were also tested. To limit the wear of Chrome-Magnesia bricks, the level of MgO in the slag was kept close to saturation.

5.2.2 Data Gathering

After the end of each test period or campaign, the furnace was cooled and opened up for refractory inspection. A plumb line is dropped from the centre of the top opening of the vessel. At 30° increments around the vessel, the distance from the plumb line to the centre of each brick coarse was measured using a tape measure. This provides a significant amount of information that is used to validate the refractory wear models. Figure 5.12 shows the wear lines for the refractory at the end of campaign 8-2.

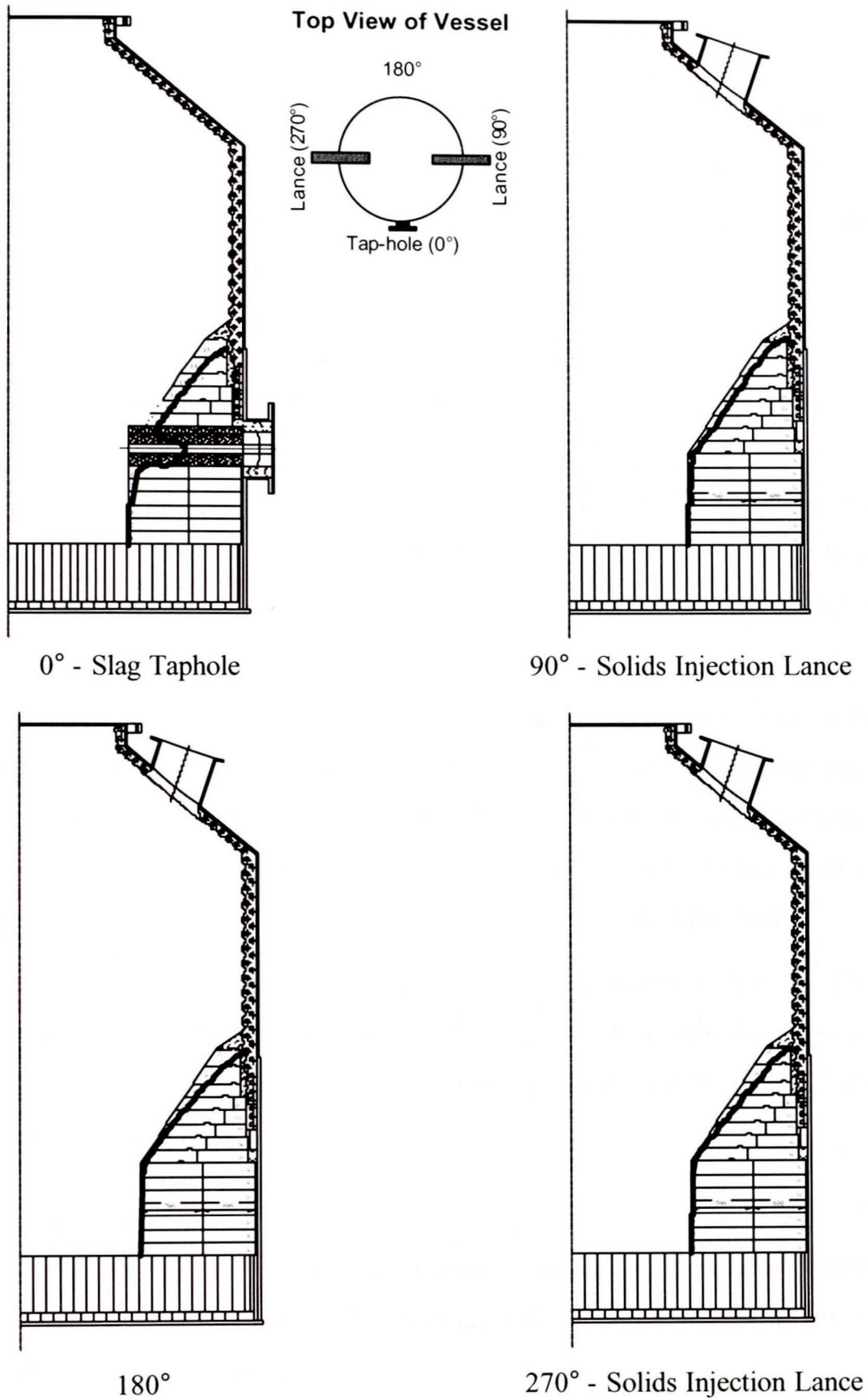


Figure 5.12 – Refractory Wear Measurements after Campaign 8-2¹²⁴

There are a couple of important features to note about this data. The wear is not concentric or even around the vessel. Taking into account the extra wear due to the location of the tap-hole, the wear is lowest at the location of the lances, and highest at 90° to the lances.

5.2.3 Model Formulation

This model takes into account the results from the induction furnace model, which modelled the penetration of Hismelt slag into the Magnesia-Chrome refractory used in this model. The induction furnace results have provided values for the penetration parameters. The extent of the domain, boundary conditions and turbulence considerations whilst developing this model are discussed in this section.

5.2.3.1 Domain

It is recognised that the Hismelt process requires a fully 3-dimensional model to accurately capture all of the physics that is involved within the process. Of particular note for this work, is the way the droplets of molten slag and iron travel through the top gas reaction space is not uniform with respect to the angle around the vessel. In particular droplets were found to fall back onto the regions in between the solids injection lances – something that has been observed in water modelling² studies.

To set up all of the required physics to model the fountain in the top-space within PHYSICA would have required a significant amount of time and effort. This modelling exercise has already been undertaken by Phil Schwarz at CSIRO in Melbourne and more recently by Mark Davis at Rio Tinto Technical Services in Perth. The slag flows from this work will be used to set up the flows of slag through the small “wedge” being modelled in this work.

Refractory bricks are used to line the bottom portion of the furnace as is shown in Figure 5.12. On top of the top ring of bricks, castable refractory is used to finish off the slope. In this model, the slope of the refractory bricks is continued up to intersect the vessel wall, and the same type of refractory is used.

5.2.3.2 Boundary Conditions

Flow and temperature boundary conditions are used in this model. The flow conditions at the boundary are chosen to imitate the results from the bath model. The temperature conditions amount to a fixed bath temperature.

Flow

As the bath and corresponding fountain of metal and slag droplets is an involved modelling task, the flow field for the slag has been based on the results from calculations performed using the bath model at Rio Tinto Technical Services in Perth.

Mark Davis supplied the velocity plot shown in Figure 5.13, which is used to direct the set up of the flow of slag within this model. This plot of the velocity vectors takes a snapshot in time. The model has only been run for a few seconds due to the long periods of time that it takes to run these complex calculations. To obtain a statistically meaningful average, more data than is available is required. Therefore the flows are used to guide the set up of the mesh and sensitivities to the flow have been carried out to test the effect of these assumptions.

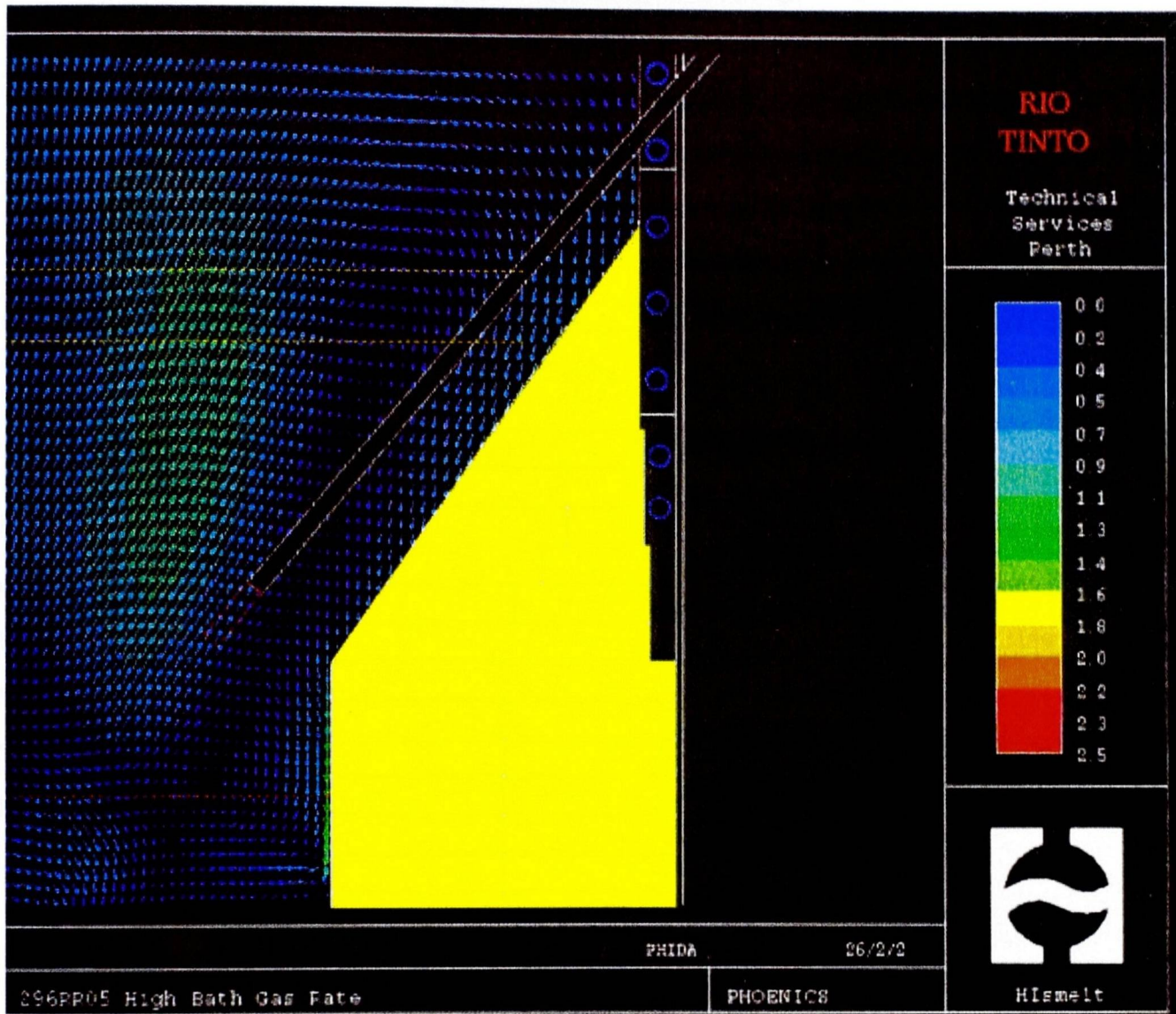


Figure 5.13 – Bath Model results Supplied by Mark Davis¹²⁰

To simulate the flow of slag within this model a mesh was constructed to model the areas where slag and refractory come into contact within the vessel. This mesh is shown in Figure 5.14 with the refractory elements shown in red, and the slag region in blue. The entire vessel has not been modelled as no additional benefit would be obtained. The refractory is modelled to the bottom of the metal bath.

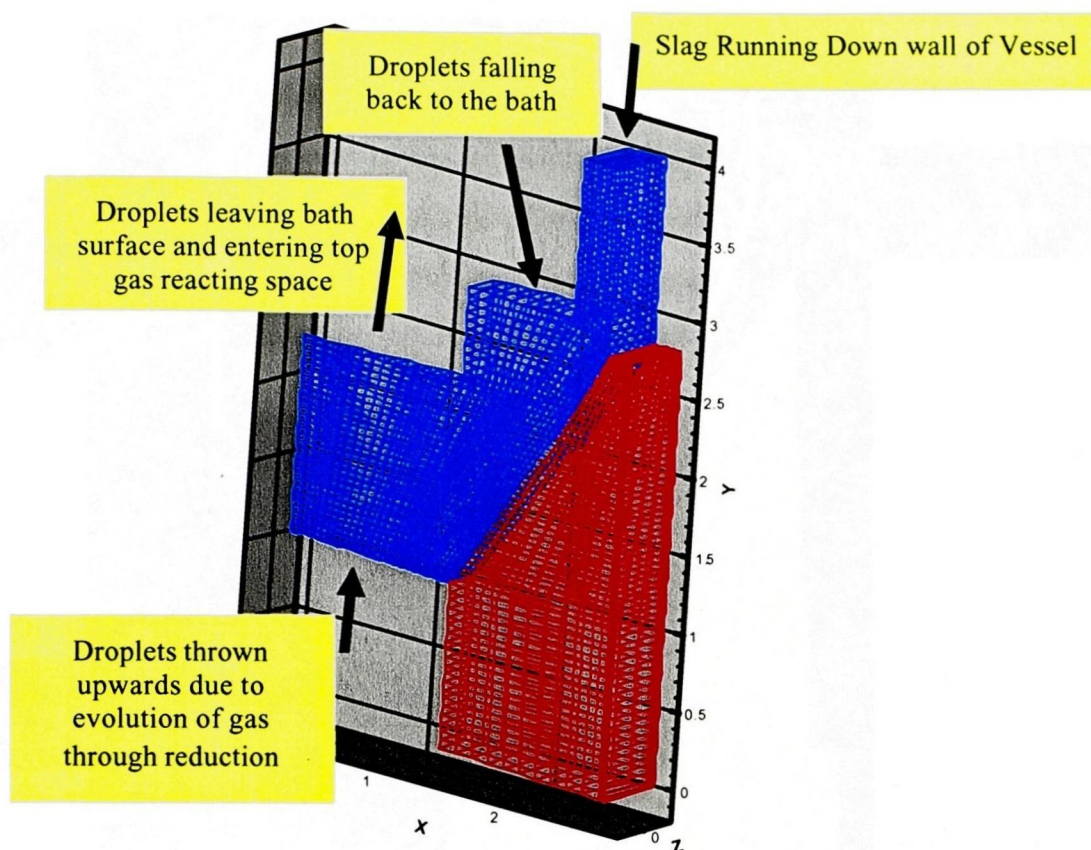


Figure 5.14 – Mesh of HIs melt HRDF pilot plant model indicating the slag flow boundary conditions

From the bath model results, the general flow pattern is used to set up flows for the boundary conditions as shown in Figure 5.15. Fixed velocities have been used to represent the droplets falling back to the bath and slag running down the walls. At the bottom of the slag region, the values from the bath model were taken and an equation fitted to this data is used for the velocity of slag at this boundary. The droplets leaving the top of the bath and entering the top gas space region are not specified as this surface is defined as an outflow within the model.

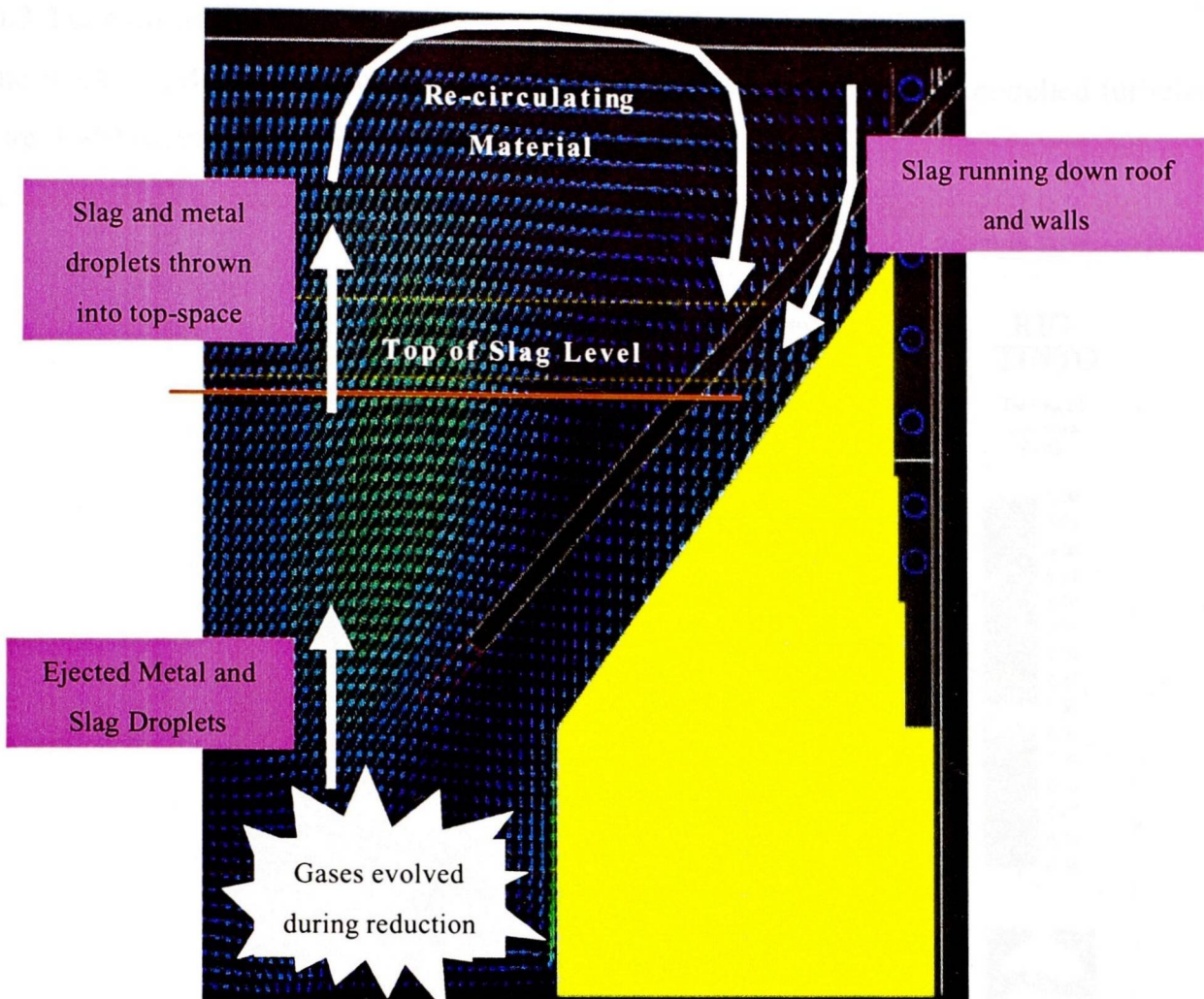


Figure 5.15 – General Bath Flow pattern on Bath Model Results

The slag running down the wall has inflow velocity of 1.0 ms^{-1} down the wall. The re-circulating droplets have a velocity set to 0.5 ms^{-1} in the downwards (y-direction) with a 0.2 ms^{-1} component towards the wall (x-direction).

Temperature

The temperature of the bath is assumed to be 1450°C , which is the normal operating temperature of the HIs melt pilot plant. This temperature is applied to the edge of the domain at the centre of the vessel and for material re-entering the bath from the top-space either directly or by running down the wall of the vessel.

The shell or cold side of the refractories uses ambient temperature of 25°C for this boundary. Other boundaries of the domain are symmetry planes that do not have any heat transfer occurring across them.

5.2.3.3 Turbulence

As the work by Mark Davis, of Rio Tinto Technical Services Perth, has modelled turbulence (Figure 5.16) directly within the top-space, the turbulent viscosity that was calculated in this work was used as a multiplier to the laminar viscosity for slag. The factor used is 1000.

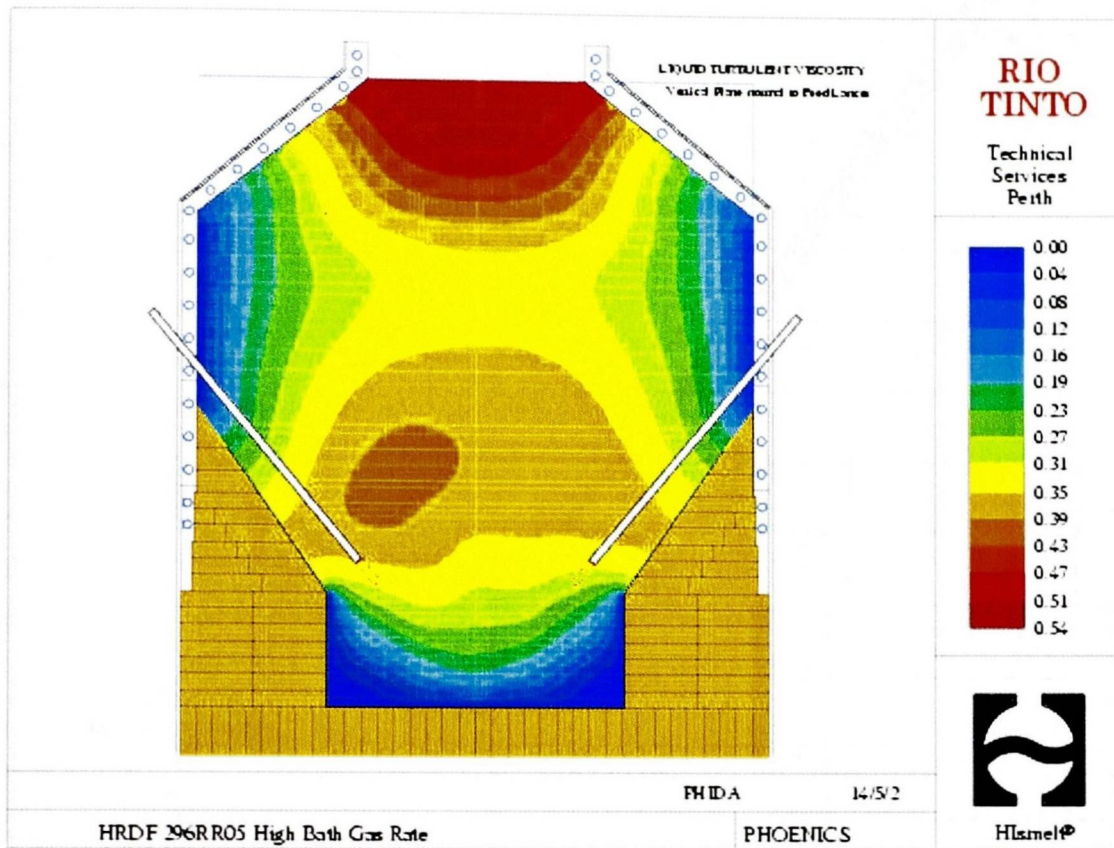


Figure 5.16 – Liquid Turbulent Viscosities Supplied by Mark Davis ¹²⁵

5.2.4 Verification of Assumptions

As the flow field used in this work is based on other modelling results, the sensitivity of the results to this is examined by varying the slag inflow rate. Additionally the sensitivity of the result to the mesh is also tested with different mesh densities.

5.2.4.1 Flow Boundary Condition

The slag running down the wall that then impacts on the sloping refractory section is set to 1ms^{-1} in the initial set up for this problem. 0.5 and 1.5ms^{-1} were also run to examine the sensitivity of the results to this inflow boundary condition as these values are the maximum and minimum values predicted from the bath model (see Figure 5.13). The wear predicted shows that at the top of the domain, the refractory wear is increasing with increasing inflow velocity. These results show that the flow rates in the range predicted by the bath model will not make these results unrepresentative of the measured values.

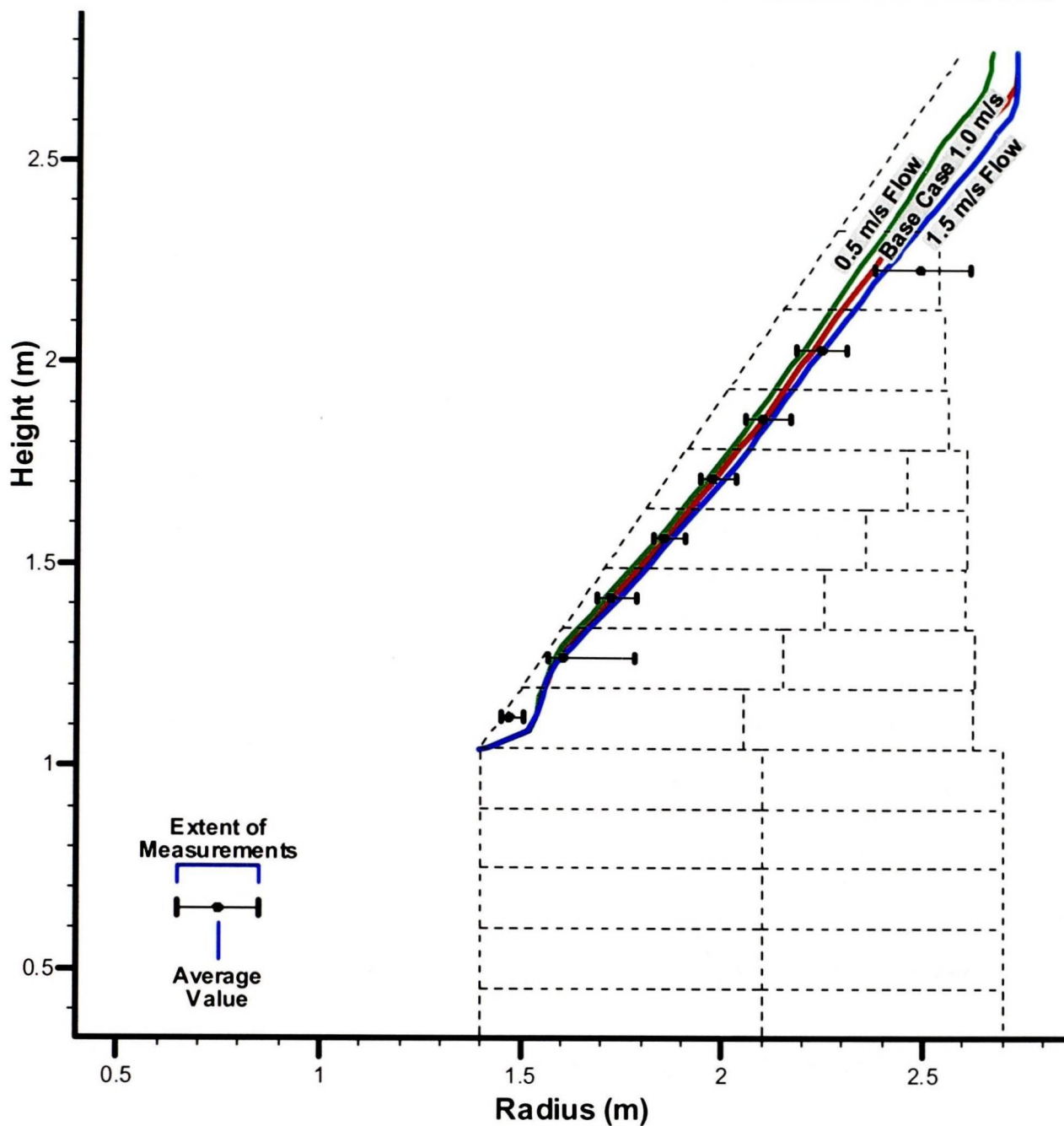


Figure 5.17 – Refractory Wear Contour Sensitivity to Inflow Boundary Condition

5.2.4.2 Mesh

As the mesh that was originally generated is seen to be quite fine already containing 2236 elements, the mesh was coarsened to ascertain the effect of the mesh on the results obtained. Two cases were run: with cells double (containing 574 elements) and 1.5 times (containing 994 elements) the size of the original mesh. Figure 5.18 shows the refractory wear lines for these various meshes. The only appreciable difference that can be seen is at the top of the refractory slope. In this region the mesh is quite fine and it is where the flow is changing direction the most – therefore more elements in this area will be better able to resolve this change in direction. This will lead to slightly different velocities which will affect the erosion in this area of the mesh.

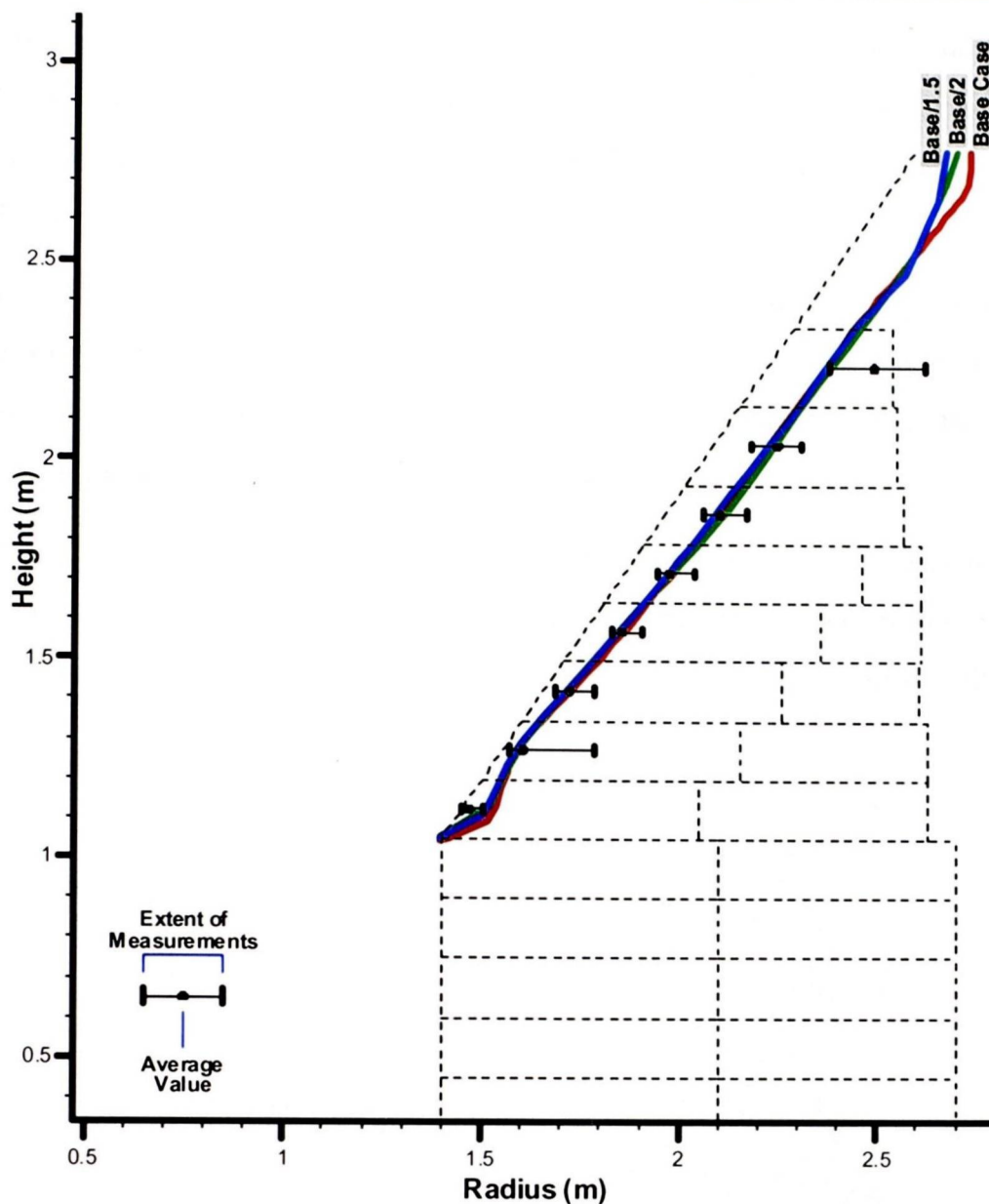


Figure 5.18 – Refractory Wear Contour Sensitivity to Mesh Density

5.2.5 Results and Discussion

The results for the model set up to represent the first part of campaign 8 are summarised in Figure 5.19. The shaded area indicates the location of the refractory, with the initial location of the bricks indicated by the dotted line. The red line shows the extent of the slag penetrating into the refractory. The vector field shows the flow of slag within the model at the end of the simulation.

The measured location for the centre of each refractory ring is shown by the error bar like marks at the interface. The range of the bars indicates the maximum and minimum values for the wear at the various locations around the vessel.

The measured values agree very well with the model results. The top measurement has the worst agreement with the modelled results. This is due to the fact that above the top ring, castable refractory is used. This refractory does not have the structure or strength to resist

wear like the Magnesium-Chrome refractories that have been compressed and fired during manufacture. The castable refractory is likely to have larger pore sizes as it is likely to be hand rammed into place on top of the refractory rather than the compression developed in a press used to make pre-fired bricks.

The castable refractory is virtually worn away completely as is shown in Figure 5.12. The top ring will therefore be exposed to a different flow condition that is more favourable for wear. The large range of wear measured for the top ring represents the different flow of slag at different parts of the vessel.

The second bottom ring also shows a large range of measured values. This representation is skewed by the measurement at the slag tap-hole area. For all the other measurements only a small amount of wear was observed. The model results compare favourably with the average of these results.

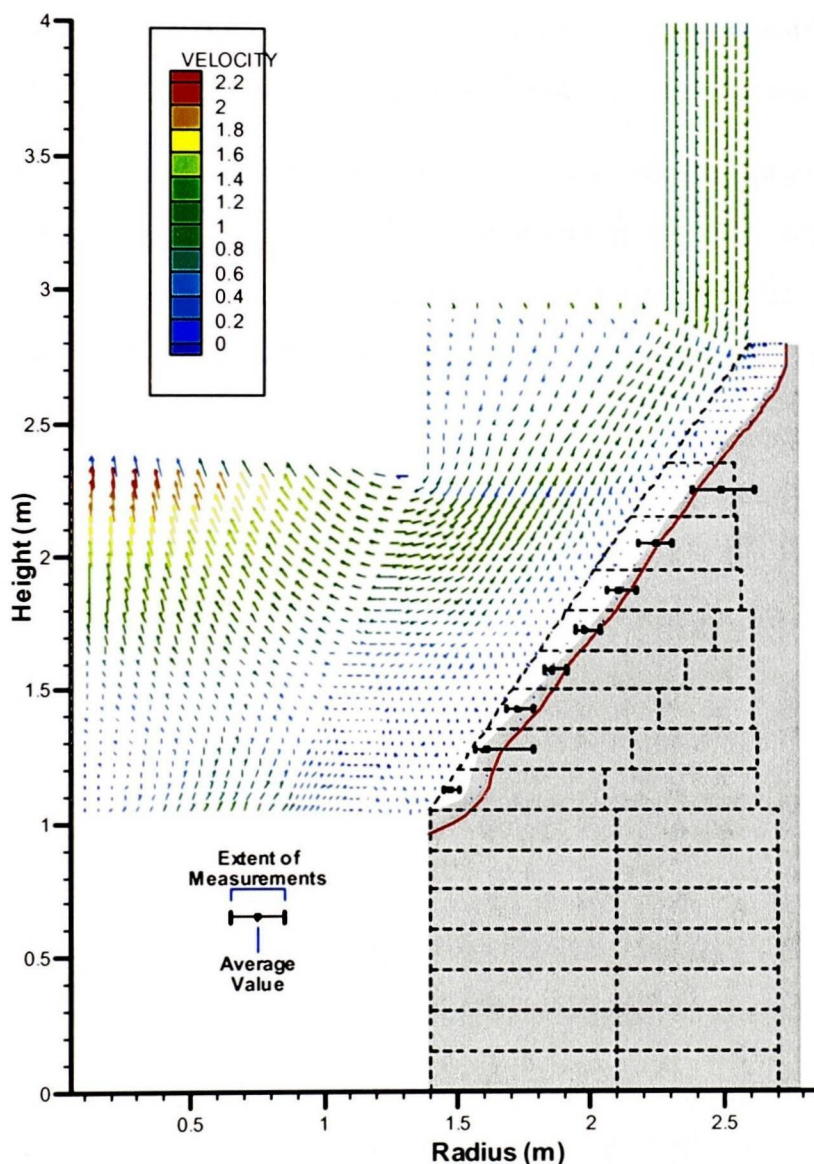


Figure 5.19 – Predicted Refractory wear for Campaign 8-2 compared to measured results

The factor that has the largest influence on these results is the flow field of the slag. The sensitivity to the inflow boundary condition demonstrates this fact very well impacting on the wear that is seen at the top of the vessel. The wear predicted with this model fits well within the range of the measured values.

To improve the prediction of the wear occurring, different properties for the castable refractory should be implemented. In particular a larger pore size could be used that would lead to increased penetration within the castable, and inevitably increased wear through erosion. By using a fully three dimensional model that accounts for the a-centric flow of slag in the vessel the different wear rates observed in the measured results could be replicated for the various locations around the vessel..

5.2.6 Concluding Remarks

The predicted wear from this model follows the measured values very well. Further improvement to these results would be obtained if a more complete treatment of the flow of slag within the top-space and down the refractory and water-cooled surfaces.

This model demonstrates how the refractory wear models can be applied to a large scale vessel. It is important to note that only the slag interactions with refractory have been accounted for in this work. The metal interaction should be able to be modelled using the same framework that has been established here, although further work will be required to validate this hypothesis.

APPLICATION TO SIMILAR SMELTING PROCESSES

To provide further verification of the refractory wear mechanisms, in particular the erosion mechanisms, the rotary slag test is modelled. The rotary slag test is widely used as it is able to set up a temperature gradient through the refractory along with having a constantly refreshed supply of slag to minimise the chemical effects. Additionally this work demonstrates how the modelling of the refractory wear mechanisms can be applied to similar smelting processes to HIs melt.

6.1 Description of the Process

The rotary slag refractory wear test is a commonly applied test for refractories for industrial applications. A cross section of the furnace is shown in Figure 6.1. This test method is described by the ASTM standard C874-85⁴⁸.

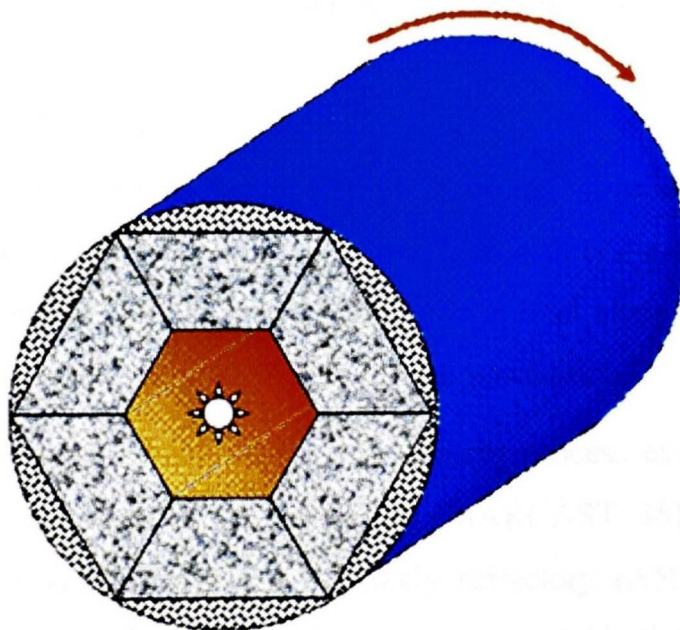


Figure 6.1 – Rotary Slag Test Arrangement

This test is popular because unlike other tests employed to test refractories a temperature gradient is established, and with the supply of fresh slag and the draining of slag from the furnace (due to its slight slope) the slag chemistry can also be controlled.

Six refractory test pieces are cut to the size shown in Figure 6.2 and to a length of 228mm. Castable refractory is used to fill the space between the test pieces and the furnace shell. The furnace is preheated and slag is added and rotated for 5 hours. After the furnace is cooled and the test pieces removed from the furnace, the samples are sectioned length wise. Points along the length of the test piece are measured for wear and the penetrated area. These are then expressed as a volume percentage of the total refractory sample tested.

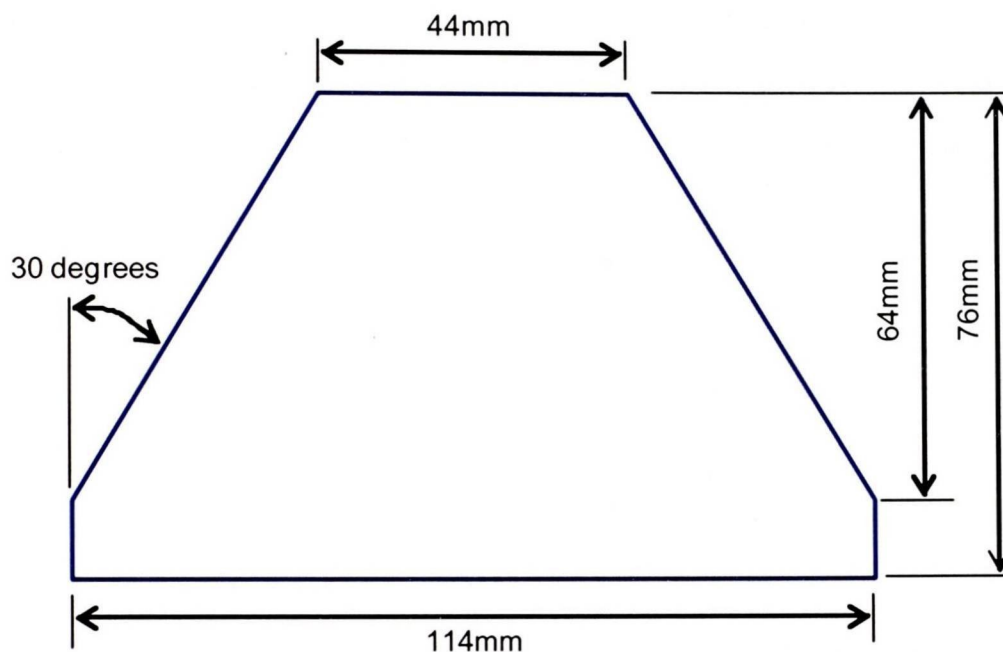


Figure 6.2 – Test Piece Dimensions

6.2 Experimental Setup

The experimental work was carried out by Rio Tinto Iron & Titanium (RTIT) at their Sorel technology centre just outside of Montreal, Quebec Canada. RTIT processes Titania rich ores using Electric Arc Furnace (EAF) technology to produce steel along with high TiO_2 content slags that are further processed into a form for pigment production.

The refractory wear test-work is part of a benchmarking process examining the refractories that RTIT use in their processes. The refractory (MARCAST 561 SP) selected for this modelling work is a refractory to match the likely refractory (ANKOCAST-ZV97M) that Hismelt proposes to substitute for the Chrome containing castable that is currently used. This material is a High Alumina, low cement, spinel forming castable.

The results¹²⁶ for this test with molten slag (of composition is listed in Table 6.1) are 4% erosion and 19% corrosion by volume. The corrosion value does not refer to the amount of the refractory that has been corroded by the slag, but rather the amount of the refractory that has

been worn away, affected or penetrated by the slag. This is a different definition to the way the mechanisms are defined for corrosion in this model – rather it is a measure of the penetration.

6.2.1 Slag and Refractory Chemistry Considerations

The slag chemistry (Table 6.1) is significantly different to that of the Hismelt slag. In particular the high iron oxide content within the RTIT slag has been linked to higher refractory wear. A typical Hismelt slag has much less than 5% iron oxide. This slag is not the typical RTIT slag which has a significantly higher concentration of TiO_2 and the operating temperatures are a couple of hundred degrees higher than those used in the Hismelt process.

Component	Composition Mass %
FeO	45
CaO	27
SiO_2	11
TiO_2	10
Al_2O_3	5

Table 6.1 – RTIT Slag Composition

As MTDATA is deficient in Titania species, FACT has been used to perform the required phase equilibria calculations for the slag (Figure 6.3), refractory (Figure 6.4) and a combination of them both (Figure 6.5).

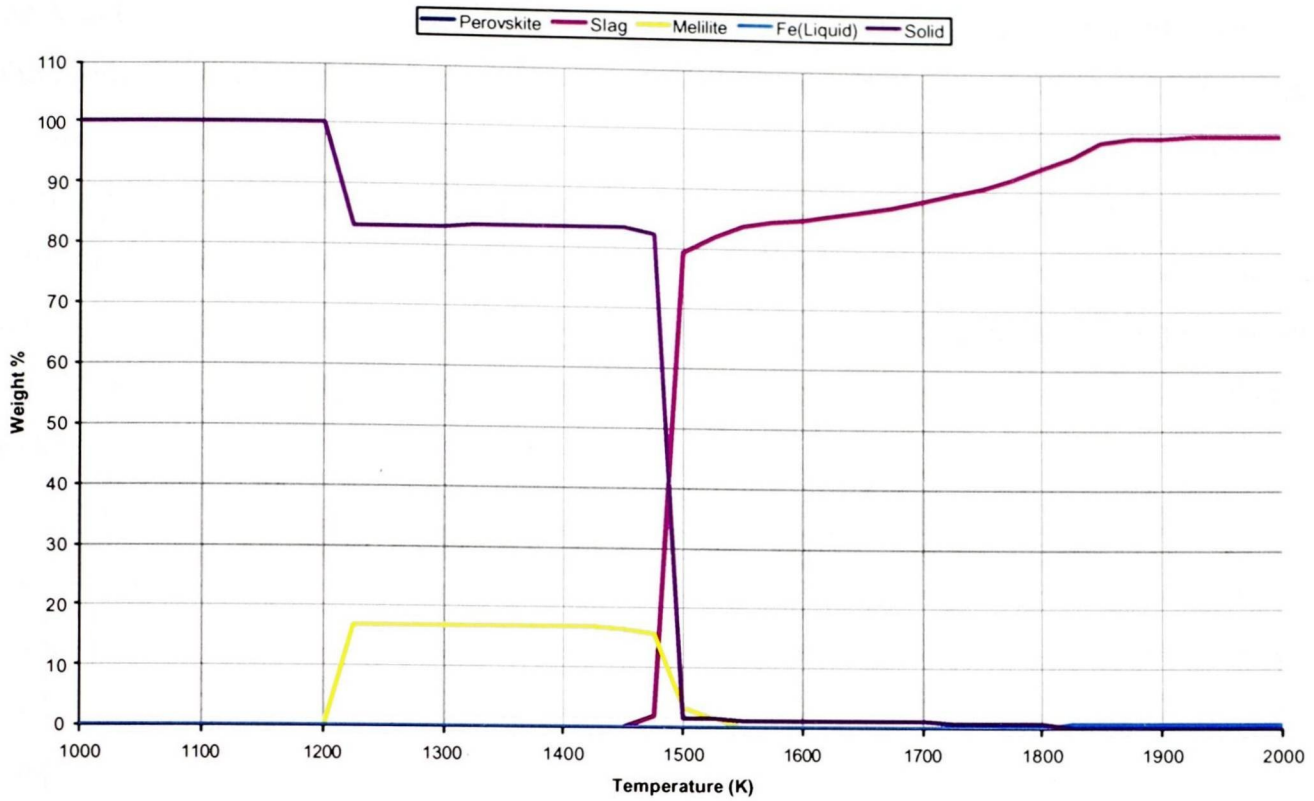


Figure 6.3 - FACT calculation for the RTIT Slag

The refractory calculation (Figure 6.4) shows the alumina spinel is the predominant phase present. This is consistent with the description of this refractory given by the manufacturer – a spinel forming castable.

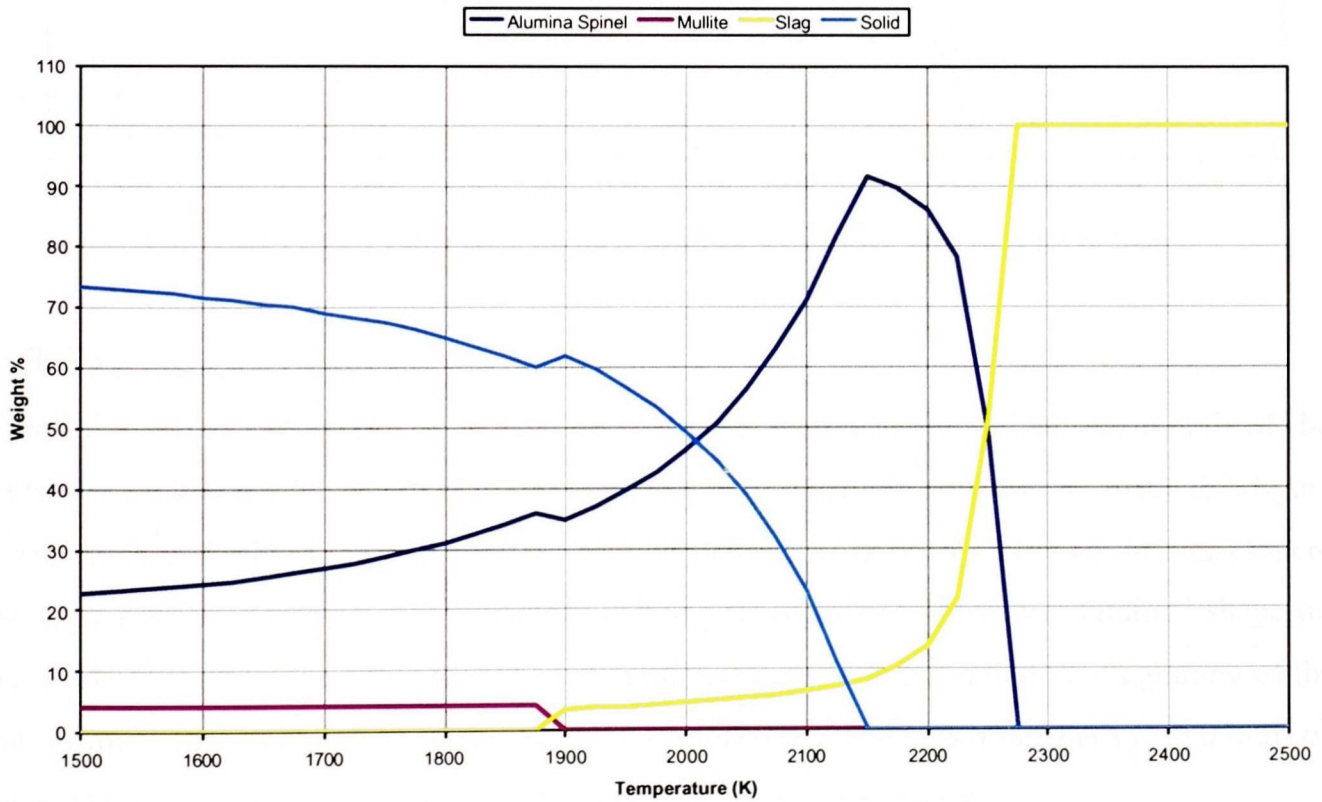


Figure 6.4 - FACT calculation for the Marcast refractory

The results for the FACT calculations (Figure 6.5) for a composite material created from 90% of the refractory and 10% of the slag show that the reacting temperature* range is 1550 – 2200 K. This is somewhat similar to the reacting range for the HIs melt refractories where the reacting temperature range has been determined to be 1680 – 2400 K. Due to the Arrhenius scaling that is performed the difference in the lower limit will be extremely small. For this fact, and the almost negligible corrosion occurring due to the slag practices employed, the same corrosion parameters have been used for this work as has been used in the HIs melt models.

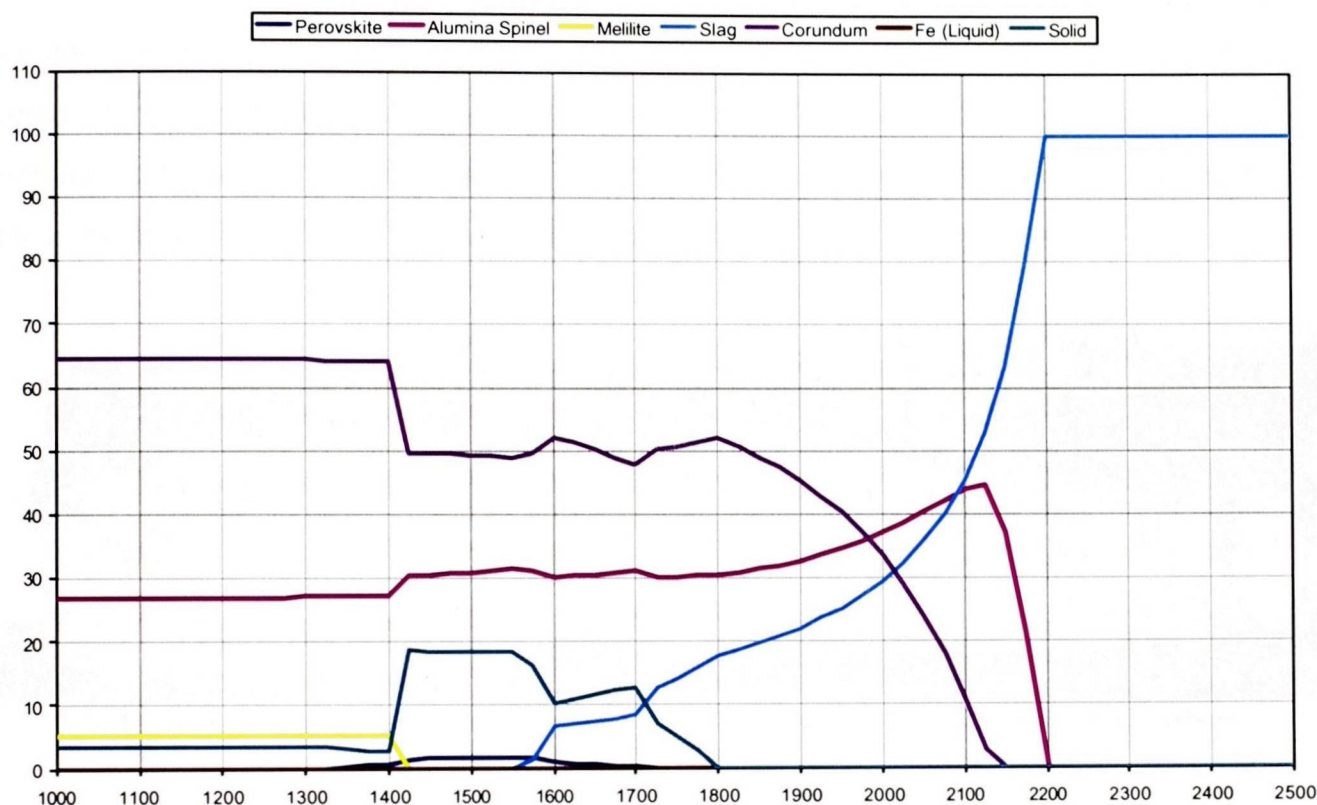


Figure 6.5 - FACT calculation for 90% Marcast Refractory with 10% RTIT Slag

6.3 Data Gathering

Figure 6.6 shows the sectioned MARCAST 561 SP sample. Points along the length of the sectioned sample are measured to obtain the amount of wear and penetration. From this figure it can be seen that it is the centre of the sample (where it has been sectioned through) where the most wear is occurring. The refractory is being worn away to form a cylindrical shape on the inside of the furnace rather than the hexagon that it started out with at the beginning of the test. From the original height of the sample (76mm) the 4% erosion translates to 3.04mm of wear. The 19% corrosion translates to 11.4mm of penetrated refractory.

* see section 3.1.2 for a description of the reaction temperature required for the corrosion mechanism



Figure 6.6 – Picture of the MARCAST 561 SP Sample tested with Molten Slag after Sectioning.

RTIT have also performed the same test using metal rather than slag. The resulting sectioned sample is shown in Figure 6.7. Metal interactions have not been considered in this work, this result shows similarities to those obtained with slag. Similar techniques could be applied to predict the wear due to metal, although further work would be required to validate and set up these models.

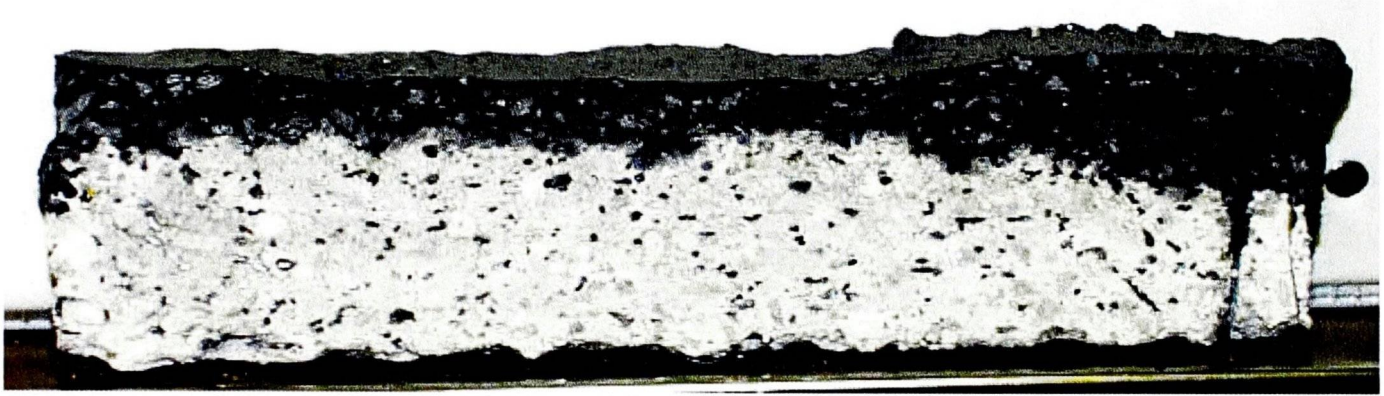


Figure 6.7 – Picture of the MARCAST 561 SP Sample tested with Molten 4.5% Carbon Metal after Sectioning.

6.4 Model Formulation

Initially the first step taken in formulating this model is to predict the location of the slag within the furnace. To accomplish this, a free-surface calculation is used. From this model information was extracted to model one of the six samples individually.

6.4.1 Free-surface

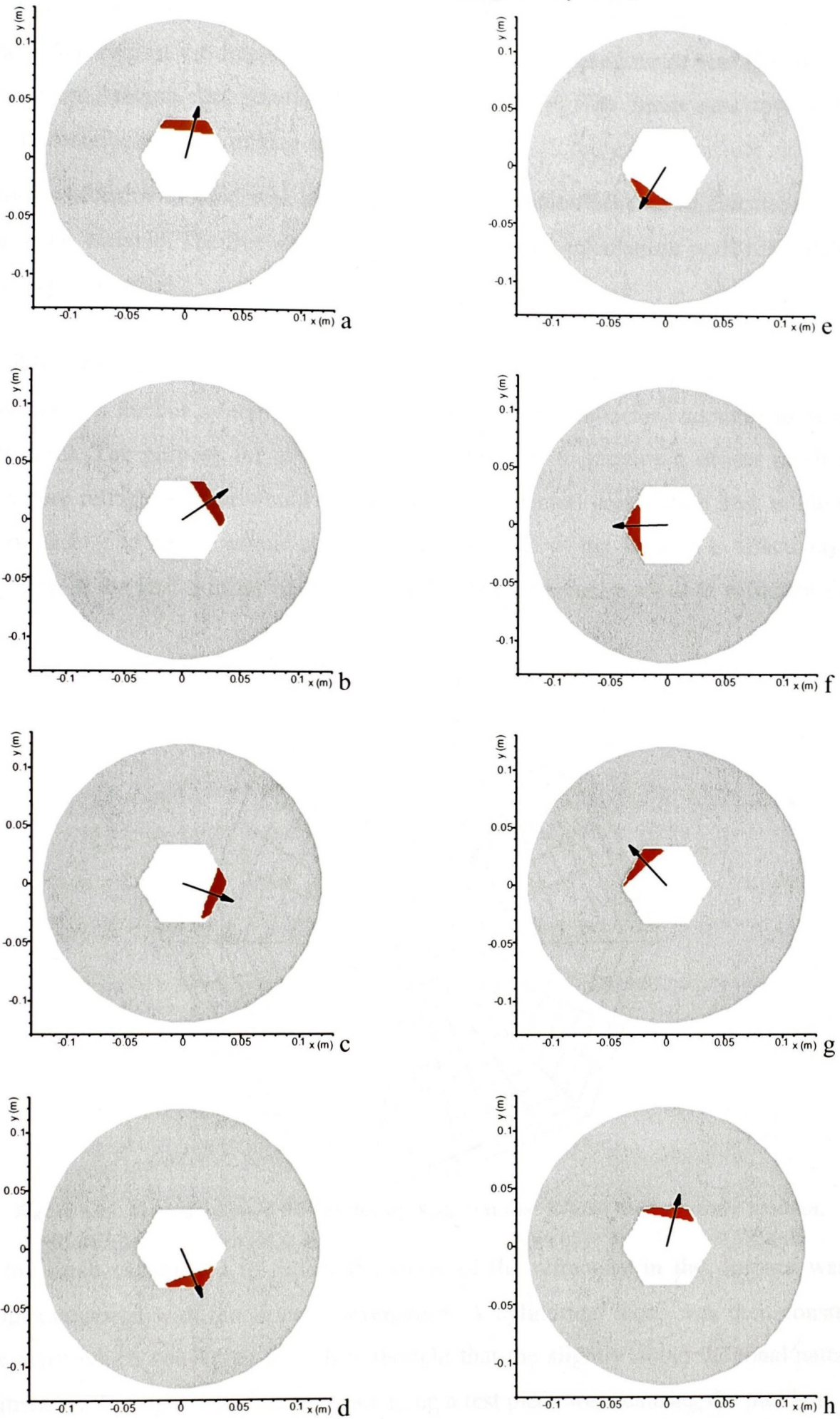
As the furnace is rotating at $2 \frac{1}{2}$ revolutions per minute the model needs to account for this. There are two possible methods that could be used to accomplish this: Moving Mesh; and Rotating Gravity.

By moving the mesh, at each time step you physically move the mesh an appropriate amount. Then you need to re-calculate or adjust the solved quantities throughout the domain to adjust for the movement of the mesh. By rotating the gravity vector, the slag will move due to the

moving gravity field. The resulting velocities then need to be adjusted to reflect the moving frame of reference.

As the rotating gravity field appeared to be simpler to implement, this approach was taken. Figure 6.8 shows six snapshots of the free-surface as it passes around the furnace. The arrow indicates the direction of the gravity vector. The free-surface was calculated using the Scalar Equation Algorithm (SEA) solving explicitly for the free-surface and using the GALA algorithm to improve the conservation of the free-surface.

Figure 6.8 – Free-surface Rotating Gravity Vector



One of the early challenges with this calculation was to prevent the diffusion of the free-surface through the domain. Initially the Van Leer advection scheme was used to prevent the numerical smearing of the free-surface. Even though an improved result was obtained using the Van Leer scheme, the result was still unsatisfactory. The mesh was too coarse to accurately describe the flow of slag around the furnace.

The Donor-Acceptor method was then used as the advection scheme to calculate the free-surface scalar variable. The free-surface did not smear in the calculations performed using the donor-acceptor method.

6.4.2 Mesh Considerations

The first meshes for this system were designed to follow the refractory contours as is shown in Figure 6.9. The purpose for attempting to do this was to provide a denser mesh in the region where refractory wear would take place and the central combustion area in the centre of the furnace. The region extending out to the cold side of the furnace is effectively only participating in the heat transfer calculations and therefore a coarse mesh is sufficient for this region.

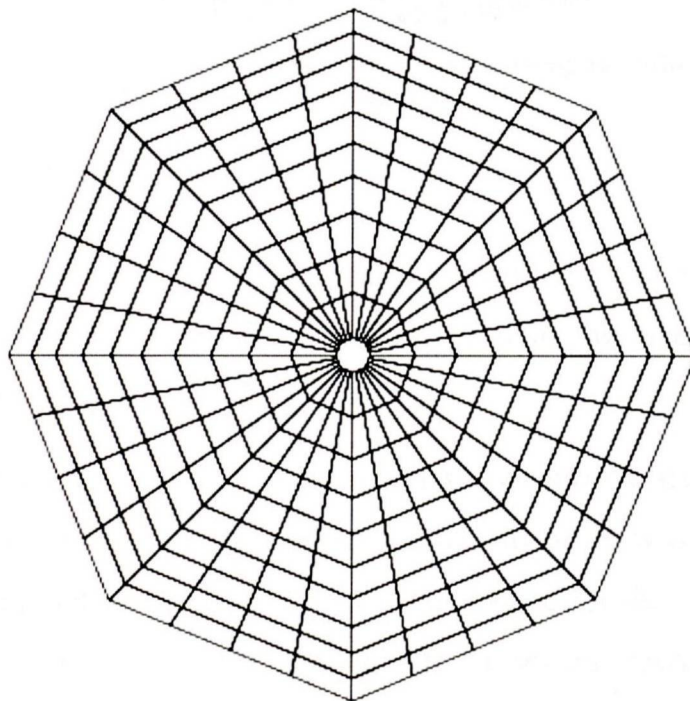


Figure 6.9 – Mesh developed for the Rotary Slag Test that follows the refractory location

When the mesh constructed to follow the shape of the refractory in the furnace was run, difficulties occurred with numerical convergence. A cylindrical mesh was then constructed (Figure 6.10) which converges well. It is thought that the slightly non-orthogonal nature of the elements at the edge of each sector containing a test piece were causing the problem.

This approach requires enough mesh density in the region of the hot face of the refractory to adequately resolve this interface. The initial location of the refractory is set up using code rather than explicitly locating the refractory when the mesh is generated. Another issue to be wary of is that when the mesh is refined, this impacts on the possible size of the time-steps as discussed below.

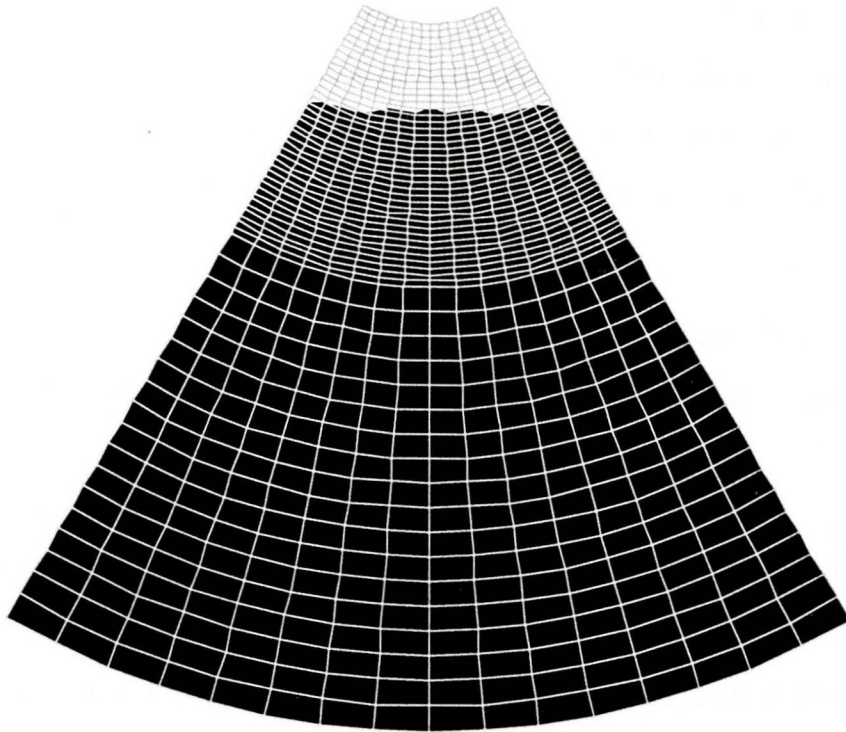


Figure 6.10 – Mesh developed for the Rotary Slag Test showing the initialised location of the refractory (shaded black)

6.4.3 Simulation Time

In reducing the size of the elements within the domain, the requirement to maintain the Courant Number below 0.35 for stability reasons leads to the size of the time-step to be limited to a smaller value.

In calculating the free-surface the maximum time-step was approximately 0.001s. To simulate only a couple of revolutions (each one taking 24s in real time) was taking days, and it was apparent that it was impractical to calculate the free-surface for the entire 5 hour test period. Therefore the free-surface calculation has been run for several revolutions to obtain a time averaged result that could be used to provide information for a simplified model.

6.4.4 Model Simplification

To simplify the model, and reduce the time that the simulations would take, it was decided to find the average location for the free-surface. This average location would be read in or stored into the free-surface variable for each time-step, eliminating the free-surface calculation that

is relatively expensive to carry out. Additionally there was no reason to model the entire furnace, and therefore only one sixth of the furnace is modelled – the region that one of the test pieces occupies.

Implementing the average location of the free-surface is not straightforward. In a normal free-surface calculation the free-surface is advected through the domain primarily by the flow of fluid. By explicitly defining the location of the free-surface at each time step, creates issues with the calculation of the flow. As the main usefulness of the fluid (slag) velocities in this model is for the calculation of shear, the momentum calculations are not solved in this simplified model. The required information can be obtained from the main free-surface calculations.

By not solving the momentum equation the convection terms within the various transport equations are zero. This in particular impacts on the heat transfer calculations.

6.4.5 Free-surface Location

After the first couple of revolutions of the furnace have been simulated, the start-up transient effects disappear. The calculated shear of the slag on the refractory is written to a data file to allow for post processing. Figure 6.8 demonstrates how the location is consistent and can be represented by a straight line with a slight slope. Figure 6.11 shows how the free-surface relates to the angle of the furnace for a fixed point in time.

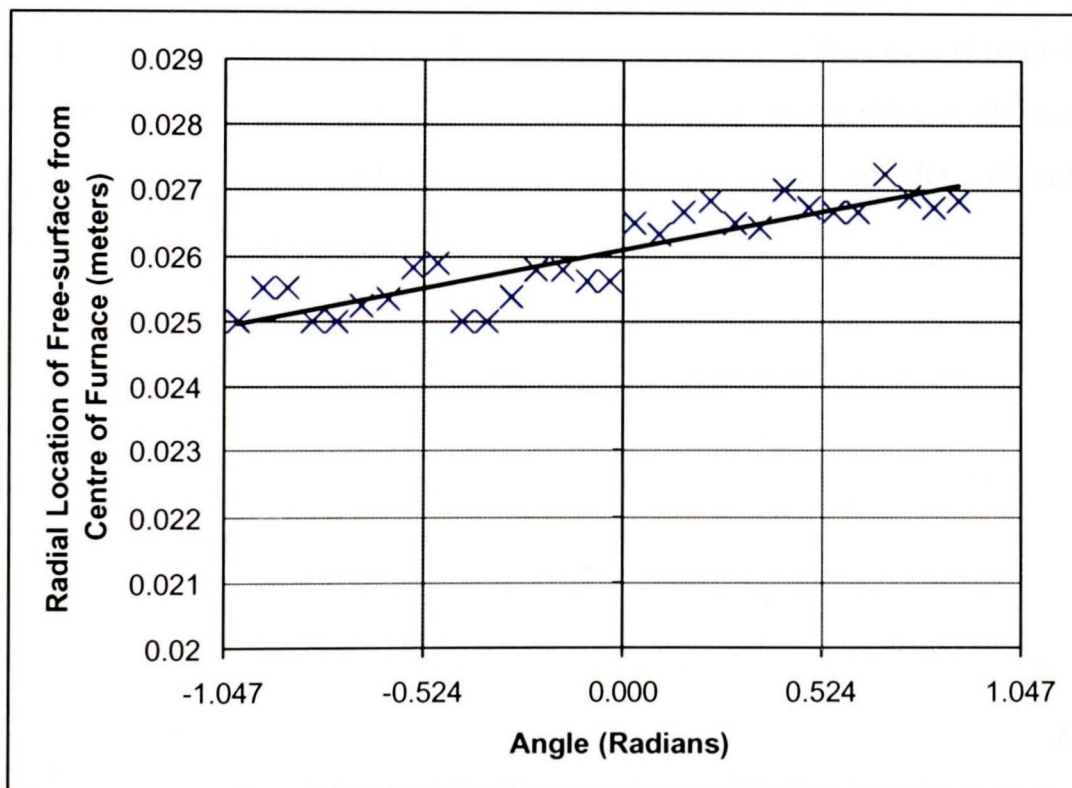


Figure 6.11 – Free-surface Location

To implement code to set the value of the free-surface throughout the domain, two points on the ends of the line are selected. The angle of rotation is calculated from the modulus of the simulation time and the time of a single revolution (Equation 6.1), which is used to rotate these points. The rotated points are then used to calculate a new linear equation that is used to determine whether a cell contains any of the free-surface variable that represents the slag.

$$\theta = \frac{t \% T}{T} 2\pi \quad (6.1)$$

where θ is the angle that the furnace has rotated to (radians)

t is the time (s)

$\%$ is the mathematical modulus operator

T is the period of a revolution (s)

6.4.6 Shear

Due to the complications caused by explicitly defining the location of the free-surface, the solution of the momentum/velocity equations is impractical. The shear, calculated from the slag velocities, also needs to be saved and re-inserted into the simplified model. Similarly to the location of the free-surface, the shear values for an entire revolution are saved to a data file from the larger free-surface calculation.

To provide a better representation of the shear, the shear values are rotated such that each of the six test pieces is aligned. This effectively gives six instances where the slag is moving past the refractory which are then averaged. Figure 6.12 shows one of the several snapshots in time for this averaging process. The important feature is the peak of the shear at the middle of the refractory face. The start and end of each of the six refractory samples coincide with the vertical gridlines of the graph.

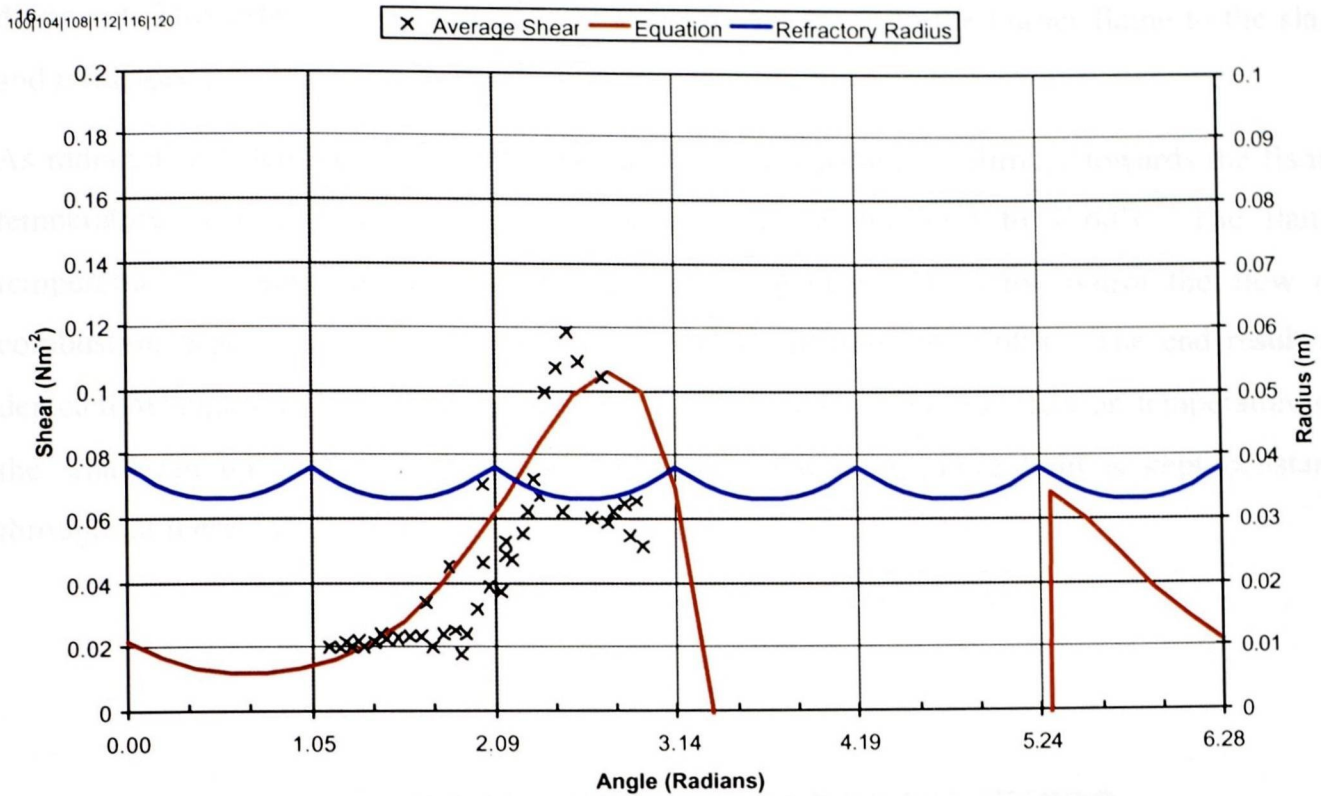


Figure 6.12 – Co-located Averaged Shear Values

The equation referred to in Figure 6.12 is the equation that has been fitted to the data to be used for the shear value within the simplified model. The equation is fitted to reflect the main features within the area of interest – the peak and the residual shear of 0.02 N/m^2 .

The magnitude of the shear is significantly lower than the values calculated in the Hismelt HRDF model. The first factor influencing this is the viscosity of the slag. Within the Hismelt model a factor of 1000 was used on the laminar viscosity – which flows through to the magnitude of the shear stress that is calculated. In this model, laminar viscosity is used due to the low Reynolds numbers that are involved.

Secondly the flows calculated within the system are relative to the mesh. Although the mesh is not physically moving within the calculations – the velocity vector is. The net effect is that the mesh has an angular velocity that needs to be added to all the velocities within the mesh. As the angular velocities will be nearly the same for all of the faces where slag is in contact with the refractory – the velocities were left unadjusted as it is easier to adjust the shear limits in the erosion mechanism than to adjust all of the velocities.

6.4.7 Temperature

In the free-surface runs the temperatures within the system are almost constant. In choosing not to solve the momentum equations, the convection term within the heat transfer equation

drops out. This affects the transfer of energy in the model from the burner flame to the slag and refractory.

As radiation will tend to drive the hot surfaces and slag within the furnace towards the flame temperature, a steady state solution is used to set the hot face to 1760°C. The flame temperature is measured by an optical pyrometer which is used to control the flow of combustion gases to the furnace to maintain the temperature at 1760°C. The end result is depicted by Figure 6.13. As the temperature is not changing, and the effect on temperature of the small amount of refractory wear that occurs, the temperature field is kept constant throughout these calculations.



Figure 6.13 – Temperature Conditions for the Rotary Slag Test

6.5 Verification of Assumptions

To test the sensitivity to the mesh size, three additional meshes were created to test the mesh that was developed during the modelling of this test. The different meshes used in this work along with the colours used in the plots following are:

- Standard Density (Red)
- Double Mesh Density (Green)
- Half the Mesh Density (Blue)
- $\frac{3}{4}$ Mesh Density (Black)

These meshes are shown in Figure 6.14, Figure 6.15, and Figure 6.16 being compared to the standard mesh. The dense part of the standard mesh has elements that are approximately 1mm wide in the radial direction.

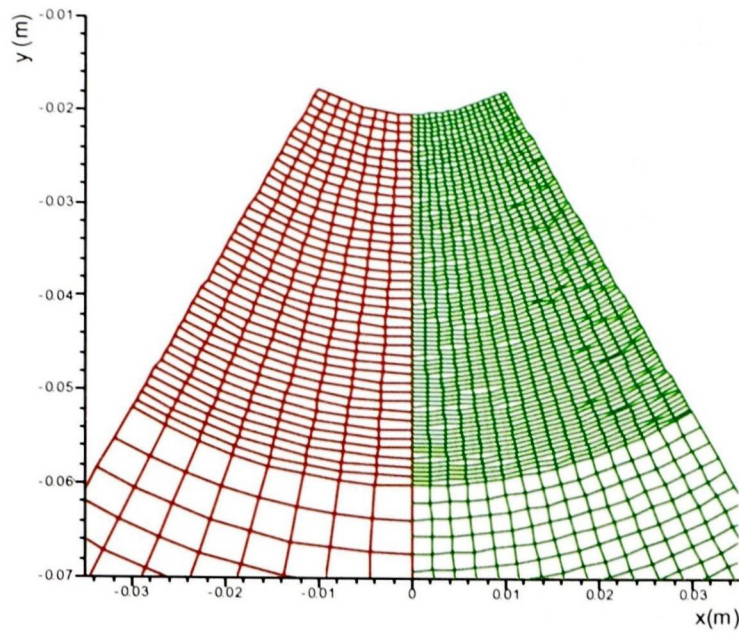


Figure 6.14 – Standard (red) and Double Density Mesh (green)

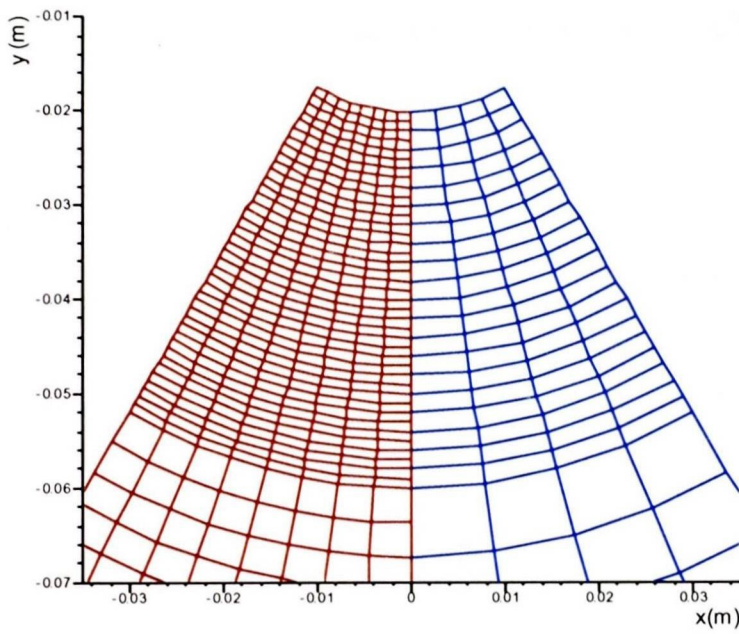


Figure 6.15 – Standard (red) and Half Density Mesh (blue)

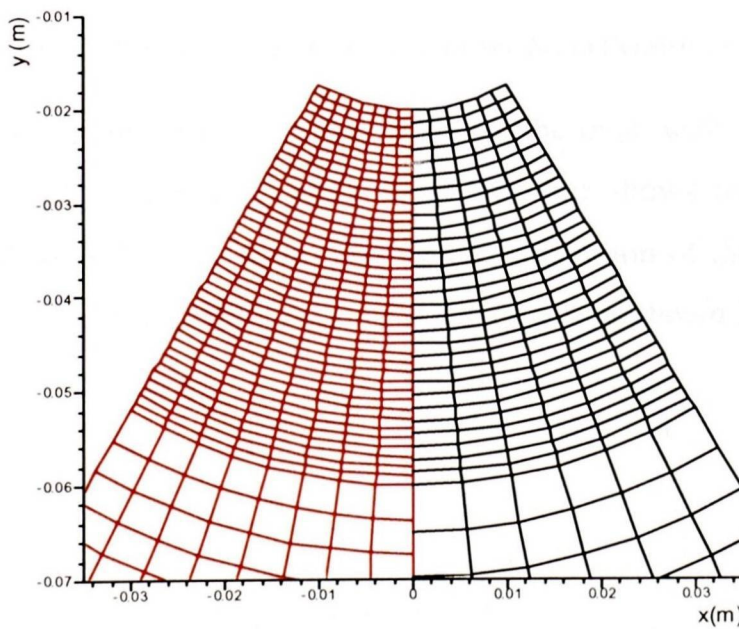


Figure 6.16 – Standard (red) and $\frac{3}{4}$ Density Mesh (black)

The plots of the 0.5 refractory contours in Figure 6.17 shows a peculiar result for the double density mesh (Green) whereas all the other results are quite similar. During the use of the refractory wear mechanisms, it has been noticed that for extremely fine meshes numerical rounding starts to cause problems with the code, which is the reason for the very dense mesh producing the unrealistic result.

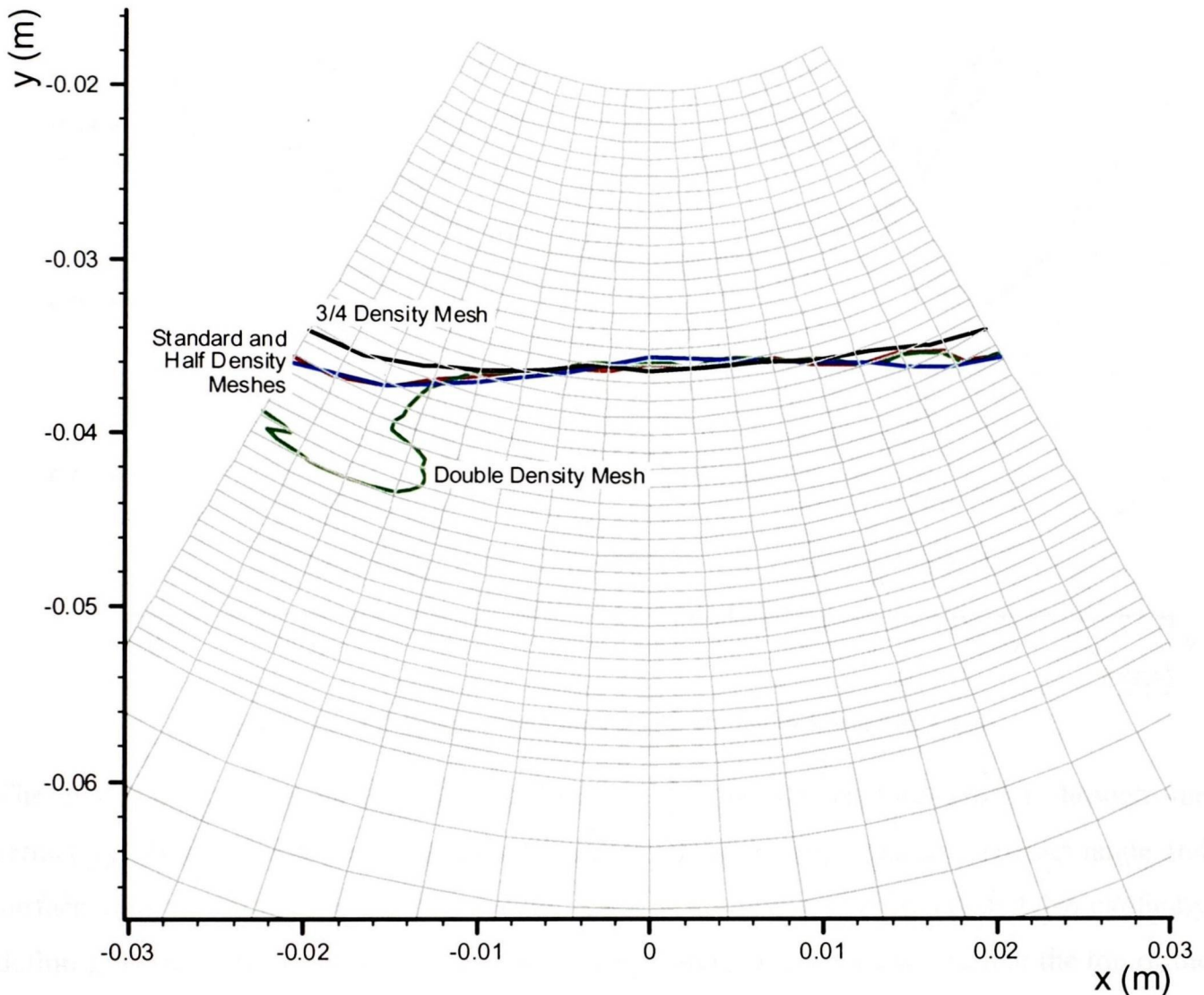


Figure 6.17 – 0.5 Refractory Contours for the Mesh Sensitivity Cases

The mesh penetration (Figure 6.18) is similar in all but the mesh with half the density of the standard mesh (Blue). The Double Density mesh (Green) shows some deviation in the location of the unrealistic refractory wear. The higher penetration of the half density mesh is due to the different temperature profile present for this case as is shown in Figure 6.19.

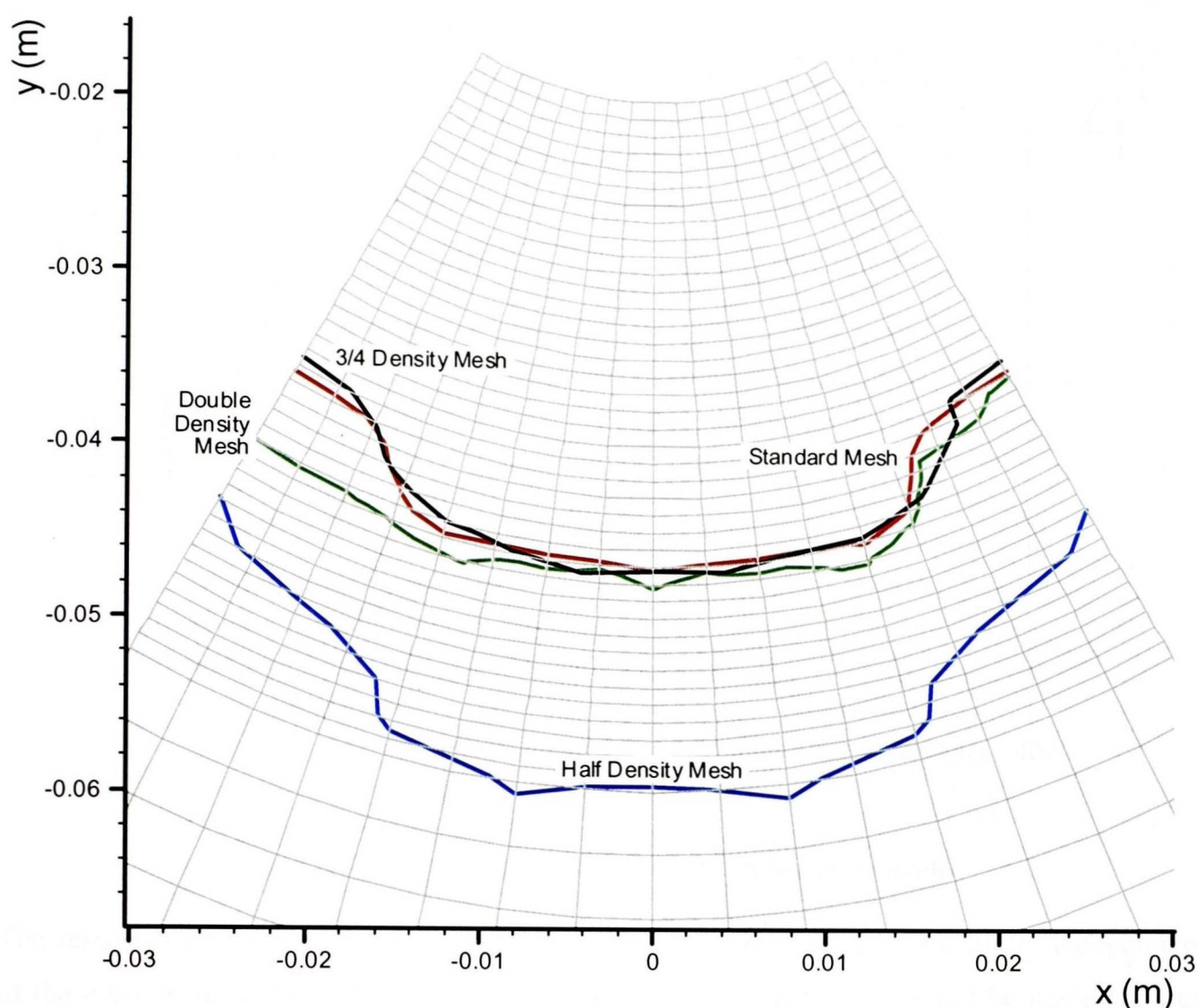


Figure 6.18 – 0.5 Penetration Contours for the Mesh Sensitivity Cases

The penetration equation is heavily influenced by the temperature profile through the refractory. This is due to the temperature dependence of the slag viscosity, contact angle and surface tension. In setting up this model, and due to the problems created by explicitly defining the free-surface location, the burner temperature boundary condition at the top of the mesh is adjusted to give the slag surface the temperature measured for the burner during the test work.

For the half density mesh, the refractory is hotter in the region where the penetration occurs, which leads to the higher penetration observed. Although this particular case is not exactly set up as intended, it demonstrates the large influence that the temperature profile has on the result.

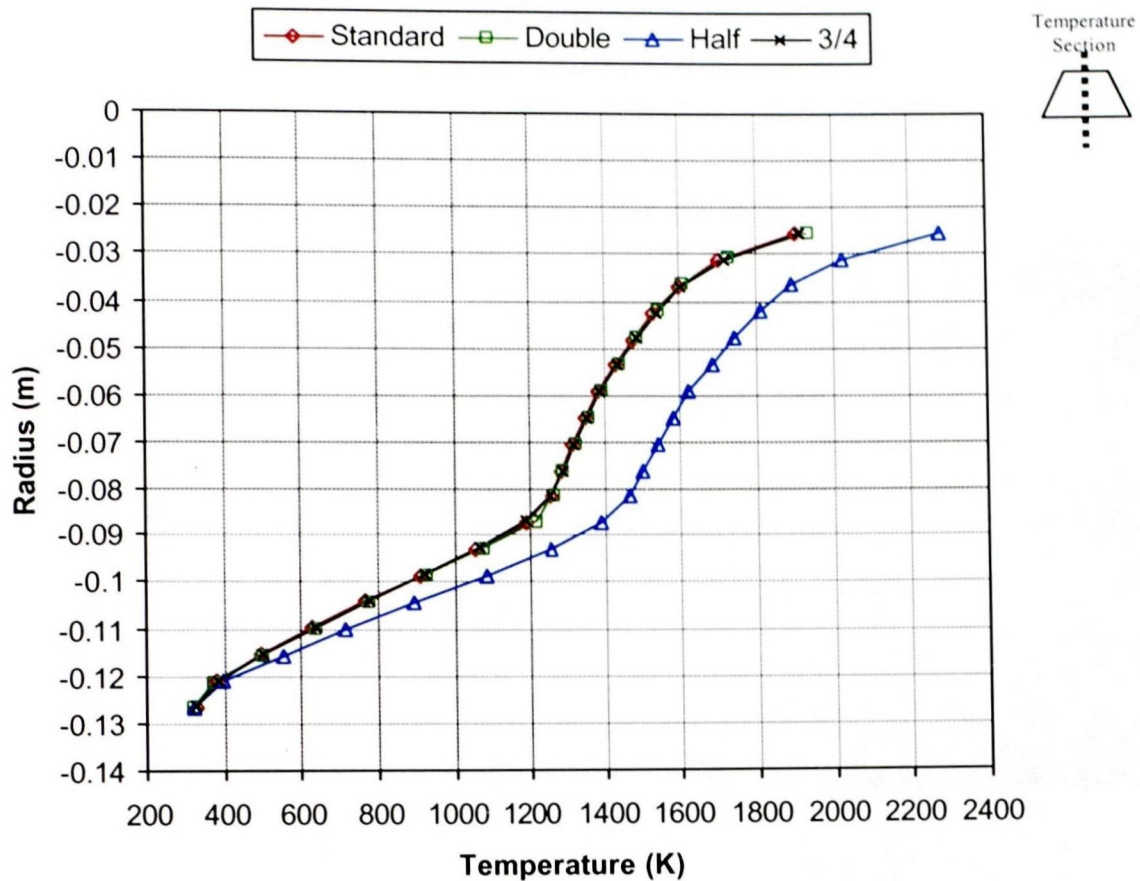


Figure 6.19 – Temperatures taken down the centre of the meshes

The results from these various meshes demonstrate how the result is essentially independent of the mesh at these mesh densities. The exception is that the mesh can not be made too fine as rounding errors influence the result.

6.6 Results and Discussion

The results from this model for the 5 hour test, shown in Figure 6.20, show refractory wear of 3mm and a penetration of 11mm at the centre of the test piece. The blue line shows the initialised location of the refractory within the model. The inset picture (scaled to match the plot scale) shows how well the wear and penetration is matched.

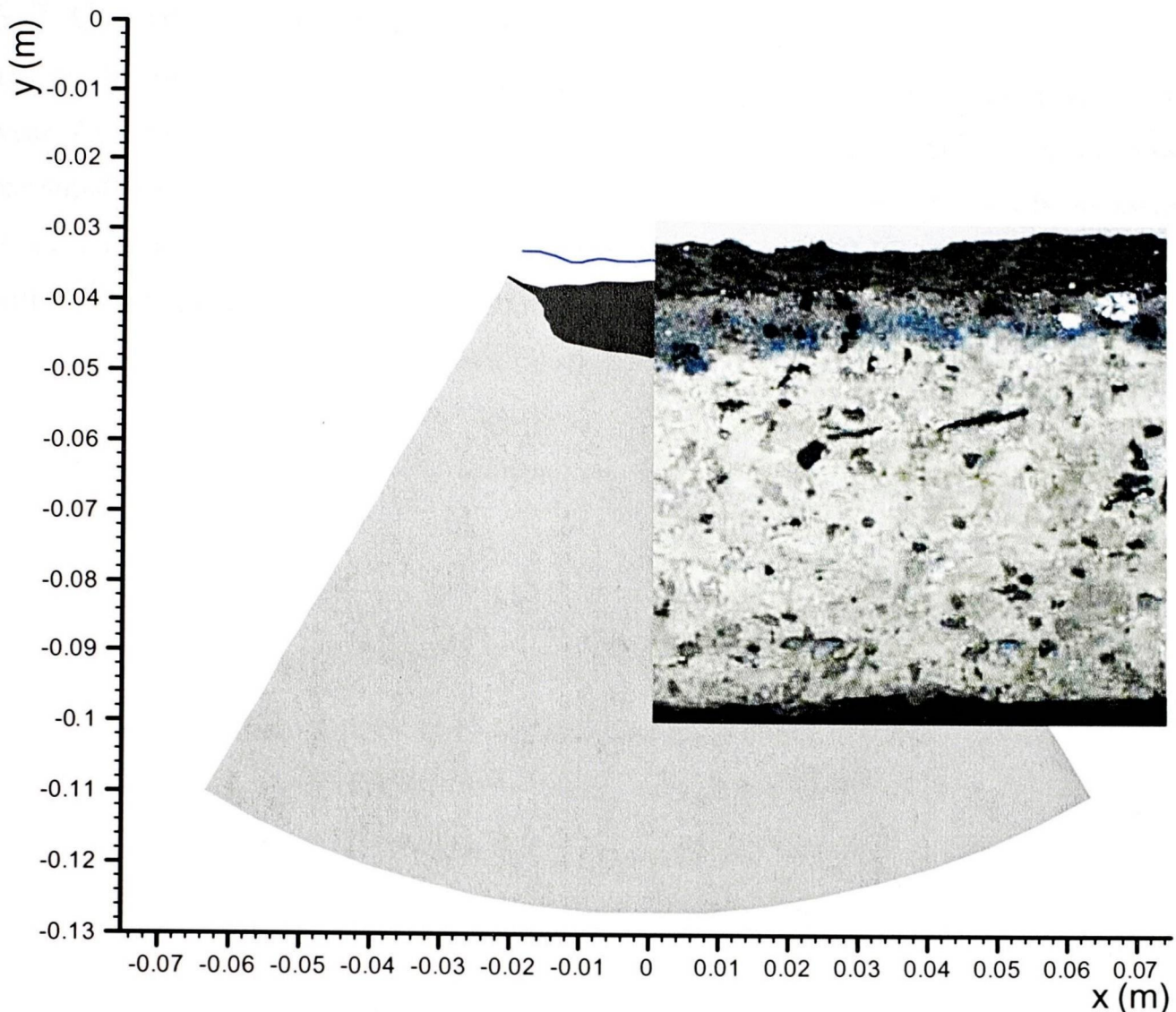


Figure 6.20 – Result from Rotary Slag Test

The image of the sectioned sample, inset into Figure 6.20, shows that the wear at the edge of the sample is less than the centre of the sample. It appears that the wear at the edge of the sample is over-predicted and is likely to be an effect of the assumptions made during the simplification of the model.

The erosion mechanism is driven by the shear stresses that have been extracted from the free-surface runs. Further adjustment of the lower stress limit would lead to a change in the amount of refractory removed. Without more accurate data making such adjustments would simply be “shooting in the dark”. In any case the standard indicates that the test is to be measured down the centre of the sample rather than at the edges, and it is this result that is represented well by the modelling results.

Some accuracy has been lost by storing averaged values from the free-surface simulation, which is later read back into the simplified model. These results could be improved by fully modelling the slag motion for the entire test period. This is not practical due to the time that such a simulation would take to complete.

6.7 Concluding Remarks

The results from this model of the rotary slag test provide further verification of the refractory wear mechanism, in particular the erosion mechanism. The model results match those measured from the laboratory test work carried out by RTIT. The model could be improved by fully modelling the free-surface flow of slag around the furnace. This is impractical as it will take a couple of years to run on a Sun Ultra 5 to run such a simulation.

APPLICATION OF REFRACTORY WEAR AND FREEZE LAYER MODELLING

This model seeks to pull together the previous modelling components - solidification and refractory wear mechanisms. Water-cooling in the sloping refractory slag zone of the proposed development plant is modelled in this section. This model can be modified to allow various water-cooling designs to be evaluated.

7.1 Objectives of Modelling the Water-cooled stove

The fundamental objective of this research is to develop techniques to determine the feasibility of using water-cooling lower down in the HIs melt Smelt Reduction Vessel. A particular concern is over whether it is safe to use water-cooling so close to molten metal.

This model seeks to put together the refractory wear models and the solidification work performed examining the elephant's trunks to provide a model that will be able to perform calculations on any particular design that may be proposed for the HIs melt plant.

7.2 Water-cooled elements

Water-cooled elements have various design features. The first consideration taken is the material that they are fabricated from. Typically the elements are made from either steel or copper. Generally steel is used for applications where the heat load is moderate, whereas copper is used for higher heat loads due to its higher thermal conductivity*. Due to the higher potential heat loads due to the presence of molten metal, the cooling elements used in this model will be assumed to be constructed from copper. HIs melt designed and fabricated copper test panels that were to be installed in the sloping refractory region, although these panels were not installed as it was viewed as too big a risk to install the panels and have them fail when at that point in the development of the process good operational results were required.

* Thermal Conductivity of Pure Copper is approximately $400 \text{ W.m}^{-1}\text{K}^{-1}$ (commercially used grades have thermal conductivities of $200\text{-}300 \text{ W.m}^{-1}\text{K}^{-1}$) versus approximately $60 \text{ W.m}^{-1}\text{K}^{-1}$ for Carbon Steel.

There are several ways that copper cooling elements are fabricated: cast; rolled; or welded. The welding of copper requires specialised welding techniques. After welding, the stresses built up during welding, need to be removed from the piece in an oven. This is the method by which the copper serpentine water cooling panels are fabricated from tube stock.

Rolling and casting are more favoured methods for the production of water cooled staves as it allows the construction of water passages through the block. The complication is that a method is required to join the water passages together. Generally machining of the interconnecting passages and plugs inserted to block outlets are used to create the water passages through the copper block.

Most water-cooled elements are designed to have a layer of refractory applied to their hot face. The advantage of this is that such a layer will reduce the amount of heat lost from the system, leading to improved process economics. To help retain the refractory layer manufacturers have come up with an array of techniques. These include copper fingers and grooved faces on the copper blocks as pictured in Figure 7.1.

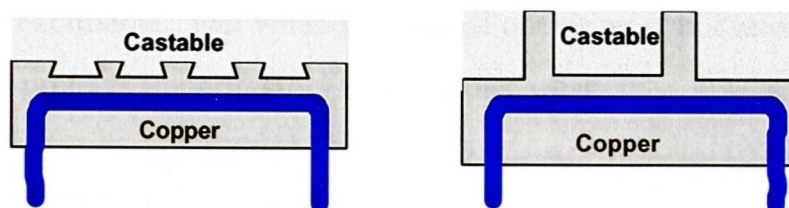


Figure 7.1 – Various Refractory Retaining Techniques

One of the problems that can occur with water-cooled elements is what is called thin film boiling. This occurs when the water is heated rapidly and the water boils. This produces gas, typically at the wall, which is a poor conductor of heat leading to a build up of heat at the wall. Generally this will lead to the physical failure of the cooling element, and in terms of smelting a hot metal explosion can occur causing significant damage to plant and endangering the safety of the operators.

7.2.1 Dynamic Nature of the Process

During the operation of the pilot plant freeze layers have been observed on the water-cooled panels in the upper parts of the panels. The initial design of the vertical vessel had water-cooled panels in the upper part of the vessel. A high chrome containing castable was slip cast around these serpentine pipe cooling panels. In the first few campaigns, a row of refractory bricks was installed in front of the cooling panels. It became obvious quite quickly that these

bricks were wearing quickly and that the cooling panels could withstand the process conditions.

To be able to penetrate the refractory, and hence wear it away, the slag needs to be above its liquidus temperature. The penetration is stopped by the contact angle – which is a function of temperature and is set to 90° which produces zero penetration rate as the cosine of the contact angle is considered in the penetration calculation. If the process is operated at a constant temperature, the refractory would wear away until it has worn away to such an extent that the hot face of the refractory is at the solidus temperature of the slag.

In reality the process is never operated at exactly the same temperature, and in particular the pilot plant trials were nothing like this as the process was changed on a frequent basis as different materials and operating conditions were trialled. Additionally the slag is batch tapped from the vessel causing the top-space conditions (temperature and the amount of slag flying around) to vary between slag taps. In particular it has been observed that the accretion is similar to the slag of a particular part of the operation¹²⁷ that corresponds to a higher operating temperature. The conclusion is that the refractory has been worn away by such an amount by process excursions, that when the normal operating conditions return a freeze layer is formed that then protects the refractory from further wear.

7.3 Model Formulation

Due to the potential for a significant heat load to be present due to metal splashing, it is assumed that any water-cooled element that will be installed in this region of the vessel will be fabricated from copper. The lowest water cooling panels in the HIsmelt vertical vessel were made from copper.

In the HIsmelt vessel, high chrome refractories have been used as these have been found to provide the best performance in the process conditions found within HIsmelt. The problem with chrome containing refractories is that Cr^{6+} has been found to be carcinogenic⁷. In a number of countries, restrictions have been placed on the disposal of materials that may be able to leach into the groundwater system. This makes it expensive to dispose of the spent refractory bricks. The alternative that has been proposed is a low cement high alumina spinel castable. This material will be used to line the hot face of the cooling element in this model.

As the slag flow is predominantly flowing down the wall of the furnace, although there will be a degree of “sloshing” in the bath, the slag is modelled to flow down the surface of the

refractory lining the hot face of the water-cooled element. Figure 7.2 shows a schematic of the HIs melt vessel indicating the region that is to be modelled.

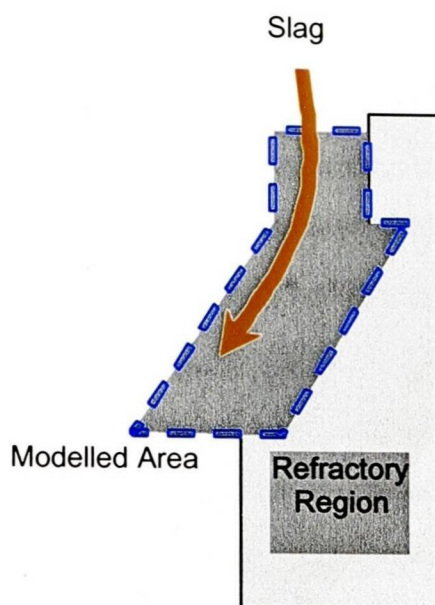


Figure 7.2 - Schematic of the Area of the Vessel Modelled

The computational domain has been created with a refractory and slag regions shown in Figure 7.3. The copper layer is not modelled as the temperature drop through the cooling element wall is negligible due to the high thermal conductivity of copper. Figure 7.4 shows the mesh that has been developed to model the water cooled stave. This figure shows a two dimensional slice through the mesh, it has been swept radially for 10° about the z-axis to form a wedge like shape.

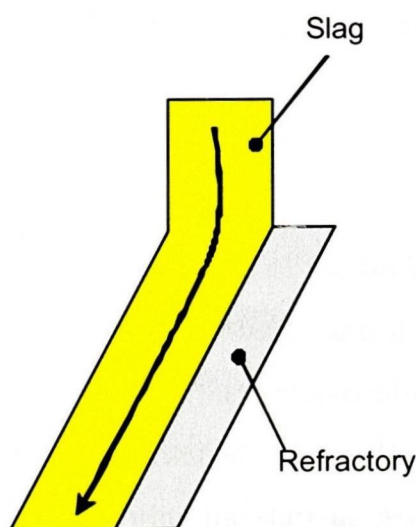


Figure 7.3 - Schematic of the extent of the Computational Domain

The model has been run transiently for a period of time with an elevated slag temperature. The effect of this is to wear away the refractory such that when the slag temperature is returned to the normal operating temperature that a slag layer will form.

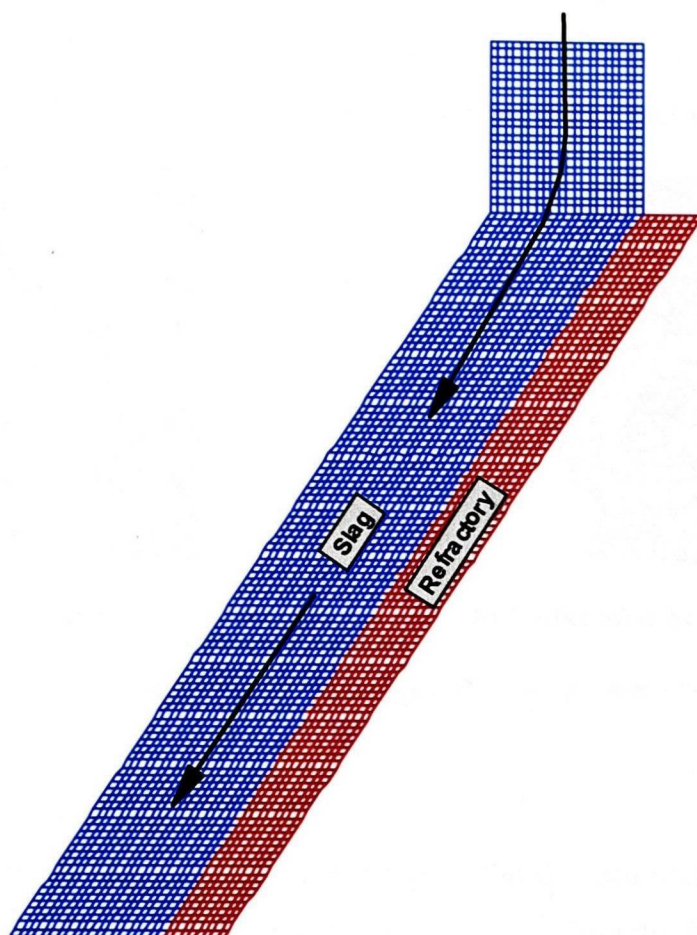


Figure 7.4 - Schematic of the Mesh Developed for the Water-Cooled Stave Model

As this model has been developed to bring together the modelling of the refractory wear with freeze layer formation, it uses the various parameter values that have been established through the modelling of other systems. This is particularly important for the refractory wear mechanisms.

7.4 Observed Results

Initially the water-cooled panels on the side walls of the SRV had a brick lining in front of the castable. These bricks wore away reasonably quickly and it was decided not to replace them. The initial castable that was slip cast around the water-cooling panels was not removed. After some of the campaigns a castable was gunned (sprayed) onto the water-cooling panels to provide some extra protection to them during the start-up period.

On occasions pieces of the accretion and refractory were broken away from the water-cooling panels. This showed a region of refractory that was un-penetrated near the water-cooling tubes. Towards the hot face, the refractory had been penetrated and on the outside a small

layer of solidified slag could be found. As the campaigns progressed the refractory around the water-cooling wore away, in particularly in between the front cooling pipes. A cross-section of the water-cooling panels on the side of the vessel is shown in Figure 7.5. This figure shows how over a considerable amount of time, that the refractory has been worn away in between the front cooling pipes. It is this case where the refractory has been worn away that the solidified layer is particularly noticeable on the hot face of the refractory.

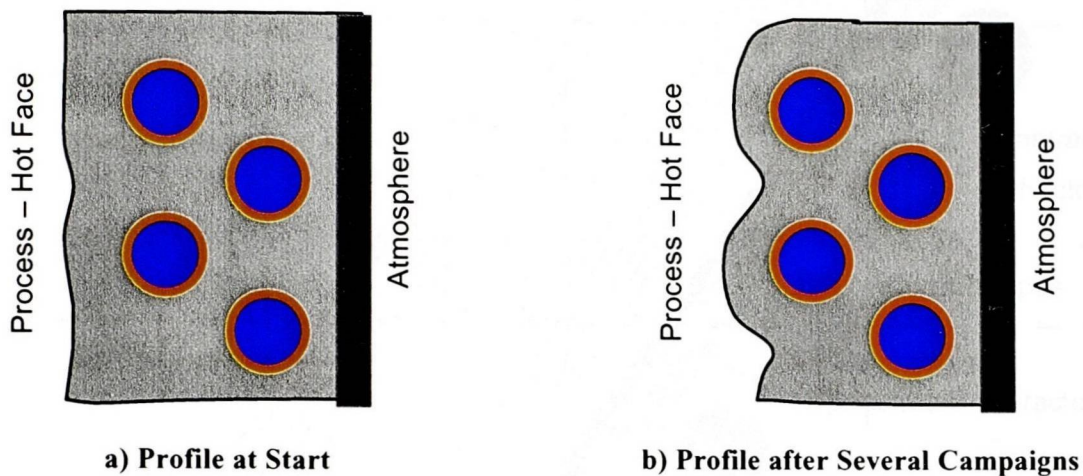


Figure 7.5 – Progression of Wear Around Cooling Pipes over time

7.5 Boundary Conditions

The flow of slag within the domain is from the top of the domain and leaves it at the bottom. The inflow boundary condition is a fixed velocity of 1 ms^{-1} directly downwards. The outlet is a constant pressure boundary condition set to a reference pressure of 0 Pa.

The remaining two boundary conditions are for the heat transfer within the system. The inflow slag is set to the required temperature. The normal operating temperature for the Hismelt process is 1450°C (1723K). A process excursion will add $100\text{-}200^\circ\text{C}$ to this. 1923K is used as the temperature for such excursions in this work. The other boundary condition is the cooler temperature which is set to the water temperature of 30°C (303K). The heat flux can be back calculated from temperatures calculated for the centres of the elements adjacent to this boundary.

7.6 Results and Discussion

The model has been run with an elevated temperature of 1923K for a simulated time of 10 days. These results (shown in Figure 7.6) show how the refractory is penetrated by slag and has been eroded by the flow of slag from the top of the vessel.

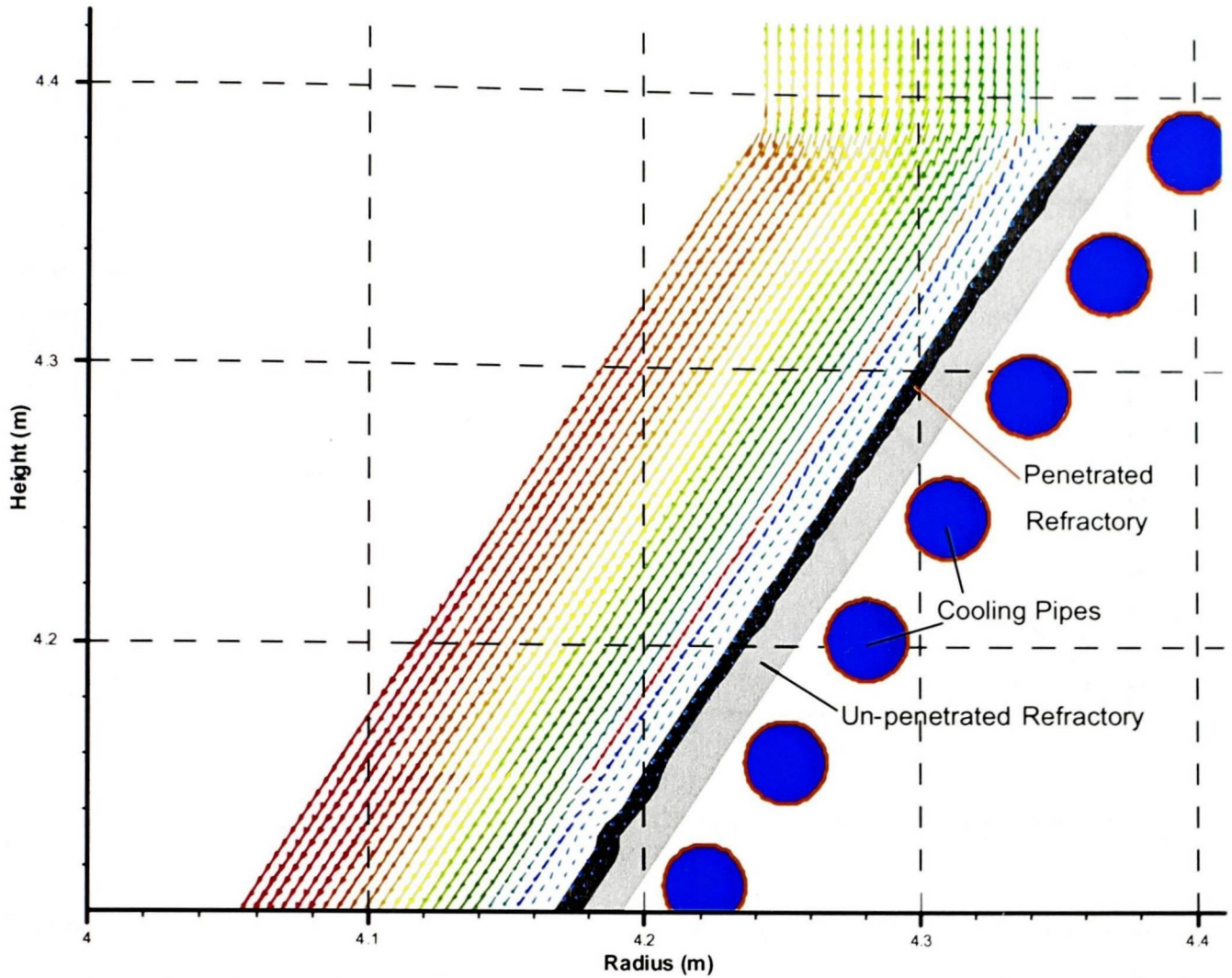


Figure 7.6 - Results after running model for simulated 10 days with an elevated temperature of 1923K

These results show how the refractory has been worn away by the higher temperature and no freeze layer is formed. Figure 7.7 plots the values of temperature, penetration and refractory fractions at a height of 3.4m. The liquidus and solidus temperatures are also plotted onto the graph. When the same values are also plotted after running the model for a further 2 days at the normal operating temperature (1450°C), the slag on the hot face of the refractory is cool enough to freeze.

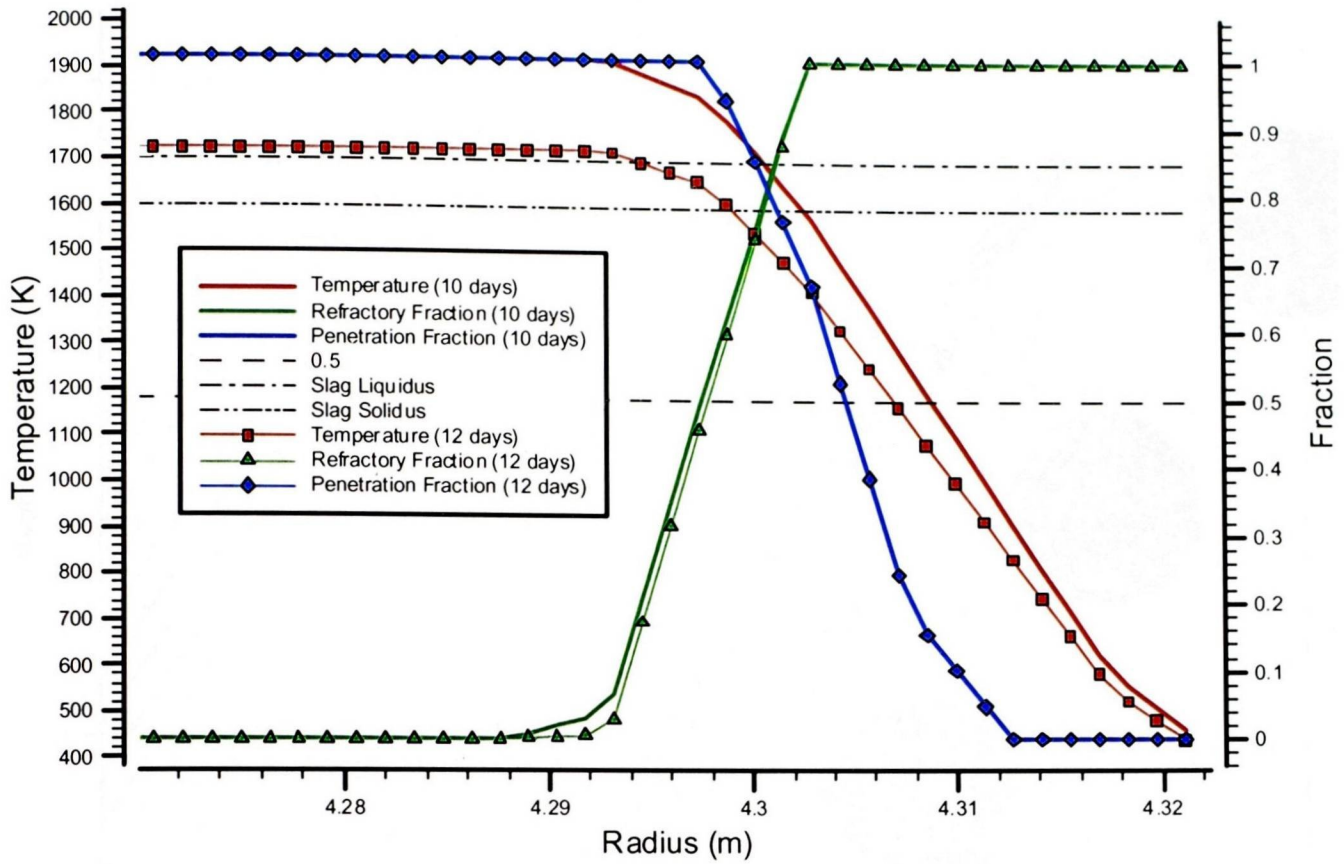


Figure 7.7 - Temperature Profile at a height of 4.3m after 10 days at 1923K and a further 2 days at 1723K

The results (Figure 7.8) from the normal slag operating temperature are practically the same as those at the higher temperature, except for the existence of the solidified slag layer (in yellow). This slag layer builds up quickly as is demonstrated by the thickness of the layers at various heights shown in Figure 7.9.

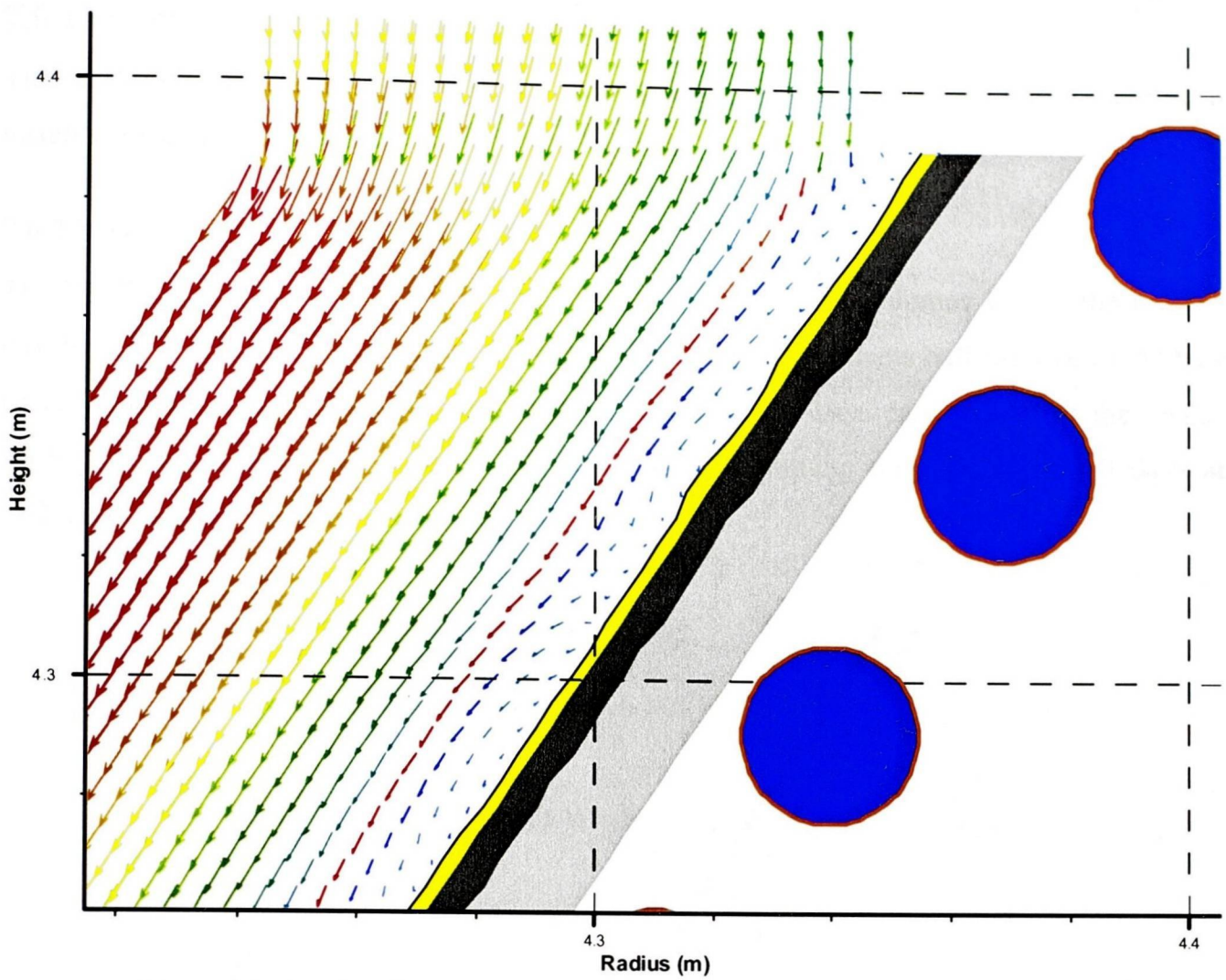


Figure 7.8 - Results after running model for a further 2 days at normal operating temperature of 1723K

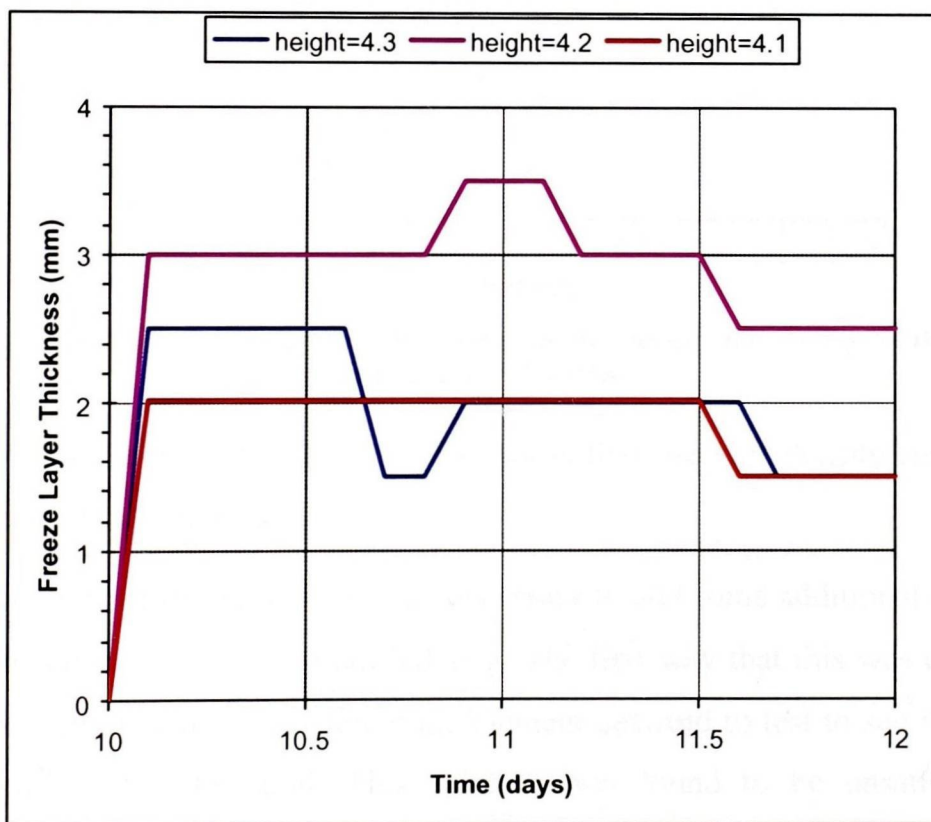


Figure 7.9 - Growth of Freeze Layers with respect to Time

7.6.1 Sensitivities

The sensitivity of the result to the mesh density and inflow boundary condition have been tested to examine their effect on the results obtained.

7.6.1.1 Mesh

To test the dependence of the result on the size of the control volumes within the meshes developed, two further meshes were developed. The first has elements half the size of the base case, whilst the second has elements double the size of the base case. As all of the results show the same trend, just the refractory location after running the models for 10 days at 1923K has been plotted in Figure 7.10.

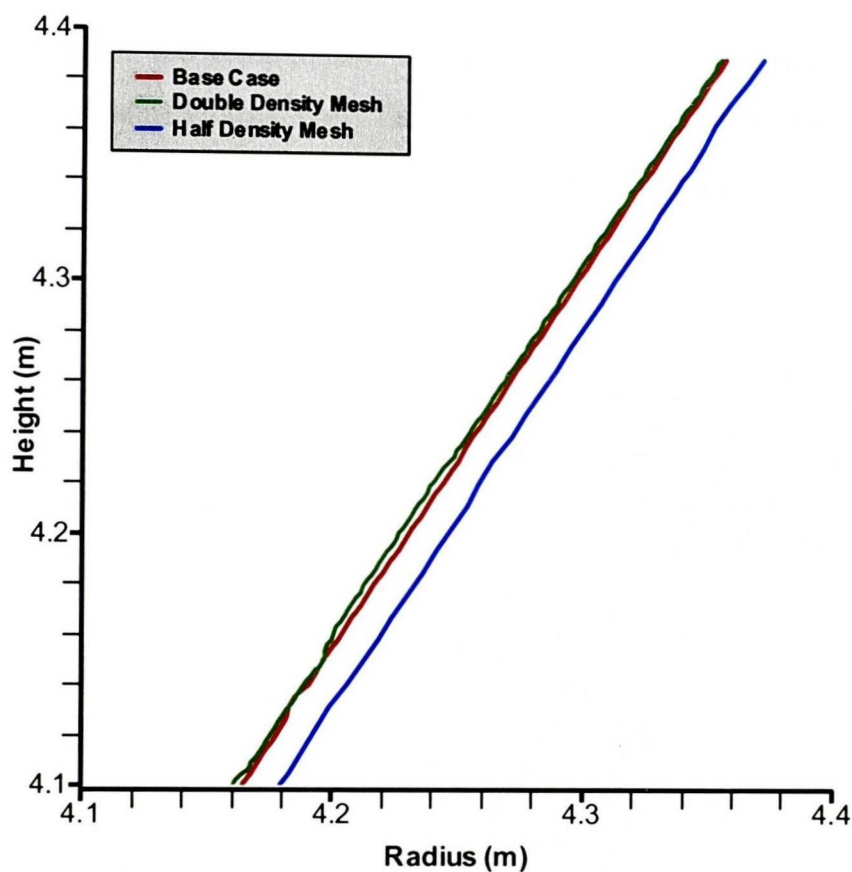


Figure 7.10 – Refractory locations for the various meshes tested after 10 days at the elevated temperature of 1923K

The noticeable feature of this sensitivity analysis is that the half density mesh (that is the mesh is coarser) exhibits more wear.

During the modelling of this case, it became necessary to add some additional code to stop the erosion mechanism eroding away solidified slag. The first way that this was carried out, was to use the temperature value calculated at the element centroid to test to see if the penetrated refractory would in fact be solid. This solution was found to be unsatisfactory as the temperature at the centroid of the control volume is not necessarily the temperature at the

slag-refractory interface. A more precise method of determining the liquid/solid state of the refractory at the slag-refractory interface was required.

To improve on this situation, the temperature at the interface is calculated. As the location of the refractory is already available through a location vector that is calculated to determine the previous time-step penetration, this is used to calculate the temperature at the interface in conjunction with the temperature gradients within the system. This provides further confirmation that it is the temperature profile that is very important in these processes.

Figure 7.11 shows an enlarged view of the base case mesh (red) and the coarser mesh (blue) with the 0.5 penetration contour lines plotted (in their respective colours). It is important to note that the base case mesh lines are underneath the coarse mesh lines. With the penetration calculation dependent on the temperature of the cell, the coarser mesh will allow more penetration to occur as the code “believes” that the entire cell is at that temperature rather than a temperature gradient running through it. This effect can be decreased by decreasing the size of the elements used within the mesh.

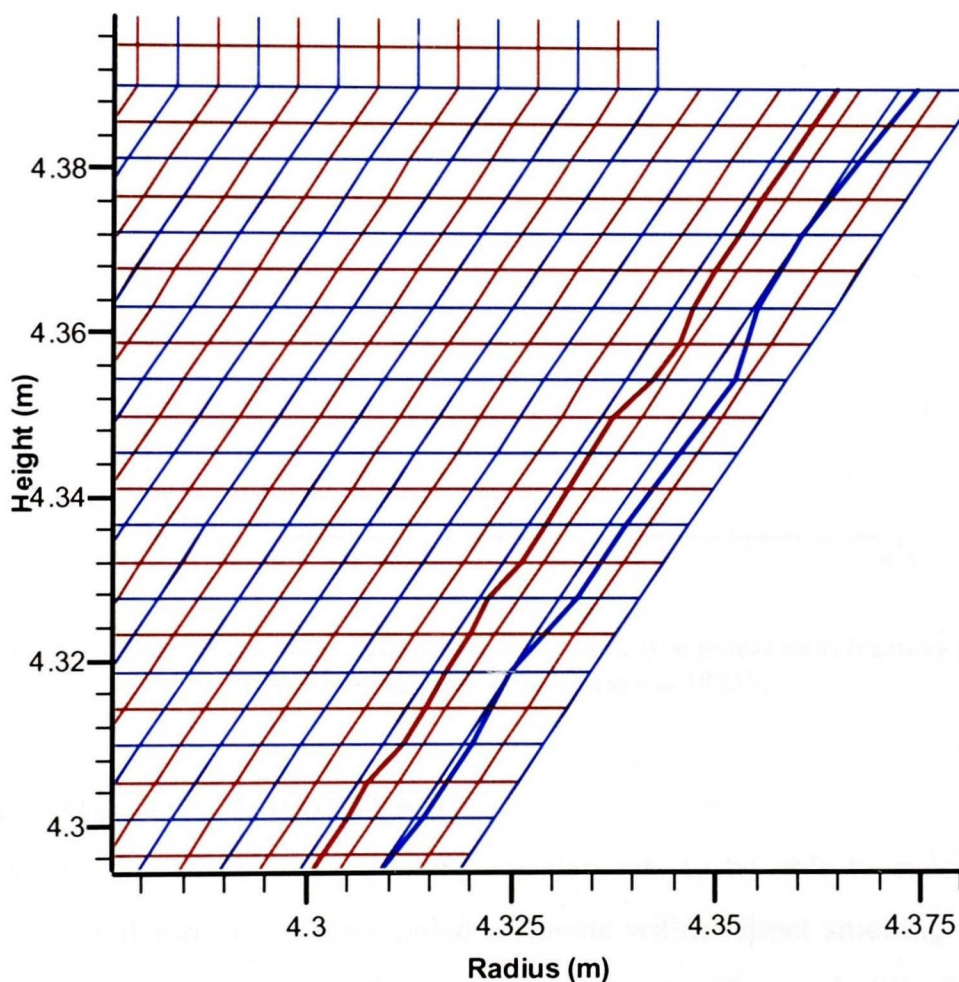


Figure 7.11 – View of the Base Case and Coarse Mesh results for Penetration

Having used an improved temperature for determining if the refractory can be eroded, it was thought that the other temperature dependent properties that influence the penetration

mechanism could benefit from a similar approach. The penetration mechanism was changed such that the viscosity used was evaluated using the temperature at the penetration front. The other temperature dependent parameters, surface tension and contact angle, were left dependent on the cell centred value. A quick calculation was performed using the induction furnace model and no discernable change was observed.

7.6.1.2 Flow Boundary Condition

Two additional inflow rates (3ms^{-1} and 5ms^{-1}) for slag have been compared to the results from the base case of 1ms^{-1} . From the refractory contours shown in Figure 7.12, very little effect can be seen between these cases. The other results for penetration and the solidified layer produce similar results to this.

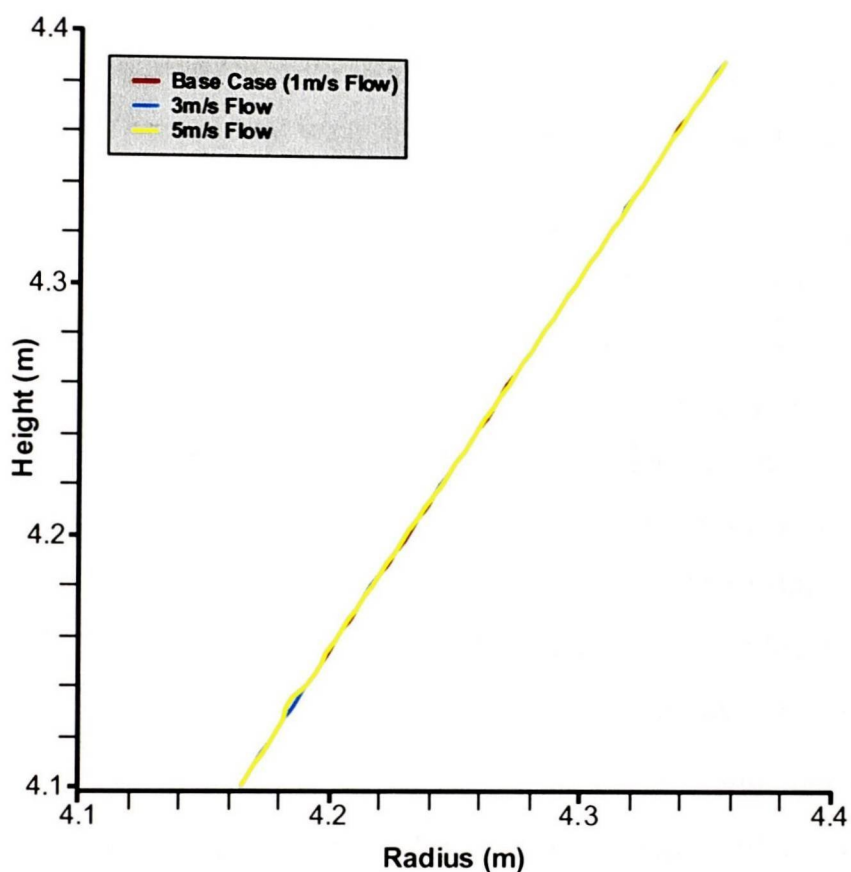


Figure 7.12 - Effect of different in-flow boundary condition model on refractory position after running model for 10 days at 1923K

7.7 Concluding Remarks

This model successfully brings together all the elements to be able to successfully model freeze layers that will form on water-cooled elements within direct smelting applications as such as HIs melt. The model exhibits the properties that were observed of the HIs melt cooling panels.

This work has set out to examine the freeze layer formation and refractory wear in direct smelting processes. This chapter summarises the findings of this work, the limitations of the models developed and suggestions for further research. The models demonstrate how this work can be used to evaluate various cooling designs for the future.

8.1 Summary of Findings

During the course of this research several models have been developed to model accretions within the HIs melt SRV, refractory wear in the HIs melt HRDF pilot plant, and refractory wear in laboratory tests.

A model of accretions formed on pneumatically injecting solid feed materials into the molten HIs melt bath was used to determine if the pipe like accretions, termed elephant trunks, would indeed form under the hot and cold injection conditions expected in the design of the commercial development plant. The results of modelling the HRDF injection conditions, match the observed trunks found on inspecting the vessel after campaigns. Elephant's trunks are predicted to form for both the hot and cold injection cases. The trunk formed for the hot injection case exhibits a transiently occurring mushy zone near where the trunk attaches to the water-cooled injection lance which may lead to this accretion coming away from the lance.

In setting up the refractory penetration mechanism, results from induction furnace test work carried out by Veitsch-Radex commissioned by HIs melt, was used to adjust the thermo-chemical properties that affect the penetration. The same penetration by slag was computed as it was measured in this test work. These parameters were then used in the modelling of the wear observed in the HIs melt HRDF campaigns.

A model of a part of the HIs melt HRDF vessel has been created to simulate campaigns 8-1 and 8-2. The results fall within the range of measurements taken after these campaigns. This model has taken the flow field from the bath modelling work that has previously been performed. On performing a sensitivity analysis (between the range of flows predicted by the bath model) on the flow boundary conditions the results can be seen to change at the top of

the domain although still remain within the range of wear measurements taken from the pilot plant.

To provide further information regarding erosion, a rotary slag test was modelled. Information was obtained from Rio Tinto Iron and Titanium (RTIT) in Tracey, Quebec Canada. Initially the full furnace was modelled, examining the free-surface flow of the slag as the furnace rotated. As it took several days to compute a couple of revolutions, a pseudo steady free-surface location was used in a simplified model. The simplified model examines one of the six samples that are tested. The results from this model are in reasonable agreement with the sectioned sample.

Finally a model of a water-cooled element in the commercial development plant has been created. This model brings together the refractory wear mechanisms and the work done on modelling the accretions formed within the furnace. The model is run for a period at an elevated temperature, during which the refractory wears away. On running the model for a further period at the normal operating temperature no wear occurs, but rather a small solidified slag layer forms on the hot face of the refractory. This is in accord with the observations from the HIs melt HRDF vessel, obtained when the refractory was chipped from the cooling panels from the top gas reaction space.

8.2 Research Achievements

This research set out to model the feasibility of water-cooling the lower parts of the HIs melt Smelt Reduction Vessel (SRV). To be able to achieve this, a mechanism is required to predict the thickness of the refractory layer applied to these cooling elements. Previous work in this area focuses on thermo-mechanical analysis of refractory linings. This work is unique as it models the individual mechanisms of refractory wear (penetration; corrosion; and erosion) in conjunction with the formation of freeze layers.

The refractory wear mechanisms have been coded generically and take a macro view of the refractory wear occurring. The penetration is modelled using a transport equation to model the progression of the slag through the refractory. Corrosion and erosion are examined at the end of each time-step, to determine how much refractory material each of these mechanisms will remove.

On combining the refractory wear mechanisms with the well established and validated solidification algorithms of PHYSICA, a model of a water-cooled element in the sloping refractory area washed by slag has been developed. This model exhibits a thin freeze layer

forming, similar to the freeze layers observed on the cooling panels in the top gas reaction space of the SRV.

8.3 Limitations of the Work

From the point of view of the application of the model, the most significant limitation is that this research has examined the refractory slag interactions when examining refractory wear. The amount of metal thrown up from the bath, as opposed to slag, within the vertical Hismelt SRV design is low (predicted to be less than 5%). The refractory of particular interest, the sloping refractory region above the hearth area, is completely submerged in slag and the incidence of metal coming into contact with this refractory is quite low.

Through the various models developed during this work, the refractory wear mechanisms have been validated. The penetration and erosion mechanisms are particularly well validated. The corrosion mechanism does not lead to a significant amount of wear in these models. This is not totally unexpected as it is general practice to maintain the slag chemistry at levels to minimise corrosion. This mechanism would benefit from further validation, although this will necessitate specifically targeted experimental work.

A macro modelling approach to the wear mechanisms was taken, as to model the complex porous structure of the refractory would be impractical. In particular this led to the development of the notion of a "cooking time" to represent the corrosion mechanism. This concept accounts for the interaction of the slag with the refractory but does not account for any boundary layers that may form. In the reported work examining the wear of magnesia-chrome refractories, a layer is not found to form and therefore this is not an issue for this refractory system. On the other hand, for the High Alumina refractories a layer which is high in gehlenite is found to form which will have an effect on the corrosion occurring.

The modelling of the Hismelt vessel uses results taken from a computational model of the bath to set up the slag flows within the vessel. As the erosion mechanism is directly related to the shear developed from these flows, the results will be dependent on the assumptions made about the flow of slag through the vessel.

8.4 Future Work

This work has successfully developed mechanisms for modelling refractory wear although this work has focused on the slag-refractory wear without examining the effect of metal. Further work to examine how the wear mechanisms created in this work are affected by metal

and other refractory systems should be carried out to be able to extend the capability of this model to these systems. Additionally these models can be used to help evaluate proposed designs for water-cooling within smelters.

8.4.1 Application to Other Refractory Slag Systems

It is not possible to directly take this work and apply it to any refractory slag system due to the assumptions that have been made in this work. The wear mechanisms should be re-validated for different systems. Of particular note, if a stable layer forms on the interface between the refractory and the slag, this will impact on the wear behaviour of the refractory as this mechanism is not accounted for within this model. To make this model applicable to a wider range of systems, mechanisms for the existence of this layer should be built into the model.

8.4.2 Application to Metal

This work has examined the wear mechanisms between slag and refractory as this is the particular condition of interest within this study. In the experimental induction furnace test, the metal can be seen to penetrate into the refractory to a similar depth as the slag. The metal penetration appears to occur similarly to that of slag although the amount of work that has been done in this area is quite limited in contrast to the work that has been carried out for slag. Further studies should be carried out to validate the various wear mechanisms developed within this work.

8.4.3 Spalling Mechanisms

The thermal cycling of refractories can cause the penetrated refractory layers to fall off or come away from the main body of the refractory in a process that is known as spalling. This process occurs due to the penetrated refractory having different thermal expansion properties to the un-penetrated refractory. On the cycling of the temperature stresses build up to such a point where the surface layer shears away from the bulk of the refractory.

In this work spalling was not examined as the part of the process that is examined is continuously submerged by slag and the fluctuations in temperature will not be significant. By performing stress calculations it will be possible to determine when spalling occurs within the refractory.

8.4.4 Alternative Cooler Designs

The flash smelting process to produce copper is one of the most intense smelting processes. Through the development of the flash smelting process over the last 50 years, the water-cooling requirements have changed as the furnaces are typically operating at many times their design ratings. Coolers have been used where the equilibrium heat flux is up to 250 kW.m^{-2} with a peak load of 5 MW.m^{-2} .

There are several novel techniques that have been used to improve the cooling in flash smelters, and more importantly to cool the protective refractory lining. The methods that particularly look useful to the HIs melt context are where either copper fingers or rods are attached to the main water-cooled part of the water-cooled element. These extensions to the cooler cool the surrounding refractory, limiting the amount of wear in the refractory. Another elegant innovation is to machine grooved slots within the cooler to provide improved attachment of the refractory layer to the cooler.

As these techniques have been “tried and tested” within the copper flash furnaces, these techniques should be examined in any future design for water-cooling of the lower parts of the HIs melt vessel. The models developed within this work provide the perfect vehicle to analyse the various cooling options available for this region of the furnace.

8.4.5 Investigate Heat Pipe Technology

The major concern with using water-cooled elements closer to the molten metal bath is whether they can withstand direct contact with the molten metal and retain their integrity. If the water-cooled elements fail, and the molten metal comes into contact with the cooling water, a hot metal explosion occurs due to the rapid expansion of the liquid water into gas spraying the molten material everywhere.

Heat pipe technology^{128,129} allows for the separation of the molten metal from the cooling water adding a degree of safety. Heat pipes work by boiling a working fluid at the hot face, and re-condensing to a liquid at the water-cooled face. Another attraction is that it is possible to have an enlarged heat transfer area on the water-cooled surface as compared to the hot face of the heat pipe. These devices are not in widespread commercial use and predominantly have been used for small scale casting work although they have been able to transfer up to 1 MW.m^{-2} .

As this technology provides a method of separating the molten metal and cooling water, this technology should be examined periodically to see if it provides a viable and safer water-cooling solution than utilising direct cooling of the refractory.

8.4.6 Porous Flows

The penetration mechanism could be simply applied to solve for flows through porous media. An example is the flow of wax into moulds in investment casting.

8.5 Concluding Remarks

This work has concentrated on the development of mathematical models, representing the mechanisms to predict refractory wear with a view to modelling the refractory layer left on water-cooled elements within direct smelting furnaces. The results of the Finite Volume computations demonstrate the capability of these mechanisms to predict the refractory wear. To complete the modelling objectives, freeze layers have been predicted in conjunction with these wear mechanisms. The models provide a tool that can be utilised to investigate future water-cooling designs for smelters.

BOF

A Basic Oxygen Furnace is a top blown steelmaking vessel.

B Ratio

A measure of the slag composition. See also *V Ratio* and *Slag Basicity*.

$$B = \frac{[CaO] + 1.4 \times [MgO]}{[SiO_2] + 0.84 \times [P_2O_5]}$$
$$B_{LF} = \frac{[CaO] + 1.4 \times [MgO]}{[SiO_2] + 0.6 \times [Al_2O_3]}$$

Castable

Refractory that is supplied as a powder, mixed with water and then formed or applied to the required shape or surface.

Contact Angle

Refers to the angle that a liquid makes with a solid surface or substrate.

Control Volume

The area that is being modelled, the computational domain, is divided into parts (Control Volumes) to allow for the transport equation that is in the form of a partial differential equation can be solved.

CSIRO

The [Australian] Commonwealth Scientific & Industrial Research Organisation.

Element

See *Control Volume*

Grid Point

The points formed by the corners of the *Control Volumes*. see also *Node Point*.

HAB

Hot Air Blast (HAB) is air that is heated using Hot Blast Stoves. These stoves contain refractory which is heated using a fuel and then air is blown through the refractory to produce hot air of temperature of 900 - 1200°C. This hot air is used for combustion in the top gas reaction space.

HRDF

HIsmelt Research and Development Facility (HRDF) is the purpose built facility in Perth, Western Australia, where the pilot plant for the HIsmelt process has been built and successfully operated.

HTE

Heat Transfer Efficiency (HTE) measures how much energy is transferred to the process rather than is lost to the water-cooling and the off-gas.

KOBM

Klockner Oxygen Blowing Method refers to a steelmaking process using bottom blown oxygen.

Node Point

The corners of the *Control Volumes*, used within a Finite Difference formulation.

OBM

A steelmaking process using bottom blown oxygen.

PC

Post Combustion (PC) is the combustion of gases produced in the process. In particular the gases CO and H₂ have a significant amount of energy that can be liberated through combustion.

PCR

The Post Combustion Ratio (PCR) measures the degree that the off-gas from the process has been combusted. This ratio is calculated in the following manner:

$$\%PCR = \frac{[CO] + [H_2]}{[CO] + [CO_2] + [H_2] + [H_2O]} \times \frac{100}{1}$$

Slag Basicity

A common measure of the slag composition, taking the ratio of various slag components. Different ratios are used for different slags. See also *B Ratio* and *V Ratio*.

SRV

Smelt reduction Vessel (SRV) is the HIs melt terminology for the central furnace where all the smelting and reduction occurs.

Tuyere

Inlet lance or pipe used for injecting various materials into furnaces. This may range from gases to pneumatically conveyed solids.

Wetting Angle

See *Contact Angle*

V Ratio

A measure of the slag composition. See also *B Ratio* and *Slag Basicity*.

$$V = \frac{[CaO]}{[SiO_2]}$$

APPENDICES

A	HISMELT COMMERCIAL DEVELOPMENT PLANT.....	168
A1	GENERAL FLOWSHEET ARRANGEMENT	168
A2	PRE-TREATMENT	170
A3	OFF-GAS TREATMENT.....	173
A4	ENERGY RECOVERY AND RE-USE.....	173
B	CD-ROM CONTENTS.....	175

A HIs melt Commercial Development Plant

The core element of the HIs melt process is the central furnace unit, the Smelt Reduction Vessel. A significant amount of effort has been waged at making this part of the process operate economically and safely. The overall economics of the process depends on what raw materials are available at what cost. These choices impact on the ancillary equipment as such as grinding and drying equipment and gas treatment equipment. This appendix sets out some of the entire process involving this ancillary equipment.

A1 General Flowsheet Arrangement

A flowsheet has to be developed for the specific requirements of each potential site. The flowsheet will be affected primarily by the raw materials available and the existing equipment that can be used. The flowsheet contains various stages: Pre-treatment of the raw materials; the core furnace – the Smelt reduction Vessel (SRV); Treatment of the Off-gas; and the recovery of energy leaving the process through the off-gas. A simple block process flow diagram is shown in Figure 8.1.

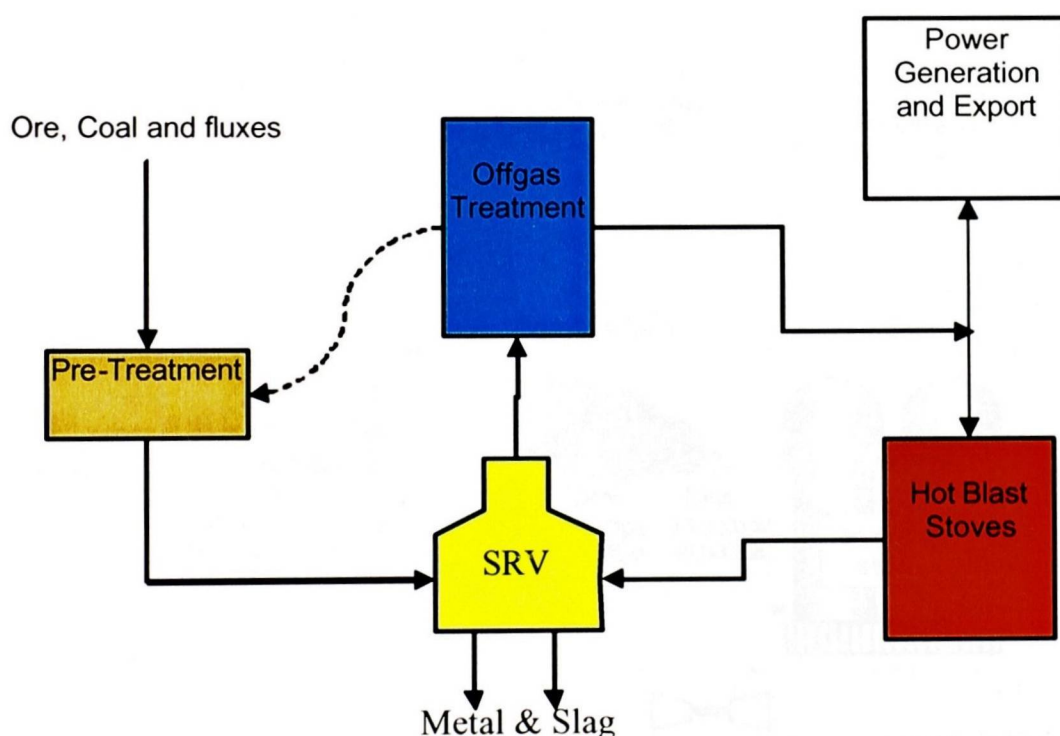


Figure 8.1 - General Arrangement of the HIs melt Flowsheet

The next sections provide a brief description of each of these stages, except for the SRV which is described in some detail in the main part of this work. The different options within each of these stages is also discussed. The first plant to commercially exploit the HIs melt

technology is to be built in Kwinana, Western Australia. Figure 8.2 shows the flowsheet for this plant.

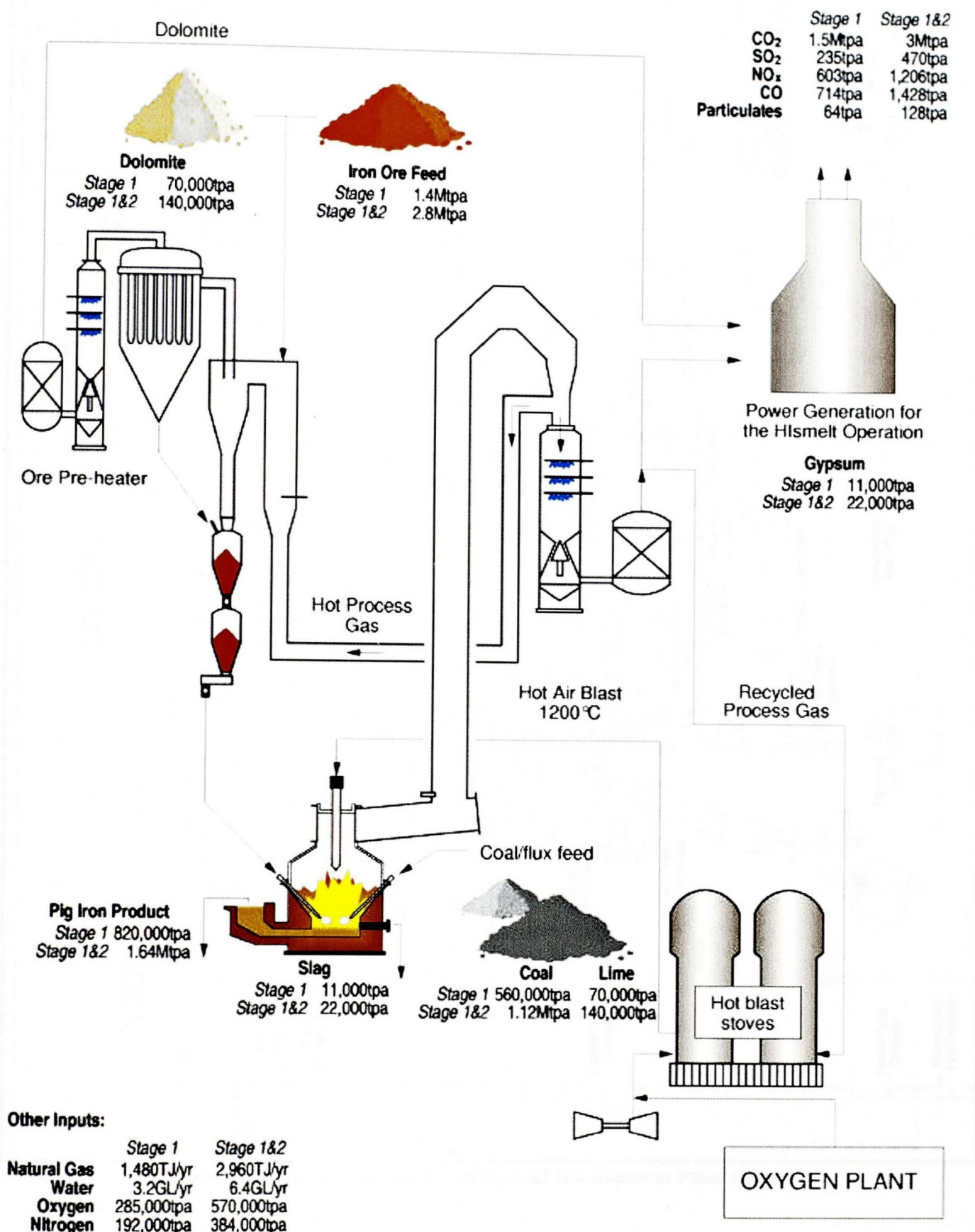


Figure 8.2 – Process Flow Diagram for the Commercial HIs melt development plant

direct impact on the product produced and the economics of the whole process. There are three levels of pre-treatment that can be carried out: physical treatment; drying or pre-heating; and pre-reduction. The aim of any pre-treatment processes is to improve the performance, and hence the economics, of the process by reducing the work that needs to be carried out within the furnace.

Physical

Depending on how the material is supplied the raw materials will be screened to remove any foreign mater. In the HIs melt pilot plant the coal was ground to ensure that all the injected material was less than 1mm in diameter whilst all of the ore injected was less than 6mm in diameter. The size of the particles is somewhat important as it is desired that all of the reduction of the ore occurs within the bath and that the coal will dissolve within the metal. Therefore a grinding stage may be required that also may drive off any free water*

Pre-heating and Drying

When water is injected into the process, this takes energy to vaporise it and bring it up to the off-gas temperature. As this can be a significant drain of energy from the process which could otherwise be used for smelting purposes, the water contained within the materials can be removed.

The free water is relatively easily removed and largely removed during grinding processes. The intrinsically bound water is more difficult to remove as this requires higher temperatures. A common method that is used is to use a Circulating Fluidised Bed (CFB) to heat and liberate the intrinsically bound water. CFB's are commonly used within the cement industry as calciners.

An advantage of using a pre-heating stage is that fluxes as such as dolomite (CaCO_3) and magnesite (MgCO_3) can also be calcined. After pre-heating the resultant treated ore is not completely cooled but rather injected into the SRV at an elevated temperature further helping the energy balance of the furnace. It is this approach that the HIs melt commercial flowsheet uses.

* Free water refers to water that is free to move around as opposed to water that is tightly bound up within the structure of the mineral.

Pre-reduction

By taking the pre-heat process further with a hotter temperature, longer residence times, and a reducing atmosphere it is possible to remove oxygen from the iron bearing feeds¹³⁰. These processes are either coal or gas based processes. Table A.1 lists the various processes that can be used for the direct reduction of iron.

Base Fuel	Process Type	Process Name
Coal	Rotary Kiln	SL/RN
		Krupp-CODIR
		DRC
		ACCAR/OSIL
	Rotary Hearth	Inmetco
		FASTMET
	Fluidised Bed	Circofer ¹³¹
Gas	Shaft	MIDREX
		HYL
		Purofer
	Fluidised Bed	FIOR/FINMET
		Iron Carbide
		Circored ¹³¹

Table A.1 – Direct Reduction Processes¹³⁰

Gas based processes crack reform gas (predominantly Methane, CH₄) using steam to produce Hydrogen. In shaft based processes the iron ore is fed into the top of the cylindrical vessel. The heated reductant (H₂) is then passed through the top part of the bed to heat and reduce the ore. The bottom part of the vessel is used to cool the reduced material to temperatures that are practical to handle when the material it is removed at the bottom of the vessel. The fluidised bed systems fluidise the iron ore particles with the hot reducing process gasses causing reduction to occur.

With the coal based processes, the coal can act in two ways – the carbon acting as a reductant; or the volatile material being gasified to produce a reducing atmosphere conducive to reduction. In the rotary hearth process layers of ore and coal are alternatively layered onto the rotating hearth. In the rotary kiln process the ore and coal are fed into the kiln where it becomes well mixed. A natural gas burner is then used to heat the ore and combust any volatile matter that is liberated from the coal. Through this heat and the presence of carbon from the coal the ore is reduced. The Circofer process is similar to the gas based fluidised bed systems except for the fact that Carbon Monoxide (CO) is used as the reductant.

These processes are reasonably difficult to operate, in particular the fluidised beds. This is due to the fine particles that are created in them along with the stickiness of the particles at higher temperatures. This is something that was experienced with the HIs melt pre-reduction system which was a Circulating Fluidised Bed (CFB) which development was discontinued when a decision was made to focus purely on the core SRV furnace unit.

During the operation of the HIs melt pilot plant, it was shown that it is possible to smelt DRI of a high metallization. The problem is that the process requires a certain amount of material to reduce such that enough gases are given off by the reduction process. These evolved gases from the ore and coal eject molten slag and iron into the top transfer space that is vital to return the heat from the top-space to the bath.

A3 Off-gas Treatment

The off-gas needs to be treated before being vented so as not to have an impact on the surrounding environment. This essentially involves wet scrubbing the gas. As the gas has a significant amount of sensible heat, the off-gas can be used in a pre-heater. Alternatively a BOF hood[†] can be used to generate steam before the off-gas scrubber.

A4 Energy recovery and re-use

The scrubbed off-gas still has a significant amount of chemical energy. This can be used to power the Hot Blast stoves which in turn heats the air that is used within the SRV. The balance of the fuel gas then can be used for other requirements or used to generate electricity for export to the power grid.

[†] A BOF hood is a membrane cooler created by welding pipes together to form the wall of the cooler. The pipes then can be used to generate steam

B CD-Rom Contents

To assist in the dissemination of this research electronic copies of the files developed during this work have been placed on the CD-Rom attached to the inside back cover of this thesis. This appendix details the files within each of the folders or directories created on the CD-ROM.

Thesis

The Thesis folder contains the electronic version of this thesis.

Publications

The publications folders contains the various publications written during this research as listed in Table B.1.

Conference, Journal	Title
Iron & Steelmaker	Modeling of Freeze Layers and Refractory Wear in Direct Smelting Processes ¹³²
Fifth World Congress on Computational Mechanics	Computational Modelling of Reduction and Smelting Processes in the Primary Metals Industries ¹³³
61st Ironmaking Conference	Modelling of Freeze Layers and Refractory Wear in Direct Smelting Processes ¹³⁴
TMS Fall Extraction and Process Metallurgy Meeting: Computational Modeling of Materials, Minerals, and Metals.	Computational Modelling of Freeze Layers in Smelting Processes ¹³⁵
ECCOMAS CFD Conference 2001	Freeze Layers in Direct Smelting Processes ¹³⁶

Table B.1 – Publication List

Source Code

The source code directory contains the entire contents of the PHYSICA source directory. Of particular note is the code within the sub-directory “ref” which contains the code for the refractory wear mechanisms. The “user” sub-directory contains the various parts of user code required for setting up the physical properties and boundary conditions required.

Models

The various model directories (summarised in Table B.2) contain the inform* and geometry† files for the various models created during this project.

Directory	Model Description
brickstep	A step made out of refractory used to illustrate the wear mechanisms during development
indfurn	The induction furnace model
HRDF	The HIs melt pilot plant refractory wear model
Rotary	The rotary slag refractory wear test
Trunks	The model of slag accretions on the solids injection lances
Stave	The model applying the refractory wear mechanisms and freeze layer formation to the development plant.

Table B.2 – Summary of Models Included on the CD-ROM

* The inform file contains the setup information for a particular PHYSCIA run. The file selects the solution method required and supplies information on the physical properties and boundary conditions.

† The geometry file contains the way the computational domain is divided into control volumes along with information regarding what material and boundary patch number.

REFERENCES

- ¹ Brotzmann, K. (1987) New Concepts and Methods for Iron and Steel Production. 70th Steelmaking Conference Proceedings. 29 March - 1 April 1987. pp.3-12.
- ² Davis, M.P. et.al. (1998) Mathematical modelling tools for the optimisation of direct smelting processes. Applied Mathematical Modelling. 22(11):921-940.
- ³ Dry, R.J. and Bates, C.P. and Price, D.P. (1999) Hismelt - The Future in Direct Ironmaking. 58th Ironmaking Conference Proceedings. March 1999 Chicago.
- ⁴ Gurr, M. (1998) Hismelt - Development of the new Ironmaking Technology: A Refractories Perspective. the 18th Biennial International Conference of the Australian Ceramics Society. 28 - 30 September 1998 Melbourne, Australia
- ⁵ Bates, C.P. and Coad, A.J. (2000) Hismelt - the future in ironmaking technology. 4th European Coke and Ironmaking Congress. June 2000 Paris.
- ⁶ (2002) Public Environmental Review Document: Commercial Hismelt Plant, Kwinana Western Australia.
- ⁷ Lee, Y. and Nassaralla, C.L. (1999) Minimization of Hexavalent Chromium in Magnesite-Chrome Refractory. Metall. Mater. Trans. B. 28(5):855-859
- ⁸ Lee, Y. and Nassaralla, C.L. (1998) Formation of Hexavalent Chromium by Reaction between Slag and Magnesite-Chrome Refractory. Metall. Mater. Trans. B. 29(2):405-410
- ⁹ Croft, T.N. (1998) Unstructured Mesh - Finite Volume Algorithms for Swirling, Turbulent, Reacting Flows. PhD Thesis, the University of Greenwich.
- ¹⁰ Schwarz, M.P. (1996) Simulation of gas injection into liquid melts. Applied Mathematical Modelling. 20(1):41-51
- ¹¹ D.B. Spalding (1980) Numerical computation of multi-phase fluid flow and heat transfer. In: C. Taylor and K. Morgan. (Eds) Recent advances in numerical methods in fluids, Pineridge Press, Swansea. pp.139-168
- ¹² Campbell, A.P. and Dry, R.J. and Perazzelli, P.A. (1999) Coal and the Versatile Hismelt Process. Advanced Clean Coal Technology International Symposium. 1 - 2 November 1999 Tokyo, Japan.
- ¹³ Hardie, G.J. and Cross, M. and Batterham, R.J. and Davis, M.P. and Schwarz, M.P. (1992) The Role of Mathematical Modelling in the Development of the Hismelt Process. 10th Process Technology Conference Proceedings. 5 - 8 April 1992 Toronto, Canada. pp.109-121
- ¹⁴ Schwarz, M.P. and Musgrove, A.R. and Hooper, J.D. and Dang, P. (1992) Validation of Numerical Simulation of Gas Driven Bath Circulation by LDV Measurements. 10th Process Technology Conference Proceedings. 5 - 8 April 1992 Toronto, Canada. pp.123-132

- 15 Taylor, I.F. (1993) Gas blowthrough of liquid metal bath by an upward direct submerged jet. *ISIJ International*. 33(7):748-756
- 16 Moodie, J.P. and Davis, M.P. and Cross, M. (1988) Numerical Modelling for the Analysis of Direct Smelting Processes. 7th Process Technology Conference Proceedings. 17 - 20 April 1988 Toronto, Canada. pp.55-64
- 17 Varnas, S.R. and Truelove, J.S. (1995) Simulating radiative transfer in flash smelting furnaces. *Applied Mathematical Modelling*. 19(8):456-464
- 18 Viskanta, R. and Menguc, M.P. (1987) Radiation Heat Transfer in Combustion Systems. *Prog. Energy Combust. Sci.* 13:97-160
- 19 Hismelt Internal Memorandum Osborne, D. (1998) Slag Zone Cooler Design.
- 20 www.multi-physics.com
- 21 Lee, W.E. and Zhang, S. (1999) Melt corrosion of oxide and oxide-carbon refractories. *Int. Mat. Reviews*. 44(3):77-104
- 22 Banerjee, S. (1998) *Monolithic Refractories: a comprehensive handbook*. World Scientific Publishing Co., Singapore.
- 23 Fruehan, R.J. (1999) *The Making, Shaping and Treating of Steel: Ironmaking Volume*. 11th Ed. Iron & Steel Society, Warrendale, PA.
- 24 Buchebner, G. and Molinari, T. and Rumpf, D. (2000) Developing Basic High-Performance Products for Furnaces in the Nonferrous Metals Industries. *Journal of Metals*. 52(2):68-72
- 25 Bear, J. (1972) *Dynamics of Fluids in Porous Media*. Dover, New York.
- 26 Mukai, K. et.al. (2000) In-situ Observation of Slag Penetration into MgO Refractory. Sixth International Conference on Molten Slags, Fluxes and Salts. 12 - 17 June 2000 Stockholm, Sweden.
- 27 Kuromitsu, Y. et.al. (1997) Interaction between Alumina and Binary Glasses. *J. Am. Ceram. Soc.* 80(6):1583-1587
- 28 Yu, Z. and Mukai, K. and Kawasaki, K. and Furusato, I. (1993) Relation between Corrosion rate of Magnesia Refractories by Molten Slag and Penetration Rate of Slag into refractories. *J. Ceram. Soc. Jpn.* 101(5):533-539
- 29 Bradley, L. and Li, L. and Stott, F.H. (2000) Flame-assisted laser surface treatment of refractory materials for crack-free desulfurization. *Mat. Sci. Eng. A*. 278:204-212
- 30 Bradley, L. and Li, L. and Stott, F.H. (2000) Surface modification of alumina-based refractories using a xenon arc lamp. *Appl. Surf. Sci.* 154-155:675-681
- 31 Sandhage, K.H. and Yurek, G.J. (1988) Indirect Dissolution of Sapphire into Silicate Melts. *J. Am. Ceram. Soc.* 71(6):478-489
- 32 Sandhage, K.H. and Yurek, G.J. (1990) Direct and Indirect Dissolution of Sapphire in Calcia-Magnesia-Alumina-Silica Melts: Dissolution Kinetics. *J. Am. Ceram. Soc.* 73(12):3633-3642

- 33 Dunkl, M. and Bruckner, R. (1987) Corrosion of refractory material under the action of forced convection flow by means of the rotating cylinder face area at 1500°C. *Glass Science and Technology*. 60(8):261-267
- 34 Rehner, H.H. and Toma, N. (1991) Mathematical Modeling of the Corrosion Processes of Refractories by Glass Melts. EURO-CERAMICS II: Electroceramics and Ceramics for Special Applications. September 1991 Augsburg, Germany. pp.2621-2625
- 35 Chen, Z. and Wu, X. (1992) The Corrosion of MgO-CaO and Magnesite-Chrome Refractories by Steelmaking Slags. Proceedings of International Symposium on Refractories: refractory Raw Materials and High Performance Refractory Products. pp.505-517
- 36 Ichikawa, K. and Minato, K. and Horita, S. (1990) Corrosion Resistance of Magnesia-Chrome Bricks to Low Basicity Slag. *Taikabutsu Overseas*. 10(3):154-156
- 37 Cherepanov, A.M. and Popov, O.N. and Ginter, S.E. (1980) Corrosion-Resistant refractory based on Chromium-Oxide. *Glass and Ceramics*. 37(3):174-176
- 38 Bates, J.L. (1987) Heterogeneous Dissolution of Refractory Oxides in Molten Calcium-Aluminium Silicate. *J. Am. Ceram. Soc.* 70(3):C55-C57
- 39 Guha, J.P. (1997) Reaction chemistry in dissolution of polycrystalline alumina in lime-alumina-silica slag. *Br. Ceram. Trans.* 96(6):231-236
- 40 McCallum, N. and Barrett, L.R. (1952) Some Aspects of the Corrosion of Refractories. *Trans. Brit. Cer. Soc.* 51(11):523-548
- 41 Reed, L. and Barrett, L.R. (1955) The Slagging of Refractories. Part 1. The Controlling Mechanism in Refractory Corrosion. *Trans. Brit. Cer. Soc.* 54:671-676
- 42 Reed, L. and Barrett, L.R. (1964) The Slagging of Refractories Part 2. The Kinetics of Corrosion. *Trans. Brit. Cer. Soc.* 63(10):509-534
- 43 Zhang, S. and Rezaie, H.R. and Sarpoolaky, H. and Lee, W.E. (2000) Alumina Dissolution into Silicate Slag. *J. Am. Ceram. Soc.* 83(4):897-903
- 44 Lee, W.E. and Korgul, P. and Goto, K. and Wilson, D.R. (1996) Microstructural analysis of corrosion mechanisms in oxide-spinel steelmaking refractories. 35th Annual conference of metallurgists of CIM: Advances in refractories for the metallurgical industries II. August 1996, Montreal, Canada. pp.453-465
- 45 Coulson, J.M. et.al. (1999) *Chemical Engineering: Volume 1 - Fluid Flow, Heat Transfer and Mass Transfer*. 6th Ed. Butterworth-Heinemann, Oxford. p. 75
- 46 Flanagan, D.C. and Nearing, M.A. (1995) USDA - Water Erosion Prediction Document: Hillslope Profile and Watershed Model Documentation. USDA-ARS National Soil Erosion Laboratory, West Lafayette, Indiana.
- 47 Antwort: Hismelt Refractories. Email communication from Molinari, T. on the 15 May 2000.
- 48 ASTM standard C874-85: Standard Practice for Rotary Slag Testing of Refractory Materials
- 49 Kojo, I.V. and Jokilaakso, A. and Hanniala, P. (2000) Flash Smelting and Converting Furnaces: A 50 Year Retrospect. *Journal of Metals*. 52(2):57-61

- 50 Stephens, R.L. (2000) Vessel Integrity for High-temperature Metallurgical Processing. *Journal of Metals*. 52(2):56
- 51 Merry, J. and Sarvinis, J. and Voermann, N. (2000) Designing Modern Furnace Cooling Systems. *Journal of Metals*. 52(2):62-64
- 52 MacRae, A. and Wallgren, M. and Wasmund, B. and Lenz, J. and Majumdar, A. and Zuliani, P. and Elvestad, P. (1998) Converting Furnace Upgrades at the Kidd Creek Metallurgical Division Copper Smelter. *Sulfide Smelting '98: Current and Future Practices*. 14 - 19 February 1998 San Antonio, TX. pp.387-397
- 53 Voermann, N. and Ham, F. and Merry, J. and Veenstra, R. and Hutchinson, K. (1999) Furnace Cooling Design for Modern, High-Intensity Pyrometallurgical Processes. *Fourth International Conference Copper 99-Cobre 99*. 10 -13 October 1999 Phoenix, AZ. pp.573-582
- 54 Kyllö, A.K. and Gray, N.B. and Papazoglou, D. and Elliot, B.J. (2000) Developing Composite Furnace Module Cooling Systems. *Journal of Metals*. 52(2):66
- 55 Sampson, P. and Gibson, R.D. (1981) Solidification of a liquid metal flowing through a circular pipe: a prediction of nozzle blockage. *Adv. Eng. Software*. 3(1):17-25
- 56 Sampson, P. and Gibson, R.D. (1982) A Mathematical Model of Nozzle Blockage by Freezing - II. Turbulent Flow. *Int. J. Heat Mass Transfer*. 25(1):119-126
- 57 Hibbert, S.E. and Markatos, N.C. and Voller, V.R. (1988) Computer simulation of moving - interface, convective, phase - change processes. *Int. J. Heat Mass Transfer*. 31(9):1785-1795
- 58 Lazaridis, A. (1970) A Numerical Solution of the Multidimensional Solidification (or Melting) Problem. *Int. J. Heat Mass Transfer*. 13:1459-1477
- 59 Voller, V.R. and Prakash, C. (1987) A fixed grid numerical modelling methodology for convection - diffusion mushy region phase - change problems. *Int. J. Heat Mass Transfer*. 30(8):1709-1719
- 60 Schneider, M.C. and Beckermann, C. (1995) A numerical study of the combined effects of microsegregation, mushy zone permeability and flow, caused by volume contraction and thermosolutal convection, on macrosegregation and eutectic formation in binary alloy solidification. *Int. J. Heat Mass Transfer*. 38(18):3455-3473
- 61 Pericleous, K.A. and Chan, K.S. (1994) The SEA Method for Free Surface Problems with Heat Transfer and Change of Phase. *Numerical Methods in Multiphase Flows 1994 - 1994 ASME Fluids Engineering Division Summer Meeting*. June 1994 Lake Tahoe, NV. pp.227-236
- 62 Pericleous, K.A. et.al. (1996) Free surface Navier-Stokes flows with simultaneous heat transfer and solidification/melting. *Adv. Comp. Mathematics*. 6:295-308
- 63 Bounds, S.M. and Moran, G.J. and Pericleous, K.A. and Cross, M. and Croft, T.N. (2000) A Computational Model for Defect Prediction in Shape Castings Based on the Interaction of free Surface Flow, Heat Transfer, and Solidification Phenomena. *Metall. Mater. Trans. B*. 31:515-527
- 64 Kyllö, A.K. and Gray, N.B. (1995) GK Williams Centre Report: Accretion formation in Iron Bath Smelting.

- 65 Xu, C. and Sahai, Y. and Guthrie, R.I.L. (1984) Formation of Thermal Accretions In Submerged Gas Injection Processes. *Ironmaking & Steelmaking*. 11(2):101-107
- 66 Kylo, A.K. and Richards, G.G. (1996) Accretion growth on shrouded tuyeres. *Ironmaking & Steelmaking*. 23(5):416-424
- 67 Chen, E.S. and Buyukozturk, O. (1985) Thermomechanical Behaviour and Design of Refractory Linings for Slagging Gasifiers. *Am. Ceram. Soc. Bull.* 64(7):988-994
- 68 Fujiwara, A. and Fujino, M. and Shimomura, K. (1986) Mechanical and Crack Behaviour of Refractories under Constraint of Thermal Expansion. *Process Technology Proceedings - Fifth International Iron and Steel Congress*. pp.933-936
- 69 Chang, W.S. and Knight, C.E. and Hasselman, D.P.H. and Mitchiner, R.G. (1983) Analysis of Thermal Stress Failure of Segmented Thick-Walled Refractory Structures. *J. Am. Ceram. Soc.* 66(10):708-713
- 70 Bradley, F. and Chaklader, A.C.D. and Mitchell, A. (1987) Thermal Stress Fracture of Refractory Lining Components: Part I Thermoelastic Analysis. *Metallurgical Trans. B.* 18:355-363
- 71 Buyukozturk, O. and Tseng, T.M. (1982) Thermomechanical Behaviour of Refractory Concrete Linings. *J. Am. Ceram. Soc.* 65(6):301-307
- 72 Chen, E.S. and Buyukozturk, O. (1985) Methodology for Thermochemical Analysis of Brittle Systems. *Am. Ceram. Soc. Bull.* 64(7):982-988
- 73 Rubesa, D. (1999) Thermal Stress Fracture and Spalling of Well Blocks in Steel Ladels - Modelling and Numerical Simulation. *Veitsch-Radex Rundschau*. 2:3-24
- 74 Zhang, L. and Jahanshahi, S. (1998) Review and Modelling of Viscosity of Silicate Melts: Part I. Viscosity of Binary and Ternary Silicates Containing CaO, MgO and MnO. *Metall. Mater. Trans. B.* 29:177-186.
- 75 Zhang, L. and Jahanshahi, S. (1998) Review and Modelling of Viscosity of Silicate Melts: Part II. Viscosity of Melts Containing Iron Oxide in the CaO-MgO-MnO-FeO-Fe₂O₃-SiO₂ System. *Metall. Mater. Trans. B.* 29:187-195.
- 76 Zhang, L. and Jahanshahi, S. (2000) Modelling Viscosity of Alumina-containing Silicate Melts. *Sixth International Conference on Molten Slags, Fluxes and Salts*. 12 - 17 June 2000 Stockholm, Sweden.
- 77 Nexhip, C. and Sun, S. (2000) Rapid/Dynamic Wetting of Molten Slag Droplets on Refractory Surfaces. *Sixth International Conference on Molten Slags, Fluxes and Salts*. 12 - 17 June 2000 Stockholm, Sweden.
- 78 Zhang, J. and Shu, Q. and Wei, S. (2000) Prediction of Surface Tension in Molten Ionic Systems. *Sixth International Conference on Molten Slags, Fluxes and Salts*. 12 - 17 June 2000 Stockholm, Sweden.
- 79 Holtzer, M. and Retel, K. (2000) Effect of Temperature and Sulphur Content on the Surface Tension of Fe - C (3.9%) - Si (1.6%) Alloy. *Canadian Metallurgical Quarterly*. 39(3):339-344
- 80 Divakar, M. and Hajra, J.P. (1997) The effect of temperature on the surface tension and adsorption function of the Fe-S-O melts - an analysis based on interaction parameters. *Steel Res.* 68(10):417-423

- 81 Perry, R.H. and Green, D.W. and Maloney, J.O. (1997) Perry's Chemical Engineers' Handbook. 7th Ed. McGraw-Hill, New York. p.4-10
- 82 Davies, R.H. and Dinsdale, A.T. and Gisby, J.A. and Hodson, S.M. and Ball, R.G.J. (1994) Thermodynamic Modelling using MTDATA: A Description showing applications involving oxides, alloys and aqueous solutions. Applications of Thermodynamics in the Synthesis and Processing of Materials. 2 - 6 October 1994 Rosemont, IL. pp.371-384
- 83 Bale, C.W. and Eriksson, G. (1990) Metallurgical Thermochemical Databases - A Review. Canadian Metallurgical Quarterly. 29(2):105-132
- 84 www.npl.co.uk/mtdata
- 85 www.crct.polymtl.ca/fact/fact.htm
- 86 Pelton, A.D. (1997) 'Solution models' in Advanced Physical Chemistry for Process Metallurgy. Academic Press pp.85-117.
- 87 Patankar, S.V. (1980) Numerical Heat Transfer and Fluid Flow. Hemisphere Publishing Corporation, Singapore.
- 88 Versteeg, H.K. and Malalasekera, W. (1995) An Introduction to Computational Fluid Dynamics: The Finite Volume Method. Longman, Essex, England.
- 89 Stroud, K.A. (1996) Further Engineering Mathematics. 3rd Ed. Palgrave, Houndmills Basingsoke, UK.
- 90 Rhie, C.M. and Chow, W.L. (1983) Numerical Study of the Turbulent Flow Past an Airfoil with Trailing Edge Separation. AIAA J. 21(11):1525-1532
- 91 Patel, M.K. and Markatos, N.C. (1986) An Evaluation of Eight Discretization Schemes for Two-Dimensional Convection-Diffusion Equations. Int. J. Numer. Methods Fluids. 6:129-154
- 92 Leonard, B.P. (1979) A Stable and Accurate Convective Modelling Procedure Based on Quadratic Upstream Interpolation. Comput. Methods Appl. Mech. Eng. 19:59-98
- 93 Pollard, A. and Siu, A.L.W. (1982) The Calculation of some Laminar Flows using Various Discretisation Schemes. Comput. Methods Appl. Mech. Eng. 35:293-313
- 94 Gaskell, P.H. and Lau, A.K.C. (1988) Curvature-Compensated Convective Transport: SMART, A New Boundless Preserving Transport Algorithm. Int. J. Numer. Methods Fluids. 8:617-641
- 95 Van Leer, B. (1977) Towards the Ultimate Conservative Difference Scheme. IV. A New Approach to Numerical Convection. J. Comput. Phys. 23:276-299
- 96 Van Leer, B. (1973) Towards the Ultimate Conservative Difference Scheme. I. The Quest of Monotonicity. Lecture Notes in Physics. 18:163-168
- 97 Van Leer, B. (1974) Towards the Ultimate Conservative Difference Scheme. II. Monotonicity and Conservation Combined in a Second-Order Scheme. J. Comput. Phys. 14:361-370
- 98 Van Leer, B. (1977) Towards the Ultimate Conservative Difference Scheme. III. Upstream-Centred Finite-Difference Schemes for Ideal Compressible Flow. J. Comput. Phys. 23:263-275

- 99 Van Leer, B. (1979) Towards the Ultimate Conservative Difference Scheme. V. A Second-Order Sequel to Godunov's Method. *J. Comput. Phys.* 32:101-136
- 100 Vetterling, W.T. et.al. (1985) Numerical Recipes Example Book (FORTRAN). Cambridge University Press, Cambridge. p. 829
- 101 Vetterling, W.T. et.al. (1985) Numerical Recipes Example Book (FORTRAN). Cambridge University Press, Cambridge. p. 846
- 102 Doormaal, J.P. and Raithby, G.D. (1984) Enhancements of the SIMPLE Method for Predicting Incompressible Fluid Flows. *Numerical Heat Transfer.* 7:147-163
- 103 Jun, L. and Spalding, D.B. (1988) Numerical Simulation of Flows with Moving Interfaces. *PhysicoChemical hydrodynamics.* 10(5/6):625-637
- 104 Pericleous, K.A. and Chan, K.S. and Cross, M. (1995) Free Surface Flow and Heat Transfer in Cavities: The SEA Algorithm. *Numer. Heat Transfer B.* 27:487-507
- 105 Ramshaw, J.D. and Trapp, J.A. (1976) A Numerical Technique for Low-Speed Homogeneous Two-Phase Flow with Sharp Interfaces. *J. Comput. Phys.* 21:438-453
- 106 Hirt, C.W. and Nichols, B.D. (1981) Volume of Fluid (VOF) Method for the Dynamics of Free Boundaries. *J. Comput. Phys.* 39:201-225
- 107 Voller, V.R. and Swaminathan, C.R. (1991) General Source-based Method for Solidification Phase Change. *Numer. Heat Transfer B.* 19:175-189
- 108 Croft, T.N. (2002) PHYSICA Version 2.12 Theory Manual. the University of Greenwich, London, UK.
- 109 Levenspiel, O. (1972) Chemical Reaction Engineering. 2nd Ed. John Wiley & Sons, New York.
- 110 Nield, D.A. and Bejan, A. (1999) Convection in Porous Media. 2nd Ed. Springer-Verlag, New York.
- 111 Incropera, F.P. and DeWitt, D.P. (1996) Fundamentals of Heat and Mass Transfer. 4th Ed. John Wiley & Sons, New York. pp. 839
- 112 Incropera, F.P. and DeWitt, D.P. (1996) Fundamentals of Heat and Mass Transfer. 4th Ed. John Wiley & Sons, New York. pp. 829.
- 113 Low Cement Castables with Spinel. Email communication from Cardarelli, F. on the 17 January 2002.
- 114 Incropera, F.P. and DeWitt, D.P. (1996) Fundamentals of Heat and Mass Transfer. 4th Ed. John Wiley & Sons, New York. pp. 837
- 115 Fruehan, R.J. (1999) The Making, Shaping and Treating of Steel: Steelmaking Volume. 11th Ed. Iron & Steel Society, Warrendale, PA. pp. 102
- 116 Incropera, F.P. and DeWitt, D.P. (1996) Fundamentals of Heat and Mass Transfer. 4th Ed. John Wiley & Sons, New York. pp. 838
- 117 Antwort: Ankrom Refractory Question. Email communication from Molinari, T. on the 20 September 2000.
- 118 <http://www.unige.ch/sciences/chifi/cpb/windig.html>
- 119 Email Communication from Carolyn McCarthy 31 May 2001

- 120 Personal communication with Mark Davis February 2002
- 121 Incropera, F.P. and DeWitt, D.P. (1996) *Fundamentals of Heat and Mass Transfer*. 4th Ed. John Wiley & Sons, New York. p. 445.
- 122 Email Communication from Carolyn McCarthy 20 June 2001
- 123 Personal Communication from Matt Gurr, Hismelt 9 March 2001.
- 124 Personal Communication from Matt Gurr, Hismelt 9 March 2001
- 125 Personal Communication from Mark Davis, Rio Tinto Technical Services Perth. 15 May 2002
- 126 Refractory Wear Information. Email communication from Cardarelli, F. on the 3 June 2002.
- 127 Gurr, M. (1998) Vessel Refractory Condition - Campaign 8-2. Hismelt Internal Memorandum
- 128 Cao, Y. and Gao, M. (2000) Wickless network heat pipes for high heat flux spreading applications. *Int. J. Heat Mass Transfer*. 45:2539-2547
- 129 Zhang, N. (2001) Innovative Heat Pipe Systems using a new Working Fluid. *International Communications in Heat and Mass Transfer*. 28(8):1025-1033
- 130 Feinman, J. and Mac Rae, D.R. eds. (1999) *Direct Reduced Iron: Technology and Economics of production and Use*. Iron and Steel Society, Warrendale, PA.
- 131 Von Bitter, R.W. et.al. (1999) Experiences with two new fine ore reduction processes - Circored and Circofer. METEC Congress 99. 13 - 15 June 1999 Dusseldorf, Germany.
- 132 Campbell, A.P. and Pericleous, K.A. and Cross, M. (2002) Modeling of Freeze Layers and Refractory Wear in Direct Smelting Processes. *Iron & Steelmaker*. 29(9):41-45
- 133 Cross, M. and Campbell, A.P. and Croft, T.N. and Pericleous, K.A. and Williams, A.J. (2002) Computational Modelling of Reduction and Smelting Processes in the Primary Metals Industries. Fifth World Congress on Computational Mechanics. 7 - 12 July 2002 Vienna, Austria.
- 134 Campbell, A.P. and Pericleous, K.A. and Cross, M. (2002) Modelling of Freeze Layers and Refractory Wear in Direct Smelting Processes. 61st Ironmaking Conference Proceedings. 10 - 13 March 2002 Nashville, Tennessee. pp.471-491
- 135 Campbell, A.P. and Pericleous, K.A. and Cross, M. (2001) Computational Modelling of Freeze Layers in Smelting Processes. 2001 TMS FALL EXTRACTION AND PROCESS METALLURGY MEETING: Computational Modeling of Materials, Minerals, and Metals. 23 - 26 September 2001 San Diego, California. pp.347-356
- 136 Campbell, A.P. (2001) Freeze Layers in Direct Smelting Processes. European Congress on Computational Methods in Applied Sciences and Engineering ECCOMAS CFD Conference 2001. 4-7 September 2001 Swansea, Wales, UK.